

**Development and Application of Advanced  
Fluorescence Microscopy Techniques for the  
Investigation of Inflammatory Processes**

**Dissertation**

zur Erlangung des Grades eines  
'Doctor rerum naturalium (Dr. rer. nat.)' der Fachbereiche:  
08 - Physik, Mathematik und Informatik,  
09 - Chemie, Pharmazie und Geowissenschaften,  
10 - Biologie,  
Universitätsmedizin  
der Johannes Gutenberg-Universität

verfasst und vorgelegt von  
Jan Neumann

Geb. 16.03.1988  
in Cottbus

Max Planck Graduate Center mit der Johannes Gutenberg-Universität  
Mainz  
angefertigt am Max-Planck-Institut für Chemie

Mainz, 2018



1. Berichterstatter:

2. Berichterstatter:

Tag der mündlichen Prüfung: 17.10.2018

I hereby declare that I wrote the dissertation submitted without any unauthorized external assistance and used only sources acknowledged in the work. All textual passages which are appropriated verbatim or paraphrased from published and unpublished texts as well as all information obtained from oral sources are duly indicated and listed in accordance with bibliographical rules. In carrying out this research, I complied with the rules of standard scientific practice as formulated in the statutes of Johannes Gutenberg-University Mainz to insure standard scientific practice.

## Abstract

The innate immune system is the first barrier against pathogens and induces fast immune responses. Hereby the Toll-like receptor 4 (TLR4) plays a key role by detecting damage- and pathogen-associated molecular patterns (DAMPs, PAMPs) like lipopolysaccharides (LPS), an outer cell wall component of gram-negative bacteria. Activation of TLR4 leads to a nuclear factor kappa-light-chain-enhancer of activated B cells (NF- $\kappa$ B) dependent signal transduction into the cell nucleus. TLR4 can be activated not only by LPS, but also by amylase trypsin inhibitors (ATI). ATI comprise a family of small proteins that are associated with gluten containing grains like wheat, barley or rice. Consumption of food containing ATI can therefore cause intestinal inflammation. Studies that microscopically investigate the effect of ATI on the molecules involved in the TLR4 signaling pathway are limited.

In this study, single molecule localization microscopy (SMLM) and high-content screening microscopy (HCS) were used to study both, the membrane distribution of TLR4 and the translocation of NF- $\kappa$ B into the cell nucleus in primary human macrophages after ATI or LPS stimulation. To investigate the membrane distribution of TLR4 below the optical diffraction limit, a SMLM microscope was constructed during this thesis and algorithms for quantitative evaluation of the measured distribution of TLR4 molecules were implemented.

SMLM microscopy revealed that more than 60 % of TLR4 molecules are part of a cluster, with diameters between 46 nm to 57 nm. Upon stimulation with ATI or LPS a tendency towards the formation of smaller and less dense clusters was observed. At the same time, the percentage of molecules that are part of a cluster increased. These results suggest that TLR4 molecules are recruited into specific domains consisting of monomers or lower order oligomers, which indicates the formation of signaling platforms. In addition, the use of HCS microscopy showed that ATI treatment induces the translocation of NF- $\kappa$ B into the cell nucleus. Quantitative differences in the response between the individual donors were observed. Together, the results show a comparable influence of ATI on both the supramolecular distribution of TLR4 and the translocation of NF- $\kappa$ B into the cell nucleus, as observed for LPS. In addition, the algorithms implemented for evaluating the membrane distribution of TLR4 will be helpful in future experiments for quantifying SMLM data with high signal densities and a large number of samples.

## Zusammenfassung

Das angeborene Immunsystem spielt eine wichtige Rolle, indem es eindringende Krankheitserreger erkennt und zu einer schnellen Immunreaktion führt. Der Toll-like Rezeptor 4 (TLR4) erkennt schaden- und pathogen-assoziierte molekulare Muster (DAMP, PAMP) wie zum Beispiel Lipopolysaccharide (LPS), welches ein Hauptbestandteil der äußeren Zellwand von gramnegativen Bakterien ist. Die Aktivierung von TLR4 führt zu einer NF- $\kappa$ B abhängigen Signalübertragung in den Zellkern. Dabei kann die Aktivierung von TLR4 nicht nur durch LPS erfolgen, sondern auch durch Amylase-Trypsin-Inhibitoren (ATI). ATI sind eine Proteinfamilie, die in glutenhaltigem Getreide wie Weizen, Gerste oder Reis vorkommen. Der Verzehr von ATI-haltigen Lebensmitteln kann daher Darmentzündungen verursachen. Nur wenige mikroskopische Studien haben sich bisher mit ATI induzierter TLR4 Aktivierung und die an der Signaltransduktion beteiligten Moleküle befasst.

In dieser Studie wurden Einzelmolekül-Lokalisationsmikroskopie (SMLM) und High-Content-Screening-Mikroskopie (HCS) verwendet, um sowohl die Membranverteilung von TLR4, als auch die Translokation von NF- $\kappa$ B in den Zellkern, auf primären menschlichen Makrophagen nach ATI- und LPS-Stimulation zu untersuchen. Um die Membranverteilung von TLR4 unterhalb der optischen Beugungsgrenze zu untersuchen, wurde im Rahmen dieser Arbeit ein SMLM-Mikroskop konstruiert und Algorithmen zur quantitativen Auswertung der gemessenen Verteilung von TLR4-Molekülen implementiert.

Mittels SMLM-Mikroskopie konnte gezeigt werden, dass mehr als 60 % der TLR4 Moleküle Teil eines Rezeptorclusters sind. Die Cluster wiesen einen Durchmesser von 46 nm bis 57 nm auf. Stimulierung mit ATI und LPS führte dazu, dass eine Tendenz zur Bildung von kleineren und weniger dichten Clustern zu beobachten war. Gleichzeitig stieg der Anteil der Moleküle, die Teil eines Clusters sind. Diese Resultate deuten darauf hin, dass TLR4-Moleküle in bestimmte Domänen rekrutiert werden, die aus Monomeren oder Oligomeren niedriger Ordnung bestehen, was eine Bildung von Signalplattformen nahelegt. Ergänzend konnte durch die Benutzung der HCS-Mikroskopie gezeigt werden, dass ATI Stimulation im weiteren Signalverlauf die Translokation von NF- $\kappa$ B in den Zellkern induziert. Dabei konnten quantitative Unterschiede in der Reaktion zwischen den einzelnen Spendern beobachtet werden.

Zusammengefasst zeigen die Resultate einen vergleichbaren Einfluss von ATI, sowohl auf die supramolekulare Verteilung von TLR4 als auch auf die Translokation von NF- $\kappa$ B in den Zellkern, wie es auch für LPS beobachtet wurde. Darüber hinaus werden die implementierten Algorithmen, welche zur Auswertung der Membranverteilung von TLR4 benutzt wurden, in zukünftigen Experimenten helfen, SMLM Daten mit hohen Signaldichten und einer großen Probenanzahl auszuwerten.



# Contents

<b>1</b>	<b>Introduction</b>	<b>1</b>
1.1	Inflammatory Processes . . . . .	1
1.2	Microscopy Techniques . . . . .	2
1.3	Research Objectives . . . . .	5
<b>2</b>	<b>Results</b>	<b>6</b>
2.1	Overview . . . . .	6
2.2	Individual Studies . . . . .	7
2.2.1	Conversion of a Confocal Laser Scanning Microscope into a Single Molecule Localization Microscope . . . . .	7
2.2.2	Integrated Localization Environment (ILE): A Software Package to Evaluate and Process Blinking Based Single Molecule Localization Microscopy Data . . . . .	7
2.2.3	Integrated Localization Analyzer for Nanoscale Distributions (ILAND): A Software Package for Spatial Point Pattern Analysis of Localization Microscopy Data . . . . .	7
2.2.4	Membrane Distribution of TLR4 in Primary Human Macrophages after Stimulation with ATI or LPS using Localization Microscopy . . . . .	8
2.2.5	Nitration of Wheat Amylase Trypsin Inhibitors Increases their Innate and Adaptive Immunostimulatory Potential <i>in vitro</i> . . . . .	8
<b>3</b>	<b>Conclusions and Outlook</b>	<b>9</b>
3.1	Localization Microscope and Software Packages . . . . .	9
3.2	TLR4 Signaling Pathway . . . . .	9
<b>A</b>	<b>References</b>	<b>11</b>
<b>B</b>	<b>Abbreviations</b>	<b>18</b>
<b>C</b>	<b>Personal List of Publications</b>	<b>19</b>
<b>D</b>	<b>Individual Studies</b>	<b>22</b>
D.1	Neumann <i>et al.</i> , in preparation, 2018 . . . . .	23
D.2	Neumann <i>et al.</i> , to be submitted, 2018 . . . . .	54
D.3	Neumann <i>et al.</i> , in preparation, 2018 . . . . .	78
D.4	Neumann <i>et al.</i> , to be submitted, 2018 . . . . .	117
D.5	Ziegler <i>et al.</i> , submitted, 2018 . . . . .	151



# 1 Introduction

## 1.1 Inflammatory Processes

The human body is continuously exposed to pathogens such as fungi, bacteria or viruses which constitute potential health hazards. Further environmental factors like chemicals or ionizing radiation steadily challenge the homeostasis of human health. To counteract this, there are in the first place physical barriers of the body, such as the skin or the mucous membranes of lung and gut. If these barriers are penetrated, innate and adaptive immune reactions will be induced to protect the body from invaders. Adaptive immune reactions are characterized as late reactions which are adapted and expanded throughout life. In these reactions, B cells, antibodies and cytotoxic T cells develop a highly specific immune response over time. In contrast to this, innate immune reactions happen immediately and are directed against damage- and pathogen-associated molecular patterns (DAMPs, PAMPs). Detection of these molecular patterns is performed by so-called pattern recognition receptors (PRRs). The family of the PRRs play a central role in innate immunity, wherein Toll-like receptor 4 (TLR4) is the most intensive studied (Moresco et al. 2011; Kawasaki et al. 2014). TLR4 is a transmembrane receptor and is not only expressed by cells of the immune system but also by different non-immune cells i.e. epithelial cells and fibroblasts. TLR4 plays a key role in the recognition of lipopolysaccharides (LPS), an outer cell wall component of gram-negative bacteria (Chow et al. 1999; Beutler et al. 2001). Several molecules are involved to facilitate the recognition of LPS by TLR4. The process starts with lipopolysaccharide binding protein (LBP), which transports LPS to the co-receptor cluster of differentiation 14 (CD14). CD14 in turn transports LPS to myeloid differentiation protein-2 (MD-2), which forms a heterodimer with TLR4 (da Silva Correia et al. 2001; Gioannini et al. 2004; Park et al. 2009). Dimerization of the TLR4/MD-2 complex together with LPS causes a change in receptor conformation and a signal transfer through the cell membrane into the cytoplasm.

The dimerization of TLR4 leads to activation of two different downstream signaling cascades by the recruitment of specific intracellular adaptor molecules - myeloid differentiation primary response 88 (MyD88) and TIR-domain-containing adapter-inducing interferon- $\beta$  (TRIF). The MyD88 dependent signaling pathway leads to the activation and subsequent translocation of the transcription factor nuclear factor kappa-light-chain-enhancer of activated B cells (NF- $\kappa$ B) from the cytoplasm into the cell nucleus. Subsequently, relevant cytokines like interleukins (IL-1, IL-6, IL-8) and tumor necrosis factor alpha (TNF $\alpha$ ) are transcribed and released by the cell, which attracts further immune cells. In parallel, increased amounts of reactive oxygen and nitrogen species (ROS/RNS) are produced by the cell. The purpose of these highly reactive molecules

is to destroy the harmful pathogens, but they may also cause damage in the surrounding tissue by oxidation processes. Some in these way modified molecules have the ability to stimulate TLR4 and other pattern recognition receptors. They are part of a class of molecules which are summarized as DAMPs. DAMPs in turn can contribute to a feedback loop of inflammation (Lucas et al. 2013). Furthermore, the released cytokines can activate other membrane receptors such as interleukin-1 receptor (IL-1R) and tumor necrosis factor receptor 1 (TNFR1), whose signaling pathways in turn lead to the activation of NF- $\kappa$ B (Verstrepen et al. 2008; Lee et al. 2009). Overall, the TLR4 receptor plays a decisive role in the recognition and transmission of inflammatory agents. It is associated with various diseases such as chronic obstructive pulmonary disease (COPD), Parkinson's disease or Alzheimer's disease (MacRedmond et al. 2007; Walter et al. 2007; Panaro et al. 2008).

Inflammation can also be caused by nutritional compounds. Amylase trypsin inhibitors (ATI) are a family of proteins related to gluten containing grains like wheat, rye or barley (Zevallos et al. 2017). Notably they can bind and activate TLR4 directly, thereby causing intra- and extraintestinal inflammation (Junker et al. 2012).

In addition to the various activators of TLR4, differences in their source and chemical composition can have a distinct influence on the agonistic properties and thus the downstream signaling pathway (Płóciennikowska et al. 2014; Zeuner et al. 2016; Krüger et al. 2017). Moreover, environmental factors that lead to the nitration of proteins may have an influence on their immunogenicity (Franze et al. 2005; Gruijthuijsen et al. 2006; Reinmuth-Selzle et al. 2017).

Studies elucidating the effect of ATI and nitrated ATI on molecules involved in the TLR4 signaling pathway are mostly based on molecular biological techniques, thus providing limited information on the structural level. Therefore, different microscopy techniques have been applied to gain insight into the aforementioned processes.

## 1.2 Microscopy Techniques

Microscopy allows to resolve and observe biological processes, which are below the resolution of the human eye. Structural changes can be related to functional differences and vice versa. Starting from conventional bright field microscopy, various methods have been developed to increase the contrast and make specific structures and processes visible. These include fluorescence microscopy methods such as confocal laser scanning microscopy (CLSM), multi-photon microscopy (MPM) (Denk et al. 1990) or light sheet fluorescence microscopy (LSFM) (Voie et al. 1993; Huisken et al. 2004). Despite the different fluorescence microscopy techniques, the sample preparation is based on the specific coupling of emitters to the target structure. The labeling techniques can be divided into three groups: (i) transfection with a fluorescent fusion protein coupled to the target protein, (ii) fluorescent dyes that bind directly to the target structure or, (iii) that are attached to a linker such as an antibody or DNA strand, which then binds to the target structure. The selected method depends on the target structure and whether measurements are to be carried out on living or fixed

specimens. Furthermore, it determines the accuracy with which the target structures can be localized.

In addition to the contrast and visualization of specific structures, the resolution of the microscopy system plays an important role. Due to the diffraction-limitation of optics, resolution of conventional far-field fluorescence microscopy is limited to about 200 nm (Abbe 1873; Rayleigh 1896). Other techniques such as electron microscopy, X-ray microscopy, atomic force microscopy (AFM) or optical near-field microscopy exist (for review on resolution enhancement techniques see Cremer et al. 2013), which can resolve structures down to the molecular range, but with the disadvantage of a relative harsh sample preparation and imaging environment as well as the need of a complex instrumentation in contrast to conventional light microscopy techniques. This may lead to additional artifacts and makes live-cell imaging challenging, which is contrary to the aim to examine the biological object in a natural state. To circumvent those limitations several so called super-resolution microscopy techniques like stimulated emission depletion (STED) microscopy (Hell et al. 1994), structured illumination microscopy (SIM) (Heintzmann et al. 1999; Gustafsson 2000) and single molecule localization microscopy (SMLM) (Lidke et al. 2005; Betzig et al. 2006; Hess et al. 2006; Rust et al. 2006; Sharonov et al. 2006; Heilemann et al. 2008; Lemmer et al. 2008; Jungmann et al. 2010) have been developed.

Unlike the other methods mentioned above, SMLM is based on the detection of single molecules i.e. point-like emitters. The basic concept of blinking-based SMLM is (i) the detection of optically isolated signals and (ii) the determination of their position with a precision of a few nanometers (Figure 1.1). Optically isolation can be achieved by separating the emitters spatially and temporally and thus imaging only a subset of the emitters at any given time. This is usually done by switching fluorophores between two different spectral states - a dark state and a fluorescent state, or by transient binding of fluorophores to the target structure, which is accompanied by an increase in fluorescence emission (Jungmann et al. 2010; Szczurek et al. 2017). Subsequent detection and determination of the molecule positions is normally done by computer algorithms (Small et al. 2014; Deschout et al. 2014). In contrast to conventional fluorescence microscopy techniques, in which an image is directly obtained and further quantification is image-based, SMLM results in a list containing the coordinates of the detected signals. The list can be used to reconstruct an image (Baddeley et al. 2010; Nieuwenhuizen et al. 2014), but more importantly, it allows to perform coordinate-based quantification, which makes it possible to derive changes in the distribution of the target structure at the single molecule level (Sengupta et al. 2011; Sengupta et al. 2012; Veatch et al. 2012; Sengupta et al. 2013; Levet et al. 2015; Rubin-Delanchy et al. 2015; Mazouchi et al. 2016; Griffié et al. 2016; Andronov et al. 2016; Andronov et al. 2018).

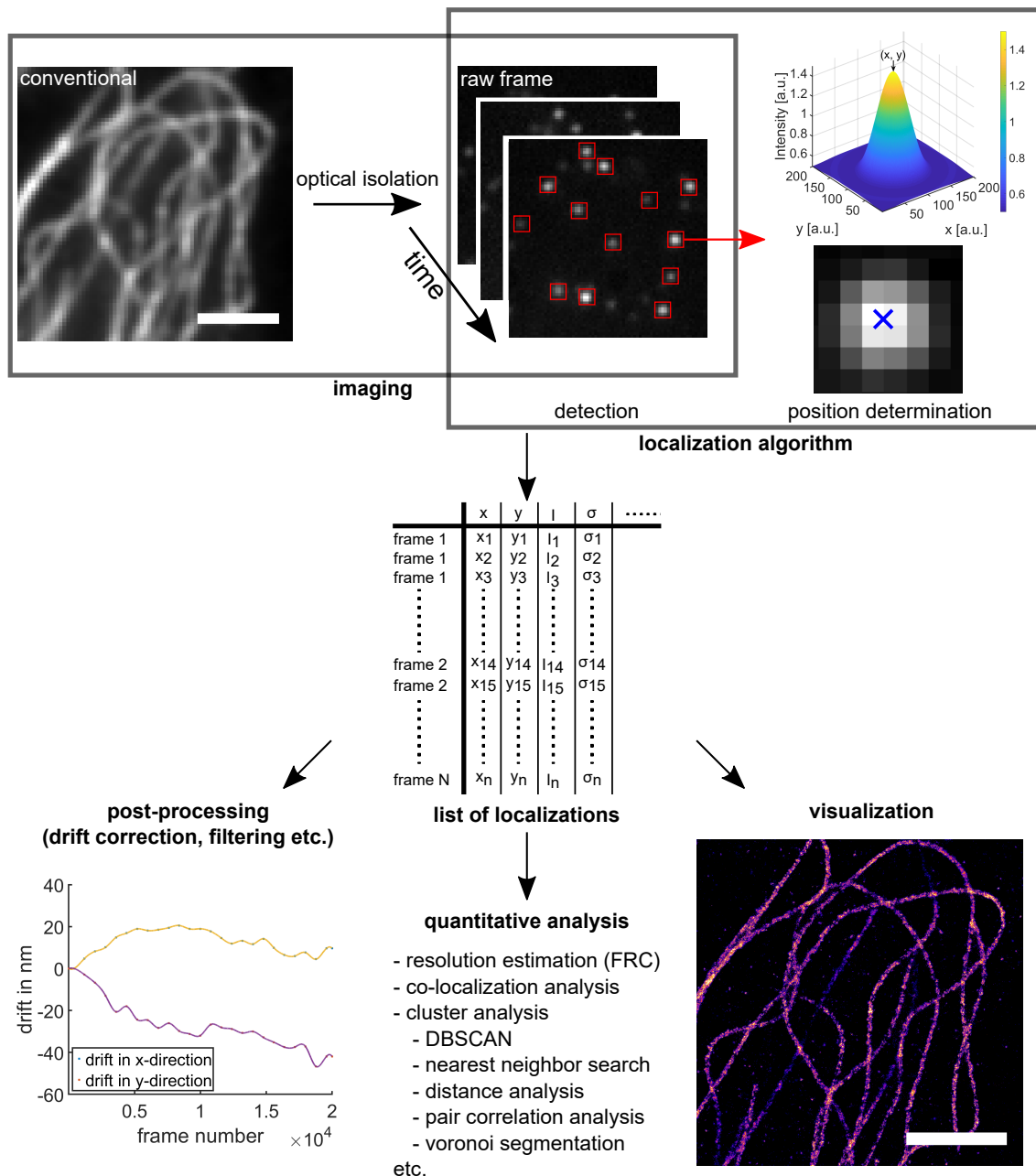


Figure 1.1: **Workflow of single molecule localization microscopy.** In a first step spatially and temporally isolated single molecule signals are imaged. Next, these signals are detected using computer algorithms and their position is determined with a precision of a few nanometers. The position coordinates of every detected molecule are collected in a list. The entries of the list can be used to perform post-processing steps such as filtering the data according to certain criteria or correcting the sample drift, which may occurred during the measurement. Furthermore, the information contained in the list can be used to generate the super-resolution image. The list of localizations is also starting point for further quantitative analysis like co-localization or cluster analysis. Scale bar = 2  $\mu\text{m}$ .

## 1.3 Research Objectives

Common molecular biology techniques such as enzyme-linked immunosorbent assay (ELISA), western blot or polymerase chain reaction (PCR) are restricted by providing information at a functional level only. Light microscopy overcomes this limitation by additionally making structural processes and changes visible down to the single cell and even single molecule level. Since structure and function are related to each other, the combination of light microscopy and classical molecular biology techniques allows one to examine their interplay.

Therefore, the main points of this PhD project were (i) to build a SMLM microscope, (ii) to implement algorithms for further data analysis and (iii) to apply these to investigate the distribution of TLR4 and NF- $\kappa$ B with regard to the effects of both inflammatory and anti-inflammatory compounds. The detailed objectives of the work were:

1. *Conversion of a confocal laser scanning microscope into a SMLM microscope.* Considering the planned applications such as the imaging of membrane receptors or transcription factors, the microscope should be capable to be operated in highly inclined and laminated optical sheet (HILO) or total internal reflection fluorescence (TIRF) mode in addition to epi-illumination. Furthermore, astigmatism-based localization microscopy should be implemented to obtain three-dimensional information about the distribution of single molecule signals (Huang et al. 2008).
2. *Development and implementation of algorithms for quantitative evaluation of SMLM data.* Current advanced microscopy techniques such as high-content screening (HCS) microscopy or SMLM make it possible to image thousands to millions of cells or molecules. Especially in SMLM, a limited number of fast and efficient algorithms are available for extracting quantitative information and analyzing the point distribution.
3. *Measurement and quantification of the membrane distribution of TLR4 using the custom-built SMLM and the implemented evaluation algorithms.* The main focus is on the influence of LPS, ATI and nitrated ATI on the membrane distribution of TLR4 in immune cells. Changes in the distribution of TLR4 could indicate increased signaling and thus an increased immune response.
4. *HCS fluorescence microscopy of the transcription factor NF- $\kappa$ B.* A simple and rapid method should be established to image and quantify the translocation of NF- $\kappa$ B into the cell nucleus. The nuclear translocation of NF- $\kappa$ B should be measured at the single cell level depending on different compounds, which allows conclusions to be drawn on their inflammatory or anti-inflammatory potential. This included compounds such as ATI and nitrated ATI, as well as certain herbal extracts such as cinnamon.

## 2 Results

### 2.1 Overview

The individual studies of the PhD project are summarized in the following pages. A graphical overview of the studies and their connections is shown in Figure 2.1. Detailed information on the studies can be found in Appendix D.

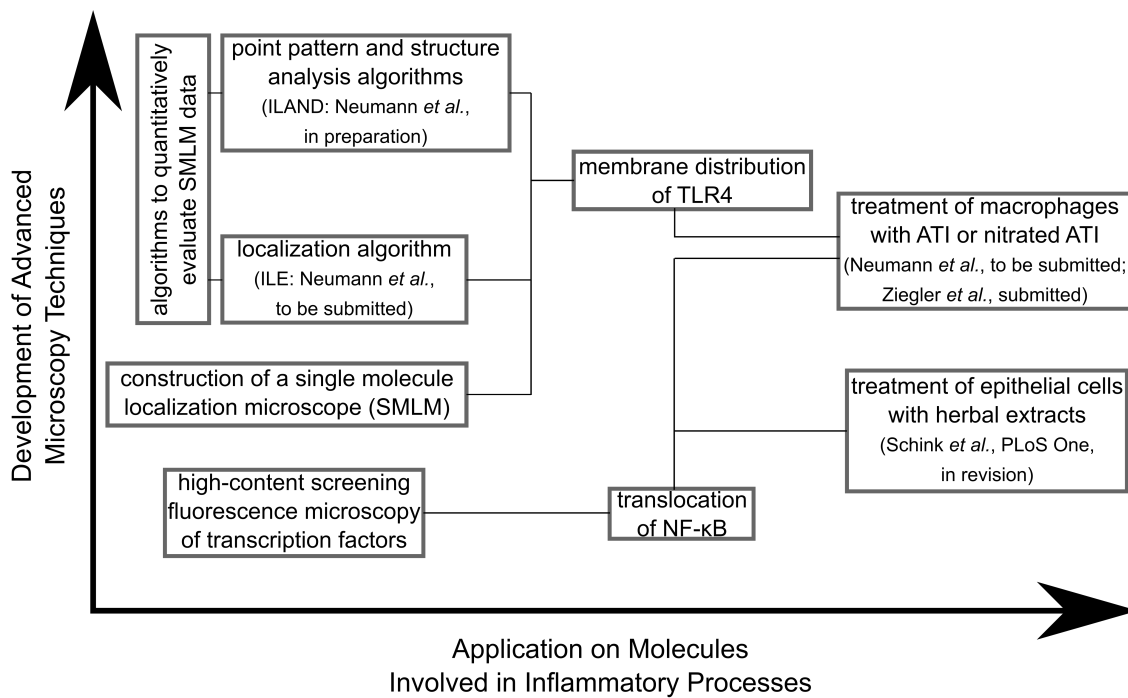


Figure 2.1: **Graphical overview of the PhD project.** The PhD project consisted of the development of advanced microscopy techniques on the one hand and their application on molecules involved in inflammatory processes on the other hand. The boxes represent the individual projects and methods used. The lines show the connection between the projects. Abbreviations: ILE: Integrated Localization Environment; ILAND: Integrated Localization Analyzer for Nanoscale Distributions.

## **2.2 Individual Studies**

### **2.2.1 Conversion of a Confocal Laser Scanning Microscope into a Single Molecule Localization Microscope**

In this project a confocal laser scanning microscope was converted into a single molecule localization microscope. The confocal microscope has been equipped with components and optics necessary for SMLM. Two lasers have been externally coupled into the back port of the microscope and an external setup allows switching between conventional widefield illumination and a localization mode. Furthermore, it allows measurements under epi-, TIRF- and HILO-illumination and is equipped with a weak cylindrical lens for astigmatism-based 3D localization microscopy (Huang et al. 2008). The performance of the custom-built SMLM was evaluated using fluorescent beads, DNA-PAINT nanorulers and microtubule. For details see Appendix D.1.

### **2.2.2 Integrated Localization Environment (ILE): A Software Package to Evaluate and Process Blinking Based Single Molecule Localization Microscopy Data**

With ILE a software package was developed to determine and visualize the position of single molecule signals in raw SMLM data. ILE uses fastSPDM (Grüll et al. 2011) as localization algorithm, which was further developed and extended with post-processing routines such as filtering and drift correction as well as several visualization routines. We demonstrate the performance of ILE on different biological structures comprising different levels of background and emitter densities. Furthermore, we show that ILE with its focus on simple user guidance has a similar execution time as other commonly used localization algorithms. For details see Appendix D.2.

### **2.2.3 Integrated Localization Analyzer for Nanoscale Distributions (ILAND): A Software Package for Spatial Point Pattern Analysis of Localization Microscopy Data**

A software package was developed to evaluate the spatial distribution and the resulting structure of single molecule localizations quantitatively. It includes algorithms for distance and cluster analysis like density-based spatial clustering of applications with noise (DBSCAN, Ester et al. 1996), Ripley's function or radial density function as well as algorithms to analyze chromatin compaction. The software package has been specifically developed to work with data sets containing several million detected single molecule signals in a computational and memory efficient manner. The software package and its application to investigations of the structure of the cell nucleus and the distribution of proteins, such as transcription factors or membrane proteins, shall be soon published. For details see Appendix D.3.

## **2.2.4 Membrane Distribution of TLR4 in Primary Human Macrophages after Stimulation with ATI or LPS using Localization Microscopy**

Localization microscopy was used to determine the membrane distribution of TLR4 in primary human macrophages upon stimulation with ATI, nitrated ATI or LPS. We show that TLR4 is not randomly distributed in the cell membrane and that more than 60 % of TLR4 molecules are located in clusters. The diameter of those clusters is about 46 nm to 57 nm, whereby a tendency towards smaller clusters was found for all treated samples. Furthermore, a decrease in the density of TLR4 molecules around the center of the clusters was observed. Those changes were accompanied by an increased density of receptor molecules in the membrane and an increased percentage of clustered molecules. For details see Appendix D.4.

## **2.2.5 Nitration of Wheat Amylase Trypsin Inhibitors Increases their Innate and Adaptive Immunostimulatory Potential *in vitro***

ATI have been chemically modified using different nitration methods simulating endogenous and exogenous nitration mechanisms. The modified ATI were tested for their inflammatory and allergenic potential *in vitro*. HCS fluorescence microscopy was used to quantify the activation of the transcription factor NF- $\kappa$ B after treatment with LPS, ATI and ATI nitrated with tetranitromethane (TNM). It was found that stimulation of human macrophages, derived from primary cells of healthy donors, with ATI and ATI TNM induces the translocation of NF- $\kappa$ B into the cell nucleus. The response to the stimuli was donor-dependent, whereby individual donors showed a tendency towards increased translocation upon stimulation with nitrated ATI. Overall, we found in syngeneic DC-T cell co-cultures of primary cells, that nitrated ATI led to an significant increased T cell proliferation and an increased release of Th1 and Th2 cytokines. For details see Appendix D.5.

## 3 Conclusions and Outlook

In this PhD project, SMLM and HCS microscopy were further developed and applied to investigate key molecules involved in inflammatory processes. With the microscopy methods used, the membrane distribution of TLR4 and the localization of NF- $\kappa$ B in response to external stimuli such as ATI could be resolved and quantified. Structural insights at the single cell and single molecule level could be gained that would not be detectable with classical molecular biological methods and conventional microscopy techniques.

### 3.1 Localization Microscope and Software Packages

To investigate biological structures at the single molecule level, a SMLM microscope was built and algorithms to determine the position of single molecule signals and to quantify their distribution were developed and extended. With ILE a software package was presented which is designed to reduce the optimization steps that have to be made by the user to determine the position of single molecule signals. To detect single molecule signals above background, ILE uses a simple thresholding algorithm based on predefined parameters provided by the user or calculated internally by the software. However, machine learning methods like convolutional neural networks are gaining more and more importance in traditional computer vision tasks due to their high performance. ILE could be extended by algorithms derived from machine learning like faster R-CNN (Ren et al. 2017) to detect single molecule signals. First approaches of deep learning in SMLM, which directly output the reconstructed super-resolution image instead of a list of localizations, have been recently published (Ouyang et al. 2018; Nehme et al. 2018).

With ILAND a software package for quantitative analysis of the distribution of the single molecule point pattern was developed. It is specifically designed to handle data sets with high number of points, which can be achieved with the combination of current staining and imaging methods (Olivier et al. 2013; Szczurek et al. 2017). The software package thus also addresses future challenges such as high emitter densities or large sample sizes.

### 3.2 TLR4 Signaling Pathway

The custom-built SMLM microscope and software algorithms were used to study and quantify the membrane distribution of TLR4 in primary human macrophages after treatment with LPS, ATI or nitrated ATI. Clusters consisting of TLR4 receptors could

be visualized and their size and the radial distribution of TLR4 molecules around the centers of these clusters could be measured. After treatment, recruitment of TLR4 molecules into specific membrane domains was observed, leading to changes in physical properties such as diameter and density in the total population of the clusters. These results indicate the significance of the membrane organization of receptors, especially their recruitment into specific membrane domains as an important feature for the regulation of the signaling process (Garcia-Parajo et al. 2014).

Furthermore, an assay was established to quantify the nuclear translocation of NF- $\kappa$ B within the TLR4 downstream signaling pathway on the single cell level. Using HCS microscopy, it was shown that ATI and nitrated ATI induce a donor-dependent translocation of NF- $\kappa$ B into the cell nucleus. Together with the SMLM measurements of TLR4, these results suggest that ATI have a comparable influence on the TLR4 signaling pathway and cause inflammation as it is observed by LPS.

Going forward, the established microscopy methods and developed algorithms provide a valuable tool in the search for compounds that inhibit ATI-induced inflammation. These include compounds that inhibit the dimerization of TLR4 or directly interfere with the signaling pathway. The established HCS microscopy assay has already been used to study various herbal extracts for their ability to inhibit LPS-induced translocation of NF- $\kappa$ B (Schink et al. 2018).

## A References

- Abbe, E. (Dec. 1873). "Beiträge zur Theorie des Mikroskops und der mikroskopischen Wahrnehmung". In: *Arch. für Mikroskopische Anat.* 9 (1), pp. 413–418. DOI: 10.1007/BF02956173.
- Andronov, L., Michalon, J., Ouararhni, K., Orlov, I., Hamiche, A., Vonesch, J.-L., and Klaholz, B. P. (Apr. 2018). "3DClusterViSu: 3D clustering analysis of super-resolution microscopy data by 3D Voronoi tessellations". In: *Bioinformatics*. DOI: 10.1093/bioinformatics/bty200.
- Andronov, L., Orlov, I., Lutz, Y., Vonesch, J.-L., and Klaholz, B. P. (Apr. 2016). "ClusterViSu, a method for clustering of protein complexes by Voronoi tessellation in super-resolution microscopy". In: *Sci. Rep.* 6, p. 24084. DOI: 10.1038/srep24084.
- Baddeley, D., Cannell, M. B., and Soeller, C. (Feb. 2010). "Visualization of Localization Microscopy Data". In: *Microsc. Microanal.* 16 (01), pp. 64–72. DOI: 10.1017/S143192760999122X.
- Betzig, E., Patterson, G. H., Sougrat, R., Lindwasser, O. W., Olenych, S., Bonifacino, J. S., Davidson, M. W., Lippincott-Schwartz, J., and Hess, H. F. (Sept. 2006). "Imaging Intracellular Fluorescent Proteins at Nanometer Resolution". In: *Science*. 313 (5793), pp. 1642–1645. DOI: 10.1126/science.1127344.
- Beutler, B., Du, X., and Poltorak, A. (2001). "Identification of Toll-like receptor 4 (Tlr4) as the sole conduit for LPS signal transduction: genetic and evolutionary studies." In: *J. Endotoxin Res.* 7 (4), pp. 277–80.
- Chow, J. C., Young, D. W., Golenbock, D. T., Christ, W. J., and Gusovsky, F. (Apr. 1999). "Toll-like receptor-4 mediates lipopolysaccharide-induced signal transduction." In: *J. Biol. Chem.* 274 (16), pp. 10689–92.
- Cremer, C. and Masters, B. R. (2013). "Resolution enhancement techniques in microscopy". In: *Eur. Phys. J. H* 38 (3), pp. 281–344. DOI: 10.1140/epjh/e2012-20060-1. arXiv: 1012.0734.
- da Silva Correia, J., Soldau, K., Christen, U., Tobias, P. S., and Ulevitch, R. J. (June 2001). "Lipopolysaccharide Is in Close Proximity to Each of the Proteins in Its Membrane Receptor Complex". In: *J. Biol. Chem.* 276 (24), pp. 21129–21135. DOI: 10.1074/jbc.M009164200.

- Denk, W., Strickler, J., and Webb, W. (Apr. 1990). "Two-photon laser scanning fluorescence microscopy". In: *Science*. 248 (4951), pp. 73–76. DOI: 10.1126/science.2321027.
- Deschout, H., Cella Zanacchi, F., Mlodzianoski, M., Diaspro, A., Bewersdorf, J., Hess, S. T., and Braeckmans, K. (Mar. 2014). "Precisely and accurately localizing single emitters in fluorescence microscopy." In: *Nat. Methods* 11 (3), pp. 253–66. DOI: 10.1038/nmeth.2843.
- Ester, M., Kriegel, H.-P., Sander, J., and Xu, X. (1996). "A Density-Based Algorithm for Discovering Clusters in Large Spatial Databases with Noise". In: *Proc. Second Int. Conf. Knowl. Discov. Data Min.* Pp. 226–231. DOI: 10.1.1.71.1980.
- Franze, T., Weller, M. G., Niessner, R., and Pöschl, U. (2005). "Protein nitration by polluted air". In: *Environ. Sci. Technol.* 39 (6), pp. 1673–1678. DOI: 10.1021/es0488737.
- Garcia-Parajo, M. F., Cambi, A., Torreno-Pina, J. A., Thompson, N., and Jacobson, K. (Dec. 2014). "Nanoclustering as a dominant feature of plasma membrane organization". In: *Journal of Cell Science* 127 (23), pp. 4995–5005. DOI: 10.1242/jcs.146340.
- Gioannini, T. L., Teghanemt, A., Zhang, D., Coussens, N. P., Dockstader, W., Ramaswamy, S., and Weiss, J. P. (Mar. 2004). "Isolation of an endotoxin-MD-2 complex that produces Toll-like receptor 4-dependent cell activation at picomolar concentrations". In: *Proc. Natl. Acad. Sci.* 101 (12), pp. 4186–4191. DOI: 10.1073/pnas.0306906101.
- Griffié, J., Shannon, M., Bromley, C. L., Boelen, L., Burn, G. L., Williamson, D. J., Heard, N. A., Cope, A. P., Owen, D. M., and Rubin-Delanchy, P. (Nov. 2016). "A Bayesian cluster analysis method for single-molecule localization microscopy data". In: *Nat. Protoc.* 11 (12), pp. 2499–2514. DOI: 10.1038/nprot.2016.149.
- Gruijthuijsen, Y. K., Grieshuber, I., Stöcklinger, A., Tischlera, U., Fehrenbach, T., Weller, M. G., Vogel, L., Vieths, S., Pöschl, U., and Duschl, A. (2006). "Nitration enhances the allergenic potential of proteins". In: *Int. Arch. Allergy Immunol.* 141 (3), pp. 265–275. DOI: 10.1159/000095296.
- Grüll, F., Kirchgessner, M., Kaufmann, R., Hausmann, M., and Kechschull, U. (2011). "Accelerating image analysis for localization microscopy with FPGAs". In: *Proc. - 21st Int. Conf. F. Program. Log. Appl. FPL 2011.* 2, pp. 1–5. DOI: 10.1109/FPL.2011.11.
- Gustafsson, M. G. (May 2000). "Surpassing the lateral resolution limit by a factor of two using structured illumination microscopy." In: *J. Microsc.* 198 (Pt 2), pp. 82–7.

- Heilemann, M., Van De Linde, S., Schüttpelz, M., Kasper, R., Seefeldt, B., Mukherjee, A., Tinnefeld, P., and Sauer, M. (2008). "Subdiffraction-resolution fluorescence imaging with conventional fluorescent probes". In: *Angew. Chemie - Int. Ed.* 47 (33), pp. 6172–6176. DOI: 10.1002/anie.200802376.
- Heintzmann, R. and Cremer, C. G. (Jan. 1999). "Laterally modulated excitation microscopy: improvement of resolution by using a diffraction grating". In: *Proc. SPIE 3568, Optical Biopsies and Microscopic Techniques III*, pp. 185–196. DOI: 10.1117/12.336833.
- Hell, S. W. and Wichmann, J. (June 1994). "Breaking the diffraction resolution limit by stimulated emission: stimulated-emission-depletion fluorescence microscopy". In: *Opt. Lett.* 19 (11), p. 780. DOI: 10.1364/OL.19.000780.
- Hess, S. T., Girirajan, T. P. K., and Mason, M. D. (Dec. 2006). "Ultra-high resolution imaging by fluorescence photoactivation localization microscopy." In: *Biophys. J.* 91 (11), pp. 4258–72. DOI: 10.1529/biophysj.106.091116.
- Huang, B., Wang, W., Bates, M., and Zhuang, X. (Feb. 2008). "Three-Dimensional Super-Resolution Imaging by Stochastic Optical Reconstruction Microscopy". In: *Science*. 319 (5864), pp. 810–813. DOI: 10.1126/science.1153529.
- Huisken, J., Swoger, J., Del Bene, F., Wittbrodt, J., and Stelzer, E. H. K. (Aug. 2004). "Optical Sectioning Deep Inside Live Embryos by Selective Plane Illumination Microscopy". In: *Science*. 305 (5686), pp. 1007–1009. DOI: 10.1126/science.1100035.
- Jungmann, R., Steinhauer, C., Scheible, M., Kuzyk, A., Tinnefeld, P., and Simmel, F. C. (2010). "Single-molecule kinetics and super-resolution microscopy by fluorescence imaging of transient binding on DNA origami". In: *Nano Lett.* 10 (11), pp. 4756–4761. DOI: 10.1021/nl103427w.
- Junker, Y., Zeissig, S., Kim, S.-J., Barisani, D., Wieser, H., Leffler, D. A., Zevallos, V., Libermann, T. A., Dillon, S., Freitag, T. L., Kelly, C. P., and Schuppan, D. (Dec. 2012). "Wheat amylase trypsin inhibitors drive intestinal inflammation via activation of toll-like receptor 4". In: *J. Exp. Med.* 209 (13), pp. 2395–2408. DOI: 10.1084/jem.20102660.
- Kawasaki, T. and Kawai, T. (2014). "Toll-like receptor signaling pathways". In: *Front. Immunol.* 5 (SEP), pp. 1–8. DOI: 10.3389/fimmu.2014.00461.
- Krüger, C. L., Zeuner, M. T., Cottrell, G. S., Widera, D., and Heilemann, M. (2017). "Quantitative single-molecule imaging of TLR4 reveals ligand-specific receptor dimerization". In: *Sci. Signal.* 10 (503). DOI: 10.1126/scisignal.aan1308.

- Lee, T. K., Denny, E. M., Sanghvi, J. C., Gaston, J. E., Maynard, N. D., Hughey, J. J., and Covert, M. W. (Oct. 2009). "A Noisy Paracrine Signal Determines the Cellular NF- $\kappa$ B Response to Lipopolysaccharide". In: *Sci. Signal.* 2 (93), ra65–ra65. DOI: 10.1126/scisignal.2000599.
- Lemmer, P., Gunkel, M., Baddeley, D., Kaufmann, R., Urich, A., Weiland, Y., Reymann, J., Müller, P., Hausmann, M., and Cremer, C. (Sept. 2008). "SPDM: light microscopy with single-molecule resolution at the nanoscale". In: *Appl. Phys. B* 93 (1), pp. 1–12. DOI: 10.1007/s00340-008-3152-x.
- Levet, F., Hosy, E., Kechkar, A., Butler, C., Beghin, A., Choquet, D., and Sibarita, J.-B. (Sept. 2015). "SR-Tesseler: a method to segment and quantify localization-based super-resolution microscopy data". In: *Nat. Methods* 12 (11), pp. 1065–1071. DOI: 10.1038/nmeth.3579.
- Lidke, K., Rieger, B., Jovin, T., and Heintzmann, R. (Sept. 2005). "Superresolution by localization of quantum dots using blinking statistics." In: *Opt. Express* 13 (18), pp. 7052–62.
- Lucas, K. and Maes, M. (Aug. 2013). "Role of the Toll Like receptor (TLR) radical cycle in chronic inflammation: possible treatments targeting the TLR4 pathway." In: *Mol. Neurobiol.* 48 (1), pp. 190–204. DOI: 10.1007/s12035-013-8425-7.
- MacRedmond, R. E., Greene, C. M., Dorscheid, D. R., McElvaney, N. G., and O'Neill, S. J. (Dec. 2007). "Epithelial expression of TLR4 is modulated in COPD and by steroids, salmeterol and cigarette smoke". In: *Respir. Res.* 8 (1), p. 84. DOI: 10.1186/1465-9921-8-84.
- Mazouchi, A. and Milstein, J. N. (Mar. 2016). "Fast Optimized Cluster Algorithm for Localizations (FOCAL): a spatial cluster analysis for super-resolved microscopy". In: *Bioinformatics* 32 (5), pp. 747–754. DOI: 10.1093/bioinformatics/btv630.
- Moresco, E. M. Y., LaVine, D., and Beutler, B. (2011). "Toll-like receptors". In: *Curr. Biol.* 21 (13), R488–R493. DOI: 10.1016/j.cub.2011.05.039.
- Nehme, E., Weiss, L. E., Michaeli, T., and Shechtman, Y. (Apr. 2018). "Deep-STORM: super-resolution single-molecule microscopy by deep learning". In: *Optica* 5 (4), p. 458. DOI: 10.1364/OPTICA.5.000458.
- Nieuwenhuizen, R., Stallinga, S., and Rieger, B. (Oct. 2014). "Visualization and Resolution in Localization Microscopy". In: *Cell Membr. Nanodomains*. CRC Press, pp. 409–430. DOI: 10.1201/b17634-23.

- Olivier, N., Keller, D., Rajan, V. S., Gönczy, P., and Manley, S. (June 2013). “Simple buffers for 3D STORM microscopy”. In: *Biomed. Opt. Express* 4 (6), p. 885. DOI: 10.1364/B0E.4.000885.
- Ouyang, W., Aristov, A., Lelek, M., Hao, X., and Zimmer, C. (Apr. 2018). “Deep learning massively accelerates super-resolution localization microscopy”. In: *Nat. Biotechnol.* 36 (5), pp. 460–468. DOI: 10.1038/nbt.4106.
- Panaro, M. A., Lofrumento, D. D., Saponaro, C., De Nuccio, F., Cianciulli, A., Mitolo, V., and Nicolardi, G. (Jan. 2008). “Expression of TLR4 and CD14 in the Central Nervous System (CNS) in a MPTP Mouse Model of Parkinson’s-Like Disease”. In: *Immunopharmacol. Immunotoxicol.* 30 (4), pp. 729–740. DOI: 10.1080/08923970802278557.
- Park, B. S., Song, D. H., Kim, H. M., Choi, B.-S., Lee, H., and Lee, J.-O. (Apr. 2009). “The structural basis of lipopolysaccharide recognition by the TLR4–MD-2 complex”. In: *Nature* 458 (7242), pp. 1191–1195. DOI: 10.1038/nature07830.
- Płóciennikowska, A., Hromada-Judycka, A., Borzecka, K., and Kwiatkowska, K. (2014). “Co-operation of TLR4 and raft proteins in LPS-induced pro-inflammatory signaling”. In: *Cell. Mol. Life Sci.* 72 (3), pp. 557–581. DOI: 10.1007/s00018-014-1762-5.
- Rayleigh (Aug. 1896). “XV. On the theory of optical images, with special reference to the microscope”. In: *London, Edinburgh, Dublin Philos. Mag. J. Sci.* 42 (255), pp. 167–195. DOI: 10.1080/14786449608620902.
- Reinmuth-Selzle, K., Kampf, C. J., Lucas, K., Lang-Yona, N., Fröhlich-Nowoisky, J., Shiraiwa, M., Lakey, P. S., Lai, S., Liu, F., Kunert, A. T., Ziegler, K., Shen, F., Sgarbanti, R., Weber, B., Bellinghausen, I., Saloga, J., Weller, M. G., Duschl, A., Schuppan, D., and Pöschl, U. (2017). “Air Pollution and Climate Change Effects on Allergies in the Anthropocene: Abundance, Interaction, and Modification of Allergens and Adjuvants”. In: *Environ. Sci. Technol.* 51 (8), pp. 4119–4141. DOI: 10.1021/acs.est.6b04908. arXiv: arXiv:1011.1669v3.
- Ren, S., He, K., Girshick, R., and Sun, J. (June 2017). “Faster R-CNN: Towards Real-Time Object Detection with Region Proposal Networks”. In: *IEEE Trans. Pattern Anal. Mach. Intell.* 39 (6), pp. 1137–1149. DOI: 10.1109/TPAMI.2016.2577031.
- Rubin-Delanchy, P., Burn, G. L., Griffié, J., Williamson, D. J., Heard, N. A., Cope, A. P., and Owen, D. M. (Oct. 2015). “Bayesian cluster identification in single-molecule localization microscopy data”. In: *Nat. Methods* 12 (11), pp. 1072–1076. DOI: 10.1038/nmeth.3612.

- Rust, M. J., Bates, M., and Zhuang, X. (Oct. 2006). "Sub-diffraction-limit imaging by stochastic optical reconstruction microscopy (STORM)". In: *Nat. Methods* 3 (10), pp. 793–796. DOI: 10.1038/nmeth929.
- Schink, A., Neumann, J., Leifke, A. L., Ziegler, K., Fröhlich-Nowoisky, J., Cremer, C., Thines, E., Weber, B., Pöschl, U., Schuppan, D., and Lucas, K. (2018). "Screening of herbal extracts for TLR2- and TLR4-dependent anti-inflammatory effects". *PLoS One*, under revision.
- Sengupta, P., Jovanovic-Taliman, T., and Lippincott-Schwartz, J. (Feb. 2013). "Quantifying spatial organization in point-localization superresolution images using pair correlation analysis." In: *Nat. Protoc.* 8 (2), pp. 345–54. DOI: 10.1038/nprot.2013.005.
- Sengupta, P., Jovanovic-Taliman, T., Skoko, D., Renz, M., Veatch, S. L., and Lippincott-Schwartz, J. (Sept. 2011). "Probing protein heterogeneity in the plasma membrane using PALM and pair correlation analysis". In: *Nat. Methods* 8 (11), pp. 969–975. DOI: 10.1038/nmeth.1704.
- Sengupta, P. and Lippincott-Schwartz, J. (May 2012). "Quantitative analysis of photoactivated localization microscopy (PALM) datasets using pair-correlation analysis." In: *Bioessays* 34 (5), pp. 396–405. DOI: 10.1002/bies.201200022.
- Sharonov, A. and Hochstrasser, R. M. (Dec. 2006). "Wide-field subdiffraction imaging by accumulated binding of diffusing probes". In: *Proc. Natl. Acad. Sci.* 103 (50), pp. 18911–18916. DOI: 10.1073/pnas.0609643104.
- Small, A. and Stahlheber, S. (Mar. 2014). "Fluorophore localization algorithms for super-resolution microscopy." In: *Nat. Methods* 11 (3), pp. 267–79. DOI: 10.1038/nmeth.2844.
- Szczurek, A., Klewes, L., Xing, J., Gourram, A., Birk, U., Knecht, H., Dobrucki, J. W., Mai, S., and Cremer, C. (Jan. 2017). "Imaging chromatin nanostructure with binding-activated localization microscopy based on DNA structure fluctuations". In: *Nucleic Acids Res.* 45 (8). DOI: 10.1093/nar/gkw1301.
- Veatch, S. L., Machta, B. B., Shelby, S. A., Chiang, E. N., Holowka, D. A., and Baird, B. A. (2012). "Correlation functions quantify super-resolution images and estimate apparent clustering due to over-counting". In: *PLoS One* 7 (2). DOI: 10.1371/journal.pone.0031457. arXiv: 1106.6068.
- Verstrepen, L., Bekaert, T., Chau, T. L., Tavernier, J., Chariot, A., and Beyaert, R. (2008). "TLR-4, IL-1R and TNF-R signaling to NF- $\kappa$ B: Variations on a common theme". In: *Cell. Mol. Life Sci.* 65 (19), pp. 2964–2978. DOI: 10.1007/s00018-008-8064-8.

- Voie, A. H., Burns, D. H., and Spelman, F. A. (June 1993). "Orthogonal-plane fluorescence optical sectioning: Three-dimensional imaging of macroscopic biological specimens". In: *J. Microsc.* 170 (3), pp. 229–236. DOI: 10.1111/j.1365-2818.1993.tb03346.x.
- Walter, S., Letiembre, M., Liu, Y., Heine, H., Penke, B., Hao, W., Bode, B., Manietta, N., Walter, J., Schulz-Schüffer, W., and Fassbender, K. (2007). "Role of the Toll-Like Receptor 4 in Neuroinflammation in Alzheimer's Disease". In: *Cell. Physiol. Biochem.* 20 (6), pp. 947–956. DOI: 10.1159/000110455.
- Zeuner, M.-T., Krüger, C. L., Volk, K., Bieback, K., Cottrell, G. S., Heilemann, M., and Widera, D. (Sept. 2016). "Biased Signalling is an Essential Feature of TLR4 in Glioma Cells". In: *Biochim. Biophys. Acta - Mol. Cell Res.* DOI: 10.1016/j.bbamcr.2016.09.016.
- Zevallos, V. F., Raker, V., Tenzer, S., Jimenez-Calvente, C., Ashfaq-Khan, M., Rüssel, N., Pickert, G., Schild, H., Steinbrink, K., and Schuppan, D. (2017). "Nutritional Wheat Amylase-Trypsin Inhibitors Promote Intestinal Inflammation via Activation of Myeloid Cells". In: *Gastroenterology* 152 (5), 1100–1113.e12. DOI: 10.1053/j.gastro.2016.12.006.

## B Abbreviations

AFM	atomic force microscopy
ATI	amylase trypsin inhibitor
CD14	cluster of differentiation 14
CLSM	confocal laser scanning microscopy
COPD	chronic obstructive pulmonary disease
DAMP	damage-associated molecular pattern
DBSCAN	density-based spatial clustering of applications with noise
DNA	deoxyribonucleic acid
DNA-PAINT	DNA points accumulation for imaging in nanoscale topography
ELISA	enzyme-linked immunosorbent assay
HCS	high-content screening
HILO	highly inclined and laminated optical sheet
ILAND	Integrated Localization Analyzer for Nanoscale Distributions
ILE	Integrated Localization Environment
IL	interleukins
IL-1R	interleukin-1 receptor
LBP	lipopolysaccharide binding protein
LPS	lipopolysaccharide
LSFM	light sheet fluorescence microscopy
MD-2	myeloid differentiation protein-2
MPM	multi-photon microscopy
MyD88	myeloid differentiation primary response 88
NF- $\kappa$ B	nuclear factor kappa-light-chain-enhancer of activated B cells
PAMP	pathogen-associated molecular pattern
PCR	polymerase chain reaction
PRR	pattern recognition receptors
RNS	reactive nitrogen species
ROS	reactive oxygen species
SIM	structured illumination microscopy
SMLM	single molecule localization microscopy
STED	stimulated emission depletion
TIRF	total internal reflection fluorescence
TLR4	toll-like receptor 4
TNF $\alpha$	tumor necrosis factor alpha
TNFR1	tumor necrosis factor receptor 1
TNM	tetranitromethane
TRIF	TIR-domain-containing adapter-inducing interferon- $\beta$

## C Personal List of Publications

### Journal Articles

Neumann, J., Ziegler, K., Gelléri, M., Fröhlich-Nowoisky, J., Fobang, L., Bellinghausen, I., Schuppan, D., Birk, U., Pöschl, U., Cremer, C. and Lucas, K.: Membrane Distribution of TLR4 in Primary Human Macrophages after Stimulation with ATI or LPS using Localization Microscopy, *to be submitted*, (2018).

Neumann, J., Hagmann, M., Grüll, F., Kaufmann, R., Szczurek, A., Prakash, K., Lopez Perez, R., Lucas, K., Pöschl, U., Cremer, C., and Birk, U.: Integrated Localization Environment (ILE): A Software Package to Evaluate and Process Blinking Based Single Molecule Localization Microscopy Data, *to be submitted*, (2018).

Neumann, J., Gourram, A., Gelléri, M., Szczurek, A., Birk, U., Lucas, K., Pöschl, U., and Cremer, C.: Integrated Localization Analyzer for Nanoscale Distributions (ILAND): A Software Package for Spatial Point Pattern Analysis of Localization Microscopy Data, *in preparation*.

Ziegler, K., Neumann, J., Liu, F., Fröhlich-Nowoisky, J., Cremer, C., Saloga, J., Reinmuth-Selzle, K., Pöschl, U., Schuppan, D., Bellinghausen, I., and Lucas, K.: Nitration of Wheat Amylase Trypsin Inhibitors Increases their Innate and Adaptive Immunostimulatory Potential *in vitro*, *submitted*, (2018).

Schink, A., Neumann, J., Leifke, A. L., Ziegler, K., Fröhlich-Nowoisky, J., Cremer, C., Thines, E., Weber, B., Pöschl, U., Schuppan, D., and Lucas, K.: Screening of herbal extracts for TLR2- and TLR4-dependent anti-inflammatory effects, *in revision*, (2018).

### Other Publications

Neumann, J., Scherhag, A., Otten, S., Shen, F., Leifke, A. L., Birk, U., Greb, C., Lucas, K., and Cremer, C.: Chronic Inflammation Under the Microscope, *Microscopy Today* **24** (06), 38-45, (2016).

## Oral Presentations

Ziegler, K., Bellinghausen, I., Neumann, J., Liu, F., Schuppan, D., Pöschl, U., and Lucas, K.: Nitration of wheat derived alpha amylase trypsin inhibitors (ATIs) increases their immunostimulatory capacity, 30. Mainzer Allergie Workshop, Mainz, Germany, 22<sup>th</sup> - 23<sup>th</sup> March 2018.

Gourram, A., Szczurek, A., Neumann, J., Cremer, C., and Birk, U.: SMLM-Context, a Software Tool for the Analysis of Conformation and Texture in Single Molecule Localization Microscopy Images, Focus on Microscopy, Bordeaux, France, 09<sup>th</sup> - 12<sup>th</sup> April 2017.

Neumann, J., Ziegler, K., Zevallos, V., Birk, U., Lucas, K., Schuppan, D., Cremer, C., and Pöschl, U.: Microscopic localization of molecules involved in chronic inflammatory processes, 29. Mainzer Allergie Workshop, Mainz, Germany, 30<sup>th</sup> - 31<sup>th</sup> March 2017.

## Poster Presentations

Schock, F., Neumann, J., Leifke, A. L., Pöschl, U., Lucas, K., and Cremer, C.: Detecting intracellular-changes below the optical resolution limit to investigate inflammation, Frühjahrstagung der Deutschen Physikalischen Gesellschaft, Berlin, Germany, 11<sup>th</sup> - 16<sup>th</sup> March 2018.

Neumann, J., Ziegler, K., Szczurek, A., Gourram, A., Birk, U., Lucas, K., Zevallos, V., Schuppan, D., Cremer, C., and Pöschl, U.: Investigation of Molecules Involved in Chronic Inflammatory Processes Using Single Molecule Localization Microscopy in Cells, Focus on Microscopy, Bordeaux, France, 09<sup>th</sup> - 12<sup>th</sup> April 2017.

Birk, U., Szczurek, A., Neumann, J., Gourram, A., and Cremer, C.: Quantitative Single Molecule Localization Microscopy Visualization, Focus on Microscopy, Bordeaux, France, 09<sup>th</sup> - 12<sup>th</sup> April 2017.

Neumann, J., Cui, S., Birk, U., Lucas, K., Cremer, C., and Pöschl, U.: Spatial organization of Toll-like receptor 4 on the cell membrane, International Conference on Nanoscopy, Basel, Switzerland, 07<sup>th</sup> - 10<sup>th</sup> June 2016.

Birk, U., Szczurek, A., Prakash, K., Neumann, J., Schock, F., Gourram, A., and Cremer, C.: Drift Correction in Single Molecule Localization Microscopy Using Nearest Neighbor Analysis, Focus on Microscopy, Taipei, Taiwan, 20<sup>th</sup> - 23<sup>th</sup> March 2016.

# Acknowledgements

## D Individual Studies

- D.1 Conversion of a Confocal Laser Scanning Microscope into a Single Molecule Localization Microscope (Neumann *et al.*, in preparation, 2018)
- D.2 Integrated Localization Environment (ILE): A Software Package to Evaluate and Process Blinking Based Single Molecule Localization Microscopy Data (Neumann *et al.*, to be submitted, 2018)
- D.3 Integrated Localization Analyzer for Nanoscale Distributions (ILAND): A Software Package for Spatial Point Pattern Analysis of Localization Microscopy Data (Neumann *et al.*, in preparation, 2018)
- D.4 Membrane Distribution of TLR4 in Primary Human Macrophages after Stimulation with ATI or LPS using Localization Microscopy (Neumann *et al.*, to be submitted, 2018)
- D.5 Nitration of Wheat Amylase Trypsin Inhibitors Increases their Innate and Adaptive Immunostimulatory Potential *in vitro* (Ziegler *et al.*, submitted, 2018)

## D.1 Neumann *et al.*, in preparation, 2018

# Conversion of a Confocal Laser Scanning Microscope into a Single Molecule Localization Microscope

Tentative author list. To be extended/adjusted.

Jan Neumann<sup>1,2</sup>, Kurt Lucas<sup>1</sup>, Ulrich Pöschl<sup>1</sup>, Udo Birk<sup>2,‡</sup> and Christoph Cremer<sup>1,2\*</sup>

<sup>1</sup>Multiphase Chemistry Department, Max Planck Institute for Chemistry,  
Hahn-Meitner-Weg 1, 55128 Mainz, Germany

<sup>2</sup>Institute of Molecular Biology, Ackermannweg 4, 55128 Mainz, Germany

<sup>‡</sup>Current address: Hochschule für Technik und Wirtschaft Chur,  
Pulvermühlestrasse 57, 7000 Chur, Switzerland

\*Correspondence to C. Cremer (c.cremer@imb-mainz.de)

### **Author contributions.**

CC, UB and JN conceived the study. JN constructed the microscope and performed the calibration. JN wrote the manuscript. All authors contributed to the writing.

# Conversion of a Confocal Laser Scanning Microscope into a Single Molecule Localization Microscope

Tentative author list. To be extended/adjusted.

Jan Neumann<sup>1,2</sup>, Kurt Lucas<sup>1</sup>, Ulrich Pöschl<sup>1</sup>, Udo Birk<sup>2,‡</sup> and Christoph Cremer<sup>1,2\*</sup>

<sup>1</sup>Multiphase Chemistry Department, Max Planck Institute for Chemistry,  
Hahn-Meitner-Weg 1, 55128 Mainz, Germany

<sup>2</sup>Institute of Molecular Biology, Ackermannweg 4, 55128 Mainz, Germany

<sup>‡</sup>Current address: Hochschule für Technik und Wirtschaft Chur,  
Pulvermühlestrasse 57, 7000 Chur, Switzerland

\*Correspondence to C. Cremer (c.cremer@imb-mainz.de)

# 1 Introduction

Super-resolution microscopy techniques such as stimulated emission depletion (STED) microscopy (Hell et al. 1994), structured illumination microscopy (SIM) (Heintzmann et al. 1999; Gustafsson 2000) and single molecule localization microscopy (SMLM) (Betzig et al. 2006; Hess et al. 2006; Rust et al. 2006; Sharonov et al. 2006; Heilemann et al. 2008; Lemmer et al. 2008; Jungmann et al. 2010) have become an essential tool in the investigation of biological structures below the diffraction limit of the optics used (Abbe 1873; Rayleigh 1896). Among these, single molecule localization microscopy (SMLM) allows to localize the position of individual molecules with a precision of a few nanometers. Normally, this happens by imaging optical isolated single molecule signals. Optical isolation can be achieved on the one hand by switching fluorophores between their fluorescent and dark state using a specific combination of fluorescent dyes, embedding medium and illumination intensities (Heilemann et al. 2008; Lemmer et al. 2009; Dempsey et al. 2011). On the other hand, certain dye molecules or dye-labeled DNA strands that transiently bind to the target structure can be used to obtain optical isolation (Jungmann et al. 2010; Szcurek et al. 2017). Since in both cases only a subset of the molecules is in the fluorescent state or transiently binds at a certain time point, several frames must be taken to sufficiently sample the target structure. However, independent of the method used on the sample side, the gain in structural information in the sub-diffraction regime does not need a complex and cost intensive instrumentation as it is necessary for electron microscopy. Although electron microscopy can achieve an even higher structural resolution, the gain in resolution paired with simpler sample preparation in SMLM may be sufficient for a variety of biological applications.

The additional instrumentation needed to perform SMLM measurements, can be easily added at almost any existing research grade fluorescence microscope. In principle such a conversion of an existing microscope comes down to three important aspects that must be fulfilled. First, the SMLM system needs a sufficient illumination intensity in the sample plane, which is usually done by coupling an external laser source into the microscope excitation beam path. Second, to sufficiently sample the optical isolated single molecule signals a fast and sensitive detector is needed. Finally, care must be taken that the sample drift during imaging due to temperature fluctuations and mechanical instabilities is reduced to a minimum.

Here we describe the conversion of a confocal laser scanning microscope into a single molecule localization microscope. We give an overview about the components used and describe the calibration of the setup in detail. The provided details can be easily adapted and used as an orientation for the conversion of other fluorescence microscopes into a SMLM system.

## 2 Methods

### Optical setup

A scheme of the constructed microscope setup with the main components is depicted in Figure 1. A confocal microscope (Leica DM RBE), positioned on top of an optical table (Newport, RS4000), served as microscope body. It has been equipped with a 488 nm (Coherent Sapphire) and a 647 nm laser (Coherent Obis), which were combined using a dichroic mirror (DM1). To achieve a sufficient sample illumination as well as high laser intensities as necessary for blinking-based SMLM, lasers have been  $3.125\times$  expanded using a  $f=40$  mm and a  $f=125$  mm lens (both Thorlabs). To illuminate the whole field of view homogeneously and to avoid unnecessary photobleaching during sample search, a second parallel beam path with  $10\times$  expansion of the laser beam consisting of a  $f=10$  mm and a  $f=100$  mm lens (both Thorlabs), has been constructed. Using two flipping mirrors (FLM) it was possible to switch between both beam paths. Next, the collimated laser beams were coupled into the back port of the microscope body after passing a periscope. The upper mirror of the periscope was placed in the front focal plane of the focusing lens (FL,  $f=300$  mm, Thorlabs). By tilting the upper mirror of the periscope using two attached piezoelectric actuators (Thorlabs), it was possible to switch between epifluorescence, total internal reflection (TIRF) and highly inclined and laminated optical sheet (HILO) illumination mode. Laser beams were focused on the back focal plane of the  $100\times/NA 1.49$  objective (Olympus). The objective was mounted on a piezo objective scanner (Physik Instrumente) for fine focusing. Coarse focusing could be accomplished by moving the sample stage using the z-drive integrated in the microscope body. Lateral adjustment of the sample stage was done using stepper motors. To discriminate the excitation light of the lasers from the emitted fluorescent light a dichroic mirror (DM2, dual line zt488/647rpc, AHF Analysetechnik) placed in a filter cube was used. To block illumination from unwanted wavelengths a clean-up filter (ZET488/647, AHF Analysetechnik) was incorporated into that cube. Remaining excitation light was removed using a dual notch filter (488/647 nm, AHF Analysetechnik). The emission path consisted also of a separate filter wheel incorporated into a custom-made camera adapter. It contained two emission filters (HQ500LP and ET700/75m, both Chroma Technology) and an additional empty position for bright-field illumination. Bright-field illumination could be applied using a mercury lamp (Leica) attached to the microscope body. The emission pathway further consisted of a  $f=300$  mm tube lens (TL, Thorlabs), which focuses the emission light onto the detector of an electron multiplying charge-coupled device (EMCCD) camera (Andor iXon+). A  $f=1.000$  mm cylindrical lens (Thorlabs) could be placed in front of the detector to enable astigmatism-based 3D localization microscopy (Huang et al. 2008).

A complete list of components used can be found in Supplementary Note 1.

### Electronics and software

All devices like lasers, camera and stage controllers were connected to a computer running open source microscopy software  $\mu$ Manager (Version 2.0.0-beta3 20170424, Edel-

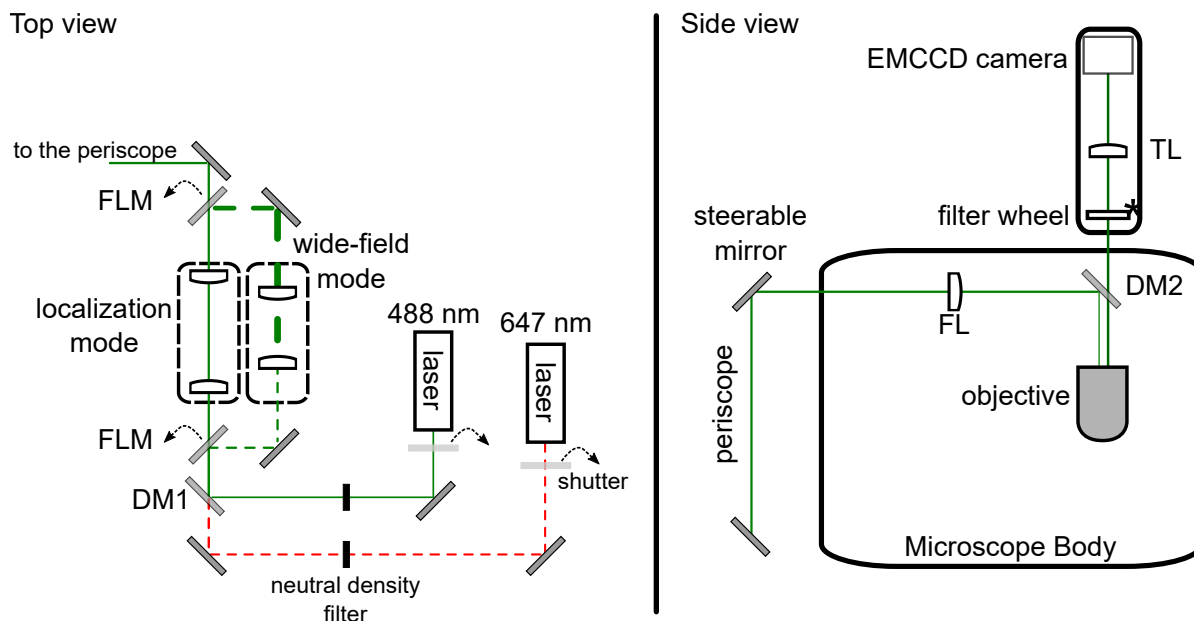


**Figure 1: Scheme of the constructed SMLM microscope.** Excitation pathway outside of the microscope body (top view). DM1 and FLM denote dichroic mirror 1 and flipping mirror, respectively. Excitation pathway from the periscope to the objective as well as the emission pathway (side view). FL is the focusing lens, DM2 the dichroic mirror 2 and TL denotes the tube lens.

stein et al. 2010).  $\mu$ Manager was configured to control those devices (Figure 2). Custom-made laser shutters and servo motors for flipping mirrors and the filter wheel were connected via the Arduino platform to  $\mu$ Manager. More detailed, each of the two laser shutters was controlled by a MOSFET driver module connected to an Arduino Uno board. The servo motors were driven by an Adafruit servo driver module connected to an Arduino Mega 2560. The Arduino Mega was programmed to place the motors, attached to the flipping mirrors, in either "wide-field" or "localization mode" and the digital servo of the filter wheel to one of the three filter positions. Another Arduino Uno was used as interface between  $\mu$ Manager and the Arduino Mega by setting the voltage of the pins and thus transmitting a high or low voltage signal. Each pin was coded to a specific state of the microscope i.e. "wide-field" or "localization mode" and filter position.

The stepper stage of the microscope body was used at the beginning of the experiment to move the sample towards the objective. Therefore, it was not controlled by  $\mu$ Manager. Instead the Leica DM SDK (Version 4.2.1) software was used. All further adjustments in z-direction were done by the piezo objective scanner, because of its smaller step size. The motors controlling the mirror used to switch between epifluorescence, TIRF and HILO illumination were controlled by APT software (Thorlabs).

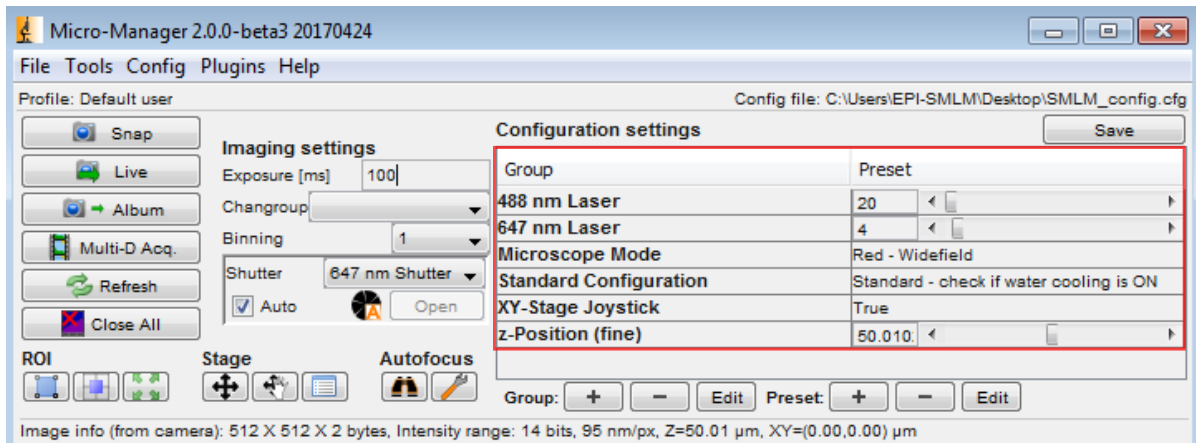


**Figure 2: Interface of  $\mu$ Manager (Edelstein et al. 2010).** Software was configured to directly adjust laser power, microscope mode and microscope configuration (red box). The "microscope mode" group communicates directly with the Arduinos controlling the servo motors, thus enabling the user to change the emission filters and switch between "widefield" and "localization mode". The standard configuration group comprises settings for the camera like EM gain or cooling.

## Sample preparation

### Preparation of bead samples

Fluorescent beads (TetraSpeck Microspheres, Thermo Fisher Scientific) were vortexed and diluted 1 to 100 or 1 to 1000 in ddH<sub>2</sub>O. Diluted beads were sonicated in an ultrasonic bath for 20 min to remove aggregates of beads. Meanwhile, coverslips (R. Langenbrinck GmbH, 22 x 22 mm, thickness: 0.17 mm  $\pm$  0.005 mm) were coated with poly-L-lysine (Sigma Aldrich) for 15 min to 30 min and rinsed afterwards with ddH<sub>2</sub>O. 100  $\mu$ l of diluted and sonicated beads were placed on parafilm and the coverslips were placed on top of it with the coated side facing down. Incubation was done for 1 h to 2 h. Next, the bead sample was embedded in either ProLong Gold (Thermo Fischer Scientific) or Vectashield H-1000 (Vector Laboratories).

### Preparation of microtubule samples

To image microtubules, HeLa cells were seeded on glass coverslips (R. Langenbrinck GmbH) placed in a six well plate (Greiner). Seeded cells were incubated at 37 °C and 5 % CO<sub>2</sub> until reaching 60 % to 80 % confluency. Next, cells were pre-extracted in 0.4 % glutaraldehyde (Sigma Aldrich) and 0.25% Triton X-100 (Merck) diluted in PBS for 90 s. After washing in pre-warmed PBS, cells were fixed for 15 min in 3 % glutaraldehyde/PBS at 37 °C. Then, cells were washed three times with PBS and subsequently quenched in 0.1 % NaBH<sub>4</sub>/PBS (Sigma Aldrich). Followed from three washing steps with PBS, cells were blocked for 1 h using 3 % BSA and 0.3 % Triton X-100 diluted in PBS. Primary antibody against  $\alpha$ -tubulin (DMA1, Sigma Aldrich) was diluted 1 to 100 in antibody dilution buffer (1 % BSA/0.3 % Triton in PBS). Cells were incubated with primary antibody for 1 h at room temperature. Next, cells were washed two times in PBS for 2 min each, by

placing the plate on a shaker. Incubation of secondary antibody (Alexa Fluor 647, diluted 1 to 100 in antibody dilution buffer) was done for 1 h at room temperature. After repeating the same washing steps as done after primary antibody staining, cells were embedded in Vectashield H-1000.

### 3 Results and Discussion

The following sections provide a detailed insight into the calibration of the microscope such as laser power, camera performance and sample drift. Overall performance of the system is evaluated on nanorulers and microtubule samples.

#### Excitation path and laser lines

Two lasers with wavelengths of 488 nm (Coherent Sapphire) and 647 nm (Coherent Obis) were incorporated into the setup, thus enabling dual-color imaging of blue- and red-absorbing dyes. Furthermore, 488 nm laser line could be used simultaneously with 647 nm laser line at low intensities for re-excitation of Alexa 647 (Heilemann et al. 2008). Two different beam paths were implemented to switch between a low intensity illumination ("wide-field mode", illuminating the whole field of view of the camera) and an configuration with high intensity illumination ("localization mode", illuminating a region of interest (ROI) of typical 200 x 200 pixels). To apply the correct laser intensities needed for SMLM (typically in the order of a few kW/cm<sup>2</sup>), laser intensities were determined in the sample plane, while operating the microscope in localization mode, and calibrated to the direct output power of the lasers (Figure 3). Laser powers were determined by placing a power meter (Nova II, Ophir Photonics) in front of the lasers as well as in the sample plane (Supplementary Figure 1). To obtain laser intensities, the illuminated area in the sample plane was determined by first calculating the median image of a localization data stack. Next, the 1/e<sup>2</sup> width of a line plot through the illuminated area was used to approximate the diameter of the circular illuminated area. This yielded an illumination area of about 640 μm<sup>2</sup>. Maximum laser intensities that can be achieved in the sample plane are 8 kW/cm<sup>2</sup> for 647 nm illumination and 17 kW/cm<sup>2</sup> for 488 nm illumination, which is sufficient for SMLM.

#### Emission path and camera system

The emission pathway contained an emission filter system consisting of a dual notch filter and a separate emission filter wheel incorporated into a custom-made camera adapter. Whilst the dual notch filter rejected light within a small bandwidth of the laser lines (488 nm and 647 nm), the purpose of the additional filters (like the ET700/75m) in the emission filter wheel was to transmit a more specific wavelength range of the emitted light. This additional emission filter wheel could be of use in photoconversion experiments (Szczyrak et al. 2014) or when it is necessary to reduce potential bleed-through.

Using a f=300 mm tube lens (Thorlabs) the emitted light was focused onto the chip of an

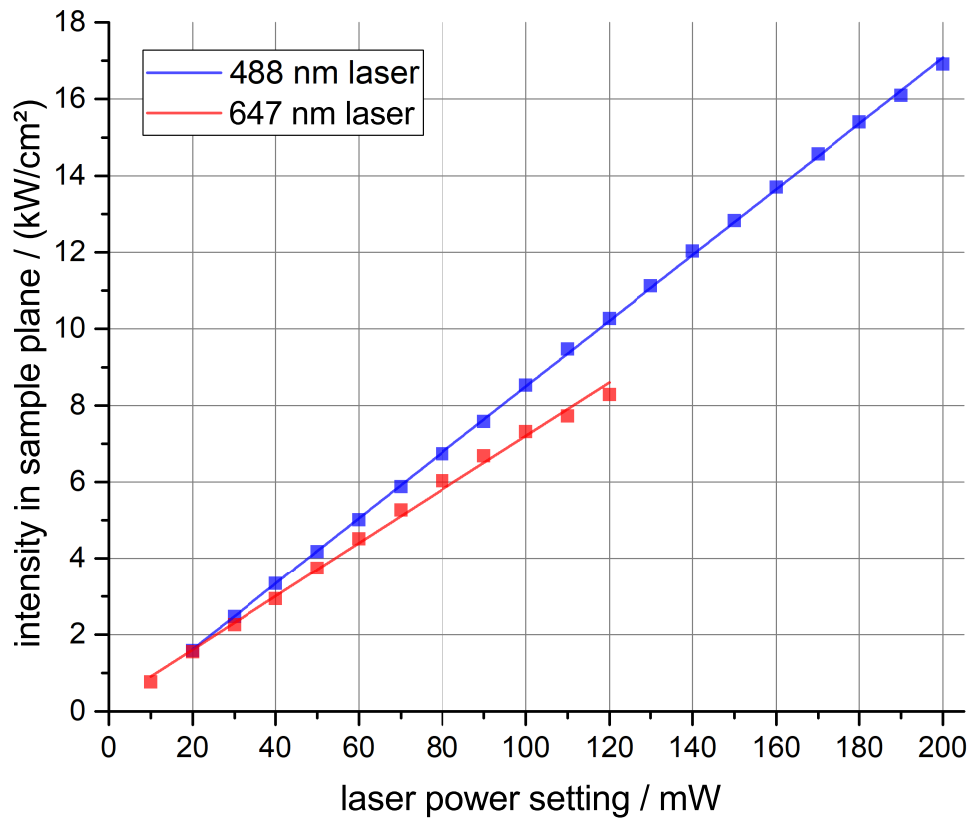


**Figure 3: Laser intensity at the sample plane for different output power settings.** Achievable intensities of 488 nm laser (blue line) and 647 nm laser (red line) in the sample plane, when operating the microscope in localization mode. Abscissa denotes laser output power as set by the software. Estimated illumination area in the sample is about  $640 \mu\text{m}^2$ .

electron multiplying charge-coupled device (EMCCD) camera (iXon 897 Ultra, DU-897E-CS0-#BV, Andor Technology). Its CCD chip contained 512 x 512 active pixels with a physical pixel size of 16 x 16  $\mu\text{m}$  and a pixel depth of 16 bit. It could be operated with (EM amplifier) or without electron multiplication (conventional amplifier). The camera was set up to be operated specialized for single molecule localization microscopy i.e. to achieve high acquisition rates, to encounter low signal intensities and having neglectable read-out noise by operating the camera in EM mode. However, for some applications, for instance DNA-PAINT (Jungmann et al. 2010), it can be more desirable to operate the camera using the conventional amplifier and therefore obtaining a higher capacity. The camera settings with the two amplifiers used are summarized in Table 1. Furthermore, the CCD chip was cooled to reduce dark current. To reduce vibrations, which can be caused by using an air ventilator, the camera was water-cooled down to about -85  $^{\circ}\text{C}$ .

It is essential in SMLM to be able to localize a single molecule point in the sample plane with high precision and accuracy. A too large pixel size would result in a worse localization precision, whereas a too small pixel size could result in a low signal-to-noise ratio (Deschout et al. 2014). Furthermore, as a prerequisite for software-based processing, the diffraction-limited spot must be optimally sampled on the detector. The optimal pixel size depends on the emission wavelength of the dyes being used and can be estimated using the resolution criteria of Rayleigh (Rayleigh 1879; Rayleigh 1896) under consideration of the Nyquist–Shannon sampling theorem :  $0.61\lambda_{\text{em}} / \text{NA} \cdot 1/2.3$ . Here  $\lambda_{\text{em}}$  is the emission wavelength and NA the numerical aperture of the objective. This results in an optimal theoretically pixel size of 93 nm (Alexa Fluor 488, emission maximum at 525 nm, NA=1.49) and 118 nm (Alexa Fluor 647, emission maximum at 665 nm, NA=1.49) for the laser wavelengths used in the setup. Depending on the resolution criteria applied, those numbers can vary. For instance when using Abbe's resolution criteria (Abbe 1873) the optimal pixel size for Alexa Fluor 488 and a NA of 1.49 would be 77 nm. Due to the small field of view of the camera when using small pixel sizes and the main use of Alexa Fluor 647, the emission pathway of the setup was adjusted to achieve a pixel size in the order of 100 nm. To do so an objective with 100 $\times$  magnification and a tube lens with a focal length of 300 mm was used. This results in a theoretically pixel size of 96 nm, which was calculated using the following equation:

$$px = \frac{d_{\text{CCD}} f_{\text{reference}}}{M f_{\text{tubelens}}}$$

Here M denotes the magnification of the objective,  $d_{\text{CCD}}$  the physical pixel size of the detector,  $f_{\text{reference}}$  the reference focal length, which is 180 mm for Olympus objectives and  $f_{\text{tubelens}}$  is the focal length of the tube lens.

The pixel size was also determined experimentally using a stage micrometer (Meiji Techno). Measuring of five different line plots perpendicular to its markings, resulted in a mean pixel size of  $(95 \pm 1)$  nm (Supplementary Figure 2). Therefore a value of 95 nm for the pixel size was used in the subsequent processing of the images.

Next, the camera was calibrated to be able to convert the data counts into number of incident photons. A proper calibration is important since most algorithms assume a Poisson

Setting	FT	Pre-Amp gain	EM gain	read-out rate / MHz	VCS / $\mu$ s	VCV / V
Mode						
14 bit EM amplifier	on	4.9x	50	10.000	0.3	+4
14 bit CON amplifier	on	4.9x	off	3.000	0.3	+4

**Table 1: Settings used for the EMCCD camera.** Depending on experimental conditions, camera was either operated using electron multiplication (EM) amplifier or conventional (CON) amplifier. FT = frame transfer, VCS=vertical clock speed, VCV=vertical clock voltage.

Property	A/D conversion factor / ( $e^-$ /count)	offset / counts	EM gain	read-out noise / ( $e^-$ rms)	QE
Mode					
14 bit EM amplifier	11.6	99	50	56.5 (1.1)	0.9
14 bit CON amplifier	1.8	88.6	off	9.2	0.9

**Table 2: Performance of the EMCCD camera.** Corresponding camera settings used for the two amplifiers are shown in Table 1. Values were used as input for localization algorithms. Value in brackets denotes the read-out noise when using the corresponding EM gain. Quantum efficiency (QE) was obtained by measurements from the manufacturer of the camera. The QE value shown, corresponds to a wavelength of 700 nm.

noise model, which relies on absolute photon counts. Calibration was done according to the protocol in Lambert et al. 2014. To perform calibration measurements, the objective was removed and a blank white screen of a smartphone was used to create a uniform illumination. Figure 4 depicts the photon transfer curve (PTC) when using the EM (without EM gain) or the CON amplifier. The A/D conversion factor was determined by measuring the x-intercept of a linear fit with a fixed slope of 0.5 to the linear part of the Poisson noise data. This results in a A/D conversion factor of  $11.6 \text{ e}^-/\text{count}$  when using the EM amplifier and  $1.8 \text{ e}^-/\text{count}$  for the conventional amplifier. All performance settings which are necessary for the localization algorithm are summarized in Table 2. Of note, that when using an EM gain of 50 the read-out noise is reduced to approximately  $1.1 \text{ e}^- \text{ rms}$ . Higher EM gain values would lead to a further reduced read-out noise, thus neglectable for localization algorithms not considering read-out noise. However, since the camera is equipped with a 14 bit A/D converter, a higher EM gain would lead to saturation of the converter for high intensity signals. Therefore, the used EM gain is a compromise between low read-out noise and subsaturating signals.

## Point spread function (PSF) of the setup

To proof the correct assembly and adjustment of the optical system, as well as the performance of the objective lens, the point spread function (PSF) of the microscope was experimentally determined using fluorescent beads.

Z-stacks of beads were acquired with a stepsize of 10 nm. Camera exposure time and laser power were set to obtain subsaturating pixels. Camera and microscope were operated in EM and widefield mode, respectively. The GDSC SMLM PSF Creator plugin (Sussex 2016) was used to create an average PSF, as shown for  $\lambda_{\text{emission}}$  at 700 nm in Figure 5. A circular diffraction pattern without any visible deformations due to aberrations in the xy-plane is visible. The axial PSF is shown in orthogonal views of the yz- and xz-plane. Slight deformations of the axial PSF, probably due to light scattering, occur when imaging deeper into the sample. Fitting a 1D Gaussian PSF to the intensity values, obtained from the PSF in the xy-plane, yields a full width at half maximum (FWHM) of 336 nm. To quantify the experimental PSF more precisely i.e. for example to correct for the bead size of 100 nm, PSFj (Theer et al. 2014) was used. Results are shown in Table 3.  $\text{FWHM}_{\text{min}}$  and  $\text{FWHM}_{\text{max}}$  were obtained by fitting a 2D elliptical Gaussian to the PSF of the beads. Experimental FWHM of lateral and axial PSF are  $(299 \pm 2) \text{ nm}$  and  $(727 \pm 87) \text{ nm}$ , respectively. Asymmetry of the PSF i.e. deviation from a circular PSF is  $0.964 \pm 0.009$ . The planarity of  $\pm 18.1 \text{ nm}$  compared to the axial FWHM indicates that the whole field of view is in focus and no component like stage, objective or camera adapter induces a significant tilt of the sample.

## Stage drift

Due to the imaging of isolated point-like emitters and their position determination in the nanometer range, combined with acquisition times ranging from minutes to hours, sam-

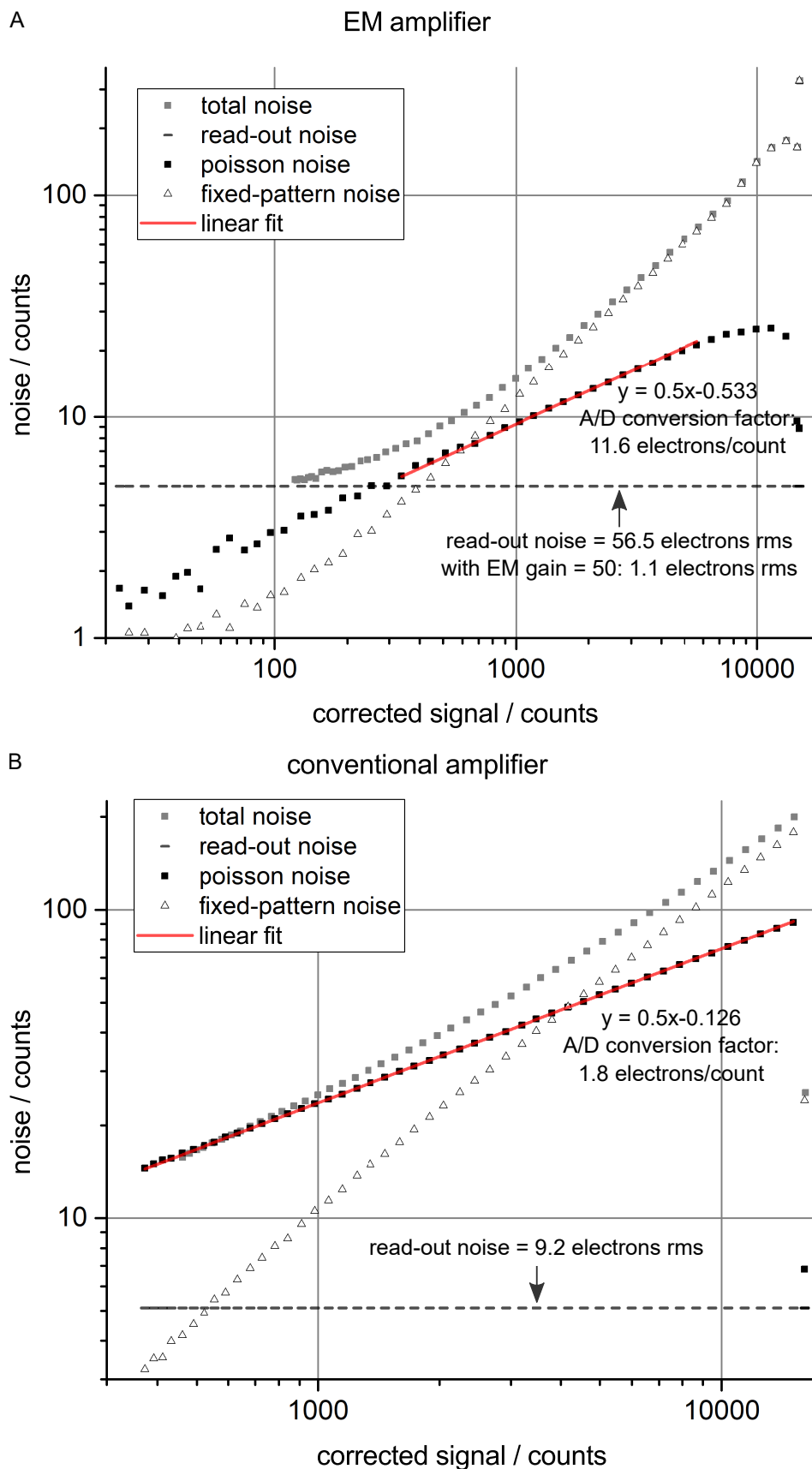


**Figure 4: Photon transfer curve (PTC) of the EMCCD camera.** A/D conversion factor as well as read-out noise was determined when using the (A) electron multiplication (EM) amplifier without EM gain or the (B) conventional amplifier. The abscissa displays the measured signal minus the camera offset, which was 99 counts in EM mode and 88.6 counts in the conventional mode.

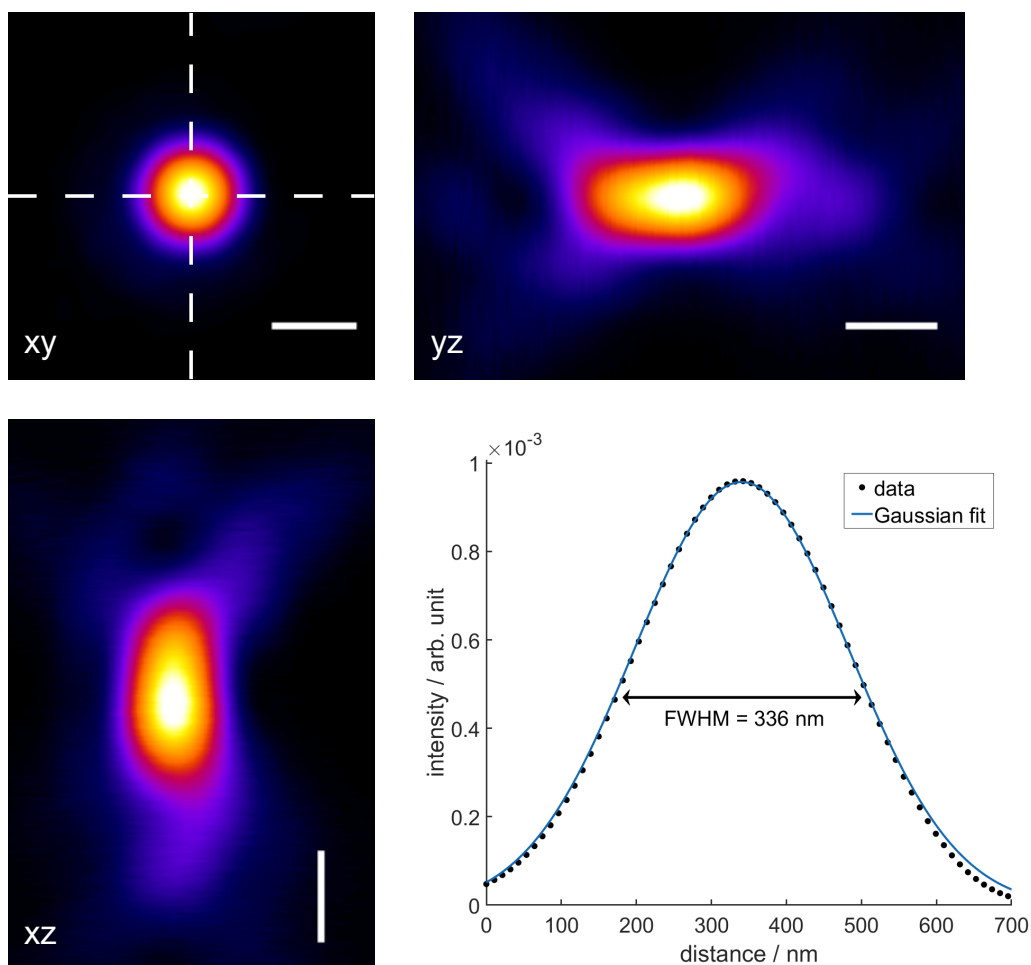


**Figure 5: Point spread function (PSF) of the setup.** Average PSF created from a z-stack of beads, measured at  $\lambda_{\text{emission}} = 700 \text{ nm}$  using GDSC SMLM PSF Creator plugin (Sussex 2016). Top left image shows the PSF in the xy-plane. Dashed lines indicate planes used for orthogonal view of yz-plane (top right) and xz-plane (bottom left). Scale bar = 400 nm. Fit of Gaussian PSF to intensity plot, obtained from the image of the xy-plane along the horizontal dashed line, is shown at the bottom right.

at $\lambda_{\text{emission}} = 700 \text{ nm}$	experimental / nm	theoretical / nm	normalized
$\text{FWHM}_{\text{min}}$ (lateral)	$299 \pm 2$	241	$1.24 \pm 0.01$
$\text{FWHM}_{\text{max}}$ (lateral)	$310 \pm 3$	241	$1.29 \pm 0.01$
FWHM (axial)	$727 \pm 87$	843	$0.9 \pm 0.1$
	experimental		
planarity	$\pm 18.1 \text{ nm}$		
asymmetry	$0.964 \pm 0.009$		

**Table 3: Properties of the PSF measured at  $\lambda_{\text{emission}} = 700 \text{ nm}$  using Tetraspeck beads.** Values were calculated using PSFj (Theer et al. 2014).  $\text{FWHM}_{\text{min}}$  and  $\text{FWHM}_{\text{max}}$  denote the smallest and largest half width as determined from the 2D elliptical Gaussian fit of the PSF to the beads. Asymmetry was determined by taking the ratio of  $\text{FWHM}_{\text{min}}$  and  $\text{FWHM}_{\text{max}}$ . Experimental values were corrected for a bead size of 100 nm and represent the median of the beads measured in the field of view. normalized = experimental value normalized to theoretical value.

ple drift is common. To estimate the expected sample drift and the waiting time between subsequent measurements after movement of the stage, fluorescent beads were imaged and their drift was calculated. First, this was done to determine the drift in lateral direction. Influences due to axial drift of the stage were reduced by waiting until the stage was stabilized i.e. through visual inspection of the camera images that beads stay in focus over time (several minutes). Next, the stage was moved in lateral direction and acquisition was started immediately after a new position was reached. In total 30,000 frames were acquired with an exposure time of 100 ms per frame. ILE software (<https://gitlab.com/microscopy/ILE.git>) was used to identify bead positions and to determine the drift. Results from this analysis are shown in Figure 6. For 80 min acquisition time, the mean lateral stage drift is about 550 nm. It is non-linear and largest at the beginning of the measurement, which is due to residual movement of the stage stepper motors. Within the first 8 min of acquisition it is 22.5 nm/min and reduces to 8 nm/min in the time window of 10 min to 25 min. This transition to a lower average stage drift indicates the minimum time that must be waited when starting a new acquisition after stage movement. Next, the axial sample drift was determined. Therefore, a cylindrical lens ( $f=1.000$  mm) was placed in front of the camera chip to enable astigmatism-based 3D localization microscopy (Huang et al. 2008). This time, the acquisition was started after waiting for at least 30 minutes until the table with the sample had been stabilized. 90,000 frames with an integration time of 40 ms were taken. For calibration of axial position of beads, a z-stack with a stepsize of 10 nm was acquired. ThunderSTORM (Ovesny et al. 2014) was used to determine relative spatial positions of the acquired beads. Positions were imported to Matlab (MathWorks) and lateral as well as axial drift was determined using the drift correction module of ILE by using the xy- and yz-projections. Results are shown in Figure 7. While the lateral drift is 150 nm and is rather linear, the axial drift accumulates to about 300 nm and shows an oscillation-like pattern, indicating that the sample is drifting slowly out of focus.

## Imaging of samples

The overall performance was accessed using different biological and non-biological samples, whereby the ground truth structure is known. A common biological sample to measure the achievable performance of a SMLM setup are microtubules.

Stained microtubule were imaged under epi-illumination using 647 nm laser with a power setting of 90 mW. 20,000 frames were taken with a camera exposure time of 40 ms. The camera was operated in EM mode. ILE software was used for evaluation, post-processing and visualization (settings: threshold: 3; multi-frame point radius:  $2.5\sigma$ ; filtering FWHM  $\leq$  155 nm). Figure 8 shows the reconstructed super-resolution image of microtubules. In the enlarged ROI the hollow-like structure of the microtubule bundle, hidden by conventional microscopy, becomes visible. An intensity plot through the cross-section of a microtubule shows a peak-to-peak distance of about 45 nm, indicating a minimum structural resolution of the setup. Furthermore, without drift correction methods applied, those structures would not have been resolved due to a drift of about 50 nm during sample acquisition.

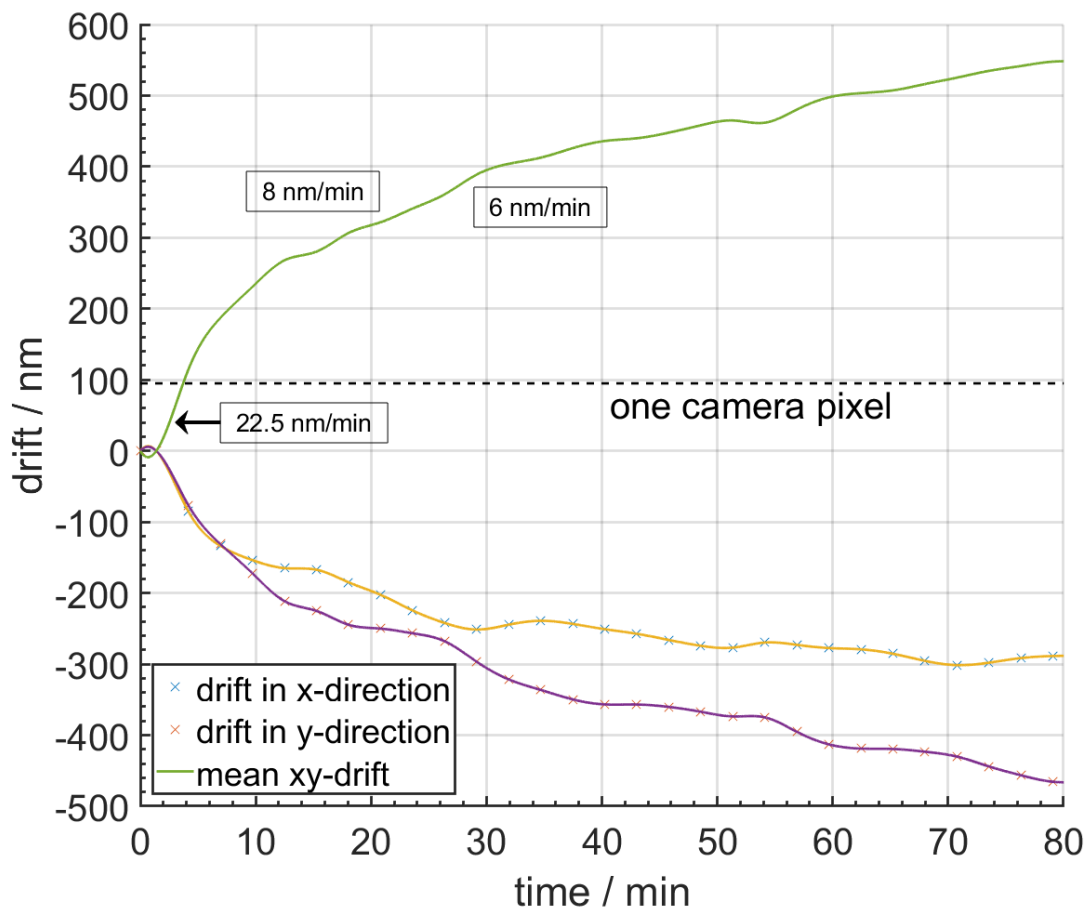


**Figure 6: Lateral stability of the setup.** The x- and y-drift of a bead sample was measured for 80 min. From this the mean drift relative to the starting position was determined (green line). Before the measurement was started, time was left until stage had been stabilized in axial direction. After that, stage was moved laterally to a new position and acquisition was started directly. Numbers in boxes indicate mean drift in certain time windows (0 min to 8 min: 22.5 nm/min, 10 min to 25 min: 8 nm/min, 20 min to 40 min: 6 nm/min). The dashed line indicates the camera pixel size of 95 nm in the sample plane.

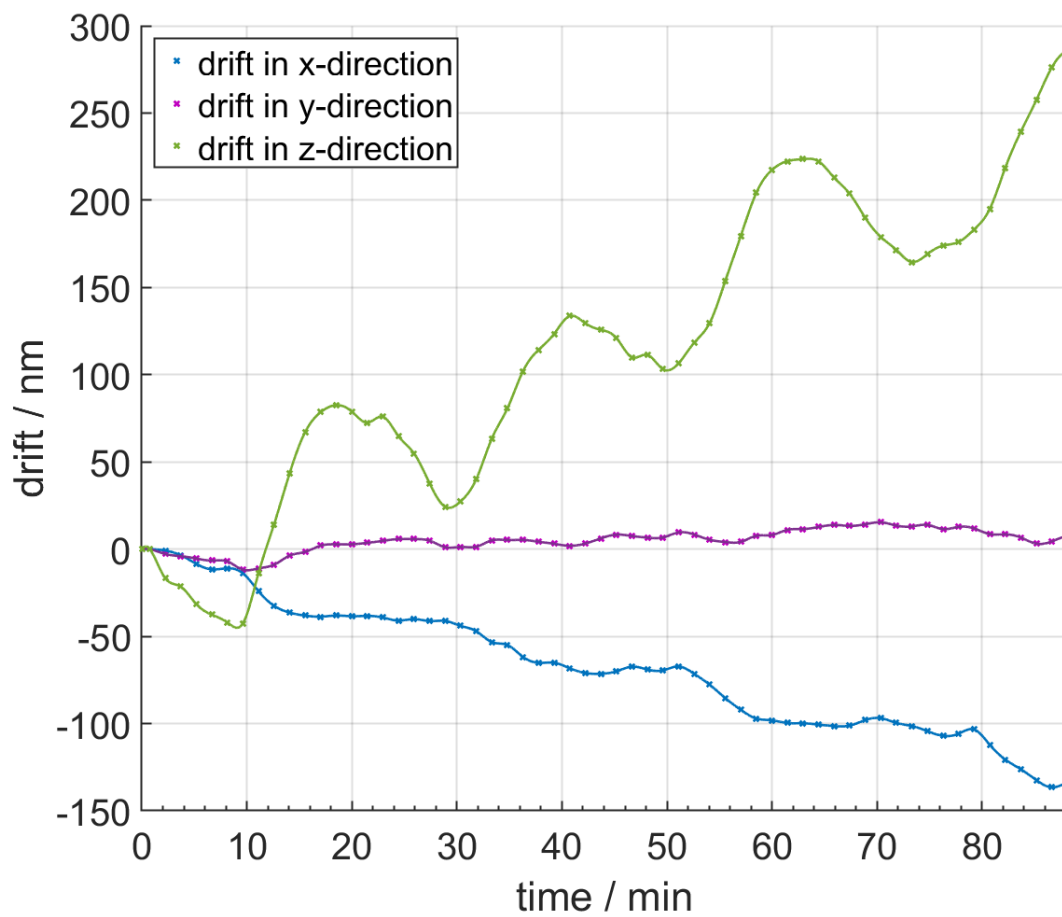


**Figure 7: Axial stability of the setup measured using fluorescent beads.** z-drift of a bead sample was measured for about 90 min (green line). Additional lateral drift in x-direction (blue line) and y-direction (purple line) is shown.

Next, nanorulers (PAINT 40RG, Gattaquant) were used for further performance evaluation. Each nanoruler consists of three marks, which are spaced 40 nm apart from each other. In contrast to the microtubule sample, where reversible photobleaching is used to achieve optical isolation needed for SMLM, here optical isolation is achieved via binding and unbinding of DNA Atto 655-labeled imager strands to their complementary counterparts attached at the nanorulers (DNA points accumulation for imaging in nanoscale topography (DNA-PAINT), Jungmann et al. 2010). Since the mean binding time between DNA strands determines exposure time of the camera and is usually designed with the purpose to achieve high photon emissions during a frame to improve localization precision, the camera was operated using the conventional amplifier, hence avoiding saturation of the A/D converter. Furthermore, the microscope was operated in TIRF-configuration, since imager strands are non-fluorogenic i.e. emitting weak fluorescence when floating in embedding medium and are not bound to a complementary docking strand. In total 20,000 frames were taken with an camera exposure time of 100 ms and a laser power of 50 mW. ILE software was used to evaluate and visualize the data set (Figure 9A). Single nanorulers can be seen, where most of them consist of three marks. To obtain the distances between the marks of the nanorulers GATTAnalysis software (Gattaquant) was used. A mean mark-to-mark distance of 44.8 nm with a standard error of the mean of 0.6 nm could be determined (Figure 9B). Mean localization precision of a emitter was 1.6 nm, as determined experimentally by nearest neighbor based analysis (NeNA, Endesfelder et al. 2014, Figure 9C). For estimation of the resolution Fourier ring correlation (FRC) was used (Nieuwenhuizen et al. 2013). An FRC value of 23.0 nm  $\pm$  0.1 nm was obtained (Figure 9D). The drift during the 33 minutes of imaging was in the order of 200 nm.

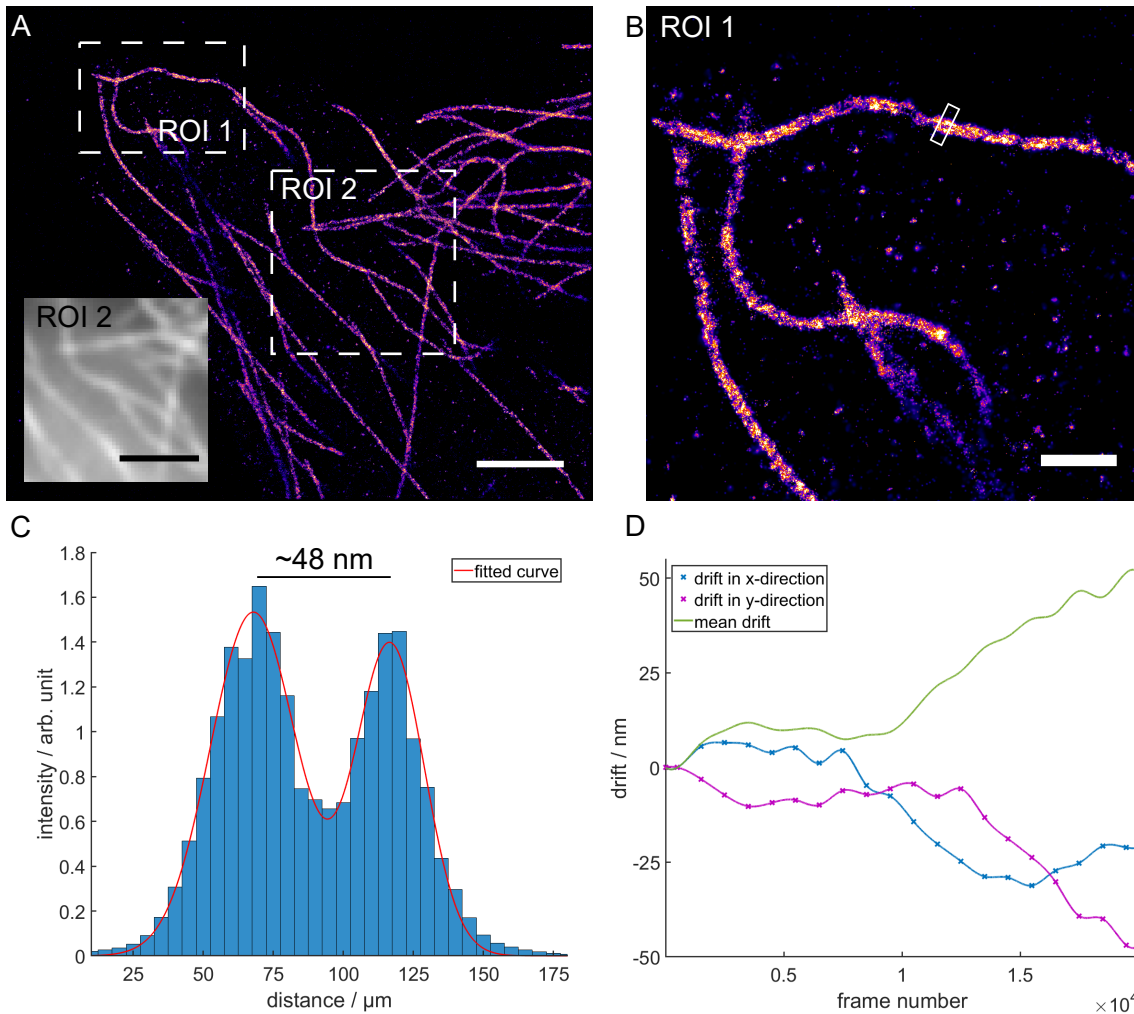


**Figure 8: Performance of the setup shown at a microtubule sample.** (A) Super-resolved image of microtubule. Inset shows conventional image of ROI 2. Scale bar = 2  $\mu\text{m}$ . (B) Enlarged section of ROI 1 from A, visualizing single microtubule bundles. Scale bar = 500 nm. (C) A cross-section was taken (B, white box) to show the intensity distribution perpendicular to the microtubule bundle. The red line represents the fit of the sum of two Gaussians. (D) Drift of the sample during acquisition. The exposure time per frame was 40 ms, resulting in a total recording time of 13 minutes.

## 4 Conclusions

Not only optimization of sample preparation is important in SMLM, also a proper calibration and setting of the microscope components is necessary, to achieve optimal blinking behavior of the emitters during imaging and a precise determination of the emitter positions. Therefore, the components of the constructed microscope were calibrated for optimal performance.

One key aspect in many SMLM imaging modalities based on reversible photobleaching or methods that rely on transient binding like DNA-PAINT (Jungmann et al. 2010) or DNA

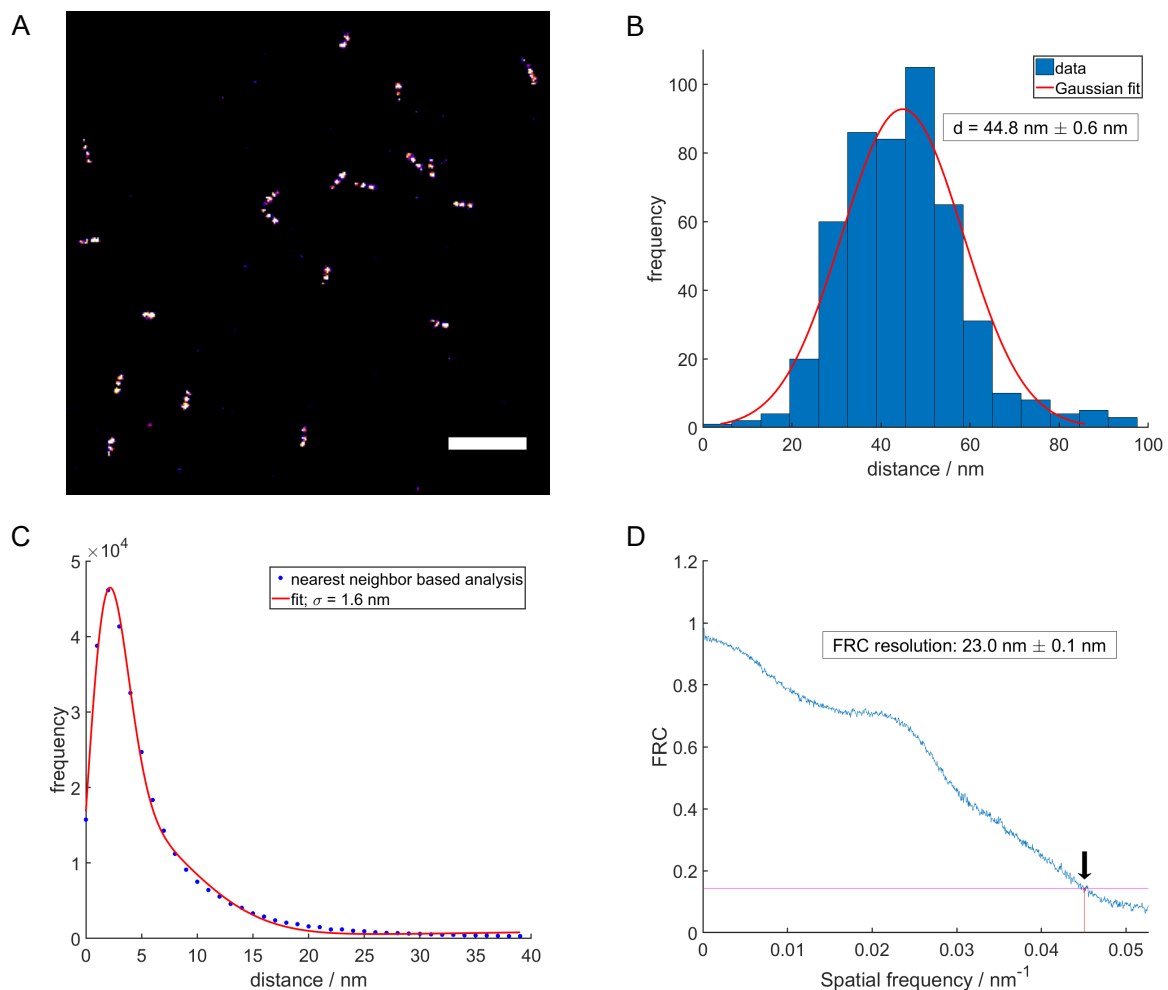


**Figure 9: Performance evaluation of the setup using Gattaquant DNA-PAINT nanorulers.** (A) Excerpt of a reconstructed SMLM image of nanorulers. Scale bar = 500 nm. (B) Frequency distribution of the mark-to-mark distances of about 500 nanorulers. Values in the box indicate mean distance between two marks ( $\pm$  SEM) as obtained by the Gaussian fit. (C) Experimental determination of the localization precision of DNA-PAINT probes using nearest neighbor based analysis (NeNA, Endesfelder et al. 2014). (D) Resolution estimation by means of Fourier ring correlation (FRC) (Nieuwenhuizen et al. 2013).

structure fluctuation-assisted BALM (fBALM, Szczurek et al. 2017) is to achieve sufficient laser intensities in the sample plane. Here both lasers have shown to provide several kW/cm<sup>2</sup>, enough for typical SMLM measurements.

Furthermore, all optical components must be configured that the theoretically expected diffraction limited PSF is achieved. It must be also validated that no optical aberrations due to misaligned optical elements occur. Therefore, the PSF was determined experimentally using fluorescent beads. Median values of the experimentally determined lateral FWHM's showed deviations from the theoretical ones by about 30%. This is within the normal range observed for different objectives (Theer et al. 2014). The asymmetry of the measured PSF was  $0.964 \pm 0.009$ , which indicates a nearly circular PSF and is also within tolerances (Theer et al. 2014).

Sample drift, resulting from mechanical instabilities of the setup or temperature fluctuations, is common. It can be divided in a lateral and in an axial drift component. The lateral drift is normally corrected using software based post-processing routines. Basically, those correlation-based routines split the data stack in several subsets and the shift is obtained by correlating the reconstructions of each subset with the reconstruction of a reference subset (Mlodzianoski et al. 2011; Geisler et al. 2012; Wang et al. 2014). Typical those correlation-based methods assume that the drift within a subset is linear and that a sufficient number of molecules are imaged within that subset for proper determination of the shift. Where the latter one can be partially controlled by the choice of the fluorophores and the embedding medium, the chosen subset size depends mostly on the specific drift characteristics of the setup. A typical subset size are 1,000 frames, which means that for an camera exposure time of 100 ms, the drift should be linear for about 2 min. Measurements of the lateral drift of the constructed setup have shown that time intervals in the order of several minutes exist where the drift is mostly linear. In those intervals the expected drift is below 10 nm/min. Oscillations or steep slopes, which would make it necessary to image enough emitters in a short amount of time, could not be observed. Only when moving the sample stage to a different position it is appropriate to wait a few minutes until acquiring a new image, due to residual movement of the sample stage stepper motors. In applications where a sufficient number of molecules within the minimum possible subset can not be imaged, the use of fiduciary markers may be an option (Rust et al. 2006; Betzig et al. 2006).

Using those software-based post-processing methods, it is also possible to correct the axial drift as long as it does not exceed the focal depths. Since the focal depths is usually only a few hundred micrometers in size, corrections can be made usually for short term acquisitions only. From the axial drift measurements it could be seen that the sample is drifting out-of-focus within 90 min. More considerable are the oscillations and steep slopes, making it challenging to apply post-processing drift correction methods. One solution could be to use methods not requiring spatial binning of molecule positions for reconstructions and instead using directly their positions, thus allowing drift correction with a lower number of molecules per subset (Han et al. 2015). More appropriate would be drift correction methods that are already applied during imaging. Additional they would also avoid out-of-focus drift during long term sample acquisitions. Those methods can be divided in active hardware based stabilization methods (Carter et al. 2007; Bathe-Peters

et al. 2018) or so called online drift correction methods (Ma et al. 2017). Where the latter requires fiducial markers introduced into the sample, hardware based methods, which are measuring the axial drift using the reflection of an infrared beam, are most common in commercial microscopes. Furthermore, they allow to hold the selected axial position, since the focus system is mostly independent of the imaging system. Although challenging due to structural constraints of the microscope body, implementation of such an autofocus system in the existing setup should be considered in future extensions, when long term or 3D acquisitions are desired. Alternatively, one may also think of an online drift correction method in astigmatism based localization microscopy, where the mean axial displacement of the elliptical shape of the PSF of a subset of molecules is used as a measure of the shift in axial direction and is directly compensated by using the PIFOC objective scanner. Of course this method also assumes a linear axial drift within the subset.

For calibration of the overall performance of the microscope, microtubule were chosen. Aside from nuclear pores they are a biological sample with well defined structures so that the resolution performance can be directly accessed. Microtubules form a hollow-like structure with a known outer diameter of about 25 nm. Here, the hollow-like structure could be resolved and peak-to-peak distance of about 49 nm was measured. The increased distance, compared to the theoretical value, can be explained by the attachment of the fluorescently labeled linker to the target structure of the microtubule. In this case the linker are two antibodies (indirect immunostaining), with an estimated size of 10 nm per antibody. This explains the 24 nm difference observed when also considering that the binding orientation and the position of fluorophores on the antibody is unknown. Furthermore, the SMLM images also represent a 2D projection of the probe.

One drawback of using a biological sample like microtubule as performance or resolution estimation of a localization microscope is that obtainable results strongly depend on the biological sample preparation. Depending on the fixation and staining methods applied (Whelan et al. 2015), it is possible that the hollow-like structure of microtubule could be not observed even if the performance of the microscope allows it. To avoid such bias due to sample preparation, Gattaquant nanorulers consisting of three marks per nanoruler, with a pre-defined mark-to-mark distance of 40 nm, were used. These nanorulers utilize also DNA-PAINT, which means that high localization precisions can be achieved as could be seen from an experimental determined value of 1.6 nm. Furthermore, the constructed microscope was able to resolve the distances between the marks of the nanorulers visually. Possible due to missing binding sites, not all nanorulers showed three marks. Averaging over several nanorulers a mean mark-to-mark distance of  $(44.8 \pm 0.6)$  nm was measured. The difference from the nominal value of 40 nm could be due to accumulations of errors in production of the sample, position determination of the signals or uncorrected residual drift of the sample.

For this calibration sample, a structural resolution of about 23 nm by means of FRC was estimated. Considered from the point of view of the microscope setup and the software evaluation routines, a structural resolution of at least 23 nm can be achieved. However, caution is granted since achievable structural resolution depends on density of detected emitters and their localization precision and can therefore also vary over the reconstructed image.

## **Acknowledgements**

We gratefully acknowledge Dr. Frank Helleis, Dr. Thomas Klimach and the workshop of the MPI for Chemistry as well as the E-lab of the IMB for constructing the camera adapter and providing support in the assembly of the electronic components. We thank the IMB Microscopy Core Facility for providing the Gattaquant nanorulers and for their continues support. We also thank for support by the Max Planck Graduate Center, the Mainz Program for Chemical Allergology (MPCA) and the joint Laboratory of Inflammation & Microscopy (LIM).

## References

- Abbe, E. (Dec. 1873). "Beiträge zur Theorie des Mikroskops und der mikroskopischen Wahrnehmung". In: *Archiv für Mikroskopische Anatomie* 9 (1), pp. 413–418. DOI: 10.1007/BF02956173.
- Bathe-Peters, M., Annibale, P., and Lohse, M. J. (2018). "All-optical microscope autofocus based on an electrically tunable lens and a totally internally reflected IR laser". In: *Optics Express* 26 (3), p. 2359. DOI: 10.1364/OE.26.002359.
- Betzig, E., Patterson, G. H., Sougrat, R., Lindwasser, O. W., Olenych, S., Bonifacino, J. S., Davidson, M. W., Lippincott-Schwartz, J., and Hess, H. F. (Sept. 2006). "Imaging Intracellular Fluorescent Proteins at Nanometer Resolution". In: *Science* 313 (5793), pp. 1642–1645. DOI: 10.1126/science.1127344.
- Carter, A. R., King, G. M., Ulrich, T. A., Halsey, W., Alchenberger, D., and Perkins, T. T. (Jan. 2007). "Stabilization of an optical microscope to 01 nm in three dimensions". In: *Applied Optics* 46 (3), p. 421. DOI: 10.1364/AO.46.000421.
- Dempsey, G. T., Vaughan, J. C., Chen, K. H., Bates, M., and Zhuang, X. (Dec. 2011). "Evaluation of fluorophores for optimal performance in localization-based super-resolution imaging." In: *Nature methods* 8 (12), pp. 1027–36. DOI: 10.1038/nmeth.1768.
- Deschout, H., Cella Zanacchi, F., Mlodzianoski, M., Diaspro, A., Bewersdorf, J., Hess, S. T., and Braeckmans, K. (Mar. 2014). "Precisely and accurately localizing single emitters in fluorescence microscopy." In: *Nature methods* 11 (3), pp. 253–66. DOI: 10.1038/nmeth.2843.
- Edelstein, A., Amodaj, N., Hoover, K., Vale, R., and Stuurman, N. (2010). "Computer control of microscopes using manager". In: *Current Protocols in Molecular Biology* (SUPPL. 92), pp. 1–17. DOI: 10.1002/0471142727.mb1420s92.
- Endesfelder, U., Malkusch, S., Fricke, F., and Heilemann, M. (June 2014). "A simple method to estimate the average localization precision of a single-molecule localization microscopy experiment." In: *Histochemistry and cell biology* 141 (6), pp. 629–38. DOI: 10.1007/s00418-014-1192-3.
- Geisler, C., Hotz, T., Schönle, A., Hell, S. W., Munk, A., and Egner, A. (Mar. 2012). "Drift estimation for single marker switching based imaging schemes". In: *Optics Express* 20 (7), p. 7274. DOI: 10.1364/OE.20.007274.

- Gustafsson, M. G. (May 2000). "Surpassing the lateral resolution limit by a factor of two using structured illumination microscopy." In: *Journal of microscopy* 198 (Pt 2), pp. 82–7.
- Han, R., Wang, L., Xu, F., Zhang, Y., Zhang, M., Liu, Z., Ren, F., and Zhang, F. (2015). "Drift correction for single-molecule imaging by molecular constraint field, a distance minimum metric". In: *BMC Biophysics* 8 (1), p. 1. DOI: 10.1186/s13628-014-0015-1.
- Heilemann, M., Van De Linde, S., Schüttpele, M., Kasper, R., Seefeldt, B., Mukherjee, A., Tinnefeld, P., and Sauer, M. (2008). "Subdiffraction-resolution fluorescence imaging with conventional fluorescent probes". In: *Angewandte Chemie - International Edition* 47 (33), pp. 6172–6176. DOI: 10.1002/anie.200802376.
- Heintzmann, R. and Cremer, C. G. (Jan. 1999). "Laterally modulated excitation microscopy: improvement of resolution by using a diffraction grating". In: ed. by I. J. Bigio, H. Schneckenburger, J. Slavik, K. Svanberg, and P. M. Viallet, pp. 185–196. DOI: 10.1117/12.336833.
- Hell, S. W. and Wichmann, J. (June 1994). "Breaking the diffraction resolution limit by stimulated emission: stimulated-emission-depletion fluorescence microscopy". In: *Optics Letters* 19 (11), p. 780. DOI: 10.1364/OL.19.000780.
- Hess, S. T., Girirajan, T. P. K., and Mason, M. D. (Dec. 2006). "Ultra-high resolution imaging by fluorescence photoactivation localization microscopy." In: *Biophysical journal* 91 (11), pp. 4258–72. DOI: 10.1529/biophysj.106.091116.
- Huang, B., Wang, W., Bates, M., and Zhuang, X. (Feb. 2008). "Three-Dimensional Super-Resolution Imaging by Stochastic Optical Reconstruction Microscopy". In: *Science* 319 (5864), pp. 810–813. DOI: 10.1126/science.1153529.
- Jungmann, R., Steinhauer, C., Scheible, M., Kuzyk, A., Tinnefeld, P., and Simmel, F. C. (2010). "Single-molecule kinetics and super-resolution microscopy by fluorescence imaging of transient binding on DNA origami". In: *Nano Letters* 10 (11), pp. 4756–4761. DOI: 10.1021/nl103427w.
- Lambert, T. J. and Waters, J. C. (2014). *Assessing camera performance for quantitative microscopy*. 1st ed. Vol. 123. June 2014. Elsevier Inc., pp. 35–53. DOI: 10.1016/B978-0-12-420138-5.00003-3.
- Lemmer, P., Gunkel, M., Baddeley, D., Kaufmann, R., Urich, A., Weiland, Y., Reymann, J., Müller, P., Hausmann, M., and Cremer, C. (Sept. 2008). "SPDM: light microscopy with single-molecule resolution at the nanoscale". In: *Applied Physics B* 93 (1), pp. 1–12. DOI: 10.1007/s00340-008-3152-x.

- Lemmer, P., Gunkel, M., Weiland, Y., Müller, P., Baddeley, D., Kaufmann, R., Urich, A., Eipel, H., Amberger, R., Hausmann, M., and Cremer, C. (Aug. 2009). "Using conventional fluorescent markers for far-field fluorescence localization nanoscopy allows resolution in the 10-nm range." In: *Journal of microscopy* 235 (2), pp. 163–71. DOI: 10.1111/j.1365-2818.2009.03196.x.
- Ma, H., Xu, J., Jin, J., Huang, Y., and Liu, Y. (2017). "A Simple Marker-Assisted 3D Nanometer Drift Correction Method for Superresolution Microscopy". In: *Biophysical Journal* 112 (10), pp. 2196–2208. DOI: 10.1016/j.bpj.2017.04.025.
- Mlodzianoski, M. J., Schreiner, J. M., Callahan, S. P., Smolková, K., Dlasková, A., Šantorová, J., Ježek, P., and Bewersdorf, J. (Aug. 2011). "Sample drift correction in 3D fluorescence photoactivation localization microscopy". In: *Optics Express* 19 (16), p. 15009. DOI: 10.1364/OE.19.015009.
- Nieuwenhuizen, R. P. J., Lidke, K. A., Bates, M., Puig, D. L., Grünwald, D., Stallinga, S., and Rieger, B. (June 2013). "Measuring image resolution in optical nanoscopy." In: *Nature methods* 10 (6), pp. 557–62. DOI: 10.1038/nmeth.2448.
- Ovesny, M., Kříek, P., Borkovec, J., Vindrych, Z., and Hagen, G. M. (Aug. 2014). "ThunderSTORM: a comprehensive ImageJ plug-in for PALM and STORM data analysis and super-resolution imaging". In: *Bioinformatics* 30 (16), pp. 2389–2390. DOI: 10.1093/bioinformatics/btu202.
- Rayleigh (Oct. 1879). "XXXI. Investigations in optics, with special reference to the spectro-scope". In: *The London, Edinburgh, and Dublin Philosophical Magazine and Journal of Science* 8 (49), pp. 261–274. DOI: 10.1080/14786447908639684.
- Rayleigh (Aug. 1896). "XV. On the theory of optical images, with special reference to the microscope". In: *The London, Edinburgh, and Dublin Philosophical Magazine and Journal of Science* 42 (255), pp. 167–195. DOI: 10.1080/14786449608620902.
- Rust, M. J., Bates, M., and Zhuang, X. (Oct. 2006). "Sub-diffraction-limit imaging by stochastic optical reconstruction microscopy (STORM)". in: *Nature Methods* 3 (10), pp. 793–796. DOI: 10.1038/nmeth929.
- Sharonov, A. and Hochstrasser, R. M. (Dec. 2006). "Wide-field subdiffraction imaging by accumulated binding of diffusing probes". In: *Proceedings of the National Academy of Sciences* 103 (50), pp. 18911–18916. DOI: 10.1073/pnas.0609643104.
- Sussex (2016). [http://www.sussex.ac.uk/gdsc/intranet/microscopy/imagej/smlm\\_plugins](http://www.sussex.ac.uk/gdsc/intranet/microscopy/imagej/smlm_plugins).
- Szczurek, A., Klewes, L., Xing, J., Gourram, A., Birk, U., Knecht, H., Dobrucki, J. W., Mai, S., and Cremer, C. (Jan. 2017). "Imaging chromatin nanostructure with binding-activated localization microscopy based on DNA structure fluctuations". In: *Nucleic*

*Acids Research* 45 (8). DOI: 10.1093/nar/gkw1301.

Szczurek, A., Prakash, K., Lee, H.-K., Żurek-Biesiada, D. J., Best, G., Hagmann, M., Dobrucki, J. W., Cremer, C., and Birk, U. (July 2014). “Single molecule localization microscopy of the distribution of chromatin using Hoechst and DAPI fluorescent probes”. In: *Nucleus* 5 (4), pp. 331–340. DOI: 10.4161/nuc1.29564.

Theer, P., Mongis, C., and Knop, M. (2014). “PSFj: Know your fluorescence microscope”. In: *Nature Methods* 11 (10), pp. 981–982. DOI: 10.1038/nmeth.3102.

Wang, Y., Schnitzbauer, J., Hu, Z., Li, X., Cheng, Y., Huang, Z.-L., and Huang, B. (June 2014). “Localization events-based sample drift correction for localization microscopy with redundant cross-correlation algorithm”. In: *Optics Express* 22 (13), p. 15982. DOI: 10.1364/OE.22.015982.

Whelan, D. R. and Bell, T. D. M. (2015). “Image artifacts in Single Molecule Localization Microscopy : why optimization of sample preparation protocols matters”. In: *Scientific Reports*. DOI: 10.1038/srep07924.

# Supplementary Material

## Conversion of a Confocal Laser Scanning Microscope into a Single Molecule Localization Microscope

Tentative author list. To be extended/adjusted.

Jan Neumann<sup>1,2</sup>, Kurt Lucas<sup>1</sup>, Ulrich Pöschl<sup>1</sup>, Udo Birk<sup>2,‡</sup> and Christoph Cremer<sup>1,2\*</sup>

<sup>1</sup>Multiphase Chemistry Department, Max Planck Institute for Chemistry,  
Hahn-Meitner-Weg 1, 55128 Mainz, Germany

<sup>2</sup>Institute of Molecular Biology, Ackermannweg 4, 55128 Mainz, Germany

<sup>‡</sup>Current address: Hochschule für Technik und Wirtschaft Chur,  
Pulvermühlestrasse 57, 7000 Chur, Switzerland

<sup>\*</sup>Correspondence to C. Cremer (c.cremer@imb-mainz.de)

## Supplementary Note 1: Materials used for converting the confocal laser scanning microscope into a single molecule localization microscope

### SMLM setup

- microscope body (Leica DMRBE, Type 301-371.011)
- mercury lamp (Leica, Type 307-072.05B)
- laser Sapphire 488-200 (Coherent, 1137967)
- Sapphire LP Heatsink (Coherent, 1110061)
- OBIS 647nm LX 120mW (Coherent, 1196627)
- custom-made laser shutters from hard drives
- EMCCD camera (Andor iXon+, DU-897E-CS0-#BV)
- water recirculator (Thermo Fisher Scientific, WKL 26)
- custom-made camera adapter
- C-mount adapter (Thorlabs, SM1A9)
- objective thread adapter (Thorlabs, RMSA1)
- PIFOC piezo objective scanner (Physik Instrumente, P-721.SDA)
- piezo amplifier (Physik Instrumente, E-665.XR LVPZT)
- objective distance piece (Physik Instrumente, P-721.90Q)
- 100x/NA 1.49 objective (Olympus, UAPON 100XOTIRF)
- immersion oil type F (Leica, 11513 859)
- z-galvo stage (Leica)
- stage controller Corvus-2 eco TT (ITK Dr. Kassen GmbH, 100-0141-009)
- optical table (Newport, RS4000)
- optical table supports (Newport, S-2000)
- air compressor (Thorlabs, PTA514)
- f = 10 mm (Thorlabs, AC050-010-A-ML)
- f = 40 mm (Thorlabs, AC254-040-A-ML)
- f = 100 mm (Thorlabs, AC254-100-A-ML)
- f = 125 mm (Thorlabs, AC254-125-A-ML)
- f = 300 mm tube lens (Thorlabs, AC254-300-A-ML)
- f = 1000 mm Cylindrical Lenses (Thorlabs, LJ1516RM-A)
- ND Filter, OD: 1.0 (Thorlabs, NDUV10A)
- mirrors (Thorlabs, PF10-03-P01-10)
- emission filter HQ500LP (Chroma Technology)
- emission filter ET700/75m (Chroma Technology)
- beamsplitter HC BS 580 (AHF Analysetechnik, F38-580)
- Leica filter cube (AHF Analysetechnik, F91-907)
- dual-notch filter 488/647 nm - U grade (AHF Analysetechnik, F40-003SG)
- dual line laser clean-up ZET488/640 (AHF Analysetechnik, F59-640)
- dual line dichroic mirror zt488/640rpc (AHF Analysetechnik, F58-639SG)
- motorized mirror flip mounts (Radiant Dyes, RD-KLS-1"-M)
- custom-made periscope holder
- LT series base plate (Thorlabs, LT101/M)
- single axis translation stage (Thorlabs, LT1/M)
- bottom unit periscope (Newport Oriel, 13715)
- top unit periscope (Thorlabs, RS99T/M)
- 10 mm travel piezo inertia (Thorlabs, PIAK10)
- inertial piezo driver T-Cube (Thorlabs, TIM101)
- K-Cube power supply (Thorlabs, KPS101)
- dovetail optical rail 300 mm (Thorlabs, RLA300/M)
- dovetail rail carrier (Thorlabs, RC1)
- kinematic mirror mount (Thorlabs, KMS/M)

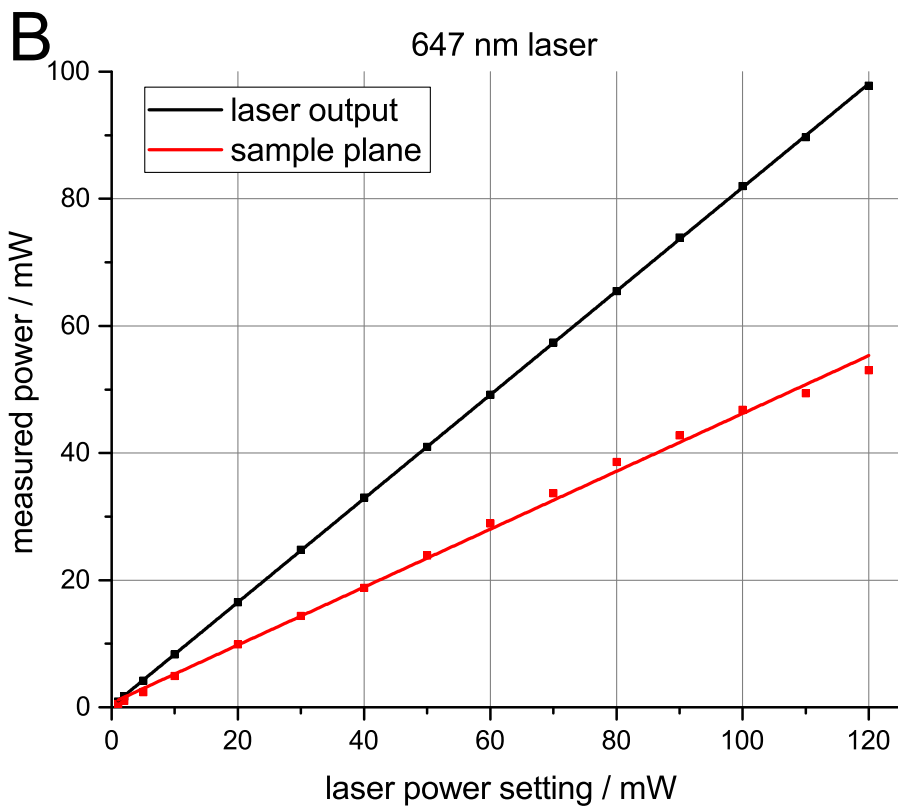
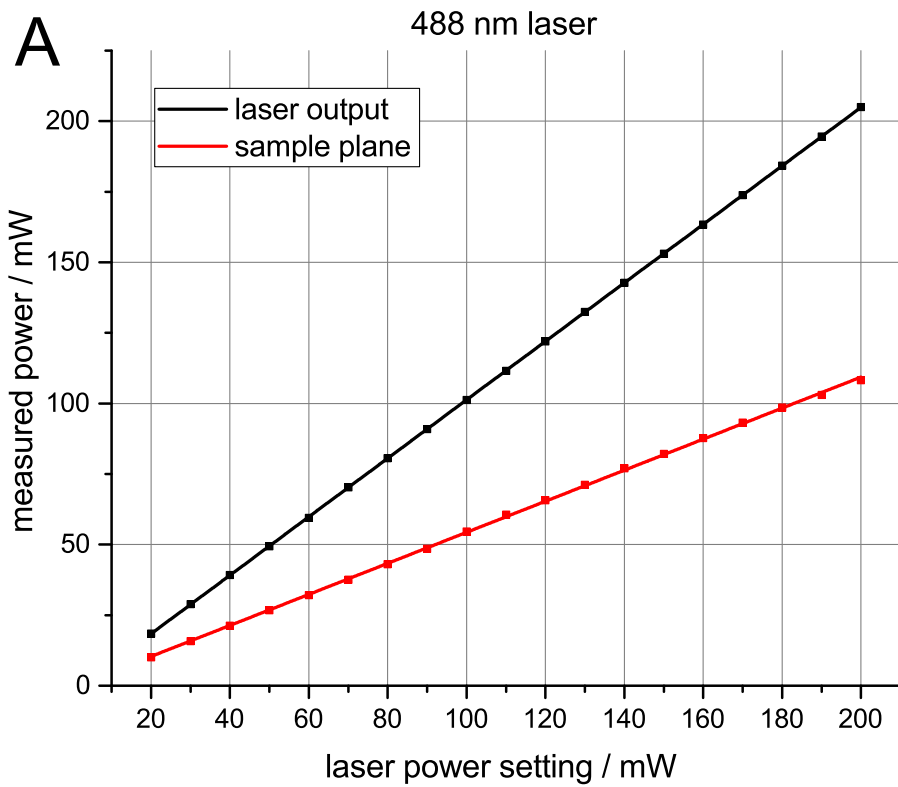
- mirror holder (Thorlabs, MH25T)
- 30 mm cage XY translator (Thorlabs, CXY1)
- XY translator for focusing lens (Thorlabs, ST1XY-A/M)
- post holder (Thorlabs, PH30/M)
- post holder (Thorlabs, PH40/M)
- pedestal style post holders (Thorlabs, PH75E/M)
- pedestal style post holders (Thorlabs, PH40E/M)
- clamping fork (Thorlabs, CF125C/M)
- clamping fork (Thorlabs, CF175)
- mounting base (Thorlabs, BA1S/M)
- mounting base (Thorlabs, BA1/M)
- cage assembly rod (Thorlabs)
- adjustable tube lens (Thorlabs, SM1V05, SM1V10, SM1V15)
- stackable lens tube (Thorlabs, SM1L05, SM1L20)
- cage plates (Thorlabs, CP02T/M, CP02/M, CP08/M)
- mirror mount (Newport, U100-A)
- flip mount for ND filters (Thorlabs, TRF90)
- hardware kit (Thorlabs)
- black masking tape (Thorlabs, T743-2.0)
- black aluminium foil (Thorlabs, BKF12)
- Arduino Uno R3 (EXP GmbH, EXP-R08-002)
- Arduino Mega 2560
- Adafruit 16-channel 12-bit PWM/servo driver (EXP GmbH, EXP-R15-017)
- filter wheel digital servo (HITEC, HS-5245MG)
- extension cables for servo motors (Conrad Electronics, 223742)
- Voltcraft SNG-1000-OW power plug (Conrad Electronics, 515511)
- Voltcraft SNG-2250-OW power plug (Conrad Electronics, 515513)
- circuit board (Conrad Electronics, 530126)
- cable set Raspberry PI (Conrad Electronics, 1182194)
- Pololu screw terminal block (EXP GmbH, EXP-R25-453)
- MOSFET IRF520 (Conrad Electronics, 162404)
- diode 1N4007 (Conrad Electronics, 162272)
- resistor set (Conrad Electronics, 535461)

### Calibration devices, samples, slides and embedding media

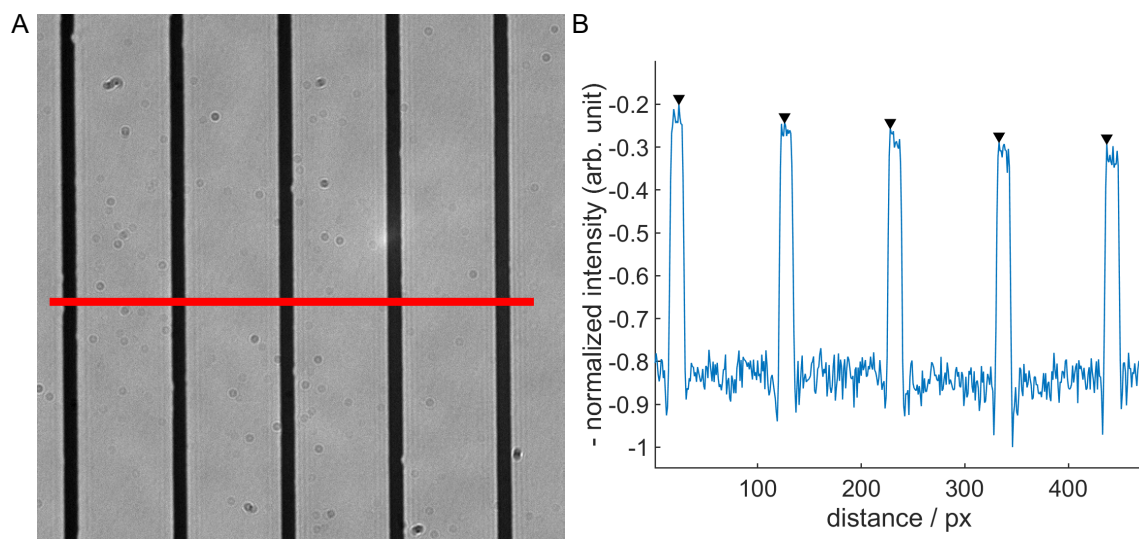
- alignment disk (Thorlabs, DG10-1500-H1-MD)
- shearing interferometer (Thorlabs, SI050)
- laser power meter (Nova II, Ophir Photonics)
- object micrometer (Meiji Techno, MA285, 0.01 mm)
- GATTA-PAINT 40 nm Nanoruler (Gattaquant, PAINT 40RG)
- fluorescent beads TetraSpeck Microspheres (Thermo Fisher Scientific, T7279)
- Vectashield H-1000 (Vector Laboratories, cat. no. H-1000)
- ProLong Gold antifade mountant (Thermo Fisher Scientific, cat. no. P36930)
- coverslips (R. Langenbrinck GmbH, 22 x 22 mm, thickness: 0.17 mm  $\pm$  0.005 mm)

### Software

- $\mu$ Manager (Edelstein et al. 2010, Version 2.0.0-beta3 20170424)
- APT software for motorized periscope mirror (Thorlabs)
- Leica DM SDK for control of Leica DM RBE stepper stage (Version 4.2.1)
- OriginPro 2016G (OriginLab, Version 93G)
- Matlab 2017b (MathWorks, Version 9.3.0.713579)
- GATTAnalysis (Gattaquant, Version 1.2)



**Supplementary Figure 1: Achievable laser power.** Laser power of (A) 488 nm and (B) 647 nm laser were measured in front of the lasers (black line) and in the sample plane (red line). Lowest possible power setting for 488 nm laser is 20 mW. Error bars are in the order of the symbol size.



**Supplementary Figure 2: Determination of camera pixel size in the sample plane.** The pixel size was determined by taking a line plot through five marks of the stage micrometer (**A**, red line) and calculating the peak to peak distances of the intensity plot along the line (**B**, indicated by arrows). Measuring of five different line plots yielded a mean pixel size of the camera in the sample of  $(95 \pm 1)$  nm. The line to line distance of the stage micrometer is 0.01 mm.

# Integrated Localization Environment (ILE): A Software Package to Evaluate and Process Blinking Based Single Molecule Localization Microscopy Data

Tentative author list. To be extended/adjusted.

Jan Neumann<sup>1,2</sup>, Martin Haggmann<sup>2</sup>, Frederik Grill<sup>3</sup>, Rainer Kaufmann<sup>4,5</sup>, Aleksander Szczurek<sup>2,†</sup>, Kirti Prakash<sup>2,‡</sup>, Ramon Lopez Perez<sup>6,7</sup>, Kurt Lucas<sup>1</sup>, Ulrich Pöschl<sup>1</sup>, Christoph Cremer<sup>1,2</sup> and Udo Birk<sup>2,\*</sup>

<sup>1</sup>Multiphase Chemistry Department, Max Planck Institute for Chemistry (MPIC),  
Hahn-Meitner-Weg 1, 55128 Mainz, Germany

<sup>2</sup>Institute of Molecular Biology (IMB), Ackermannweg 4, 55128 Mainz, Germany

<sup>3</sup>Kirchhoff-Institut für Physik, Universität Heidelberg, Im Neuenheimer Feld 227, 69120  
Heidelberg, Germany

<sup>4</sup>Division of Structural Biology, Wellcome Trust Centre for Human Genetics, University of  
Oxford, Roosevelt Drive, Oxford, OX3 7BN, United Kingdom

<sup>5</sup>Department of Biochemistry, University of Oxford, South Parks Road, Oxford, OX1 3QU,  
United Kingdom

<sup>6</sup>Department of Molecular and Radiation Oncology, German Cancer Research Center  
(DKFZ), Im Neuenheimer Feld 280, 69120 Heidelberg, Germany

<sup>7</sup>Heidelberg Institute for Radiation Oncology (HIRO), National Center for Radiation Research  
in Oncology, Im Neuenheimer Feld 280, 69120 Heidelberg, Germany

Correspondence: u.birk@imb-mainz.de; Tel.: +49-(0)-6131-39-21524

<sup>†</sup>Current address: Department of Biochemistry, University of Oxford, South Parks Road,  
Oxford OX1 3QU, United Kingdom

<sup>‡</sup>Current address: Department of Paediatrics, University of Cambridge, Box 116, Level 8,  
Cambridge Biomedical Campus, Cambridge CB2 0QQ, United Kingdom

\*Current address: Hochschule für Technik und Wirtschaft Chur,  
Pulvermühlestrasse 57, 7000 Chur, Switzerland

## Author contributions.

All authors listed, have made substantial, direct and intellectual contribution to the work, and approved it for publication. UB, CC, JN and UP conceived the study. JN drafted the manuscript; UB, CC, KL, AS contributed to the writing; UB, FG, MH, RK, JN, KP, RLP contributed to the software; AS provided the experimental data.

# Integrated Localization Environment (ILE): A Software Package to Evaluate and Process Blinking Based Single Molecule Localization Microscopy Data

Tentative author list. To be extended/adjusted.

Jan Neumann<sup>1,2</sup>, Martin Hagmann<sup>2</sup>, Frederik Gröll<sup>3</sup>, Rainer Kaufmann<sup>4,5</sup>, Aleksander Szczurek<sup>2,†</sup>, Kirti Prakash<sup>2,‡</sup>, Ramon Lopez Perez<sup>6,7</sup>, Kurt Lucas<sup>1</sup>, Ulrich Pöschl<sup>1</sup>, Christoph Cremer<sup>1,2</sup> and Udo Birk<sup>2\*</sup>

<sup>1</sup>Max Planck Institute for Chemistry (MPIC), Hahn-Meitner-Weg 1, 55128 Mainz, Germany

<sup>2</sup>Institute of Molecular Biology (IMB), Ackermannweg 4, 55128 Mainz, Germany

<sup>3</sup>Kirchhoff-Institut für Physik, Universität Heidelberg, Im Neuenheimer Feld 227, 69120 Heidelberg, Germany

<sup>4</sup>Division of Structural Biology, Wellcome Trust Centre for Human Genetics, University of Oxford, Roosevelt Drive, Oxford, OX3 7BN, United Kingdom

<sup>5</sup>Department of Biochemistry, University of Oxford, South Parks Road, Oxford, OX1 3QU, United Kingdom

<sup>6</sup>Department of Molecular and Radiation Oncology, German Cancer Research Center (DKFZ), Im Neuenheimer Feld 280, 69120 Heidelberg, Germany

<sup>7</sup>Heidelberg Institute for Radiation Oncology (HIRO), National Center for Radiation Research in Oncology, Im Neuenheimer Feld 280, 69120 Heidelberg, Germany

Correspondence: u.birk@imb-mainz.de; Tel.: +49-(0)-6131-39-21524

†Current address: Department of Biochemistry, University of Oxford, South Parks Road, Oxford OX1 3QU, United Kingdom

‡Current address: Department of Paediatrics, University of Cambridge, Box 116, Level 8, Cambridge Biomedical Campus, Cambridge CB2 0QQ, United Kingdom

\*Current address: Hochschule für Technik und Wirtschaft Chur, Pulvermühlestrasse 57, 7000 Chur, Switzerland

**Keywords:** image processing; SMLM; localization algorithm; drift correction

## Abstract

Typical algorithms used to reconstruct raw images based on single molecule localization microscopy (SMLM) offer a wide collection of routines and parameters to identify and localize single molecule signals, making it difficult and time consuming to optimize parameter settings for different SMLM experiments. Also, the underlying model to calculate the signal emitter positions can be complicated and not readily accessible to users. Here, we present Integrated Localization Environment (ILE); a software package to evaluate SMLM data. This includes post-processing routines like combination of points occurring in consecutive frames, signal candidate filtering, drift correction and various super-resolution visualization methods. The simplicity of the algorithm and the post-processing modules used makes it quick and easy to evaluate and process various SMLM data. We demonstrate the performance of our algorithm on different experimental data sets comprising different structures.

## 1 Introduction

Single molecule localization microscopy (SMLM) is a well-established tool in life sciences enabling investigations of biological processes and structures down to a few tens of nanometers - well below the diffraction-limited resolution of conventional light microscopy. To achieve this unprecedented resolution, single molecule signals need to be first acquired using a sensitive detector and then precisely and accurately localized in space using a sophisticated computer algorithm [1], [2]. The first step usually involves a thresholding algorithm that detects signals over a certain background value. A region of interest (ROI) is defined around these signals and these are then extracted from the data stack. In a second step, the position of the single molecule signal within the extracted ROI is estimated with a high precision [1], [3]. This can be done by either determining the center of intensity, by a least-square adaption (mostly by fitting a two-dimensional Gaussian point spread function (PSF) to the diffraction limited signal), by a maximum likelihood estimation (MLE) fitting [4], or by cubic splines [5]. All of these methods yield a list containing the x-, y- (and optionally z-) position coordinates of all identified single molecule signals. In addition to the positions, further information can be returned including localization precision (i.e. uncertainty of position estimation), detected number of photons, width of PSF etc.

The raw list of localizations can be further processed to remove artefacts due to blinking properties of fluorophores (e.g. overlapping signals or multiple detection of the same emitter) or stage drift during acquisition. These post-processing comprises filtering, combination of localizations occurring in consecutive frames and drift correction. Finally, after obtaining the corrected list of localizations, the position estimates and their respective localization precision values can be converted into a super-resolution image [6], [7] or can be used for further quantitative analysis like co-localization analysis [8], cluster analysis [9]–[11], resolution estimation using Fourier ring correlation (FRC) [12] or single molecule signal density distribution analysis [13]. Commonly used software packages like ThunderSTORM or rapidSTORM [14], [15] offer many settings for filtering and segmenting the images as well as for detecting the single molecule signals. This makes data evaluation cumbersome and time-consuming, especially for beginners new to the field of SMLM and experts from other fields who wish to use SMLM as a tool e.g. for their biological studies.

Therefore, in this work we present Integrated Localization Environment (ILE), an open source plugin for Matlab (<https://gitlab.com/microscopy/ILE.git>) to evaluate SMLM data. ILE puts the focus on a simple user guidance to evaluate the data quickly and easily. The core localization algorithm requires only one parameter provided by the user. This ensures a high reproducibility of the data analysis of single molecule localization microscopy experiments as an important step towards developing best practice. Additionally, our software package provides post-processing routines like combining localizations occurring in consecutive frames, single molecule candidate filtering and drift correction, as well as several visualization methods. We demonstrate the applicability on different experimental data sets, comprising different structures, imaging conditions and levels of background.

## 2 Materials and Methods

ILE consists of three separate modules: i) the algorithm to identify single molecule signals, ii) post-processing routines on list of identified single molecule signal candidates, iii) super-resolution visualization methods. A workflow of ILE is depicted in Figure 1.

### Localization algorithm

Single molecule signals are identified in raw SMLM acquisitions based on fastSPDM [16]. It assumes that the signals can be modeled by a 2D Gaussian function with a constant local background. This background is subtracted before determining the position of the signal. With this offset-correction, the maximum likelihood estimation of the signal position can be obtained from the center of mass of the input ROI [17].

The algorithm comprises four steps:

1. Background subtraction

At the beginning an initial background image is calculated by averaging over the first eight frames of the input data stack. This initial background image is subtracted from the first raw frame yielding a difference image. While looping through the frames of the raw data stack, the initial background image is continuously adjusted to account for changes in the background during acquisition. This happens by weighted-averaging the existing background image with the difference image, which is clipped by values larger than the standard deviation of the noise and scaled by a factor of 1/8. Negative values in the difference image are set to zero.

2. Segmentation

Next, signal peaks are identified from the difference image after applying a 3 x 3 median filter. Only signals with intensity higher than a certain threshold are identified as signal peaks. The threshold is defined as follows:

$$Threshold = (\alpha - 1) * \sqrt{\overline{I}_{bg}}$$

Where  $\alpha$  is a threshold parameter and  $\overline{I}_{bg}$  the mean background intensity calculated from current background image. The background is assumed to follow a Poissonian noise model, meaning that the standard deviation of the noise is equal to the square root of the background. With the threshold parameter  $\alpha$ , the user defines only one value by how much the signal peak must be above the background.

3. Position determination

The identified peaks are centered in a 7 x 7 px ROI and their position is determined using the Gaussian estimator [17]. It calculates the center of intensity of the input ROI, which in the case of zero-level background (due to the subtraction) equals to the maximum likelihood estimation of the signal position.

4. Signal separation

Single molecule signals that appeared simultaneously within a single ROI are separated in a fourth step, provided that their distance is just above the Sparrow resolution criterion applied to the digitized image. To do so, each ROI is scanned from its center towards its boundaries for local intensity minima. If a local minimum is detected, the ROI is clipped and the position of the signal will be recalculated. If more than 30 % of intensity is removed the signal is discarded from further analysis.

The algorithm then returns a list of the detected signals which we call “*Orte*”-matrix (german for locations). It contains in each line information about an individual signal, such as integrated signal level, peak height, position, or its localization precision.

To calculate the sample-based estimate localization precision an approximation to Mortensen's formula is used [4], [18]:

$$\widehat{\sigma}_{loc}^2 = \left( 1 + 4\tau + \sqrt{\frac{2\tau}{1 + 4\tau}} \right) * \frac{\sigma_p^2}{N} \quad (1)$$

with  $\sigma_p^2 = \sigma_{PSF}^2 + p^2/12$  and  $\tau = 2\pi\sigma_p^2 b/(Np^2)$ . Here,  $N$  denotes the number of detected photons,  $\sigma_{PSF}$  the width of Gaussian PSF,  $p$  the pixel size and  $b$  the noise level in the background, expressed in number of photons per pixel. If an electron multiplying charge-coupled device (EMCCD) camera is used the right-hand side of equation 1 has to be multiplied by a factor of 2 to account for excess noise [4], [19]. The thus obtained *Orte*-matrix can be further processed for the sake of post-processing or quantitative analyzes.

### Post-processing

After obtaining the raw list of localizations, several post-processing steps are advisable. In a first step, signals occurring in consecutive frames and originating from the same fluorophore should be merged to prevent from signal overcounting and improve the precision of the single molecule localization ( $\sigma_{loc}^2 \sim 1/N$ ). To combine single molecule signals that appear in one or more consecutive frames, a search radius parameter is applied. Signals in consecutive frames are combined if they are closer than (search radius parameter) x (mean localization precision). By default, a value of 2.5 times the mean localization precision is used.

The next post-processing step contains filtering of signals according to the width of the PSF, the localization precision or the peak intensity of the signals. This step is necessary to remove out-of-focus signals or signals that originate from autofluorescence of the sample. A further important aspect is to reject overlapping signals (i.e. PSF's that are not separated in the time domain during acquisition), which are particularly occurring in raw SMLM data of high signal density (see Fig. 3 for demonstration), as well as to minimize grid-like patterns. Those have been reported in reconstructions based on centroid-based position extraction methods, due to a bias in position-extraction of these overlapping signals with respect to the physical pixels of the detector array. The effects of both can be diminished by filtering *Orte*-matrix based on PSF width. Additionally, the z-extent covered by a SMLM acquisition can be decreased due to rejection of out-of-focus contributions having a larger PSF than signals within focus.

Finally, sample drift, a hallmark of mechanical instabilities or temperature fluctuation can be corrected. For this purpose, a drift correction routine based on cross-correlation of subsets of reconstructions is implemented [20]–[22]. Our routine determines the shift by correlating each subset with a reference subset. The shift among the subsets is interpolated and used to correct the position coordinates of detected signals. Correlation-based methods have shown to reliably reduce the drift down to ~5 nm precision [20] without introducing fiduciary markers into the sample [23], [24] or integrating an active stabilization system into the microscopy setup [25], [26].

## Visualization

In contrast to conventional microscopy techniques, the super-resolution image is not a direct result of e.g. camera image but rather needs to be reconstructed based on the list of localizations. To do so, the list of localizations (the *Orte*-matrix) containing the position estimates generated by the localization algorithm, must be mapped into an image. The choice of single molecule data visualization method is crucial as it needs to faithfully reflect the information on the structure which is stochastically sampled by means of single molecule signals, originating from dye molecules typically attached to the binding site via a linker. In addition, many mapping algorithms aim at visualizing features in addition to the extracted positions in the final reconstructions. Prominent examples are to visualize the localization precision by means of signal blurring, or to visualize the local signal density ([6], [7]).

Therefore, our software offers a broad range of mapping strategies, in which different visualization routines are implemented: scatter plot, histogram binning, Gaussian rendering, triangulation, Voronoi tessellation and local density-based visualization.

## Sample preparation and SMLM imaging

Detailed protocols on sample preparation and imaging conditions can be found in Supplementary Table 1. The SMLM setup used to acquire the demonstration data sets shipped with the software has been described in detail Szczurek et al. (2014) [27] (Supplementary Note 3).

## 3 Results

### Application of ILE to experimental SMLM data comprising different biological structures

To demonstrate the performance and applicability of our evaluation software, we first used three experimental data sets of various background contributions and three-dimensional extents. The first data set (Fig. 2a) comprises flat fluorescently labeled structures of the synaptonemal complex (dataset 1, "synaptonemal complex"; cell spread, less than 0.5  $\mu\text{m}$  thick) [28]. The second data set (Fig. 2b) contains data taken of antibody-stained microtubules (dataset 2, "microtubule";  $\sim 1$   $\mu\text{m}$  thick cell body), and the third data set (Fig. 2c) contains images taken of DNA staining of the cell nucleus (dataset 3, "nucleus"; nucleus equator,  $\sim 2$   $\mu\text{m}$  away from coverslip,  $\sim 4$   $\mu\text{m}$  nucleus thickness), which was imaged by using DNA structure fluctuation assisted binding activated localization microscopy (fBALM) technique [29]. As compared to the sample datasets 1 and 2, the demonstration images of the nucleus exhibit higher background levels (i.e. higher out-of-focus contribution), higher density of signals, and relatively high optical aberrations due to greater distance of the imaged sample from the coverslip surface. Our algorithm was able to reliably identify single molecule signals and reconstruct all data sets (Fig. 2).

It enables an insight into nanostructure of synaptonemal complex, revealing its two protein strands and their twisting (Fig. 2a, arrows). SMLM reconstruction of fluorescently labeled microtubules revealed their hollow structure (microtubule surface labeling using antibodies, Supplementary Fig. 1) which remains inaccessible to conventional widefield microscopy (Fig. 2a).

For all data sets we used the threshold value  $\alpha$  of 3, which is the only parameter in the localization algorithm that has to be optimized by the user. Usually this one is optimized by experimentally applying different threshold parameters (Supplementary Fig. 2). We found that a value of 3 is an optimal starting value for an initial evaluation suitable for practically all our experimental data. Smaller values may lead to

considerable amount of false positive detections, whereas when using much larger values, a considerable number of signals, which would normally contribute to structure reconstruction, are rejected during the extraction of the list of localizations. A refined value for the threshold parameter can be obtained by analysis of the photon counts and noise of the list of localizations obtained from the initial evaluation. Furthermore, we evaluated the runtime performance of ILE on those data sets (Table 1). The time values given include the time taken to read the data stack but exclude the post-processing routines and visualizations. For comparison the runtime performance of ThunderSTORM [14] on those data sets is displayed. All timing measurements were conducted on an AMD Ryzen 5 1600 CPU with a base clock of 3.20 GHz. In total our localization algorithm achieves comparable execution times as ThunderSTORM, considering that we do not use parallelization.

### **Post-processing routines in ILE**

After obtaining the list of localizations, the images shown in Fig. 2 have been subjected to post-processing involving drift correction and removal of overlapping signals via filtering localizations of broadest PSF (Fig. 3c). To show the importance of filtering and its effect on SMLM visualization, we imaged microtubules under sub-optimal photoswitching conditions (Fig. 3), resulting in poor single molecule contrast (Figure 3b). Due to their high density, many signals were overlapping. This is reflected in the distribution of the size of the different PSF's. By removing the signals with a PSF size (measured at full width at half maximum (FWHM)) of 150 nm or larger in both, x- and y-direction, the quality of the final reconstruction is improved (Figure 3e). A line plot through two closely spaced microtubule bundles indicate the improvement in image quality achieved by filtering the localizations from a data set with extremely poor switching (see raw data frame, Fig. 3b).

Since SMLM acquisitions can typically take several minutes to hours, sample drift is common. To correct drift that occurs during measurement, we implemented a correlation-based drift correction routine (Fig. 4). For demonstration a strongly drifted reconstruction of a microtubule data stack is shown, where the bundles of microtubules are smeared in x- and y-direction. By correlating 25 subsets of reconstructions, the drift correction routine, identified a drift of ~400 nm in x-direction and ~250 nm in y-direction over 30,000 frames. The drift between the subsets was interpolated and the position estimates of the identified single molecule signals had been corrected accordingly. In the final corrected reconstruction single microtubule fibers become visible. The appropriate correction of sample drift is also reflected by analyzing the mean nearest neighbor distance which is decreased by ~25 % (Fig. 4d). Using the Fourier ring correlation (FRC) method [12] we obtained a resolution estimation of  $(237 \pm 94)$  nm before drift correction compared to  $(54 \pm 3)$  nm after drift correction. We are using this routine also to correct for drift occurring in DNA acquisitions by fBALM (Suppl. Fig. 4).

The images shown in Fig. 2-4 were visualized using Gaussian rendering, however our ILE package also offers other visualization methods (Fig. 5). A detailed performance evaluation of these techniques in terms of image resolution and visual appearance is beyond the scope of this paper but can be found in the existing literature [6], [7].

## 4 Discussion

Beside optimized sample preparation and appropriate imaging conditions [30], the localization algorithm including post-processing steps and visualization plays an important role in qualitative and quantitative analysis of SMLM data. Typical algorithms [31] used to evaluate SMLM data, offer a wide range of settings, making it difficult to yield reproducible results, and often the software algorithm developed in the specific labs have a very steep learning curve for users from outside of that lab. In contrast, the simplicity of the localization algorithm used in ILE requires one parameter that must be optimized by the user. All other parameters are either specified by the microscope with which the sample was taken or are calculated by the software like the continuously adjusted background intensity. This limits greatly the number of iterations a user has to do to optimize the evaluation process. Furthermore, the localization algorithm works hand in hand with the post-processing routines. Our drift correction routine was able to reliably reduce the drift from ~400 nm down to the 10 nm range. Since it is based on cross-correlation of subsets of reconstructions it can be used for a variety of data sets, without the need for specific sample preparation i.e. introducing fiducial markers. Only a sufficient number of localizations within a subset is necessary to reliably correct the drift in lateral direction [20]. Furthermore, users have the choice between different super-resolution visualization methods.

We deem the ILE an essential step towards the development of best practice in the analysis of SMLM data. A discussion of the requirements on best practice candidate software can be found e.g. in [32]. Accordingly, the software must feature a user-friendly interface and guide the user step-by-step through the different steps in the evaluation procedure, detailing on the required parameters and what affect these parameters will have on the final reconstructions. Clearly, the user must be presented with a minimum number of options, essentially leaving two options for the implementation of the software supported by approaches from machine learning: i) parameter optimization for the particular type of data (i.e. labelled samples) at hand, or ii) automated parameter extraction based on the dataset presented.

ILE may be used to quickly process and evaluate different SMLM data sets without spending much time-consuming parameter adjustment. Nonetheless, it covers all the necessary post-processing routines to obtain state-of-the art SMLM images. In future versions of the software additional features like support for SMLM images obtained with scientific complementary metal-oxide-semiconductor (sCMOS) cameras or three-dimensional localization microscopy based on astigmatism [33] will be implemented.

### Acknowledgments

This work was supported by the Max Planck Society, the Boehringer-Ingelheim Foundation, the MPIC-IMB joint Laboratory of Inflammation and Microscopy (LIM), and the Mainz Program for Chemical Allergology (MPCA). JN acknowledges funding by the Max Planck Graduate Center with the University of Mainz (MPGC). We would like to express our gratitude to Dr. Gerrit Best for support.

### Author contributions

All authors listed, have made substantial, direct and intellectual contribution to the work, and approved it for publication. UB, CC, JN and UP conceived the study. JN drafted the manuscript; UB, CC, KL, AS contributed to the writing; UB, FG, MH, RK, JN, KP, RLP contributed to the software; AS provided the experimental data.

## Conflict of interest

The founding sponsors had no role in the design of the study; in the collection, analyses, or interpretation of data; in the writing of the manuscript, and in the decision to publish the results. UB and CC are also affiliated with LuciaOptics Forschungszentrum, a non-profit company based in Karlsruhe, Germany.

The following abbreviations are used in this manuscript:

ILE	Integrated Localization Environment
SMLM	single molecule localization microscopy
ROI	region of interest
PSF	point spread function
MLE	maximum likelihood estimation
GUI	graphical user interface
FRC	Fourier ring correlation
EMCCD	electron multiplying charge-coupled device
fBALM	DNA structure fluctuation assisted binding activated localization microscopy
FWHM	full width at half maximum
sCMOS	scientific complementary metal–oxide–semiconductor

## References

- [1] A. Small and S. Stahlheber, “Fluorophore localization algorithms for super-resolution microscopy.,” *Nat. Methods*, vol. 11, no. 3, pp. 267–79, Mar. 2014.
- [2] H. Deschout *et al.*, “Precisely and accurately localizing single emitters in fluorescence microscopy.,” *Nat. Methods*, vol. 11, no. 3, pp. 253–66, Mar. 2014.
- [3] B. Rieger, R. Nieuwenhuizen, and S. Stallinga, “Image Processing and Analysis for Single-Molecule Localization Microscopy: Computation for nanoscale imaging,” *IEEE Signal Process. Mag.*, vol. 32, no. 1, pp. 49–57, 2015.
- [4] K. I. Mortensen, L. S. Churchman, J. A. Spudich, and H. Flyvbjerg, “Optimized localization analysis for single-molecule tracking and super-resolution microscopy,” *Nat. Methods*, vol. 7, no. 5, pp. 377–381, May 2010.
- [5] H. P. Babcock and X. Zhuang, “Analyzing Single Molecule Localization Microscopy Data Using Cubic Splines,” *Sci. Rep.*, vol. 7, no. 1, p. 552, Dec. 2017.
- [6] D. Baddeley, M. B. Cannell, and C. Soeller, “Visualization of Localization Microscopy Data,” *Microsc. Microanal.*, vol. 16, no. 01, pp. 64–72, Feb. 2010.
- [7] R. Nieuwenhuizen, S. Stallinga, and B. Rieger, “Visualization and Resolution in Localization Microscopy,” in *Cell Membrane Nanodomains*, CRC Press, 2014, pp. 409–430.
- [8] S. Malkusch, U. Endesfelder, J. Mondry, M. Gelléri, P. J. Verveer, and M. Heilemann, “Coordinate-based colocalization analysis of single-molecule localization microscopy data,” *Histochem. Cell Biol.*, vol. 137, no. 1, pp. 1–10,

Jan. 2012.

- [9] R. Kaufmann, P. Müller, G. Hildenbrand, M. Hausmann, and C. Cremer, "Analysis of Her2/neu membrane protein clusters in different types of breast cancer cells using localization microscopy," *J. Microsc.*, vol. 242, no. 1, pp. 46–54, Apr. 2011.
- [10] P. Sengupta, T. Jovanovic-Talisman, and J. Lippincott-Schwartz, "Quantifying spatial organization in point-localization superresolution images using pair correlation analysis," *Nat. Protoc.*, vol. 8, no. 2, pp. 345–54, Feb. 2013.
- [11] J. Griffié *et al.*, "A Bayesian cluster analysis method for single-molecule localization microscopy data," *Nat. Protoc.*, vol. 11, no. 12, pp. 2499–2514, Nov. 2016.
- [12] R. P. J. Nieuwenhuizen *et al.*, "Measuring image resolution in optical nanoscopy," *Nat. Methods*, vol. 10, no. 6, pp. 557–62, Jun. 2013.
- [13] I. Kirmes *et al.*, "A transient ischemic environment induces reversible compaction of chromatin," *Genome Biol.*, vol. 16, no. 1, p. 246, Dec. 2015.
- [14] M. Ovesny, P. K i ek, J. Borkovec, Z. Vindrych, and G. M. Hagen, "ThunderSTORM: a comprehensive ImageJ plug-in for PALM and STORM data analysis and super-resolution imaging," *Bioinformatics*, vol. 30, no. 16, pp. 2389–2390, Aug. 2014.
- [15] S. Wolter *et al.*, "rapidSTORM: accurate, fast open-source software for localization microscopy," *Nat. Methods*, vol. 9, no. 11, pp. 1040–1041, Nov. 2012.
- [16] F. Gröll, M. Kirchgessner, R. Kaufmann, M. Hausmann, and U. Kobschull, "Accelerating image analysis for localization microscopy with FPGAs," in *Proceedings - 21st International Conference on Field Programmable Logic and Applications, FPL 2011*, 2011, no. 2, pp. 1–5.
- [17] S. Brandt, "ch. 7. The Method of Maximum Likelihood," in *Data Analysis*, Springer, 1998.
- [18] S. Stallinga and B. Rieger, "The effect of background on localization uncertainty in single emitter imaging," in *2012 9th IEEE International Symposium on Biomedical Imaging (ISBI)*, 2012, pp. 988–991.
- [19] B. Rieger and S. Stallinga, "The Lateral and Axial Localization Uncertainty in Super-Resolution Light Microscopy," *ChemPhysChem*, vol. 15, no. 4, pp. 664–670, Mar. 2014.
- [20] M. J. Mlodzianoski *et al.*, "Sample drift correction in 3D fluorescence photoactivation localization microscopy," *Opt. Express*, vol. 19, no. 16, p. 15009, Aug. 2011.
- [21] C. Geisler, T. Hotz, A. Schönle, S. W. Hell, A. Munk, and A. Egner, "Drift estimation for single marker switching based imaging schemes," *Opt. Express*, vol. 20, no. 7, p. 7274, Mar. 2012.
- [22] Y. Wang *et al.*, "Localization events-based sample drift correction for

- localization microscopy with redundant cross-correlation algorithm,” *Opt. Express*, vol. 22, no. 13, p. 15982, Jun. 2014.
- [23] M. J. Rust, M. Bates, and X. Zhuang, “Sub-diffraction-limit imaging by stochastic optical reconstruction microscopy (STORM),” *Nat. Methods*, vol. 3, no. 10, pp. 793–796, Oct. 2006.
- [24] E. Betzig *et al.*, “Imaging Intracellular Fluorescent Proteins at Nanometer Resolution,” *Science (80-. )*, vol. 313, no. 5793, pp. 1642–1645, Sep. 2006.
- [25] A. R. Carter, G. M. King, T. A. Ulrich, W. Halsey, D. Alchenberger, and T. T. Perkins, “Stabilization of an optical microscope to 01 nm in three dimensions,” *Appl. Opt.*, vol. 46, no. 3, p. 421, Jan. 2007.
- [26] R. McGorty, D. Kamiyama, and B. Huang, “Active microscope stabilization in three dimensions using image correlation,” *Opt. Nanoscopy*, vol. 2, no. 1, p. 3, 2013.
- [27] A. T. Szczurek *et al.*, “Single molecule localization microscopy of the distribution of chromatin using Hoechst and DAPI fluorescent probes,” *Nucleus*, vol. 5, no. 4, pp. 331–340, Jul. 2014.
- [28] K. Prakash *et al.*, “Superresolution imaging reveals structurally distinct periodic patterns of chromatin along pachytene chromosomes,” *Proc. Natl. Acad. Sci.*, vol. 112, no. 47, pp. 14635–14640, Nov. 2015.
- [29] A. Szczurek *et al.*, “Imaging chromatin nanostructure with binding-activated localization microscopy based on DNA structure fluctuations,” *Nucleic Acids Res.*, vol. 45, no. 8, Jan. 2017.
- [30] A. Burgert, S. Letschert, S. Doose, and M. Sauer, “Artifacts in single-molecule localization microscopy,” *Histochem. Cell Biol.*, vol. 144, no. 2, pp. 123–131, Aug. 2015.
- [31] D. Sage *et al.*, “Quantitative evaluation of software packages for single-molecule localization microscopy,” *Nat. Methods*, vol. 12, no. 8, pp. 717–724, Jun. 2015.
- [32] U. J. Birk, *Super-Resolution Microscopy: A Practical Guide*. Wiley VCH, 2017.
- [33] B. Huang, W. Wang, M. Bates, and X. Zhuang, “Three-Dimensional Super-Resolution Imaging by Stochastic Optical Reconstruction Microscopy,” *Science*, vol. 319, no. 5864, pp. 810–813, Feb. 2008.

## Figures and Tables

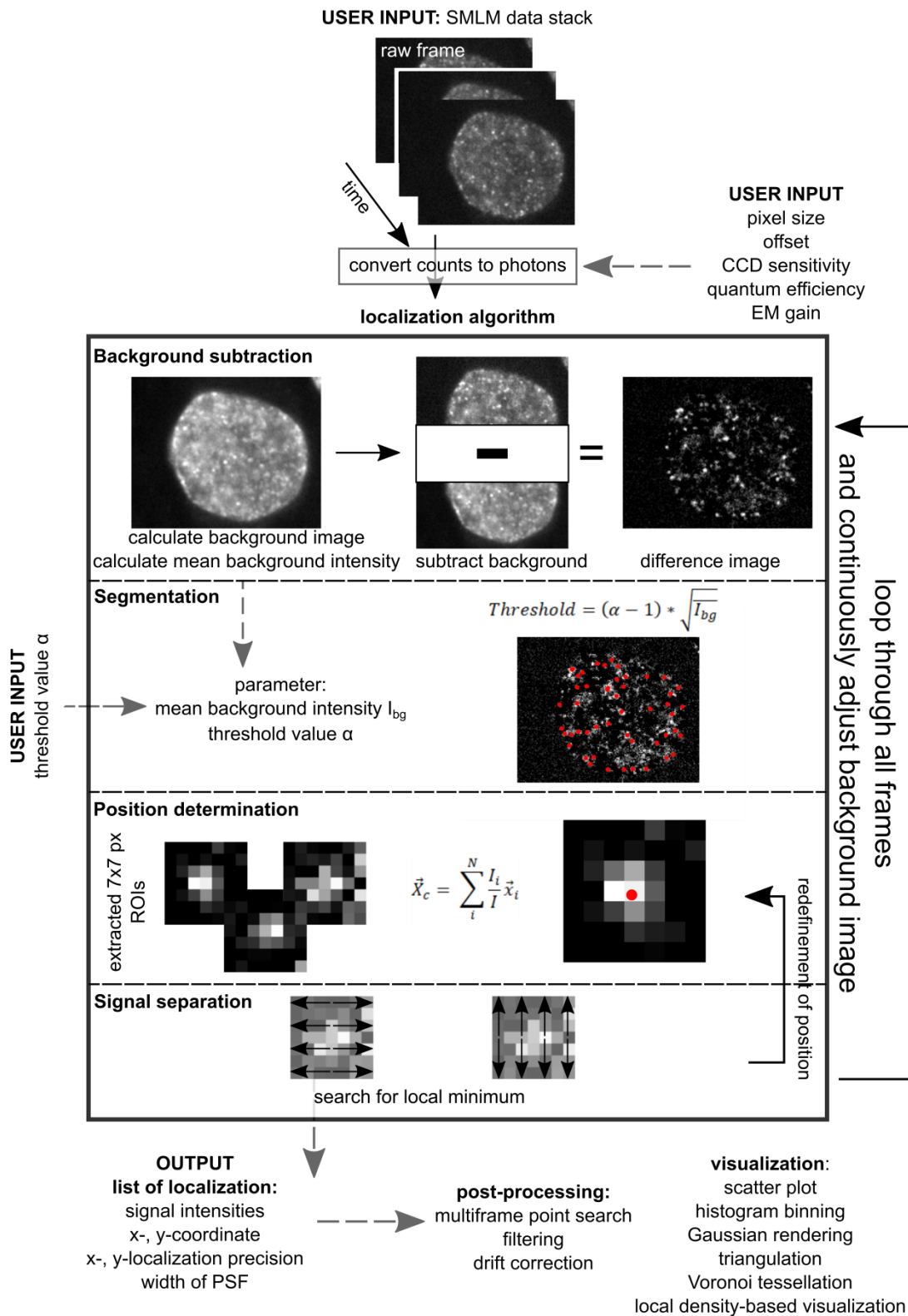


**Figure 1.** Workflow of ILE. The input data stack is converted from counts to photons before it is passed to the localization algorithm. The localization algorithm determines the position of each detected single molecule signal and outputs a list containing the localizations as described in the Materials and Methods part. To complete the analysis ILE offers different post-processing routines and visualization methods.

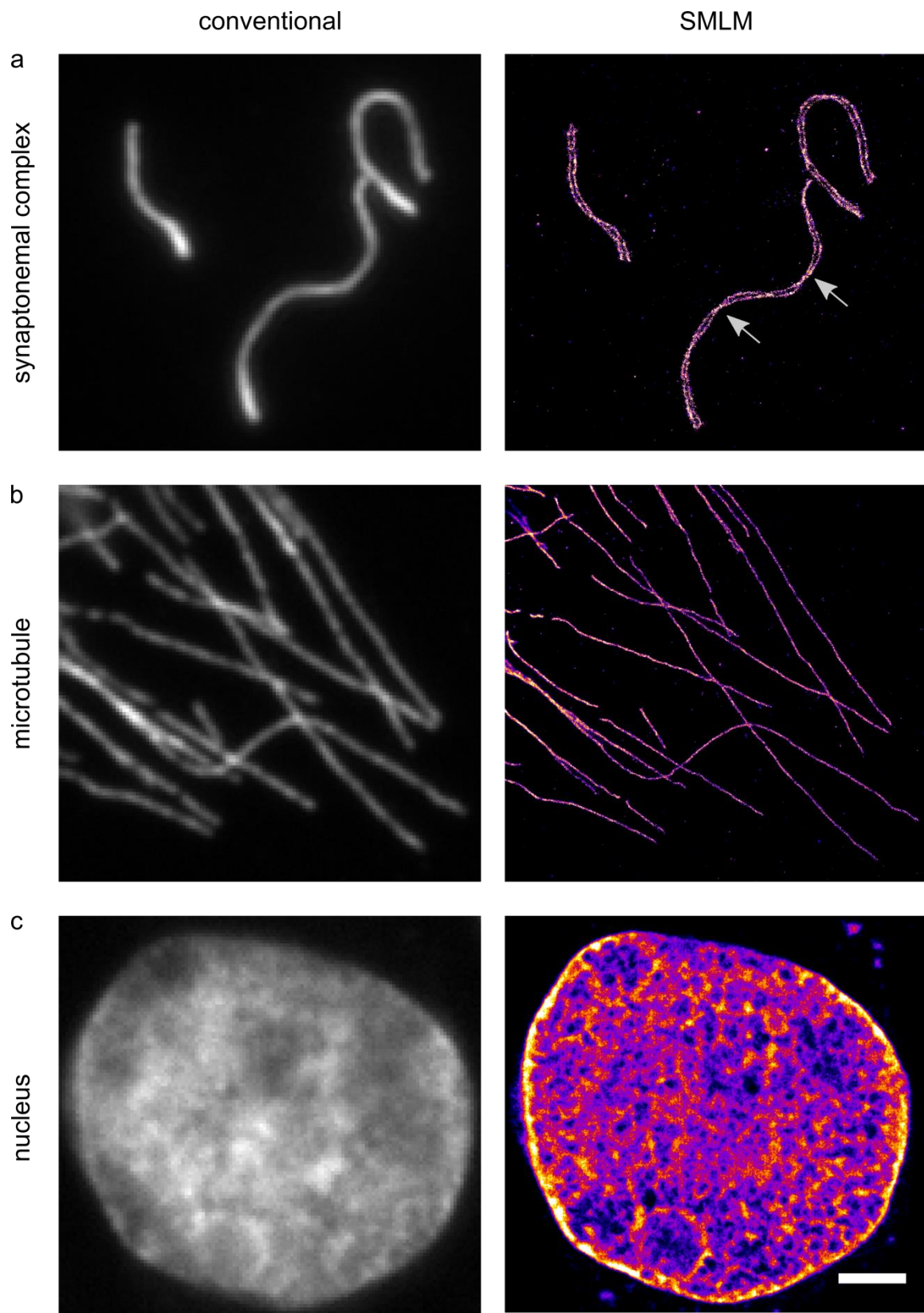


**Figure 2.** Comparison of conventional widefield image and SMLM reconstruction for three different experimental data sets by our software. **(a)** Synaptonemal complex located at a relatively short distance below the coverslip surface. **(b)** Fluorescently labeled microtubule. **(c)** Nuclear DNA imaged approx. 2 mm above the coverslip using fBALM. Scale bar = 2  $\mu$ m.

	number of detected signals	density of signals ( $1/\mu\text{m}^2$ )	localization precision (nm)	execution time (s)	execution time (s)
				ILE	ThunderSTORM
synaptonemal complex	63,000	95	10	27	15
microtubule	440,000	1,700	8	140	56
nucleus	1,500,000	7,500	18	400	200

**Table 1.** Runtime performance of ILE for the different data sets. Values displayed are without any post-processing routines.

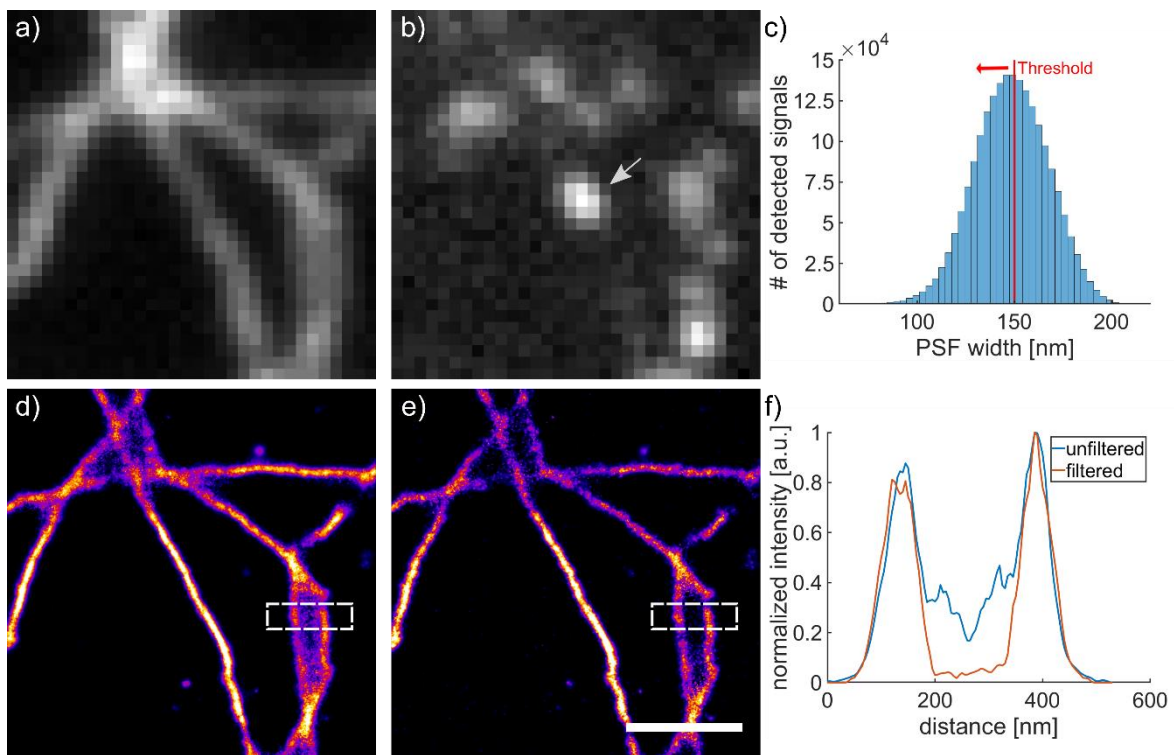


**Figure 3.** Filtering of overlapping signals improves image quality. **(a)** Conventional image of microtubules stained with AlexaFluor 647 and embedded in sub-optimal imaging buffer, yielding poor AlexaFluor 647 photoswitching. **(b)** Single raw frame from localization data stack with multiple emitters (arrow) indicating insufficient switching of fluorophores for optical isolation of single molecules. **(c)** Histogram of PSF size measured at FWHM as given by the localization algorithm. The red line indicates the threshold applied to the list of localizations to filter out signals with a large PSF width. Here, a threshold value of 150 nm was applied i.e. signals with a width of 150 nm or larger have been removed. **(d)** Reconstructed unfiltered SMLM image with overlapping localizations. **(e)** Filtered SMLM image (PSF < 150 nm) demonstrating improvement in image quality. **(f)** Intensity profile through dashed area from **(d)** and **(e)**. Scale bar = 1  $\mu\text{m}$ .

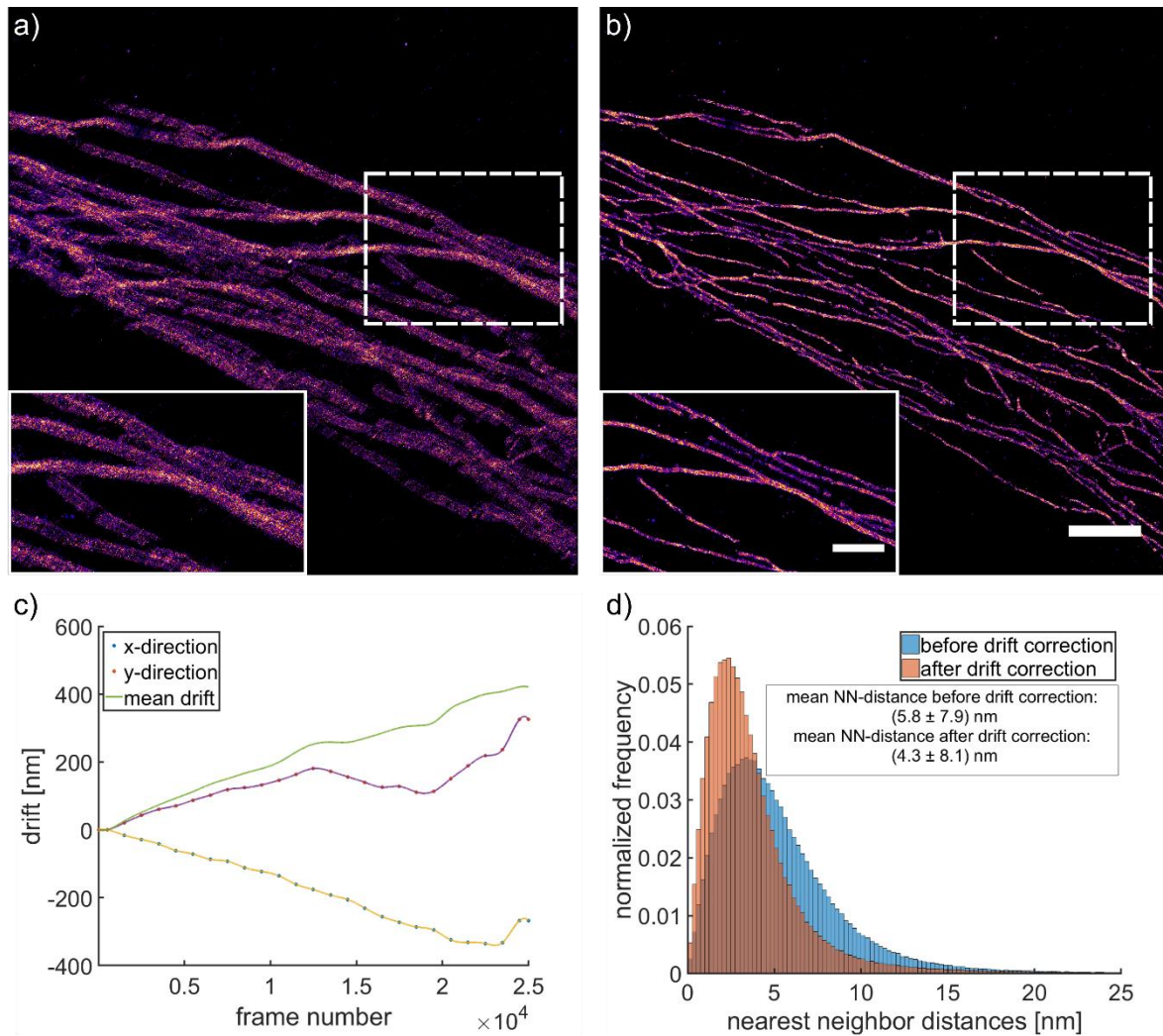


**Figure 4.** Cross-correlation based drift correction. **(a)** Reconstructed image of microtubule indicates that a lateral drift occurred during image acquisition. **(b)** After correcting the list of localizations, single microtubule bundle became visible in the drift-corrected reconstruction that had been hidden before (scale bar = 2  $\mu\text{m}$ , inset scale bar = 1  $\mu\text{m}$ ). **(c)** The drift correction routine identified a drift of  $\sim 400$  nm in x-direction and  $\sim 250$  nm in y-direction, based on cross-correlation of 25 subsets of reconstructions. **(d)** Nearest neighbor distances were reduced after drift correction.

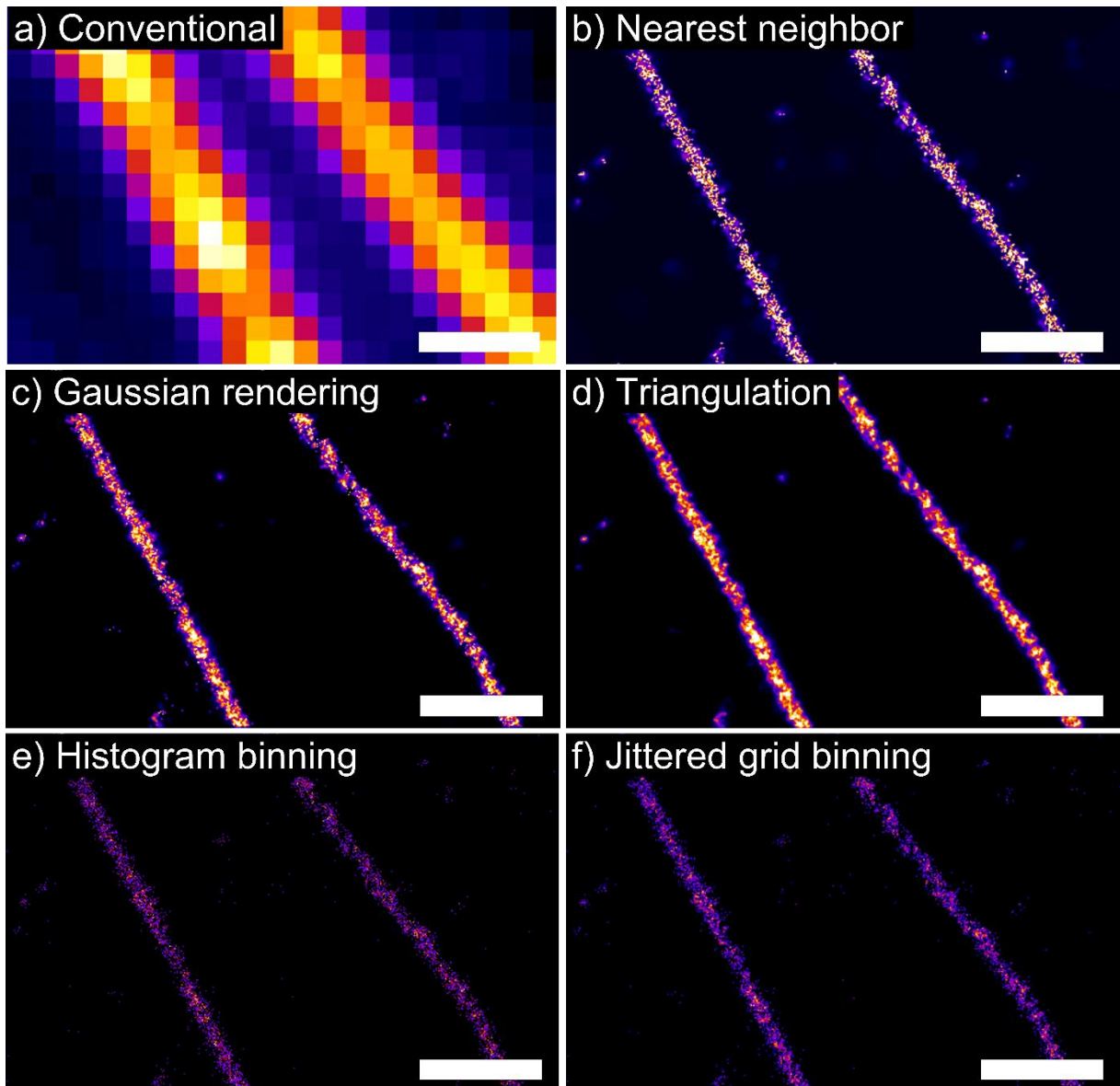


**Figure 5.** Different SMLM visualization techniques are implemented in ILE. **(a)** Conventional image of two fluorescently labeled microtubule strands. **(b)** Nearest neighbor visualization: each intensity value reflects the distance to the nearest neighbor. **(c)** Gaussian rendering: each point is convolved by a 2D Gaussian with a width corresponding to its localization precision. **(d)** Reconstruction based on triangulation. To avoid a fractal-like appearance the point positions can be jittered several times within their respective localization precision and for each set a new triangulated image can be created. The resulting image is the sum over all created images. Here the image is the result of the sum of 40 reconstructions. **(e)** Histogram binning: each point is binned into a square grid with a certain pixel size. The intensity values of each bin correspond to the number of points within this bin. **(f)** Jittered grid binning: Similar like histogram binning, but the underlying grid is jittered. All images show a subregion of the microtubule image shown in Fig. 1a-d and are reconstructed with a pixel size of 5 nm. Pixel intensities have been adapted to cover the whole dynamic range of the image for better comparison. Scale bar = 500 nm.

## Supplementary Material

# Integrated Localization Environment (ILE): A Software Package to Evaluate and Process Blinking Based Single Molecule Localization Microscopy Data

Tentative author list. To be extended/adjusted.

Jan Neumann<sup>1,2</sup>, Martin Hagmann<sup>2</sup>, Frederik Gröll<sup>3</sup>, Rainer Kaufmann<sup>4,5</sup>, Aleksander Szczurek<sup>2,†</sup>, Kirti Prakash<sup>2,‡</sup>, Ramon Lopez Perez<sup>6,7</sup>, Kurt Lucas<sup>1</sup>, Ulrich Pöschl<sup>1</sup>, Christoph Cremer<sup>1,2</sup> and Udo Birk<sup>2\*</sup>

<sup>1</sup>Max Planck Institute for Chemistry (MPIC), Hahn-Meitner-Weg 1, 55128 Mainz, Germany

<sup>2</sup>Institute of Molecular Biology (IMB), Ackermannweg 4, 55128 Mainz, Germany

<sup>3</sup>Kirchhoff-Institut für Physik, Universität Heidelberg, Im Neuenheimer Feld 227, 69120 Heidelberg, Germany

<sup>4</sup>Division of Structural Biology, Wellcome Trust Centre for Human Genetics, University of Oxford, Roosevelt Drive, Oxford, OX3 7BN, United Kingdom

<sup>5</sup>Department of Biochemistry, University of Oxford, South Parks Road, Oxford, OX1 3QU, United Kingdom

<sup>6</sup>Department of Molecular and Radiation Oncology, German Cancer Research Center (DKFZ), Im Neuenheimer Feld 280, 69120 Heidelberg, Germany

<sup>7</sup>Heidelberg Institute for Radiation Oncology (HIRO), National Center for Radiation Research in Oncology, Im Neuenheimer Feld 280, 69120 Heidelberg, Germany

Correspondence: u.birk@imb-mainz.de; Tel.: +49-(0)-6131-39-21524

†Current address: Department of Biochemistry, University of Oxford, South Parks Road, Oxford OX1 3QU, United Kingdom

‡Current address: Department of Paediatrics, University of Cambridge, Box 116, Level 8, Cambridge Biomedical Campus, Cambridge CB2 0QQ, United Kingdom

\*Current address: Hochschule für Technik und Wirtschaft Chur, Pulvermühlestrasse 57, 7000 Chur, Switzerland

**Supplementary Table 1:** Experimental description and protocols used for the demonstration data sets.

<b>Dataset 1</b>	<b>Synaptonemal complex</b>
cell line	extracted from mouse [1]
sample preparation	see [1]
imaging conditions	110 mW 561 nm laser; 3,000 frames; 90 ms exposure time
Figure	Fig. 1a,d; Suppl. Fig. 2

<b>Dataset 2</b>	<b>Microtubule</b>	<b>Microtubule with overlapping signals</b>	<b>Microtubule with drift</b>
cell line	Vero B4	Vero B4	Vero B4
sample preparation	see [2]	see [2]	see [2]
	Embedding medium: PBS, 50 mM MEA, 10% (w/v) glucose, 0.5 mg/ml glucose oxidase, 40 mg/ml catalase	Embedding medium: 90% (v/v) Vectashield H-1000, 10% (v/v) PBS, 10% (w/v) glucose, 0.5 mg/ml glucose oxidase, 40 mg/ml catalase	Embedding medium: Vectashield H-1000
imaging conditions	80 mW 647 nm laser; 25,000 frames; 30 ms exposure time	80 mW 647 nm laser; 18,000 frames; 35 ms exposure time	80 mW 647 nm laser; 25,000 frames; 30 ms exposure time
Figure	Fig. 1b,e; Fig. 4; Suppl. Fig. 1	Fig. 2	Fig. 3

<b>Dataset 3</b>	<b>Nuclear DNA</b>	<b>Nuclear DNA with drift</b>
cell line	HL-1 mouse cardiomyocyte	HL-1 mouse cardiomyocyte
sample preparation	see [3]	see [3]
imaging conditions	50 mW 491 nm laser; 30,000 frames; 12 ms exposure time	50 mW 491 nm laser; 30,000 frames; 12 ms exposure time
Figure	Fig. 1c,f	Suppl. Fig. 3

## Supplementary Figure 1

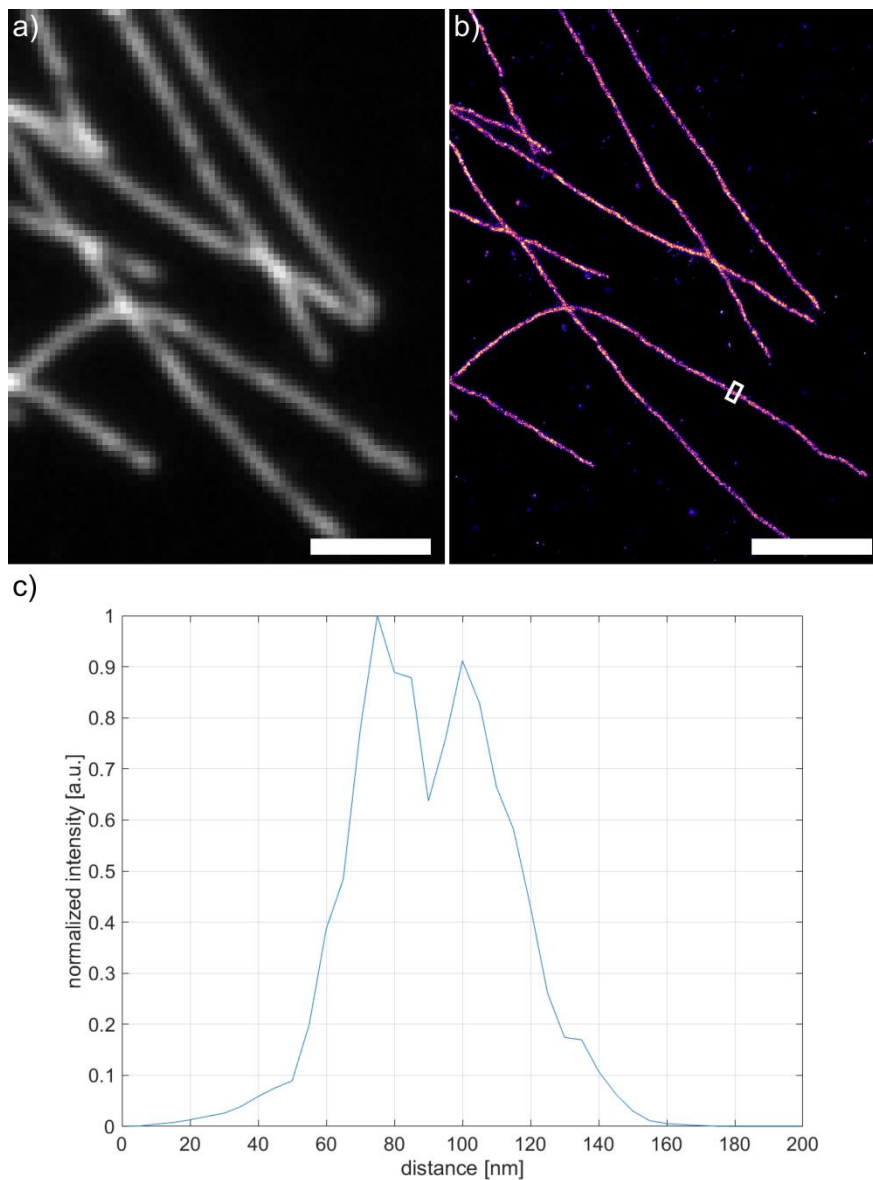


**Figure S1:** Microtubule stained with AlexaFluor 647 and imaged under optimal imaging conditions. (a) Conventional image and (b) reconstructed SMLM image of the same area as in (a) using Gaussian rendering. (c) Line plot across ROI marked in (b). A peak to peak distance of  $\sim 30$  nm can be estimated from the line plot. This value reflects the hollow structure of microtubule which is in the order of  $\sim 25$  nm under the consideration that the structure is enlarged due to antibody labeling. Scale bar =  $2 \mu\text{m}$ .

## Supplementary Figure 2

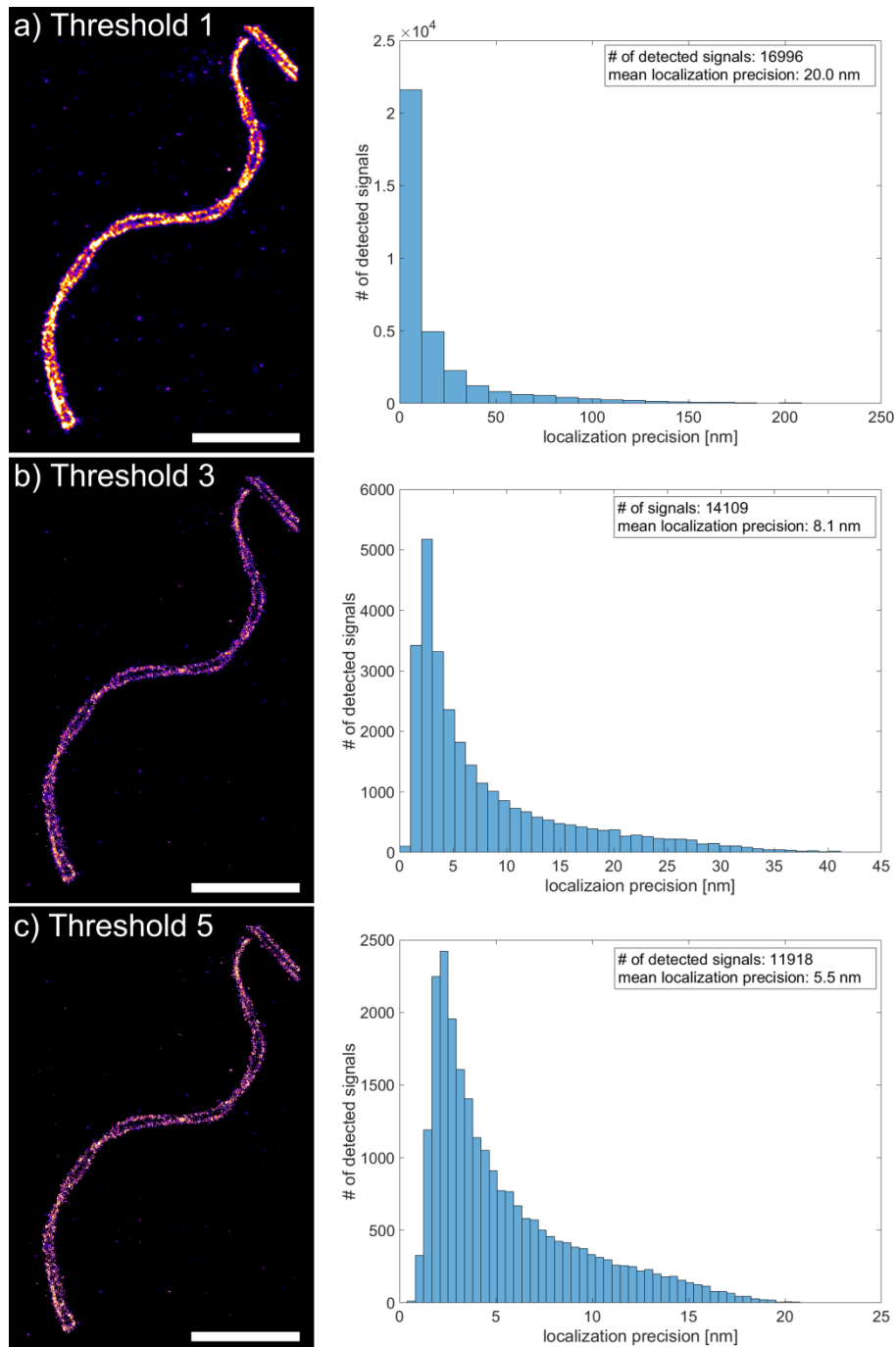


**Figure S2:** Influence of different threshold parameters shown on reconstructions of synaptonemal complex [1]. Choosing a low threshold value (a) leads to increased identification of background signals, which is reflected in the localization precision. Signals with localization precision as high as 200 nm occur. In contrast a threshold value of 3 improves the image quality by detecting less background signals (b). This can be further improved by increasing the threshold where only bright signals with therefore high localization precision are detected (c). Nonetheless it can lead to insufficient sampling due to points that are rejected by the algorithm but still originating from the true structure. A threshold value of 3 turns out to be a good initial value, which is also used for the images presented in the manuscript. Scale bar = 2  $\mu\text{m}$ .

### Supplementary Figure 3

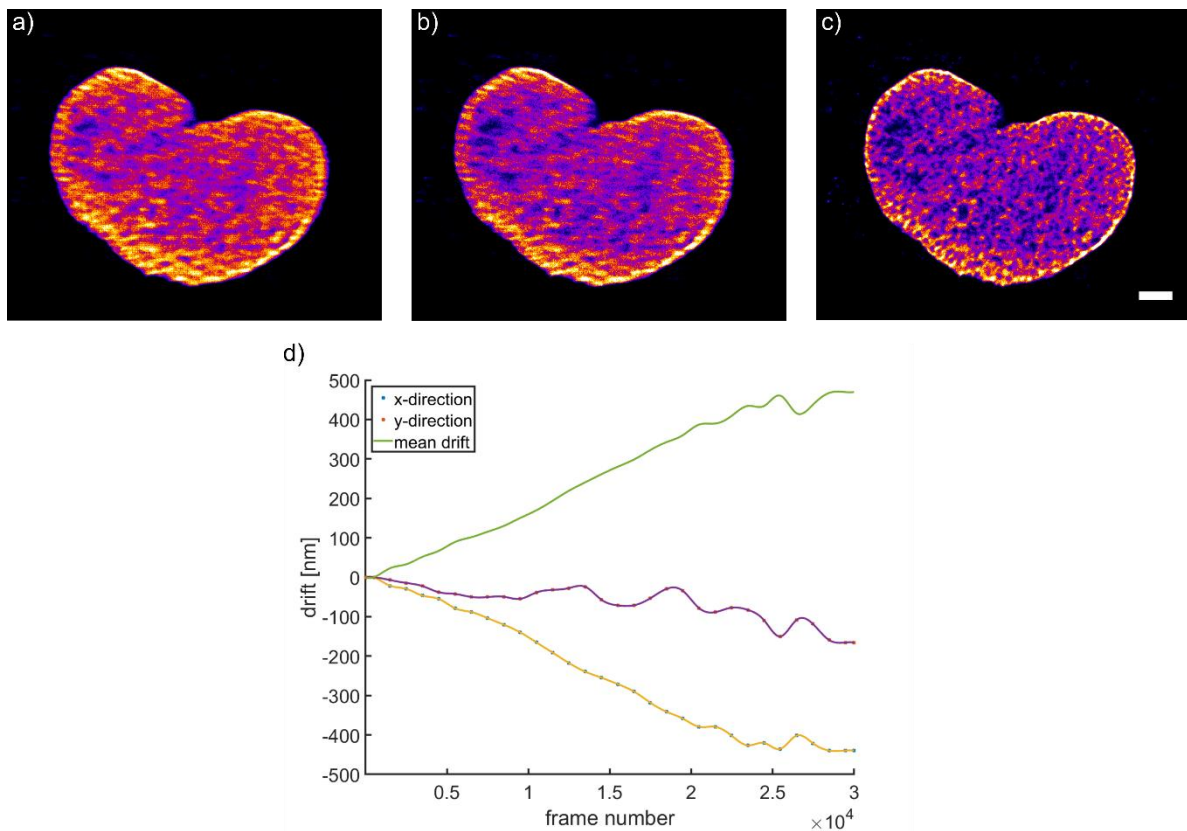


**Figure S3:** Filtering and drift correction applied on a cell nucleus stained with YOYO-1 according to fBALM [3]. (a) Raw visualization using Gaussian rendering after combining points occurring in consecutive frames. A drift of the sample during acquisition and grid-like pattern due to high-density signals is recognizable. (b) Removal of points with a PSF width of 170 nm or larger in the first post-processing step removes the grid-like pattern, but a drift of  $\sim 500$  nm in x-direction and less than  $\sim 150$  nm in y-direction is identified by the drift correction algorithm (d). (c) Shows the final reconstructed image which is corrected for drift and overlapping signals. By correlating 30 subsets of reconstructions, the drift correction routine is capable of correcting the drift. Scale bar = 2  $\mu\text{m}$ .

## Supplementary Figure 4:

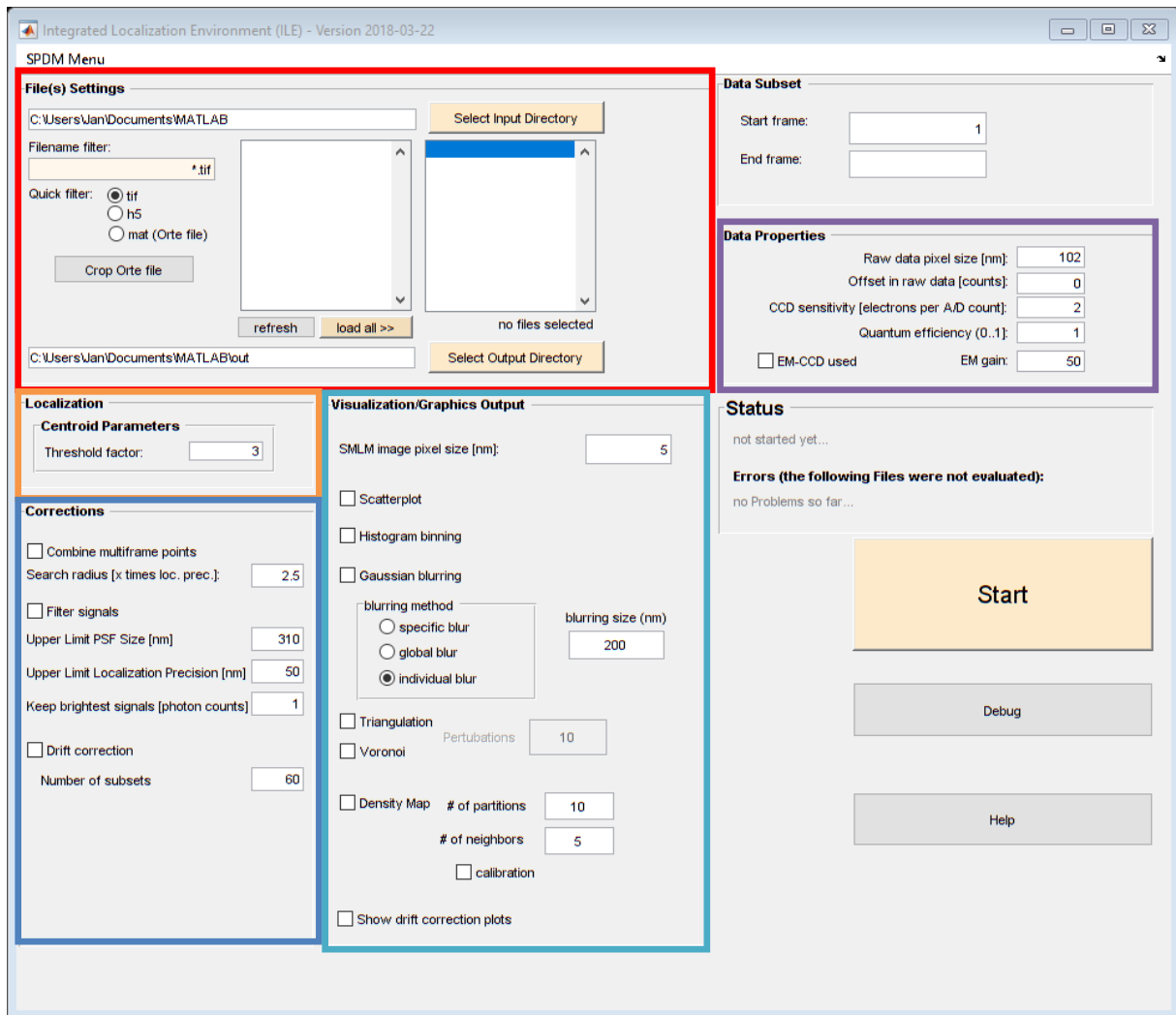


**Figure S4:** Graphical User Interface (GUI) of Integrated Localization Environment (ILE). Different modules are marked with colored panels. **Red Panel:** Selection of files for evaluation. Multiple files can be batch processed. **Purple Panel:** Camera properties of the SMLM setup used to acquire the data. **Orange Panel:** Localization algorithm module. Input for threshold parameter. **Dark Blue Panel:** Correction/Post-processing module. Options for merging points occurring in consecutive frames, single molecule candidate filtering and drift correction. **Bright Blue Panel:** Visualization module.

## Supplementary Note 2: Features of ILE:

### Requirements:

- Matlab (2012a or newer)
- *DIPImage* toolbox (free download: <http://www.diplib.org/>)

### ILE:

- graphical user interface (GUI)
- single scripts accessible via Matlab workspace

### Supported File Formats:

- tagged Image File Format (.tiff)
- hierarchical Data Format (.h5, as output by PYthon Microscopy Environment (PYME) [4])
- MAT-file (list of localizations in *Orte* format)

### Supported Camera Types:

- CCD
- EM-CCD
- sCMOS (no pixel-dependent camera noise)

### Post-processing routines:

- merging of points occurring in consecutive frames with user specified search radius
- filtering of candidates list of localizations:
  - removal of points with a larger PSF width than specified
  - removal of points with a lower localization precision than specified
  - removal of points having a peak intensity lower than specified
- drift correction based on correlation of reconstructions of subsets

### SMLM visualization routines:

- scatter plot
- histogram binning
- Gaussian rendering
- triangulation
- Voronoi tessellation
- local density-based visualization

### Supplementary Note 3: Microscope Setup

The SMLM setup used has been described previously [5]. In brief, the SMLM setup was equipped with a 491 nm laser (Calypso 05 series, Cobolt), a 561 nm laser (Jive series, Cobolt) and a 647 nm laser (LuxX diode laser, Omicron), respectively. Laser beam of all three laser lines was combined by appropriate dichroid mirrors and either expanded by 6.7-fold for widefield imaging or reduced by 0.5-fold for SMLM measurements (which corresponds to an illumination diameter of ~25  $\mu\text{m}$  in the imaging plane measured at the full width at half maximum (FWHM)). Using an f=60 mm achromatic lens the collimated laser beam is focused on the back focal plane of a 1.4 NA/63x oil immersion objective (Leica Microsystems). Emitted light was focused with a f=200 mm achromatic lens onto the CCD chip of 12 bit camera (SensiCam QE, PCO) after passing appropriate emission filters. A camera pixel corresponds to 102 nm in a sample plane.

### References:

- [1] Prakash, K.; Fournier, D.; Redl, S.; Best, G.; Borsos, M.; Tiwari, V.K.; Tachibana-Konwalski, K.; Ketting, R.F.; Parekh, S.H.; Cremer, C.; Birk, U.J. Superresolution imaging reveals structurally distinct periodic patterns of chromatin along pachytene chromosomes. *Proceedings of the National Academy of Sciences*, vol. 112, no. 47, **2015**.
- [2] N. Olivier, D. Keller, P. Gönczy, and S. Manley, "Resolution Doubling in 3D-STROM Imaging through Improved Buffers," *PLoS ONE*, vol. 8, no. 7, Jul. **2013**.
- [3] Szczurek, A.; Klewes, L.; Xing, J.; Gourram, A.; Birk, U.; Knecht, H.; Dobrucki, J.W.; Mai, S.; Cremer, C. Imaging chromatin nanostructure with binding-activated localization microscopy based on DNA structure fluctuations. *Nucleic Acids Research*, vol. 45, no. 8, **2017**.
- [4] Baddeley, D.; Cannell, M.B.; Soeller, C. Three-dimensional sub-100 nm super-resolution imaging of biological samples using a phase ramp in the objective pupil. *Nano Research*, vol. 4, no. 6, **2011**.
- [5] Szczurek, A.T.; Prakash, K.; Lee, H.K.; Żurek-Biesiada, D.J.; Best, G.; Hagmann, M.; Dobrucki, J.W.; Cremer, C.; Birk, U. Single molecule localization microscopy of the distribution of chromatin using Hoechst and DAPI fluorescent probes. *Nucleus*, vol. 5, no. 44, **2014**.

## D.3 Neumann *et al.*, in preparation, 2018

# Integrated Localization Analyzer for Nanoscale Distributions (ILAND): A Software Package for Spatial Point Pattern Analysis of Localization Microscopy Data

Tentative author list. To be extended/adjusted.

Jan Neumann<sup>1,2</sup>, Amine Gourram<sup>2,†</sup>, Márton Gelléri<sup>2</sup>, Aleksander Szczurek<sup>2,‡</sup>, Udo Birk<sup>2,\*</sup>, Kurt Lucas<sup>1</sup>, Ulrich Pöschl<sup>1</sup>, and Christoph Cremer<sup>1,2</sup>

<sup>1</sup>Multiphase Chemistry Department, Max Planck Institute for Chemistry (MPIC),  
Hahn-Meitner-Weg 1, 55128 Mainz, Germany

<sup>2</sup>Institute of Molecular Biology (IMB), Ackermannweg 4, 55128 Mainz, Germany

Correspondence to C. Cremer (c.cremer@imb-mainz.de)

<sup>†</sup>Current address: Center for Free-Electron Laser Science, Deutsches  
Elektronen-Synchrotron DESY, Notkestrasse 85, 22607 Hamburg, Germany

<sup>‡</sup>Current address: Department of Biochemistry, University of Oxford, South Parks  
Road, Oxford OX1 3QU, United Kingdom

<sup>\*</sup>Current address: Hochschule für Technik und Wirtschaft Chur,  
Pulvermühlestrasse 57, 7000 Chur, Switzerland

### Author contributions.

CC, UB, JN, KL, MG and UP designed research. JN programmed the software package. AG contributed the SMLM-ConText algorithm. AS provided the experimental data. JN drafted the manuscript. All authors contributed to the writing.

# **Integrated Localization Analyzer for Nanoscale Distributions (ILAND): A Software Package for Spatial Point Pattern Analysis of Localization Microscopy Data**

Tentative author list. To be extended/adjusted.

Jan Neumann<sup>1,2</sup>, Amine Gourram<sup>2,†</sup>, Márton Gelléri<sup>2</sup>, Aleksander Szczurek<sup>2,‡</sup>, Udo Birk<sup>2,\*</sup>, Kurt Lucas<sup>1</sup>, Ulrich Pöschl<sup>1</sup>, and Christoph Cremer<sup>2</sup>

<sup>1</sup>Multiphase Chemistry Department, Max Planck Institute for Chemistry (MPIC), Hahn-Meitner-Weg 1, 55128 Mainz, Germany

<sup>2</sup>Institute of Molecular Biology (IMB), Ackermannweg 4, 55128 Mainz, Germany

Correspondence to C. Cremer (c.cremer@imb-mainz.de)

<sup>†</sup>Current address: Center for Free-Electron Laser Science, Deutsches Elektronen-Synchrotron DESY, Notkestrasse 85, 22607 Hamburg, Germany

<sup>‡</sup>Current address: Department of Biochemistry, University of Oxford, South Parks Road, Oxford OX1 3QU, United Kingdom

<sup>\*</sup>Current address: Hochschule für Technik und Wirtschaft Chur, Pulvermühlestrasse 57, 7000 Chur, Switzerland

## 1 Introduction

Super-resolution microscopy techniques allow insight into biological processes and structures below the optical diffraction limit<sup>1–10</sup>. One of these techniques is single molecule localization microscopy (SMLM), which makes it possible to determine the position of single molecules with a precision of a few nanometers. This usually is done in two steps. First, spatially and temporally isolated single fluorophores are imaged before their position is determined in the second step using sophisticated computer algorithms<sup>11,12</sup>. These algorithms usually output a list, which contains the coordinates of every detected molecule. Subsequently, several post-processing steps like filtering or drift correction are applied to the list of localizations, before using the coordinates contained in the list to reconstruct a super-resolution image<sup>13</sup>. More importantly, the coordinates can be used to quantify the observed structures at the single molecule level using tools derived from spatial point pattern, cluster or co-localization analysis<sup>14–21</sup>.

All together this makes it necessary to have two classes of algorithms. One class which identifies and determines the position of single molecule signals and thus outputs the list of localizations. And a second class that extracts quantitative information from the list of localizations. While for the first class one can choose from a variety of localization algorithms including post-processing and visualization routines<sup>11,22,23</sup>, the choice for the second class can be more challenging. On the one hand, algorithms are available for quantitative analysis that are specialized in certain tasks such as cluster analysis of membrane receptors<sup>16</sup>. On the other hand, there are quantitative analysis tools that contain a collection of common algorithms such as Ripley's function<sup>24</sup> or density-based spatial clustering of applications with noise (DBSCAN)<sup>25</sup>, but their number is limited<sup>26,27</sup>.

Here, we present Integrated Localization Analyzer for Nanoscale Distributions (ILAND, <https://github.com/Jan-NM/ILAND>, Supplementary Note 1) a collection of different spatial point pattern and cluster analysis algorithms. ILAND is specifically tailored for the evaluation of SMLM data sets with large sample sizes and high emitter densities. Furthermore, ILAND should help to quickly quantify data sets before proceeding with more specialized algorithms which may need longer computation time or have limitations regarding the evaluable area. With ILAND, we also introduce new tools like SMLM-ConText (conformation and texture), which allows to quantify SMLM images obtained from DNA-binding dyes<sup>28,29</sup> and to differentiate between different levels of chromatin condensation. We first demonstrate the performance of our software on simulated data before showing its application on the basis of different biological questions such as the investigation of the nuclear nanostructure or the membrane distribution of receptors after treatment.

## References

1. Hell, S. W. & Wichmann, J. Breaking the diffraction resolution limit by stimulated emission: stimulated-emission-depletion fluorescence microscopy. *Opt. Lett.* **19**, 780 (1994).
2. Heintzmann, R. & Cremer, C. G. Laterally modulated excitation microscopy: improvement of resolution by using a diffraction grating. in (eds. Bigio, I. J., Schneckenburger, H., Slavik, J., Svanberg, K. & Viallet, P. M.) 185–196 (1999). doi:10.1117/12.336833
3. Gustafsson, M. G. Surpassing the lateral resolution limit by a factor of two using structured illumination microscopy. *J. Microsc.* **198**, 82–7 (2000).
4. Lidke, K. A., Rieger, B., Jovin, T. M. & Heintzmann, R. Superresolution by localization of quantum dots using blinking statistics. *Opt. Express* **13**, 7052 (2005).
5. Betzig, E. *et al.* Imaging intracellular fluorescent proteins at nanometer resolution. *Science* **313**, 1642–5 (2006).
6. Hess, S. T., Girirajan, T. P. K. & Mason, M. D. Ultra-high resolution imaging by fluorescence photoactivation localization microscopy. *Biophys. J.* **91**, 4258–72 (2006).
7. Rust, M. J., Bates, M. & Zhuang, X. Sub-diffraction-limit imaging by stochastic optical reconstruction microscopy (STORM). *Nat. Methods* **3**, 793–5 (2006).
8. Heilemann, M. *et al.* Subdiffraction-resolution fluorescence imaging with conventional fluorescent probes. *Angew. Chemie - Int. Ed.* **47**, 6172–6176 (2008).
9. Lemmer, P. *et al.* SPDM: light microscopy with single-molecule resolution at the nanoscale. *Appl. Phys. B* **93**, 1–12 (2008).
10. Jungmann, R. *et al.* Single-molecule kinetics and super-resolution microscopy by fluorescence imaging of transient binding on DNA origami. *Nano Lett.* **10**, 4756–4761 (2010).
11. Small, A. & Stahlheber, S. Fluorophore localization algorithms for super-resolution microscopy. *Nat. Methods* **11**, 267–79 (2014).
12. Deschout, H. *et al.* Precisely and accurately localizing single emitters in fluorescence microscopy. *Nat. Methods* **11**, 253–66 (2014).
13. Rieger, B., Nieuwenhuizen, R. & Stallinga, S. Image Processing and Analysis for Single-Molecule Localization Microscopy: Computation for nanoscale imaging. *IEEE Signal Process. Mag.* **32**, 49–57 (2015).
14. Sengupta, P. *et al.* Probing protein heterogeneity in the plasma membrane using PALM and pair correlation analysis. *Nat. Methods* **8**, 969–75 (2011).
15. Rubin-Delanchy, P. *et al.* Bayesian cluster identification in single-molecule localization microscopy data. *Nat. Methods* **12**, 1072–1076 (2015).
16. Griffié, J. *et al.* A Bayesian cluster analysis method for single-molecule localization microscopy data. *Nat. Protoc.* **11**, 2499–2514 (2016).
17. Andronov, L., Orlov, I., Lutz, Y., Vonesch, J.-L. & Klaholz, B. P. ClusterViSu, a method for clustering of protein complexes by Voronoi tessellation in super-resolution microscopy. *Sci. Rep.* **6**, 24084 (2016).
18. Andronov, L. *et al.* 3DClusterViSu: 3D clustering analysis of super-resolution microscopy data by 3D Voronoi tessellations. *Bioinformatics* (2018). doi:10.1093/bioinformatics/bty200
19. Levet, F. *et al.* SR-Tesseler: a method to segment and quantify localization-based super-resolution microscopy data. *Nat. Methods* **12**, 1065–1071 (2015).
20. Malkusch, S. *et al.* Coordinate-based colocalization analysis of single-molecule

- localization microscopy data. *Histochem. Cell Biol.* **137**, 1–10 (2012).
21. Mazouchi, A. & Milstein, J. N. Fast Optimized Cluster Algorithm for Localizations (FOCAL): a spatial cluster analysis for super-resolved microscopy. *Bioinformatics* **32**, 747–754 (2016).
  22. Ovesny, M., K i ek, P., Borkovec, J., Vindrych, Z. & Hagen, G. M. ThunderSTORM: a comprehensive ImageJ plug-in for PALM and STORM data analysis and super-resolution imaging. *Bioinformatics* **30**, 2389–2390 (2014).
  23. Wolter, S. *et al.* rapidSTORM: accurate, fast open-source software for localization microscopy. *Nat. Methods* **9**, 1040–1041 (2012).
  24. Ripley, B. D. Modelling spatial patterns. *J. R. Stat. Soc. Ser. B* **39**, 172–212 (1977).
  25. Ester, M., Kriegel, H.-P., Sander, J. & Xu, X. A Density-Based Algorithm for Discovering Clusters in Large Spatial Databases with Noise. *Proc. Second Int. Conf. Knowl. Discov. Data Min.* 226–231 (1996). doi:10.1.1.71.1980
  26. Caetano, F. A. *et al.* MliSR: Molecular Interactions in Super-Resolution Imaging Enables the Analysis of Protein Interactions, Dynamics and Formation of Multi-protein Structures. *PLOS Comput. Biol.* **11**, e1004634 (2015).
  27. Malkusch, S. & Heilemann, M. Extracting quantitative information from single-molecule super-resolution imaging data with LAMA – LocAlization Microscopy Analyzer. *Sci. Rep.* **6**, 34486 (2016).
  28. Żurek-Biesiada, D. *et al.* Localization microscopy of DNA in situ using Vybrant® DyeCycle™ Violet fluorescent probe: A new approach to study nuclear nanostructure at single molecule resolution. *Exp. Cell Res.* (2015). doi:10.1016/j.yexcr.2015.08.020
  29. Szczurek, A. *et al.* Imaging chromatin nanostructure with binding-activated localization microscopy based on DNA structure fluctuations. *Nucleic Acids Res.* **45**, (2017).

## ***Supplementary Material***

# **Integrated Localization Analyzer for Nanoscale Distributions (ILAND): A Software Package for Spatial Point Pattern Analysis of Localization Microscopy Data**

Tentative author list. To be extended/adjusted.

Jan Neumann<sup>1,2</sup>, Amine Gourram<sup>2,†</sup>, Márton Gelléri<sup>2</sup>, Aleksander Szczurek<sup>2,‡</sup>, Udo Birk<sup>2,\*</sup>, Kurt Lucas<sup>1</sup>, Ulrich Pöschl<sup>1</sup>, and Christoph Cremer<sup>2</sup>

<sup>1</sup>Multiphase Chemistry Department, Max Planck Institute for Chemistry (MPIC), Hahn-Meitner-Weg 1, 55128 Mainz, Germany

<sup>2</sup>Institute of Molecular Biology (IMB), Ackermannweg 4, 55128 Mainz, Germany

Correspondence to C. Cremer (c.cremer@imb-mainz.de)

<sup>†</sup>Current address: Center for Free-Electron Laser Science, Deutsches Elektronen-Synchrotron DESY, Notkestrasse 85, 22607 Hamburg, Germany

<sup>‡</sup>Current address: Department of Biochemistry, University of Oxford, South Parks Road, Oxford OX1 3QU, United Kingdom

<sup>\*</sup>Current address: Hochschule für Technik und Wirtschaft Chur, Pulvermühlestrasse 57, 7000 Chur, Switzerland

**Supplementary Note 1:** Source code of ILAND. ILAND is implemented in Matlab (MathWorks).

1. Main program (class ClusterAnalysis)
2. Methods
  - 2.1 DBSCAN
  - 2.2 Nearest Neighbor analysis
  - 2.3 Radial density function
  - 2.4 Ripley's H function
  - 2.5 Distance analysis
  - 2.6 Grid-based analysis
  - 2.7 Parameter estimation
  - 2.8 Scatterplot
  - 2.9 Visualization subroutines

## 1. Main program (class ClusterAnalysis)

```
classdef ClusterAnalysis < handle
%ClusterAnalysis Object class for performing cluster analysis of SMLM data
%
% Class constructor extracts positions and localization precision of SMLM
% data and creates automatically a random position table. Input
% localization table should be in Orte file format i.e.
% column 2/3 = x/y-position, column 4/5 = x/y-localization precision,
% column 9 = frame number
% If your localization table does not contain the x- and y-localization
% precisions, a warning will be displayed. One option to avoid possible
% errors due to missing localization precisions could be to use an average
% localization precision as calculated by nearest neighbor based analysis
% (Ulrike Endesfelder, Sebastian Malkusch, Franziska Fricke, and Mike Heilemann (June
% 2014). "A simple method to estimate the average localization precision of a single-molecule
% localization microscopy experiment." In: Histochem. Cell Biol. 141.6,
% pp. 629–38. ISSN: 1432-119X. DOI: 10.1007/s00418-014-1192-3) for example.
%
% To create an instance of this class call:
%
% e.g. cell01 = ClusterAnalysis(localization data, varargin);
%
% varargin comprise the following additional arguments that can be hand over
% varargin{1}: name or number of the sample (char or numeric value)
% varargin{2}: dimensionality of the sample (2 for 2D or 3 for 3D) - note 3D is not completely
% implemented
% varargin{3}: algorithm used to calculate local density. allows the following
% parameters: 'nearestNeighbor', 'averageDensity',
% 'convolution', 'kernelDensity', 'specificValue'
% varargin{4}: additional parameter for selected algorithm to create local density: varargin{3}
% varargin{5}: algorithm used to create random data from calculated local
% density (true = complete spatial randomness (poisson point process);
% false = same number of points as in experimental data with calculated local density))
%
% default values:
% varargin{1}: '001'
% varargin{2}: 2
% varargin{3}: 'averageDensity'
% varargin{4}: empty array
% varargin{5}: true
%
% The created position table / random table has the following order:
```



```

randomClusterStruct
positionTable
randomTable
queryData
randomQueryData
dimension
NoOfPoints
randomNoOfPoints
localDensity
physicalDimension
randomPhysicalDimension
sampleID
end

methods
% constructor
function obj = ClusterAnalysis(localizationFile, varargin)

```

---

```
% Input parser
```

```

narginchk(1, 6);

% default values
obj.dimension = 2;
obj.sampleID = '001';
% set default values if random algorithm is specified
if nargin >= 4
    randomAlgorithm = varargin{3};
    randomAlgorithm = validatestring(randomAlgorithm, ...
        {'nearestNeighbor', 'averageDensity', 'convolution', 'kernelDensity', 'specificValue'});
    switch randomAlgorithm
        case 'nearestNeighbor'
            % does not need any parameters
            randomAlgorithmValue = [];
        case 'averageDensity'
            % does not need any parameters
            randomAlgorithmValue = [];
        case {'convolution', 'kernelDensity'}
            % use half of the estimated spatial resolution
            % as filter radius (sigma)
            [~, nnDistance] = knnsearch(localizationFile(:, 2:3), localizationFile(:, 2:3), 'K', 2);
            randomAlgorithmValue = 0.5 * sqrt( (mean(nnDistance(:, 2), 1))^2 +
                mean(mean(localizationFile(:, 4:5), 2))^2 );
        case 'specificValue'
            if nargin < 5
                error('If you want to use a specific value, you must add it as argument to the
                    function!')
            end
    end
else
    randomAlgorithm = 'averageDensity';
    randomAlgorithmValue = [];
end
assumeCSR = true;
% check input arguments
switch nargin
    case 1
        % nothing to do, default values are already assigned
    case 2
        validateattributes(varargin{1}, {'char', 'numeric'}, {'nonempty'})
        obj.sampleID = varargin{1};
    case 3

```

```

validateattributes(varargin{1}, {'char', 'numeric'}, {'nonempty'})
obj.sampleID = varargin{1};
switch varargin{2}
    case 2
        obj.dimension = 2;
    case 3
        obj.dimension = 3;
    otherwise
        error('Unknown dimension!')
end
case 4
validateattributes(varargin{1}, {'char', 'numeric'}, {'nonempty'})
obj.sampleID = varargin{1};
switch varargin{2}
    case 2
        obj.dimension = 2;
    case 3
        obj.dimension = 3;
    otherwise
        error('Unknown dimension!')
end
% random algorithm already set with default values for
% randomAlgorithmValue
case 5
validateattributes(varargin{1}, {'char', 'numeric'}, {'nonempty'})
obj.sampleID = varargin{1};
switch varargin{2}
    case 2
        obj.dimension = 2;
    case 3
        obj.dimension = 3;
    otherwise
        error('Unknown dimension!')
end
switch randomAlgorithm
    case 'nearestNeighbor'
        % does not need any parameters
        randomAlgorithmValue = [];
    case 'averageDensity'
        % does not need any parameters
        randomAlgorithmValue = [];
    case {'convolution', 'kernelDensity'}
        validateattributes(varargin{4}, {'numeric'}, {'nonnegative'})
        if isempty(varargin{4})
            warning('No value for random algorithm specified. Using default values!')
        else
            randomAlgorithmValue = varargin{4};
        end
    case {'specificValue'}
        validateattributes(varargin{4}, {'numeric'}, {'nonnegative'})
        randomAlgorithmValue = varargin{4};
end
case 6
validateattributes(varargin{1}, {'char', 'numeric'}, {'nonempty'})
obj.sampleID = varargin{1};
switch varargin{2}
    case 2
        obj.dimension = 2;
    case 3
        obj.dimension = 3;
    otherwise
        error('Unknown dimension!')

```

```

end
switch randomAlgorithm
case 'nearestNeighbor'
    % does not need any parameters
    randomAlgorithmValue = [];
case 'averageDensity'
    % does not need any parameters
    randomAlgorithmValue = [];
case {'convolution', 'kernelDensity'}
    validateattributes(varargin{4}, {'numeric'}, {'nonnegative'})
    if isempty(varargin{4})
        warning('No value for random algorithm specified. Using default values!')
    else
        randomAlgorithmValue = varargin{4};
    end
case {'specificValue'}
    validateattributes(varargin{4}, {'numeric'}, {'nonnegative'})
    randomAlgorithmValue = varargin{4};
end
assumeCSR = varargin{5};
end

```

---

```
% create cluster class with specified parameters
```

---

```

obj.NoOfPoints = size(localizationFile, 1);
obj.physicalDimension = [max(localizationFile(:, 2)); max(localizationFile(:, 3)); 0];
% change to double if higher precision is needed, to reduce
% memory consumption stay with single data type
obj.positionTable = zeros(obj.NoOfPoints, 7, 'single');
obj.positionTable(:, 1) = localizationFile(:, 2);
obj.positionTable(:, 2) = localizationFile(:, 3);
% add frame numbering
obj.positionTable(:, 7) = localizationFile(:, 9);
try
    obj.positionTable(:, 4) = localizationFile(:, 4);
    obj.positionTable(:, 5) = localizationFile(:, 5);
catch
    warning('Localization precision is missing?');
end
if obj.dimension == 3
    warning('Is z-coordinate in Orte Matrix specified? Check code!')
    % During programming of this code no convention for column
    % number of z-position in Orte matrix was defined. Replace
    % xx with appropriate number.
    % obj.positionMatrix(:, 3) = localizationFile(:, xx);
    % obj.positionMatrix(:, 6) = localizationFile(:, xx);
    % obj.queryData = createns(obj.positionTable(:, 1:3));
    % obj.physicalDimension(3, 1) = max(localizationFile(:, xx));
else
    obj.positionTable(:, 3) = NaN;
    obj.positionTable(:, 6) = NaN;
    obj.queryData = createns(obj.positionTable(:, 1:2));
end
obj.clusterStruct = struct([]);
% choose algorithm for random point distribution
switch randomAlgorithm
case 'nearestNeighbor'
    % assumes that one point accumulates a circular area
    % with half of the mean 2-NN-distance
    [~, nnDistance] = knnsearch(obj.positionTable(:, 1:2), obj.positionTable(:, 1:2), 'K', 2);
    obj.localDensity = 1 / (pi*((mean(nnDistance(:, 2), 1)) / 1000 / 2)^2); % in 1/ μm^2
case 'averageDensity'

```

```

obj.localDensity = obj.NoOfPoints / (obj.physicalDimension(1, 1)/1000 *
obj.physicalDimension(2, 1)/1000); % in  $\mu\text{m}^2$ 
case 'convolution'
    % estimation of local density using a disk shaped
    % kernel and convolution
    pixelSize = ceil(randomAlgorithmValue / 2.3); % pixel size calculated from estimated
    resolution with nyquist criteria
    radius = randomAlgorithmValue; % radius of disk shaped kernel in nm
    binnedImage = double(visModuleCluster(obj.positionTable, 'histogramBinning',
    pixelSize));
    % create disk shaped kernel
    kernel = fspecial('disk', radius);
    imageConv = conv2(binnedImage, kernel);
    localArea = sum(sum(imageConv > 0)) * (pixelSize/1000)^2; % local area in  $\mu\text{m}^2$ 
    obj.localDensity = obj.NoOfPoints / localArea;
case 'kernelDensity'
    kernelSize = randomAlgorithmValue; % in nm
    radius = sqrt(-2*kernelSize^2 * log(10^(-6)) ); % in nm, calculate neglectable distance
    pointDensity = zeros(obj.NoOfPoints, 1, 'single');
    % this part is slow and should be improved in feature
    % versions
    % for waitbar
    warning('Kernel density algorithm is slow for large localization tables. This part will be
    improved in future versions!')
    multiWaitbar('computing kernel density...', 0);
    prevPercent = 0;
    counter = 0;
    for ii = 1:obj.NoOfPoints
        [~, distances] = rangesearch(obj.positionTable(ii, 1:2), obj.queryData.X, radius);
        distances = cell2mat(distances.);
        kernel = 1 / (2*pi*kernelSize^2) .* exp(- (distances).^2 ./ (2*kernelSize^2));
        pointDensity(ii, 1) = sum(kernel) / size(obj.NoOfPoints, 2) * 1000^2;
        % waitbar
        currentPercent = fix(100*counter/obj.NoOfPoints);
        if currentPercent > prevPercent
            multiWaitbar('computing kernel density...', 'Value', counter/obj.NoOfPoints);
            prevPercent = currentPercent;
        end
        counter = counter + 1;
    end
    obj.localDensity = mean(pointDensity);
case 'specificValue'
    obj.localDensity = randomAlgorithmValue;
end
if assumeCSR == true
    % create CSR with estimated localDensity
    nPoints = poissrnd(obj.localDensity*obj.physicalDimension(1,
    1)/1000*obj.physicalDimension(2, 1)/1000); % 1000 because localDensity is in  $\mu\text{m}^2$ 
    % change to double if higher precision is needed, to reduce
    % memory consumption stay with single data type
    obj.randomTable = zeros(nPoints, 6, 'single');
    obj.randomNoOfPoints = nPoints;
    obj.randomTable(:, 1) = (obj.physicalDimension(1, 1)).*rand(nPoints, 1);
    obj.randomTable(:, 2) = (obj.physicalDimension(2, 1)).*rand(nPoints, 1);
    if obj.dimension == 3
        obj.randomTable(:, 3) = (obj.physicalDimension(3, 1)).*rand(nPoints, 1);
        obj.randomQueryData = createns(obj.randomTable(:, 1:3));
    else
        obj.randomQueryData = createns(obj.randomTable(:, 1:2));
    end
end
obj.randomPhysicalDimension = [max(obj.randomTable(:, 1)); max(obj.randomTable(:, 2));
0];

```

```

else
    % place measured points randomly, uniformly distributed in
    % an area calculated from localDensity
    randomImageSize = obj.NoOfPoints / obj.localDensity; % image size to incorporate points
    with local density
    % change to double if higher precision is needed, to reduce
    % memory consumption stay with single data type
    obj.randomTable = zeros(obj.NoOfPoints, 6, 'single');
    obj.randomTable(:, 1) = (sqrt(randomImageSize)*1000).*rand(obj.NoOfPoints, 1); % image
    is squared
    obj.randomTable(:, 2) = (sqrt(randomImageSize)*1000).*rand(obj.NoOfPoints, 1);
    obj.randomNoOfPoints = obj.NoOfPoints;
    % loc. prec. of random table stays empty - if loc. prec. for
    % random data is desired, insert lines here
    if obj.dimension == 3
        obj.randomTable(:, 3) = (sqrt(randomImageSize)*1000).*rand(obj.NoOfPoints, 1);
        obj.randomQueryData = createns(obj.randomTable(:, 1:3));
    else
        obj.randomQueryData = createns(obj.randomTable(:, 1:2));
    end
    obj.randomPhysicalDimension = [max(obj.randomTable(:, 1)); max(obj.randomTable(:, 2));
    0];
end
obj.randomClusterStruct = struct([]);
if isempty(obj.randomNoOfPoints) || obj.randomNoOfPoints < 2
    warning('Number of random points is lower than 2. This could lead to errors, if random data
    is used for calculation. Maybe parameters specified in calculation of random data are not
    chosen appropriate.')
end
end

```

```

end
% implemented cluster algorithms
[varargout] = DBSCAN(obj, radius, minPoints, isRandom, maxDiameter, showImage)

[varargout] = kNNDistance(obj, k, isRandom, maxDistance, showPlot)

[varargout] = radialDensityFunction(obj, binSize, maxRadius, isRandom, showImage)

[varargout] = ripleys(obj, samplingDistance, maxRadius, isRandom, showImage)

[varargout] = voronoiCluster(obj, isRandom, showImage)

[varargout] = distanceAnalysis(obj, maxDistance, isRandom, showPlot)

[varargout] = gridAnalysis(obj, gridSize, showPlot)

[varargout] = parameterEstimation(obj, method)

[varargout] = scatterPlot(obj)

end
end

```

## 2. Methods

### 2.1 DBSCAN

```
function [] = DBSCAN(obj, radius, minPoints, isRandom, maxDiameter, showImage)
```

```

%DBSCAN for details see A Density-Based Algorithm for Discovering Clusters in Large
% Spatial Databases with Noise. Ester et al. 1996
%
% The current version is implemented for 2D data sets.
%
% Input:
% radius: radius within a certian number of points (minPoints) must be
% found to accept point as part of a cluster
% minPoints: minimum number of points within specified distance (radius)
% to fullfill cluster criteria
% isRandom: true = use random data; false = use experimental data
% maxDiameter: maximum diameter of a cluster, cluster larger than
% maxDiamter will removed (default: maximum dimension of the image)
% showImage: true = show image with noise points in black and coloured cluster
% overlaid to histogram binned image of the data. White cross
% indicates center of mass of the cluster
%
% Output
% (1) number of points in cluster
% (2) obj.clusterStruct or obj.randomclusterStruct (depending on value of isRandom)
% containing the cluster and thier properties
% (3) clusterAssignment - every point in the localization data set is
% assigned to noise (value = 0) or to a cluster (removed cluster - see maxDiameter
% will be set to 0 as well)
%
% Note:
% The current version removes clusters, which consists of two or less
% points. Cluster touching the border of an image will be not removed.
%
% Matlab version: 2014b or newer (because of boundary command).
%
% Cluster areas are calculated using Matlab's boundary and polyarea command,
% alternatively convhull could be used, but this does not allow for
% shrinkng for irregular shaped clusters.
% Diameter property assumes more or less circular clusters.
% Large localization tables will split in chunks. Next, a distance matrix
% is pre-computed and is saved as sparse matrix to save memory.
%
% Jan Neumann, 27.06.2017
%%%%%%%%%%%%%%%%%%%%%%%%%%%%%%%%%%%%%%%%%%%%%%%%%%%%%%%%%%%%%%%%%%%%%%%%
%%%%%%%%%%%%%%%%%%%%%%%%%%%%%%%%%%%%%%%%%%%%%%%%%%%%%%%%%%%%%%%%%%%%%%%%

```

```

memoryThresholdParam = 0.5; % maximum of total memory that will be used
visPixelsize = 10;

```

```

% init

```

```

multiWaitbar('computing distance matrix...', 0);
switch nargin
case 3
    isRandom = 0;
    if isRandom == true
        maxDiameter = max(obj.randomPhysicalDimension);
    else
        maxDiameter = max(obj.physicalDimension);
    end
case 4
    if isRandom == true
        maxDiameter = max(obj.randomPhysicalDimension);
    else
        maxDiameter = max(obj.physicalDimension);
    end
end

```

```

    showImage = 0;
    case 5
        showImage = 0;
    case 6

    otherwise
        error('Wrong number of input arguments!')
    end
    if isRandom == true
        positions = obj.randomTable;
        dataMat = obj.randomClusterStruct;
        nPoints = obj.randomNoOfPoints;
    else
        positions = obj.positionTable;
        dataMat = obj.clusterStruct;
        nPoints = obj.NoOfPoints;
    end

```

---

```

% pre-compute distance matrix

```

```

spaceOnRam = memory;
% limit memory consumption to memoryThresholdParam times total available memory
memoryThreshold = memoryThresholdParam*spaceOnRam.MaxPossibleArrayBytes;
maxNoOfDistances = ceil(memoryThreshold / 8 / nPoints); % /8 for data type double
if maxNoOfDistances > nPoints
    maxNoOfDistances = nPoints;
end
% split Orte matrix
chunkSize = diff(fix(linspace(0, nPoints, ceil(nPoints/maxNoOfDistances) + 1))); % + 1 should stay
splittedPositions = mat2cell(positions, chunkSize, size(positions, 2));
offset = 0;
ivec = cell(1, size(splittedPositions, 1)); % pre-allocate column and row vectors for sparse matrix
jvec = cell(1, size(splittedPositions, 1));
% for waitbar
prevPercent = 0;
counter = 1;
for ii = 1:size(splittedPositions, 1)
    distances = pdist2(splittedPositions{ii}(:, 1:2), positions(:, 1:2));
    [row, column] = find(distances <= radius); % keep distances which are smaller than radius
    % also includes distance to each point itself (which is zero) - will be
    % considered in DBSCAN algorithm (minPoints + 1)
    ivec{ii} = (row + offset).';
    jvec{ii} = column. ';
    offset = offset + size(splittedPositions{ii}, 1);
    % waitbar
    currentPercent = fix(100*counter/size(splittedPositions, 1));
    if currentPercent > prevPercent
        multiWaitbar('computing distance matrix...', 'Value', counter/size(splittedPositions, 1));
        prevPercent = currentPercent;
    end
    counter = counter + 1;
end
% create sparse matrix
jvec = (cell2mat(jvec)).';
ivec = (cell2mat(ivec)).';
xvec = true(length(ivec), 1);
distances = sparse(ivec, jvec, xvec, nPoints, nPoints);
multiWaitbar('computing distance matrix...', 'Close');

```

---

```

% DBSCAN algorithm

```

```

clusterID = 0; % number labeling of cluster
% initialize Cluster matrix - all points are at beginning
% unassigned []
clusterAssignment = zeros(nPoints, 1);
for ii = 1:nPoints
    clusterAssignment(ii, 1) = -2;
end
multiWaitbar('DBSCAN algorithm running...', 'Busy');
for ii = 1:nPoints
    if ~(clusterAssignment(ii, 1) == -2)
        % point is already assigned
        continue
    end
    clusterAssignment(ii, 1) = -1; % point is visited
    if sum(distances(:, ii), 1) < minPoints + 1 % + 1 ignore current point
        clusterAssignment(ii, 1) = 0; % point is noise
    else
        clusterID = clusterID + 1;
        clusterAssignment(ii, 1) = clusterID;
        indice = 1;
        distanceAppend = find(distances(:, ii));
        while indice < length(distanceAppend)
            ll = distanceAppend(indice);
            indice = indice + 1;
            if clusterAssignment(ll, 1) == -2 % if point is not visited
                clusterAssignment(ll, 1) = -1;
                if sum(distances(:, ll), 1) >= minPoints + 1 % + 1
                    newAppend = find(distances(:, ll));
                    distanceAppend = cat(1, distanceAppend, newAppend); % do not implement union or
unique - this may change the order of the array
                end
            end
            if clusterAssignment(ll, 1) == -1 % not member of cluster
                clusterAssignment(ll, 1) = clusterID;
            end
        end
    end
end
end
end

```

---

```

% calculate cluster properties

```

```

for kk = 1:max(clusterAssignment)
    dataMat(2).clusterDBSCAN(kk).PointsCluster = find(clusterAssignment(:, 1) == kk);
    tempCluster = [dataMat(2).clusterDBSCAN(kk).PointsCluster];
    % extract position of cluster points
    x = double(positions(tempCluster, 1));
    y = double(positions(tempCluster, 2));
    k = boundary(x,y);
    dataMat(2).clusterDBSCAN(kk).Area = polyarea(x(k), y(k));
    dataMat(2).clusterDBSCAN(kk).Molecules = size(tempCluster, 1);
    dataMat(2).clusterDBSCAN(kk).Diameter = 2.*sqrt(dataMat(2).clusterDBSCAN(kk).Area./pi); % in
nm
    dataMat(2).clusterDBSCAN(kk).Area = dataMat(2).clusterDBSCAN(kk).Area*(1/1000).^2; %  $\mu\text{m}^2$ 
    % calculate center of mass
    dataMat(2).clusterDBSCAN(kk).xCoM = 1/length(tempCluster)*sum(positions(tempCluster, 1));
    dataMat(2).clusterDBSCAN(kk).yCoM = 1/length(tempCluster)*sum(positions(tempCluster, 2));
end
% filter cluster according to diameter and calculate with remaining cluster additional properties
if ~isempty(dataMat)
    % filter data
    deleteInd = [dataMat(2).clusterDBSCAN.Diameter] > maxDiameter;
    for ii = 1:size(dataMat(2).clusterDBSCAN, 2)

```

```

    if deleteInd(ii) == 1
        tempCluster = clusterAssignment(:, 1) == ii;
        clusterAssignment(tempCluster, 1) = 0;
    end
end
dataMat(2).clusterDBSCAN([dataMat(2).clusterDBSCAN.Diameter] > maxDiameter) = [];
% filter clusters which consists of two or less points
deleteInd = [dataMat(2).clusterDBSCAN.Diameter] == 0;
for ii = 1:size(dataMat(2).clusterDBSCAN, 2)
    if deleteInd(ii) == 1
        tempCluster = clusterAssignment(:, 1) == ii;
        clusterAssignment(tempCluster, 1) = 0;
    end
end
dataMat(2).clusterDBSCAN([dataMat(2).clusterDBSCAN.Diameter] == 0) = [];
% shift cluster number in clusterAssignment, so starting from one in
% ascending order
counter = 0;
for ii = 1:max(clusterAssignment)
    tempVal = clusterAssignment(:, 1) == ii;
    if any(tempVal)
        clusterAssignment(tempVal, 1) = counter + 1;
        counter = counter + 1;
    end
end
% calculate distance to next neighboring cluster
[~, distance] = knnsearch(cat(2,vertcat(dataMat(2).clusterDBSCAN.xCoM),
vertcat(dataMat(2).clusterDBSCAN.yCoM)), cat(2,vertcat(dataMat(2).clusterDBSCAN.xCoM),
vertcat(dataMat(2).clusterDBSCAN.yCoM)), 'k', 2);
% calculate total number of molecules in cluster
dataMat(1).clusterDBSCAN = sum([dataMat(2).clusterDBSCAN.Molecules]);
for ii = 1:size(dataMat(2).clusterDBSCAN, 2)
    if ~isempty(distance) && ~isequal(distance, 0)
        dataMat(2).clusterDBSCAN(ii).NNCluster = distance(ii, 2);
    end
    % check for two points and if Area = zero
    if ~isempty(dataMat(2).clusterDBSCAN)
        dataMat(2).clusterDBSCAN(ii).ClusterDensity =
            dataMat(2).clusterDBSCAN(ii).Molecules./dataMat(2).clusterDBSCAN(ii).Area;
    end
end
else
    % no points in cluster
    dataMat(1).clusterDBSCAN = 0;
end
% save cluster assignment for distance calculation (to calculate distances from points inside and
outside of clusters)
dataMat(3).clusterDBSCAN = uint32(clusterAssignment);
multiWaitbar( 'DBSCAN algorithm running...', 'Close' );

```

---

```

% visualization

```

---

```

if showImage == true && ~isempty(clusterAssignment)
    % create histogram binned image and overlay clustered points
    clusterImage = visModuleCluster(positions, 'histogramBinning', visPixelsize);
    figure( 'Name', num2str(obj.sampleID) );
    imagesc(clusterImage);
    hold on
    multiWaitbar('creating DBSCAN image...', 0);
    % for waitbar
    prevPercent = 0;
    counter = 1;

```

```

for kk = 1:max(clusterAssignment)
    tempCluster = find(clusterAssignment(:, 1) == kk);
    % plot points inside a cluster - each cluster with different color
    scatter(double((positions(tempCluster, 2)) - min(positions(:, 2)))./visPixelsize + 0.5,
            double((positions(tempCluster, 1)) - min(positions(:, 1)))./visPixelsize + 0.5, 50, '.');
    hold on
    % plot center of mass
    scatter(double((dataMat(2).clusterDBSCAN(kk).yCoM) - min(positions(:, 2)))./visPixelsize + 0.5,
            double((dataMat(2).clusterDBSCAN(kk).xCoM) - min(positions(:, 1)))./visPixelsize + 0.5, 100,
            'wx');
    % waitbar
    currentPercent = fix(100*counter/max(clusterAssignment));
    if currentPercent > prevPercent
        multiWaitbar('creating DBSCAN image...', 'Value', counter/max(clusterAssignment));
        prevPercent = currentPercent;
    end
    counter = counter + 1;
end
% add points outside of cluster
tempCluster = find(clusterAssignment(:, 1) == 0);
scatter(double((positions(tempCluster, 2)) - min(positions(:, 2)) )./visPixelsize + 0.5,
        double((positions(tempCluster, 1)) - min(positions(:, 1)) )./visPixelsize + 0.5, 50, 'k. ');
title('Histogram binned image with points overlaid - points outside of clusters and filtered points are
black')
axis equal
axis off
hold off
end

```

---

```
% output
```

---

```

if isRandom == true
    obj.randomClusterStruct = dataMat;
else
    obj.clusterStruct = dataMat;
end
multiWaitbar('CLOSEALL');

```

---

```
end
```

## 2.2 Nearest Neighbor analysis

---

```
function [] = kNNDistance(obj, k, isRandom, maxDistance, showPlot)
```

---

```

%kNNDistance calculates distance to k-th nearest neighbor
%
% k = 2 calculates distance to next neighbor
%
% Input:
% k: number of next neighbor to calculate distance (default: 2)
% isRandom: true if random positions should be used
% maxDistance: maximum allowed distance for nearest neighbor in nm (default = size of image)
% showPlot: show histogram of NN distribution (default = true)
% Output:
% (1) k-value
% (2) nearest neighbor distances of all points
%
% Note: if clustering with DBSCAN was done before, the function
% automatically calculates NN-distance of all the points, of points
% within cluster and of the points outside of the cluster

```

```

% Additional output:
% (3) nearest neighbor distances of points within clusters
% (2) nearest neighbor distances of points outside of clusters
%
% Matlab 2014b or newer and Statistics and Machine Learning Toolbox
%
% Jan Neumann, 27.06.2017
%%%%%%%%%%%%%%%%%%%%%%%%%%%%%%%%%%%%%%%%%%%%%%%%%%%%%%%%%%%%%%%%%%%%%%%%
%%%%%%%%%%%%%%%%%%%%%%%%%%%%%%%%%%%%%%%%%%%%%%%%%%%%%%%%%%%%%%%%%%%%%%%%

```

```

% init

```

```

isDBSCAN = false; % remembers if DBSCAN data already exist
switch nargin
  case 1
    k = 2;
    isRandom = 0;
    if isRandom == true
      maxDistance = max(obj.randomPhysicalDimension);
    else
      maxDistance = max(obj.physicalDimension);
    end
    showPlot = 0;
  case 2
    isRandom = 0;
    if isRandom == true
      maxDistance = max(obj.randomPhysicalDimension);
    else
      maxDistance = max(obj.physicalDimension);
    end
    showPlot = 0;
  case 3
    if isRandom == true
      maxDistance = max(obj.randomPhysicalDimension);
    else
      maxDistance = max(obj.physicalDimension);
    end
    showPlot = 0;
  case 4
    showPlot = 0;
  case 5

  otherwise
    error('Wrong number of input arguments!')
end
if maxDistance <= 0
  error('maxDistance must be larger than zero!')
end
if isRandom == true
  positions = obj.randomTable;
  dataMat = obj.randomClusterStruct;
  treeData = obj.randomQueryData;
  if isfield(obj.randomClusterStruct, 'clusterDBSCAN')
    clusterAssignment = obj.randomClusterStruct(3).clusterDBSCAN;
    isDBSCAN = true;
  end
else
  positions = obj.positionTable;
  dataMat = obj.clusterStruct;
  treeData = obj.queryData;
  if isfield(obj.clusterStruct, 'clusterDBSCAN')
    clusterAssignment = obj.clusterStruct(3).clusterDBSCAN;

```

```

        isDBSCAN = true;
    end
end
if k == 1 || k > obj.NoOfPoints
    error('k must be larger then 1 and smaller then the maximum number of points within the data set!')
end

```

```

% k-NN-calculation for all distances

```

```

[~, nnDistance] = knnsearch(treeData.X, treeData.X, 'K', k);
% mean over NN distance
nnDistances = mean(nnDistance(:, 2:end), 2);
nnDistances = nnDistances(nnDistances(:, 1) <= maxDistance, :);

```

```

% k-NN-calculation for points inside and outside of clusters

```

```

if isDBSCAN == true
    % for outside points clusterAssignment is 0
    tempCluster = clusterAssignment(:, 1) == 0;
    outerPoints = positions(tempCluster, 1:2);
    [~, outerNNDistance] = knnsearch(outerPoints(:, 1:2), outerPoints(:, 1:2), 'K', k);
    % mean over outer NN distance
    outerNNDistance = mean(outerNNDistance(:, 2:end), 2);
    outerNNDistance = outerNNDistance(outerNNDistance(:, 1) <= maxDistance, :);
    innerNNDistance = [];
    if any(clusterAssignment)
        for kk = 1:max(clusterAssignment)
            tempCluster = clusterAssignment(:, 1) == kk;
            innerPoints = positions(tempCluster, 1:2);
            % calculate NN distance within cluster
            [~, tempInnerNNDistance] = knnsearch(innerPoints(:, 1:2), innerPoints(:, 1:2), 'K', k);
            currentInnerNNDistance = mean(tempInnerNNDistance(:, 2:end), 2);
            currentInnerNNDistance = currentInnerNNDistance(currentInnerNNDistance(:, 1) <=
                maxDistance, :);
            innerNNDistance = cat(1, innerNNDistance, currentInnerNNDistance);
        end
    end
end
end

```

```

% visualization

```

```

if showPlot == true
    figure( 'Name', num2str(obj.sampleID) );
    if isDBSCAN == true
        subplot(1, 3, 1)
        h = histogram(nnDistances, ceil(max(nnDistances(:, 1)))), 'Normalization', 'probability');
        grid on;
        title('Nearest Neighbor Distance - all points');
        xlabel('distance [nm]');
        ylabel('normalized frequency');
        ax = gca;
        ax.XLim = [0 maxDistance];
        subplot(1, 3, 2)
        h = histogram(innerNNDistance, ceil(max(innerNNDistance(:, 1))), 'Normalization', 'probability');
        grid on;
        title('Nearest Neighbor Distance - points inside of clusters');
        xlabel('distance [nm]');
        ylabel('normalized frequency');
        ax = gca;
        ax.XLim = [0 maxDistance];
        subplot(1, 3, 3)
        h = histogram(outerNNDistance, ceil(max(outerNNDistance(:, 1))), 'Normalization', 'probability');
    end
end

```

```

grid on;
title('Nearest Neighbor Distance - points outside of clusters');
xlabel('distance [nm]');
ylabel('normalized frequency');
ax = gca;
ax.XLim = [0 maxDistance];
else
h = histogram(nnDistances, ceil(max(nnDistances(:, 1))), 'Normalization', 'probability');
grid on;
title('Nearest Neighbor Distance');
xlabel('distance [nm]');
ylabel('normalized frequency');
ax = gca;
ax.XLim = [0 maxDistance];
end
end

```

```
% output
```

```

dataMat(1).kNNDistance = k;
dataMat(2).kNNDistance = nnDistances; % all points
if isDBSCAN == true
    dataMat(3).kNNDistance = innerNNDistance; % points inside of clusters
    dataMat(4).kNNDistance = outerNNDistance; % points outside of clusters
end
if isRandom == true
    obj.randomClusterStruct = dataMat;
else
    obj.clusterStruct = dataMat;
end

```

```
end
```

## 2.3 Radial density function

```
function [] = radialDensityFunction( obj, binSize, maxRadius, isRandom, showPlot )
```

```

%radialDensityFunction computes radial density function using the point
%coordinates
%
% Input:
% binSize: size of the shell (dr) in nm
% maxRadius: maximum radius for investigation in nm (only points with this
%           minimum distance to the image boundary are considered)
% isRandom: true if random positions should be used
% showPlot: plot pair correlation function
%
% Output:
% (1) g(r) values for each bin
% (2) center of each bin
%
% Jan Neumann, 27.06.2017
%%%%%%%%%%%%%%%%%%%%%%%%%%%%%%%%%%%%%%%%%%%%%%%%%%%%%%%%%%%%%%%%%%%%%%%%
%%%%%%%%%%%%%%%%%%%%%%%%%%%%%%%%%%%%%%%%%%%%%%%%%%%%%%%%%%%%%%%%%%%%%%%%

```

```
% default parameters
```

```
memoryThresholdParam = 0.8; % maximum of total memory that will be used
```

```
% init
```

```

multiWaitbar('computing distance matrix...', 0);
switch nargin
    case 3
        isRandom = 0;
        showPlot = 0;
    case 4
        showPlot = 0;
    case 5

    otherwise
        error('Wrong number of input arguments!')
end
if isRandom == true
    positions = obj.randomTable;
    dataMat = obj.randomClusterStruct;
    nPoints = obj.randomNoOfPoints;
    physicalDimension(1, :) = obj.randomPhysicalDimension(1, :);
    physicalDimension(2, :) = obj.randomPhysicalDimension(2, :);
else
    positions = obj.positionTable;
    dataMat = obj.clusterStruct;
    nPoints = obj.NoOfPoints;
    physicalDimension(1, :) = obj.physicalDimension(1, :);
    physicalDimension(2, :) = obj.physicalDimension(2, :);
end

```

---

```

% pre-compute distance matrix

```

```

spaceOnRam = memory;
% limit memory consumption to memoryThresholdParam times total available memory
memoryThreshold = memoryThresholdParam*spaceOnRam.MaxPossibleArrayBytes;
maxNoOfDistances = ceil(memoryThreshold / 8 / nPoints); % /8 for data type double
if maxNoOfDistances > nPoints
    maxNoOfDistances = nPoints;
end
% to avoid edge effects only points within a minimum distance of
% maxDiameter to the image boundaries are considered
mapSize = ceil(max(positions(:, 1:2)));
currentPositions = positions(positions(:, 1) > maxRadius & positions(:, 1) < mapSize(1)-maxRadius...
    & positions(:, 2) > maxRadius & positions(:, 2) < mapSize(2)-maxRadius, :);
% check of currentPositions is empty
if isempty(currentPositions)
    error('Image size is too small or maxRadius is too big! Can not find any points which have maxRadius
    distance from the image borders! Try to decrease maxRadius or increase image region.');
```

---

```

end
% split Orte matrix
chunkSize = diff(fix(linspace(0, size(currentPositions, 1), ceil(size(currentPositions,
1)/maxNoOfDistances) + 1))); % + 1 should stay
splittedPositions = mat2cell(currentPositions, chunkSize, size(currentPositions, 2));
offset = 0;
ivec = cell(1, size(splittedPositions, 1)); % pre-allocate column and row vectors for sparse matrix
jvec = cell(1, size(splittedPositions, 1));
xvec = cell(1, size(splittedPositions, 1));
% for waitbar
prevPercent = 0;
counter = 1;
for ii = 1:size(splittedPositions, 1)
    distances = pdist2(splittedPositions{ii}(:, 1:2), positions(:, 1:2));
    % keep distances which are smaller than maxRadius and exclude
    % self-distances
    [row, column] = find(distances <= maxRadius & distances > 0);
    ivec{ii} = (row + offset).';

```

```

jvec{ii} = column. ';
k = sub2ind([size(distances, 1) size(distances, 2)], row, column);
xvec{ii} = distances(k). ';
offset = offset + size(splittedPositions{ii}, 1);
% waitbar
currentPercent = fix(100*counter/size(splittedPositions, 1));
if currentPercent > prevPercent
    multiWaitbar( 'computing distance matrix...', 'Value', counter/size(splittedPositions, 1));
    prevPercent = currentPercent;
end
counter = counter + 1;
end
% create sparse matrix
jvec = (cell2mat(jvec)). ';
ivec = (cell2mat(ivec)). ';
xvec = double((cell2mat(xvec)). ');
distances = sparse(ivec, jvec, xvec, nPoints, nPoints);
multiWaitbar( 'computing distance

```

```

% radial density function algorithm

```

```

multiWaitbar('computing radial density function...', 0);
% create bins for radial density function
nbins = ceil(maxRadius/binSize);
[binArray, edges] = histcounts([0 maxRadius], nbins);
binArray = zeros(size(binArray, 2), 1);
% for waitbar
prevPercent = 0;
counter = 1;
for ii = 1:size(binArray, 1)
    binArray(ii, 1) = sum(nonzeros(distances(:, :) > edges(ii) ) - sum(nonzeros(distances(:, :) >=
edges(ii+1) ));
    % waitbar
    currentPercent = fix(100*counter/size(binArray, 1));
    if currentPercent > prevPercent
        multiWaitbar( 'computing radial density function...', 'Value', counter/size(binArray, 1));
        prevPercent = currentPercent;
    end
    counter = counter + 1;
end
binArray = full(binArray);
nPointsFinal = size(currentPositions, 1);

```

```

% normalize data

```

```

density = nPoints / (physicalDimension(1, :) * physicalDimension(2, :));
for ii = 1 : nbins
    innerPart = edges(1, ii) + binSize/2;
    outerPart = innerPart + binSize;
    binArray(ii) = binArray(ii) / (pi*outerPart^2 - pi*innerPart^2);
end
binArray = binArray ./ nPointsFinal ./ density ;
multiWaitbar( 'computing radial density function...', 'Close');

```

```

% visualization

```

```

if showPlot == true
    figure( 'Name', num2str(obj.sampleID) );
    % interpolatedLine = interp1(edges(1 ,1:end-1) + binSize/2, binArray, edges(1):edges(end), 'spline');
    % h = plot((edges(1):edges(end)), interpolatedLine);
    h = plot(edges(1 ,1:end-1) + binSize/2, binArray);
    % h = bar(edges(1 ,1:end-1) + binSize/2, binArray);

```

```

grid on;
title('radial density function');
xlabel('distance [nm]');
ylabel('g(r)');
end

% output

dataMat(1).RDF = binArray;
dataMat(2).RDF = (edges(1, 1:end-1) + binSize/2).';
if isRandom == true
    obj.randomClusterStruct = dataMat;
else
    obj.clusterStruct = dataMat;
end

end

```

## 2.4 Ripley's H function

```

function [] = ripley( obj, samplingDistance, maxRadius, isRandom, showPlot)

%ripley computes Ripley's function using the point
%coordinates
%
% Input:
% samplingDistance: radius of the first circle in nm
% maxRadius: maximum radius for investigation in nm (only points with this
%           minimum distance to the image boundary are considered)
% isRandom: true if random positions should be used
% showPlot: plot pair correlation function
%
% Output:
% (1) L(r)-r values for each bin
% (2) center of each bin
%
% Jan Neumann, 02.06.2018
%%%%%%%%%%%%%%%%%%%%%%%%%%%%%%%%%%%%%%%%%%%%%%%%%%%%%%%%%%%%%%%%%%%%%%%%
%%%%%%%%%%%%%%%%%%%%%%%%%%%%%%%%%%%%%%%%%%%%%%%%%%%%%%%%%%%%%%%%%%%%%%%%

% default parameters

memoryThresholdParam = 0.6; % maximum of total memory that will be used

% init

multiWaitbar('computing distance matrix...', 0);
switch nargin
    case 3
        isRandom = 0;
        showPlot = 0;
    case 4
        showPlot = 0;
    case 5

    otherwise
        error('Wrong number of input arguments!')
end
if isRandom == true
    positions = obj.randomTable;

```

```

dataMat = obj.randomClusterStruct;
nPoints = obj.randomNoOfPoints;
physicalDimension(1, :) = obj.randomPhysicalDimension(1, :);
physicalDimension(2, :) = obj.randomPhysicalDimension(2, :);
else
    positions = obj.positionTable;
    dataMat = obj.clusterStruct;
    nPoints = obj.NoOfPoints;
    physicalDimension(1, :) = obj.physicalDimension(1, :);
    physicalDimension(2, :) = obj.physicalDimension(2, :);
end

% pre-compute distance matrix

spaceOnRam = memory;
% limit memory consumption to memoryThresholdParam times total available memory
memoryThreshold = memoryThresholdParam*spaceOnRam.MaxPossibleArrayBytes;
maxNoOfDistances = ceil(memoryThreshold / 8 / nPoints); % /8 for data type double
if maxNoOfDistances > nPoints
    maxNoOfDistances = nPoints;
end
% to avoid edge effects only points within a minimum distance of
% maxDiameter to the image boundaries are considered
mapSize = ceil(max(positions(:, 1:2)));
currentPositions = positions(positions(:, 1) > maxRadius & positions(:, 1) < mapSize(1)-maxRadius...
    & positions(:, 2) > maxRadius & positions(:, 2) < mapSize(2)-maxRadius, :);
% check of currentPositions is empty
if isempty(currentPositions)
    error('Image size is too small or maxRadius is too big! Can not find any points which have maxRadius
    distance from the image borders! Try to decrease maxRadius or increase image region.');
```

```

end
% split Orte matrix
chunkSize = diff(fix(linspace(0, size(currentPositions, 1), ceil(size(currentPositions,
1)/maxNoOfDistances) + 1))); % + 1 should stay
splittedPositions = mat2cell(currentPositions, chunkSize, size(currentPositions, 2));
offset = 0;
ivec = cell(1, size(splittedPositions, 1)); % pre-allocate column and row vectors for sparse matrix
jvec = cell(1, size(splittedPositions, 1));
xvec = cell(1, size(splittedPositions, 1));
% for waitbar
prevPercent = 0;
counter = 1;
for ii = 1:size(splittedPositions, 1)
    distances = pdist2(splittedPositions{ii}(:, 1:2), positions(:, 1:2));
    % keep distances which are smaller than maxRadius and exclude
    % self-distances
    [row, column] = find(distances <= maxRadius & distances > 0);
    ivec{ii} = (row + offset).';
    jvec{ii} = column. ';
    k = sub2ind([size(distances, 1) size(distances, 2)], row, column);
    xvec{ii} = distances(k).';
    offset = offset + size(splittedPositions{ii}, 1);
    % waitbar
    currentPercent = fix(100*counter/size(splittedPositions, 1));
    if currentPercent > prevPercent
        multiWaitbar('computing distance matrix...', 'Value', counter/size(splittedPositions, 1));
        prevPercent = currentPercent;
    end
    counter = counter + 1;
end
% create sparse matrix
jvec = (cell2mat(jvec)).';
```

```
ivec = (cell2mat(ivec)).';
xvec = double((cell2mat(xvec)).');
distances = sparse(ivec, jvec, xvec, nPoints, nPoints);
multiWaitbar('computing distance matrix...', 'Close');
```

```
% ripley algorithm
```

```
multiWaitbar('computing ripleys function...', 0);
% create bins
nbins = ceil(maxRadius/samplingDistance);
[binArray, edges] = histcounts([0 maxRadius], nbins);
binArray = zeros(size(binArray, 2), 1);
% for waitbar
prevPercent = 0;
counter = 1;
for ii = 1:size(binArray, 1)
    binArray(ii, 1) = sum(nonzeros(distances(:, :)) <= edges(ii + 1) );
    % waitbar
    currentPercent = fix(100*counter/size(binArray, 1));
    if currentPercent > prevPercent
        multiWaitbar('computing ripleys function...', 'Value', counter/size(binArray, 1));
        prevPercent = currentPercent;
    end
    counter = counter + 1;
end
binArray = full(binArray);
nPointsFinal = size(currentPositions, 1);
```

```
% normalize data
```

```
density = nPoints / (physicalDimension(1, :) * physicalDimension(2, :));
binArray = binArray ./ nPointsFinal ./ density;
for ll = 1:size(binArray, 1)
    binArray(ll) = sqrt(binArray(ll, 1) / pi) - (edges(1, ll) + samplingDistance);
end
multiWaitbar('computing ripleys function...', 'Close');
```

```
% visualization
```

```
if showPlot == true
    figure('Name', num2str(obj.sampleID) );
    h = plot(edges(1, 1:end-1) + samplingDistance, binArray);
    grid on;
    title('Ripleys function');
    xlabel('distance [nm]');
    ylabel('L(r)-r');
end
```

```
% output
```

```
dataMat(1).ripley = binArray;
dataMat(2).ripley = (edges(1, 1:end-1) + samplingDistance/2).';
if isRandom == true
    obj.randomClusterStruct = dataMat;
else
    obj.clusterStruct = dataMat;
end
```

```
end
```

## 2.5 Distance analysis

```
function [] = distanceAnalysis(obj, maxDistance, isRandom, showPlot)
```

```
%distanceAnalyses calculates pairwise distances
%
% Image is divided into a grid with a cell size specified by maxDistance.
% Distances from points in the outer cells of the grid are not calculated to
% avoid edge effects.
%
% Image based waitbar displays progress of computation. This could be
% replaced in future versions using a conventional waitbar.
% Variable distances changes size in every loop iteration. Future version
% should implement a cell array.
%
% Input:
% maxDistance: maximum allowed distance to which distances are calculated in nm (default = 200)
% isRandom: true if random positions should be used
% showPlot: show histogram of NN distribution (default = true)
% Output:
% (1) distances of all points
%
% Note: if clustering with DBSCAN was done before, the function
% automatically calculates distances of all the points, of points
% within cluster and of the points outside of the cluster
% Additional output:
% (2) nearest neighbor distances of points within clusters
% (3) nearest neighbor distances of points outside of clusters
%
% Matlab 2014b or newer and Statistics and Machine Learning Toolbox
%
% Important when using histogram:
% data are normalized to all distances from 0 to maxDistance
%
%
% Jan Neumann, 13.07.2017
%%%%%%%%%%%%%%%%%%%%%%%%%%%%%%%%%%%%%%%%%%%%%%%%%%%%%%%%%%%%%%%%%%%%%%%%%
```

```
% init
```

```
isDBSCAN = false; % remembers if DBSCAN data already exist
```

```
switch nargin
```

```
case 1
```

```
maxDistance = 200;
```

```
isRandom = 0;
```

```
showPlot = 0;
```

```
case 2
```

```
isRandom = 0;
```

```
showPlot = 0;
```

```
case 3
```

```
showPlot = 0;
```

```
case 4
```

```
otherwise
```

```
error('Wrong number of input arguments!')
```

```
end
```

```
if isRandom == true
```

```
positions = obj.randomTable;
```

```
dataMat = obj.randomClusterStruct;
```

```

if isfield(obj.randomClusterStruct, 'clusterDBSCAN')
    clusterAssignment = obj.randomClusterStruct(3).clusterDBSCAN;
    isDBSCAN = true;
end
else
    positions = obj.positionTable;
    dataMat = obj.clusterStruct;
    if isfield(obj.clusterStruct, 'clusterDBSCAN')
        clusterAssignment = obj.clusterStruct(3).clusterDBSCAN;
        isDBSCAN = true;
    end
end
end

```

---

```

% distance calculation

```

```

if isRandom == true
    dataSize = min(obj.randomPhysicalDimension(1), obj.randomPhysicalDimension(2));
else
    dataSize = min(obj.physicalDimension(1), obj.physicalDimension(2));
end
if dataSize < 3*maxDistance
    disp('Image size is smaller then 3 times the cut-off distance! Try to decrease cut-off distance or increase image region.');
```

```

    return
end
% init distance matrix
distances = [];

mapSize = ceil(max(positions(:, 1:2)));
xStepSize = ceil(mapSize(1)/maxDistance);
yStepSize = ceil(mapSize(2)/maxDistance);
cellVerification = zeros(xStepSize, yStepSize, 9, 'uint16'); % for verification which pair of cells had been already visited
multiWaitbar('calculating distances...', 0);
% for waitbar
prevPercent = 0;
counter = 1;
for stripe = 2:xStepSize-1
    for line = 2:yStepSize-1
        % compute boundaries of current cell grid
        upperStripe = max(stripe-1, 1); % take only positive values
        lowerStripe = min(xStepSize, stripe+1); % prevent exceeding image boundaries
        leftStripe = max(line-1, 1); % take only positive values
        rightStripe = min(yStepSize, line+1); % prevent exceeding image boundaries
        % get signals from current position
        currentPositions = positions(positions(:, 1) >= upperStripe*maxDistance & positions(:, 1) < (lowerStripe-1)*maxDistance...
            & positions(:, 2) >= leftStripe*maxDistance & positions(:, 2) < (rightStripe-1)*maxDistance, :);
        % do something with first stripe...check first if already calculated
        currentDistance = single(pdist(currentPositions(:, 1:2))); % distance within cell
        distances = [distances; currentDistance];
        % set verification of current stripe
        horizontalPosition = line;
        verticalPosition = stripe;
        currentIdx = strcat(num2str(verticalPosition), num2str(horizontalPosition));
        cellVerification(stripe, line, 5) = str2double(currentIdx);
        % position 1
        % do something with position 1 upper left
        if ~(cellVerification(upperStripe, leftStripe, :) == str2double(currentIdx))
            pointerPositions = positions(positions(:, 1) >= (upperStripe-1)*maxDistance & positions(:, 1) < (lowerStripe-2)*maxDistance...
                & positions(:, 2) >= (leftStripe-1)*maxDistance & positions(:, 2) < (rightStripe-

```

```

    2)*maxDistance, :);
    % do something with first stripe...check first if already calculated
    currentDistance = single(pdist2(currentPositions(:, 1:2), pointerPositions(:, 1:2)));
    distances = [distances; reshape(currentDistance,[],1)];
    % set verification of current stripe
    horizontalPosition = leftStripe;
    verticalPosition = upperStripe;
    upperIdx = strcat(num2str(verticalPosition),num2str(horizontalPosition));
    cellVerification(stripe, line, 1) = str2double(upperIdx);
end
% position 2
% do something with position 2 upper
if ~(cellVerification(upperStripe, line, :) == str2double(currentIdx))
    pointerPositions = positions(positions(:, 1) >= (upperStripe-1)*maxDistance & positions(:, 1) <
(lowerStripe-2)*maxDistance...
& positions(:, 2) >= (leftStripe)*maxDistance & positions(:, 2) < (rightStripe-1)*maxDistance, :);
    % do something with first stripe...check first if already calculated
    currentDistance = single(pdist2(currentPositions(:, 1:2), pointerPositions(:, 1:2)));
    distances = [distances; reshape(currentDistance,[],1)];
    % set verification of current stripe
    horizontalPosition = line;
    verticalPosition = upperStripe;
    upperIdx = strcat(num2str(verticalPosition),num2str(horizontalPosition));
    cellVerification(stripe, line, 2) = str2double(upperIdx);
end
% position 3
% do something with position 3 upper right
if ~(cellVerification(upperStripe, rightStripe, :) == str2double(currentIdx))
    pointerPositions = positions(positions(:, 1) >= (upperStripe-1)*maxDistance & positions(:, 1) <
(lowerStripe-2)*maxDistance...
& positions(:, 2) >= (leftStripe+1)*maxDistance & positions(:, 2) < (rightStripe)*maxDistance, :);
    % do something with first stripe...check first if already calculated
    currentDistance = single(pdist2(currentPositions(:, 1:2), pointerPositions(:, 1:2)));
    distances = [distances; reshape(currentDistance,[],1)];
    % set verification of current stripe
    horizontalPosition = rightStripe;
    verticalPosition = upperStripe;
    upperIdx = strcat(num2str(verticalPosition),num2str(horizontalPosition));
    cellVerification(stripe, line, 3) = str2double(upperIdx);
end
% position 4
% do something with position 4 left
if ~(cellVerification(stripe, leftStripe, :) == str2double(currentIdx))
    pointerPositions = positions(positions(:, 1) >= (upperStripe)*maxDistance & positions(:, 1) <
(lowerStripe-1)*maxDistance...
& positions(:, 2) >= (leftStripe-1)*maxDistance & positions(:, 2) < (rightStripe-2)*maxDistance,
);
    % do something with first stripe...check first if already calculated
    currentDistance = single(pdist2(currentPositions(:, 1:2), pointerPositions(:, 1:2)));
    distances = [distances; reshape(currentDistance,[],1)];
    % set verification of current stripe
    horizontalPosition = leftStripe;
    verticalPosition = stripe;
    upperIdx = strcat(num2str(verticalPosition),num2str(horizontalPosition));
    cellVerification(stripe, line, 4) = str2double(upperIdx);
end
% position 6
% do something with position 6 right
if ~(cellVerification(stripe, rightStripe, :) == str2double(currentIdx))
    pointerPositions = positions(positions(:, 1) >= (upperStripe)*maxDistance & positions(:, 1) <
(lowerStripe-1)*maxDistance...
& positions(:, 2) >= (leftStripe+1)*maxDistance & positions(:, 2) < (rightStripe)*maxDistance, :);

```

```

% do something with first stripe...check first if already calculated
currentDistance = single(pdist2(currentPositions(:, 1:2), pointerPositions(:, 1:2)));
distances = [distances; reshape(currentDistance,[],1)];
% set verification of current stripe
horizontalPosition = rightStripe;
verticalPosition = stripe;
upperIdx = strcat(num2str(verticalPosition),num2str(horizontalPosition));
cellVerification(stripe, line, 6) = str2double(upperIdx);
end
% position 7
% do something with position 7 lower left
if ~(cellVerification(lowerStripe, leftStripe, :) == str2double(currentIdx))
    pointerPositions = positions(positions(:, 1) >= (upperStripe+1)*maxDistance & positions(:, 1) <
(lowerStripe)*maxDistance...
& positions(:, 2) >= (leftStripe-1)*maxDistance & positions(:, 2) < (rightStripe-2)*maxDistance,
:);
% do something with first stripe...check first if already calculated
currentDistance = single(pdist2(currentPositions(:, 1:2), pointerPositions(:, 1:2)));
distances = [distances; reshape(currentDistance,[],1)];
% set verification of current stripe
horizontalPosition = leftStripe;
verticalPosition = lowerStripe;
upperIdx = strcat(num2str(verticalPosition),num2str(horizontalPosition));
cellVerification(stripe, line, 7) = str2double(upperIdx);
end
% position 8
% do something with position 8 lower
if ~(cellVerification(lowerStripe, line, :) == str2double(currentIdx))
    pointerPositions = positions(positions(:, 1) >= (upperStripe+1)*maxDistance & positions(:, 1) <
(lowerStripe)*maxDistance...
& positions(:, 2) >= (leftStripe)*maxDistance & positions(:, 2) < (rightStripe-1)*maxDistance, :);
% do something with first stripe...check first if already calculated
currentDistance = single(pdist2(currentPositions(:, 1:2), pointerPositions(:, 1:2)));
distances = [distances; reshape(currentDistance,[],1)];
% set verification of current stripe
horizontalPosition = line;
verticalPosition = lowerStripe;
upperIdx = strcat(num2str(verticalPosition),num2str(horizontalPosition));
cellVerification(stripe, line, 8) = str2double(upperIdx);
end
% position 9
% do something with position 9 lower right
if ~(cellVerification(lowerStripe, rightStripe, :) == str2double(currentIdx))
    pointerPositions = positions(positions(:, 1) >= (upperStripe+1)*maxDistance & positions(:, 1) <
(lowerStripe)*maxDistance...
& positions(:, 2) >= (leftStripe+1)*maxDistance & positions(:, 2) < (rightStripe)*maxDistance, :);
% do something with first stripe...check first if already calculated
currentDistance = single(pdist2(currentPositions(:, 1:2), pointerPositions(:, 1:2)));
distances = [distances; reshape(currentDistance,[],1)];
% set verification of current stripe
horizontalPosition = rightStripe;
verticalPosition = lowerStripe;
upperIdx = strcat(num2str(verticalPosition),num2str(horizontalPosition));
cellVerification(stripe, line, 9) = str2double(upperIdx);
end
end
% waitbar
currentPercent = fix(100*counter/(xStepSize - 2));
if currentPercent > prevPercent
    multiWaitbar('calculating distances...', 'Value', counter/(xStepSize - 2));
    prevPercent = currentPercent;
end
end

```

```

counter = counter + 1;
end
% removes distances larger than maxDistance
currentIdx = (distances <= maxDistance & distances > 0);
distances = distances(currentIdx);

```

---

```

% distance calculation for points inside and outside of clusters

```

---

```

if isDBSCAN == true
    % for outside points clusterAssignment is 0
    tempCluster = clusterAssignment(:, 1) == 0;
    outerPoints = positions(tempCluster, 1:2);
    % calculate distance using cell grid based algorithm
    % check size of localization table and split localization table
    if min(obj.physicalDimension(1), obj.physicalDimension(2)) < 3*maxDistance
        disp('Image size is smaller than 3 times the cut-off distance! Try to decrease cut-off distance or
            increase image region. ');
        return
    end
    % init distance matrix
    outerDistance = [];

    mapSize = ceil(max(outerPoints(:, 1:2)));
    xStepSize = ceil(mapSize(1)/maxDistance);
    yStepSize = ceil(mapSize(2)/maxDistance);
    cellVerification = zeros(xStepSize, yStepSize, 9, 'uint16'); % for verification which pair of cells had
    % been already visited
    multiWaitbar('calculating distances outside of cluster...', 0);
    % for waitbar
    prevPercent = 0;
    counter = 1;
    for stripe = 2:xStepSize-1
        for line = 2:yStepSize-1
            % compute boundaries of current cell grid
            upperStripe = max(stripe-1, 1); % take only positive values
            lowerStripe = min(xStepSize, stripe+1); % prevent exceeding image boundaries
            leftStripe = max(line-1, 1); % take only positive values
            rightStripe = min(yStepSize, line+1); % prevent exceeding image boundaries
            % get signals from current position
            currentouterPoints = outerPoints(outerPoints(:, 1) >= upperStripe*maxDistance &
                outerPoints(:, 1) < (lowerStripe-1)*maxDistance...
                & outerPoints(:, 2) >= leftStripe*maxDistance & outerPoints(:, 2) < (rightStripe-
                1)*maxDistance, :);
            % do something with first stripe...check first if already calculated
            currentDistance = single(pdist(currentouterPoints(:, 1:2))); % distance within cell
            outerDistance = [outerDistance; currentDistance];
            % set verification of current stripe
            horizontalPosition = line;
            verticalPosition = stripe;
            currentIdx = strcat(num2str(verticalPosition), num2str(horizontalPosition));
            cellVerification(stripe, line, 5) = str2double(currentIdx);
            % position 1
            % do something with position 1 upper left
            if ~(cellVerification(upperStripe, leftStripe, :) == str2double(currentIdx))
                pointerouterPoints = outerPoints(outerPoints(:, 1) >= (upperStripe-1)*maxDistance &
                    outerPoints(:, 1) < (lowerStripe-2)*maxDistance...
                    & outerPoints(:, 2) >= (leftStripe-1)*maxDistance & outerPoints(:, 2) < (rightStripe-
                    2)*maxDistance, :);
                % do something with first stripe...check first if already calculated
                currentDistance = single(pdist2(currentouterPoints(:, 1:2), pointerouterPoints(:, 1:2)));
                outerDistance = [outerDistance; reshape(currentDistance, [], 1)];
                % set verification of current stripe
            end
        end
    end
end

```

```

horizontalPosition = leftStripe;
verticalPosition = upperStripe;
upperIdx = strcat(num2str(verticalPosition),num2str(horizontalPosition));
cellVerification(stripe, line, 1) = str2double(upperIdx);
end
% position 2
% do something with position 2 upper
if ~(cellVerification(upperStripe, line, :) == str2double(currentIdx))
pointerouterPoints = outerPoints(outerPoints(:, 1) >= (upperStripe-1)*maxDistance &
outerPoints(:, 1) < (lowerStripe-2)*maxDistance...
& outerPoints(:, 2) >= (leftStripe)*maxDistance & outerPoints(:, 2) < (rightStripe-
1)*maxDistance, :);
% do something with first stripe...check first if already calculated
currentDistance = single(pdist2(currentouterPoints(:, 1:2), pointerouterPoints(:, 1:2)));
outerDistance = [outerDistance; reshape(currentDistance,[],1)];
% set verification of current stripe
horizontalPosition = line;
verticalPosition = upperStripe;
upperIdx = strcat(num2str(verticalPosition),num2str(horizontalPosition));
cellVerification(stripe, line, 2) = str2double(upperIdx);
end
% position 3
% do something with position 3 upper right
if ~(cellVerification(upperStripe, rightStripe, :) == str2double(currentIdx))
pointerouterPoints = outerPoints(outerPoints(:, 1) >= (upperStripe-1)*maxDistance &
outerPoints(:, 1) < (lowerStripe-2)*maxDistance...
& outerPoints(:, 2) >= (leftStripe+1)*maxDistance & outerPoints(:, 2) <
(rightStripe)*maxDistance, :);
% do something with first stripe...check first if already calculated
currentDistance = single(pdist2(currentouterPoints(:, 1:2), pointerouterPoints(:, 1:2)));
outerDistance = [outerDistance; reshape(currentDistance,[],1)];
% set verification of current stripe
horizontalPosition = rightStripe;
verticalPosition = upperStripe;
upperIdx = strcat(num2str(verticalPosition),num2str(horizontalPosition));
cellVerification(stripe, line, 3) = str2double(upperIdx);
end
% position 4
% do something with position 4 left
if ~(cellVerification(stripe, leftStripe, :) == str2double(currentIdx))
pointerouterPoints = outerPoints(outerPoints(:, 1) >= (upperStripe)*maxDistance &
outerPoints(:, 1) < (lowerStripe-1)*maxDistance...
& outerPoints(:, 2) >= (leftStripe-1)*maxDistance & outerPoints(:, 2) < (rightStripe-
2)*maxDistance, :);
% do something with first stripe...check first if already calculated
currentDistance = single(pdist2(currentouterPoints(:, 1:2), pointerouterPoints(:, 1:2)));
outerDistance = [outerDistance; reshape(currentDistance,[],1)];
% set verification of current stripe
horizontalPosition = leftStripe;
verticalPosition = stripe;
upperIdx = strcat(num2str(verticalPosition),num2str(horizontalPosition));
cellVerification(stripe, line, 4) = str2double(upperIdx);
end
% position 6
% do something with position 6 right
if ~(cellVerification(stripe, rightStripe, :) == str2double(currentIdx))
pointerouterPoints = outerPoints(outerPoints(:, 1) >= (upperStripe)*maxDistance &
outerPoints(:, 1) < (lowerStripe-1)*maxDistance...
& outerPoints(:, 2) >= (leftStripe+1)*maxDistance & outerPoints(:, 2) <
(rightStripe)*maxDistance, :);
% do something with first stripe...check first if already calculated
currentDistance = single(pdist2(currentouterPoints(:, 1:2), pointerouterPoints(:, 1:2)));

```

```

outerDistance = [outerDistance; reshape(currentDistance,[],1)];
% set verification of current stripe
horizontalPosition = rightStripe;
verticalPosition = stripe;
upperIdx = strcat(num2str(verticalPosition),num2str(horizontalPosition));
cellVerification(stripe, line, 6) = str2double(upperIdx);
end
% position 7
% do something with position 7 lower left
if ~(cellVerification(lowerStripe, leftStripe, :) == str2double(currentIdx))
    pointerouterPoints = outerPoints(outerPoints(:, 1) >= (upperStripe+1)*maxDistance &
    outerPoints(:, 1) < (lowerStripe)*maxDistance...
    & outerPoints(:, 2) >= (leftStripe-1)*maxDistance & outerPoints(:, 2) < (rightStripe-
    2)*maxDistance, :);
    % do something with first stripe...check first if already calculated
    currentDistance = single(pdist2(currentouterPoints(:, 1:2), pointerouterPoints(:, 1:2)));
    outerDistance = [outerDistance; reshape(currentDistance,[],1)];
    % set verification of current stripe
    horizontalPosition = leftStripe;
    verticalPosition = lowerStripe;
    upperIdx = strcat(num2str(verticalPosition),num2str(horizontalPosition));
    cellVerification(stripe, line, 7) = str2double(upperIdx);
end
% position 8
% do something with position 8 lower
if ~(cellVerification(lowerStripe, line, :) == str2double(currentIdx))
    pointerouterPoints = outerPoints(outerPoints(:, 1) >= (upperStripe+1)*maxDistance &
    outerPoints(:, 1) < (lowerStripe)*maxDistance...
    & outerPoints(:, 2) >= (leftStripe)*maxDistance & outerPoints(:, 2) < (rightStripe-
    1)*maxDistance, :);
    % do something with first stripe...check first if already calculated
    currentDistance = single(pdist2(currentouterPoints(:, 1:2), pointerouterPoints(:, 1:2)));
    outerDistance = [outerDistance; reshape(currentDistance,[],1)];
    % set verification of current stripe
    horizontalPosition = line;
    verticalPosition = lowerStripe;
    upperIdx = strcat(num2str(verticalPosition),num2str(horizontalPosition));
    cellVerification(stripe, line, 8) = str2double(upperIdx);
end
% position 9
% do something with position 9 lower right
if ~(cellVerification(lowerStripe, rightStripe, :) == str2double(currentIdx))
    pointerouterPoints = outerPoints(outerPoints(:, 1) >= (upperStripe+1)*maxDistance &
    outerPoints(:, 1) < (lowerStripe)*maxDistance...
    & outerPoints(:, 2) >= (leftStripe+1)*maxDistance & outerPoints(:, 2) <
    (rightStripe)*maxDistance, :);
    % do something with first stripe...check first if already calculated
    currentDistance = single(pdist2(currentouterPoints(:, 1:2), pointerouterPoints(:, 1:2)));
    outerDistance = [outerDistance; reshape(currentDistance,[],1)];
    % set verification of current stripe
    horizontalPosition = rightStripe;
    verticalPosition = lowerStripe;
    upperIdx = strcat(num2str(verticalPosition),num2str(horizontalPosition));
    cellVerification(stripe, line, 9) = str2double(upperIdx);
end
end
% waitbar
currentPercent = fix(100*counter/(xStepSize - 2));
if currentPercent > prevPercent
    multiWaitbar('calculating distances outside of cluster...', 'Value', counter/(xStepSize - 2));
    prevPercent = currentPercent;
end
end

```

```

        counter = counter + 1;
    end
    currentIdx = (outerDistance <= maxDistance & outerDistance > 0);
    outerDistance = outerDistance(currentIdx);
    innerDistance = []; % assumes that size of the cluster and number of points within a cluster is small
    enough to be able to use pdist function
    if any(clusterAssignment)
        for kk = 1:max(clusterAssignment)
            tempCluster = clusterAssignment(:, 1) == kk;
            innerPoints = positions(tempCluster, 1:2);
            % calculates pairwise distances using pdist function
            templInnerDistance = single(pdist(innerPoints(:, 1:2)));
            % removes distances larger than maxDistance
            currentIdx = (templInnerDistance <= maxDistance & templInnerDistance > 0);
            innerDistance = cat(1, innerDistance, templInnerDistance(currentIdx));
        end
    end
end
end

```

```
% visualization
```

```

if showPlot == true
    figure( 'Name', num2str(obj.sampleID) );
    if isDBSCAN == true
        subplot(1, 3, 1)
        h = histogram(distances, ceil(max(distances(:, 1))), 'Normalization', 'probability');
        grid on;
        title('Distance Analysis - all points');
        xlabel('distance [nm]');
        ylabel('normalized frequency');
        ax = gca;
        ax.XLim = [0 maxDistance];
        subplot(1, 3, 2)
        h = histogram(innerDistance, ceil(max(innerDistance(:, 1))), 'Normalization', 'probability');
        grid on;
        title('Distance Analysis - points inside of clusters');
        xlabel('distance [nm]');
        ylabel('normalized frequency');
        ax = gca;
        ax.XLim = [0 maxDistance];
        subplot(1, 3, 3)
        h = histogram(outerDistance, ceil(max(outerDistance(:, 1))), 'Normalization', 'probability');
        grid on;
        title('Distance Analysis - points outside of clusters');
        xlabel('distance [nm]');
        ylabel('normalized frequency');
        ax = gca;
        ax.XLim = [0 maxDistance];
    else
        h = histogram(distances, maxDistance, 'Normalization', 'probability'); % data are normalized to all
        distances with 0 and maxDistance
        grid on;
        title('Distance Analysis - all points');
        xlabel('distance [nm]');
        ylabel('normalized frequency');
        ax = gca;
        ax.XLim = [0 maxDistance];
    end
end
end

```

```
% output
```

```

dataMat(1).allDistances = distances;
if isDBSCAN == true
    dataMat(2).allDistances = innerDistance; % points inside of clusters
    dataMat(3).allDistances = outerDistance; % points outside of clusters
end
if isRandom == true
    obj.randomClusterStruct = dataMat;
else
    obj.clusterStruct = dataMat;
end
multiWaitbar('CLOSEALL');

end

```

## 2.6 Grid-based analysis

```
function [] = gridAnalysis( obj, gridSize, showPlot )
```

```
%gridAnalysis
%%%%%%%%%%%%%%%%%%%%%%%%%%%%%%%%%%%%%%%%%%%%%%%%%%%%%%%%%%%%%%%%%%%%%%%%%
```

```
% init
```

```

switch nargin
    case 2
        showPlot = 0;
    case 3

    otherwise
        error('Wrong number of input arguments!')
end
dataMat = obj.clusterStruct;

```

```
% bin data
```

```

x1 = double(ceil(obj.positionTable(:, 1)./gridSize));
y1 = double(ceil(obj.positionTable(:, 2)./gridSize));
% random data
x1Random = double(ceil(obj.randomTable(:, 1)./gridSize));
y1Random = double(ceil(obj.randomTable(:, 2)./gridSize));

minX = min(min(x1), min(x1Random));
minY = min(min(y1), min(y1Random));
maxX = max(max(x1), max(x1Random));
maxY = max(max(y1), max(y1Random));

[xSize, ySize] = size(full(sparse(maxX-minX+1,maxY-minY+1,1)));
% bin (experimental) localization table
x1 = double(ceil(obj.positionTable(:, 1)./ gridSize));
y1 = double(ceil(obj.positionTable(:, 2)./ gridSize));
% generate histogram binned image
binnedExp = sparse(x1-min(x1) + 1, y1-min(y1) + 1, 1, xSize, ySize);
binnedExp = full(binnedExp);
% bin (random) localization table
x1 = double(ceil(obj.randomTable(:, 1)./gridSize));
y1 = double(ceil(obj.randomTable(:, 2)./gridSize));
% generate histogram binned image
binnedRan = sparse(x1-min(x1)+1, y1-min(y1)+1, 1, xSize, ySize);
binnedRan = full(binnedRan);

```

```

if showPlot == true
    compositelImage = binnedExp ./ binnedRan;
    compositelImage(compositelImage > 2) = 2;
    imagesc((compositelImage));
    axis off
    axis image
end

% calculate Variance to Mean Ration (VMR)

var = (sum(sum(binnedExp.^2)) - (sum(sum(binnedExp)).^2/ (size(binnedExp, 1) * size(binnedExp, 2)))) / ((size(binnedExp, 1) * size(binnedExp, 2)) - 1);
mean = sum(sum(binnedExp)) / (size(binnedExp, 1) * size(binnedExp, 2));
dataMat(1).VMR = var/mean;

obj.clusterStruct = dataMat;
% dof = (size(binnedExp, 1) * size(binnedExp, 2));
% value = (sum(sum(binnedExp.^2)) - (sum(sum(binnedExp)).^2/ (size(binnedExp, 1) * size(binnedExp, 2)))) / mean;

% 1-chi2cdf(value, dof)

% var = (sum(sum(binnedRan.^2)) - (sum(sum(binnedRan)).^2/ (size(binnedRan, 1) * size(binnedRan, 2)))) / ((size(binnedRan, 1) * size(binnedRan, 2)) - 1);
% mean = sum(sum(binnedRan)) / (size(binnedRan, 1) * size(binnedRan, 2));
% var/mean

end

```

## 2.7 Parameter estimation

```

function [] = parameterEstimation( obj, method)
%parameterEstimation helps to estimate appropriate parameters for DBSCAN
% Jan Neumann, 27.06.17
%%%%%%%%%%%%%%%%%%%%%%%%%%%%%%%%%%%%%%%%%%%%%%%%%%%%%%%%%%%%%%%%%%%%%%%%
%%%%%%%%%%%%%%%%%%%%%%%%%%%%%%%%%%%%%%%%%%%%%%%%%%%%%%%%%%%%%%%%%%%%%%%%
switch method
    case 'DBSCAN'

        figure('Name', 'DBSCAN parameter estimation');
        set(gcf,'units', 'normalized', 'outerposition', [0 0 1 1])
        subplot(2,2,1)

% calculate nearest neighbor distance (k=2)

        positions = obj.positionTable;
        treeData = obj.queryData;
        [~, nnDistance] = knnsearch(treeData.X, treeData.X, 'K', 2);
        nnDistances = mean(nnDistance(:, 2:end), 2);
        % plot histogram
        histogram(nnDistances, 'Normalization', 'probability');
        grid on
        xlabel('distance [nm]');
        ylabel('normalized frequency');
        title('Nearest neighbor distances');

% enter radius and do rangesearch with corresponding radius

        prompt = {'Enter radius value [nm]:'};
        dlg_title = 'Input';
        num_lines = 1;

```

```

defaultans = {'2'};
radius = inputdlg(prompt,dlg_title,num_lines,defaultans);
radius = str2double(radius{1});
[~, distance] = rangesearch(positions(:, 1:2), treeData.X, radius); % should be done on a cropped
dataset for large position tables
minPoints = cellfun(@length, distance);
subplot(2,2,2)
histogram(minPoints)
title(['Frequency of number of neighbors for radius ' num2str(radius)]);
xlabel('Number of neighbors');
ylabel('frequency');
grid on

```

% second method according to DBSCAN paper

```

prompt = {'Enter k value:'};
dlg_title = 'Input';
num_lines = 1;
defaultans = {'4'};
k = inputdlg(prompt,dlg_title,num_lines,defaultans);
k = str2double(k{1});
% calculate k-NN distance
[~, nnDistance] = knnsearch(treeData.X, treeData.X, 'K', k);
% mean over NN distance
nnDistances = mean(nnDistance(:, 2:end), 2);

```

% create k-distance graph

```

nnDistances = sortrows(nnDistances, 'ascend');
% plot figures for estimation of radius parameter
subplot(2,2,3)
histogram(nnDistances, 'Normalization', 'probability');
title([num2str(k), '-nearest neighbor distance']);
grid on
xlabel('distance [nm]');
ylabel('normalized frequency');
subplot(2,2,4)
plot(nnDistances);
title([num2str(k), '-distance graph']);
grid on;
xlabel('points');
ylabel('radius [nm]');

```

otherwise

```
disp('Choose DBSCAN as method!')
```

end

end

## 2.8 Scatterplot

```

function [] = scatterPlot(obj)
%scatterPlot creates scatterplot of experimental and random data
%
% Jan Neumann, 18.04.18
%%%%%%%%%%%%%%%%%%%%%%%%%%%%%%%%%%%%%%%%%%%%%%%%%%%%%%%%%%%%%%%%%%%%%%%%%%
%%%%%%%%%%%%%%%%%%%%%%%%%%%%%%%%%%%%%%%%%%%%%%%%%%%%%%%%%%%%%%%%%%%%%%%%%%
figure('Name', num2str(obj.sampleID) );
plot(obj.randomTable(:, 2), obj.randomTable(:, 1), '.');
title('Random data')

```

```

set(gca,'Ydir','reverse')
axis equal
axis off
figure( 'Name', num2str(obj.sampleID) );
title('Experimental data')
plot(obj.positionTable(:, 2), obj.positionTable(:, 1), '.');
title('Experimental data')
set(gca,'Ydir','reverse')
axis equal
axis off
end

```

## 2.9 Visualization subroutines

```
function [varargout] = visModuleCluster(locTable, visMethod, pixelSize)
```

```

%visModuleCluster visualization for cluster algorithm
%
% Following visualization methods are supported
% histogramBinning    [2D only]
% gaussianBlur        [2D only]
%
% input parameters
% locTable            Matrix that contains point coordinates. Rows should
%                    correspond to detected signals. Columns should be
%                    arranged in the following order (column 1 - x coordiante, column 2 - y coordiante, ,
%                    column 4 - x loc. prec., column 5 - y loc. prec.)
% visMethod           any of the specified visualization methods as string
%                    for example 'histogramBinning'
% pixelSize           final super-resolution pixel size
%
% requires Image Processing Toolbox, Statistics and Machine Learning
% Toolbox
%
% by Jan Neumann, IMB Mainz, 12.02.2018
%%%%%%%%%%%%%%%%%%%%%%%%%%%%%%%%%%%%%%%%%%%%%%%%%%%%%%%%%%%%%%%%%%%%%%%%
%%%%%%%%%%%%%%%%%%%%%%%%%%%%%%%%%%%%%%%%%%%%%%%%%%%%%%%%%%%%%%%%%%%%%%%%
nSteps = 100; % needed in gaussian blur if individual blurring method is used, specifies binning for
loc. prec.

if nargin < 3
    multiWaitbar('CloseAll');
    error('Please specify at least visualization method and pixel size!');
end

switch visMethod
case 'histogramBinning'
    x1 = double(ceil(locTable(:, 1)./pixelSize));
    y1 = double(ceil(locTable(:, 2)./pixelSize));
    % generate histogram binned image
    SRimage = sparse(x1-min(x1)+1, y1-min(y1)+1, 1);
    SRimage = full(SRimage);
case 'gaussianBlur'
    minPrecision = floor(min(min(locTable(:, 4:5))));
    maxPrecision = ceil(max(max(locTable(:, 4:5))));
    % get dimension of image
    x1 = double(round(locTable(:, 1)./pixelSize));
    y1 = double(round(locTable(:, 2)./pixelSize));
    % generate histogram binned image

```

```

[xSize, ySize] = size(full(sparse(x1-min(x1)+1, y1-min(y1)+1, 1)));
minX = min(x1);
minY = min(y1);
SRimage = zeros(xSize, ySize, 'single');
prevStep = minPrecision;
steps = linspace(minPrecision, maxPrecision, nSteps);
steps(1) = [];
for ii = steps
    % find points with specific loc prec.
    idx = (mean(locTable(:, 4:5), 2) <= ii) & (mean(locTable(:, 4:5), 2) > prevStep);
    tempPoints = locTable(idx, :);
    globalBlur = ((0.5*(ii - prevStep)) + prevStep) / pixelSize;
    % generate histogram binned with current selection of points
    x1 = double(round(tempPoints(:, 1)./pixelSize));
    y1 = double(round(tempPoints(:, 2)./pixelSize));
    templImage = sparse(x1-minX+1, y1-minY+1, 1, xSize, ySize); % check if x and y are correct
    templImage = full(templImage);
    % images should have fixed size to be able to be added
    % check version of matlab
    if verLessThan('matlab', '8.5')
        h = fspecial('gaussian', 2*ceil(2*globalBlur) + 1, globalBlur);
        SRimage = SRimage + imfilter(templImage, h, 'conv');
        % alternative implement own filter
        % maskSize = 2*ceil(2*globalBlur) + 1;
        % ind = -floor(maskSize/2) : floor(maskSize/2);
        % [X, Y] = meshgrid(ind, ind);
        % h = exp(-(X.^2 + Y.^2)/(2*globalBlur*globalBlur));
        % h = h / sum(h(:));
        % SRimage = SRimage + conv2(templImage ,h);
    else
        SRimage = SRimage + imgaussfilt(templImage, globalBlur);
    end
    prevStep = ii;
end

end
varargout{1} = SRimage;

end

```

## **Membrane Distribution of TLR4 in Primary Human Macrophages after Stimulation with ATI or LPS using Localization Microscopy**

Tentative author list. To be extended/adjusted.

Jan Neumann<sup>1,2</sup>, Kira Ziegler<sup>1</sup>, Márton Gelléri<sup>2</sup>, Janine Fröhlich-Nowoisky<sup>1</sup>, Fobang Liu<sup>1</sup>, Iris Bellinghausen<sup>3</sup>, Detlef Schuppan<sup>4,5</sup>, Udo Birk<sup>2,†</sup>, Ulrich Pöschl<sup>1</sup>, Christoph Cremer<sup>2,1</sup>, and Kurt Lucas<sup>1</sup>

<sup>1</sup>Multiphase Chemistry Department, Max Planck Institute for Chemistry (MPIC), Hahn-Meitner-Weg 1, 55128 Mainz, Germany

<sup>2</sup>Institute of Molecular Biology (IMB), Ackermannweg 4, 55128 Mainz, Germany

<sup>3</sup>Department of Dermatology, University Medical Center of the Johannes Gutenberg University, 55131 Mainz, Germany

<sup>4</sup>Institute of Translational Immunology, University Medical Center of the Johannes Gutenberg University, Langenbeckstraße 1, 55131 Mainz, Germany

<sup>5</sup>Division of Gastroenterology, Beth Israel Deaconess Medical Center, Harvard Medical School, 330 Brookline Ave, Boston, MA 02215, USA

Correspondence to K. Lucas (k.lucas@mpic.de)

<sup>†</sup>Current address: Hochschule für Technik und Wirtschaft Chur, Pulvermühlestrasse 57, 7000 Chur, Switzerland

### **Author contributions.**

UP, CC, KL, UB and JN designed the research. JN and KZ performed the experiments. JN, MG, KL and JFN analyzed and interpreted the data. FL, IB and DS contributed materials and methods. JN, MG and KL wrote the paper. All authors contributed in editing and proof reading of the manuscript.

# Membrane Distribution of TLR4 in Primary Human Macrophages after Stimulation with ATI or LPS using Localization Microscopy

Tentative author list. To be extended/adjusted.

Jan Neumann<sup>1,2</sup>, Kira Ziegler<sup>1</sup>, Márton Gelléri<sup>2</sup>, Janine Fröhlich-Nowoisky<sup>1</sup>, Fobang Liu<sup>1</sup>, Iris Bellinghausen<sup>3</sup>, Detlef Schuppan<sup>4,5</sup>, Udo Birk<sup>2,†</sup>, Ulrich Pöschl<sup>1</sup>, Christoph Cremer<sup>2,1</sup>, and Kurt Lucas<sup>1</sup>

<sup>1</sup>*Multiphase Chemistry Department, Max Planck Institute for Chemistry, Hahn-Meitner-Weg 1, 55128 Mainz, Germany*

<sup>2</sup>*Institute of Molecular Biology, Ackermannweg 4, 55128 Mainz, Germany*

<sup>3</sup>*Department of Dermatology, University Medical Center of the Johannes Gutenberg University, 55131 Mainz, Germany*

<sup>4</sup>*Institute of Translational Immunology, University Medical Center of the Johannes Gutenberg University, Langenbeckstraße 1, 55131 Mainz, Germany*

<sup>5</sup>*Division of Gastroenterology, Beth Israel Deaconess Medical Center, Harvard Medical School, 330 Brookline Ave, Boston, MA 02215, USA*

Correspondence to K. Lucas (k.lucas@mpic.de)

†Current address: Hochschule für Technik und Wirtschaft Chur, Pulvermühlestrasse 57, 7000 Chur, Switzerland

## Abstract

Activation of Toll-like receptor 4 (TLR4) by pathogen- and damage-associated molecular patterns (PAMP, DAMP) is accompanied by a complex interaction with different accessory molecules and a recruitment of TLR4 in specific membrane domains. This supramolecular membrane organization is described as an essential step in the activation process and the subsequent downstream signaling of TLR4. Beside lipopolysaccharides (LPS), TLR4 can be stimulated by amylase-trypsin inhibitors (ATI), proteins associated with gluten which cause intestinal and pulmonary inflammation. However, the influence of ATI on the membrane distribution of TLR4 at the nanoscale is unknown. Here we investigated the membrane distribution of TLR4 in primary human macrophages upon stimulation with ATI and LPS using single molecule localization microscopy (SMLM). We found that more than 60 % of TLR4 molecules are assembled in clusters with a diameter of about 46 nm to 57 nm. After ATI and LPS stimulation we observed a tendency towards the formation of smaller and less dense clusters accompanied with an increase in the percentage of clustered molecules. This suggests the recruitment of TLR4 molecules around pre-existing monomers or lower order oligomers and thus the formation of signaling platforms. Together, our results indicate comparable effects of ATI on the membrane distribution of TLR4 as observed for LPS and underlines the functional role of receptor clusters as signaling platforms.

## Introduction

Toll-like receptors (TLR) represent a family of pattern recognition receptors (PRRs) that are part of the innate immune system [1], [2]. Their function is the detection of pathogen associated molecular patterns (PAMPs), which triggers the subsequent production and release of inflammatory mediators. One of the best studied TLRs is TLR4, which is sensitive to lipopolysaccharide (LPS), a cell wall component of gram-negative bacteria [3], [4].

Stimulation of TLR4 through LPS is facilitated by a complex interaction of different molecules. It starts with binding of LPS to the soluble lipopolysaccharide binding protein (LBP) and its transfer to the co-receptor cluster of differentiation (CD14). CD14 in turn transports LPS to myeloid differentiation protein-2 (MD-2), which forms a heterodimer with TLR4 [5]–[7]. Binding of LPS leads to the dimerization of the TLR4/MD-2 complex followed by a change in receptor conformation and the activation of a NF- $\kappa$ B dependent signaling cascade.

Stimulation and subsequent downstream signaling of TLR4 is accompanied by a re-localization of TLR4 and its accessory molecules into specific domains of the cell membrane (reviewed in [8], [9]). For example, TLR4 is recruited into CD14 enriched microdomains after treatment with LPS [10]. Since these domains are smaller than 200 nm [11], [12], they are inaccessible using conventional microscopy. With the advent of super-resolution microscopy techniques ([13]–[22]), different studies investigated the membrane distribution of TLR4 at the single molecule level. It was reported that TLR4 forms cluster on the cell membrane of glioblastoma cells with a cluster size of ~50 nm, independent of the LPS stimuli [23]. In another study on mouse macrophages the cluster size of TLR4 was ~380 nm, and increased after LPS stimulation to ~520 nm [24].

In general it is assumed that the existence of receptor clusters and the recruitment of receptors into domains create a local environment that facilitates downstream signaling and thus represent a functional or regulatory mechanism [25], [26]. Specifically, for TLR4, an increase in its cluster size upon LPS stimulation as observed in mouse macrophages may promote immune responses [24]. Of note, during stimulation the entire TLR4/MD-2/CD14 complex is endocytosed [27], which results in a depletion of TLR4 on the cell surface.

In addition to LPS, TLR4 can be stimulated by a broad spectrum of other molecules such as high mobility group box 1 protein (HMGB1) and different heat shock proteins [28]. These body's own molecules are denoted as damage-associated molecular patterns (DAMPs) and play an important role in inflammation. Furthermore, some allergens (Der p 2, Nickel) are known to stimulate TLR4 [29], [30].

Of special interest in this study are amylase trypsin inhibitors (ATI) that can act as potent activators of innate immunity in monocytes, macrophages and dendritic cells [31]. They comprise a family of small proteins found in different crops like wheat, rye or barley, which are associated with gluten [32]. As wheat, which is also contained in processed food, has become a major staple in modern societies nutrition, the daily intake of ATI is estimated to be 0.5 g to 1.5 g per person [32]. As a result, consumption of ATI containing food can cause non-celiac gluten sensitivity [33]–[35] and drive intestinal inflammation [31], [32]. Amylase trypsin inhibitors can also act as allergens and are the major cause in baker's asthma [36].

However, it is known that the inflammation is triggered by direct binding of ATI to TLR4 [31], [37], but its influence on the membrane distribution of TLR4 is unknown. To investigate the influence of ATI and LPS on spatial distribution of TLR4 in primary human macrophages, we used single molecule localization microscopy (SMLM). Aim

of our study was to elucidate if ATI treatment causes a change in the surface representation and distribution of TLR4, which might indicate increased downstream signaling and hence an increased immune response. Studies have shown that environmental factors can lead to nitration of proteins and hence increase their inflammatory and allergenic potential [38]–[41]. Therefore, we have also tested tetranitromethane (TNM) nitrated ATI to investigate whether nitration of ATI induces changes in the distribution of TLR4 compared to native ATI.

## Results and Discussion

### TLR4 forms clusters on the cell membrane

The distribution of TLR4 on the cell membrane of unstimulated primary human macrophages was investigated using indirect immunostaining. TLR4 was labeled with Alexa647 and stained macrophages were imaged using conventional fluorescence and localization microscopy (Figure 1). The use of both microscopy methods allows access to the large-scale distribution of TLR4 on the single cell level and short-scale distribution of TLR4 on membrane sections at the single molecule level. Conventional fluorescence images show that macrophages express TLR4, whereby differences in the expression level of TLR4 between cells can be observed (Figure 1A). In addition, membrane sections with a size of about 5  $\mu\text{m}$  to 20  $\mu\text{m}$  exist on individual cells, which exhibit increased fluorescence intensity (Figure 1 A, arrows). These sections show that the localization of TLR4 varies at the single cell level. Next, SMLM was used to measure the distribution of TLR4 in individual membrane sections at the single molecule level. Compared to conventional fluorescence microscopy, finer structural details become visible (Figure 1B), which indicate an accumulation of TLR4 molecules in domains at the nanometer scale (Figure 1C). The domains appear to be evenly distributed in the captured membrane section. To quantitatively evaluate the observed pattern, a grid-based analysis was performed, which compares the measured distribution with that expected from a random distribution (Figure 1D). It shows that TLR4 forms clusters in the nanometer range on the cell membrane. These clusters are embedded in regions depleted by TLR4. Regions depleted by TLR4 also contain small isolated clustered regions, which are not part of a larger cluster complex. This can be attributed to fluorophores belonging to a single TLR4 receptor, which blinks multiple times during SMLM imaging. This leads to small pseudo clusters in the order of magnitude of the localization precision (Supplementary Figure 1). All together it shows that TLR4 forms cluster in unstimulated cells, which confirms previous investigations that have shown that membrane receptors can already exist in a pre-clustered state [42]–[44].

Next, we investigated whether ATI and TNM nitrated ATI have an effect on membrane distribution of TLR4. Therefore, macrophages were stimulated with these agonists for 15 min and 30 min, respectively. LPS served as positive control. The chosen stimulation times are based on previous studies using LPS as agonist, where it has shown to induce a relocation of TLR4 on the cell membrane within 15 min of stimulation [45], [46]. In addition, our own measurements on the macrophages reveal a LPS-induced translocation of NF- $\kappa$ B from the cytoplasm into the nucleus within 30 minutes (Supplementary Figure 2). The visual inspection of individual membrane sections of cells treated with ATI and ATI TNM for 15 min show a similar clustered distribution of TLR4 as in unstimulated samples (Figure 2A+B). Additionally, we calculated the index of dispersion for each sample and obtained a value of  $(2.1 \pm 0.7)$  TLR4 molecules/pixel<sup>2</sup> to  $(2.5 \pm 0.7)$  TLR4 molecules/pixel<sup>2</sup>, indicating significant clustering

of TLR4 in all samples compared to a random distribution. Notably, macrophages treated with ATI or LPS show an increase in the density of molecules on the cell membrane (Figure 2C). In addition, donor-dependent variations in the density can be observed.

### **TLR4 tends to form smaller clusters upon stimulation**

Since we could show that TLR4 forms clusters on the cell membrane in primary human macrophages, the next step was to investigate on which size scales the clusters exist and whether there are differences between untreated cells and cells treated with ATI or ATI TNM. For this purpose, Ripley's H-function was calculated for each treatment as a means of determining the degree of clustering as a function of the length scale (Figure 3). For comparison Ripley's H-function of a random distribution is displayed as well. Deviations from this line towards positive values indicate clustering, which is the case for all samples regardless of the type of stimulation used. Using the maximum of Ripley's H-function as an indicator for the cluster size of TLR4 [47], reveals a mean cluster size of 64 nm for unstimulated macrophages (Figure 3D, Supplementary Table 1). Since ATI, ATI TNM and LPS stimulated samples do not show a significantly increased cluster size, it can be concluded that the increased density of molecules observed in ATI and LPS stimulated samples is not accompanied by an increased cluster size. On the contrary, there is a tendency towards a smaller cluster size in the treated samples (Figure 3D). Previous studies focusing on the influence of LPS on the cluster size of TLR4 have come to different conclusions regarding the effects of LPS. Aaron et al. [48] reported a TLR4 cluster size of ~380 nm in unstimulated mouse macrophages, which had increased to ~520 nm after stimulation with LPS. However, our measured TLR4 cluster sizes are comparable to the ones measured on LPS stimulated glioblastoma cells [23]. Discrepancies between the studies could be attributed to the use of different cell lines, especially a different behavior of TLR4 in mouse cells or the result of inefficient photoswitching during localization imaging [23], which can lead to an apparently larger cluster size.

To elucidate if the cluster size corresponds to the diameter, we carried out simulation with a similar point density and distribution as in the experimental data but with a defined cluster diameter (Supplementary Figure 3). Our simulation shows that the cluster size obtained from Ripley's analysis reflects the diameter of the clusters. It must also be noted that the true cluster diameter should be smaller as the measured one, due to the chosen labeling system consisting of primary antibody and fluorescently labeled secondary F(ab')<sub>2</sub> fragments. This increases the distance between protein and detection molecule so that the measured cluster diameter represents an upper limit.

### **Recruitment of TLR4 upon stimulation**

Since the analysis with Ripley's function only allows statements about the level of clustering and the characteristic cluster size, further analysis was done using DBSCAN [48]. In contrast to Ripley's function, this allows to identify and visualize individual clusters of any shape (Supplementary Figure 5). Using the identified molecules within clusters, we were able to calculate the percentage of clustered molecules (Figure 4A). It reveals that the majority of TLR4 molecules on the cell membrane are distributed in clusters. In addition, stimulation leads to an increase in the molecules that are part of a cluster, with the highest increase in ATI and LPS treated samples. Next, we calculated the density of the clusters on the cell membrane (Figure 4B). On average there are 4 clusters/ $\mu\text{m}^2$  to 7 clusters/ $\mu\text{m}^2$ , which can be translated to a mean distance between neighboring clusters between 200 nm and 260 nm, respectively. Here, an

increase in the density of the clusters can be observed, especially in ATI and LPS stimulated samples. The obtained densities are in agreement with previous investigations on LPS stimulated glioblastoma cells [23]. To investigate whether the individual TLR4 clusters themselves form cluster, we used the center of mass of the clusters obtained by DBSCAN and investigated the distribution of the clusters. Our analysis reveals that the clusters are randomly distributed on the cell membrane regardless of the treatment, which shows that second-order clusters do not exist on the investigated size scale (data not shown).

Moreover, to verify the results obtained with Ripley's function we used DBSCAN to derive the cluster diameter (Figure 4C) and the number of molecules per cluster (Figure 4D) from at least 8,500 clusters. Here we obtained a value of 46 nm to 57 nm for the cluster diameter, which is slightly lower as the one obtained by Ripley's function. Apart from that it confirms the previous analyses that ATI and ATI TNM do not significantly increase cluster size, but that there is a tendency towards smaller clusters for all treated samples. Considering that the number of molecules per cluster is also decreasing after treatment, this could be explained by the recruitment of receptors around pre-existing monomers or lower order oligomers. This would increase the local density, exceeding the threshold after which DBSCAN detects the clusters. The recruitment of receptors then tends to lead to smaller clusters with few points, as observed in the treated samples in the measurement data. It also explains that the percentage of clustered molecules is increasing.

### **TLR4 stimulation reduces density of TLR4 molecules around cluster centers**

The recruitment of molecules, that leads to the formation of smaller clusters containing less molecules, should be reflected in a decrease in density around the center of mass of the cluster. Therefore, we looked at the radial density distribution of molecules around the clusters depending on the treatment (Figure 5). Samples treated with ATI and ATI TNM show a reduction in the density of molecules within the cluster and its immediate environment. LPS treated samples show a similar effect after stimulation for 30 min. However, 15 min stimulation of LPS results in an increase in the density of molecules at the border of a cluster (Figure 5A).

## **Conclusions**

Here we investigated the membrane distribution of TLR4 in primary human macrophages using SMLM. Thereby we focused on the influence of ATI and ATI TNM, which had been identified as activators of immunity in macrophages by directly binding to TLR4 [31] [41]. Using different quantitative analysis methods, we could show that more than 60 % of TLR4 molecules are located in clusters with a diameter of 46 nm to 55 nm upon treatment. With a mean inter-cluster distance between 200 nm and 260 nm, those structures would have been inaccessible using conventional fluorescence microscopy. We could show that after treatment with ATI and ATI TNM there is an increase in the percentage of clustered molecules accompanied with a tendency towards the formation of smaller clusters containing less molecules, which results in less dense clusters. Together it suggests the recruitment of receptors around pre-existing monomers or lower order oligomers, which may lead to an increase in the number of signaling platforms. This structural change could indicate functional or regulatory processes induced by ligand stimulation [26]. The formation of smaller clusters and the decreased density of molecules around the cluster center could also indicate the early formation of endosomes and continuous degradation of TLR4 from

the cluster centers [45]. As we observed a similar tendency for LPS stimulated samples, our results indicate microscopically an influence of ATI on TLR4, which was previously shown by coimmunoprecipitation [31] and surface plasmon resonance binding [37]. Furthermore, they suggest a similar role of ATI and TNM nitrated ATI in the membrane distribution of TLR4 as observed for LPS.

A recent study elucidated the ligand-specific receptor dimerization of TLR4 using stoichiometric labeling of TLR4 together with quantitative single molecule localization microscopy [49]. In this study, they were able to determine the proportion of monomeric and dimeric TLR4 complexes depending on the LPS chemotype used. An extension of these experiments from different LPS chemotypes to ATI might help to understand whether the formation of smaller and less dense clusters is accompanied by a change in the ratio of monomers to dimers upon ATI stimulation. Such effects would indicate stronger and focused signaling events, which would underline together with our results the importance of receptor clusters as signaling platforms.

## **Experimental**

### **Cell culture**

Primary human macrophages were derived from peripheral blood mononuclear cells (PBMCs) of healthy donors ( $n = 3$ ). Isolation and differentiation was done using standard methods as described by Heydenreich et al. (2014) [50]. In brief, a density centrifugation of heparinized blood samples was performed to obtain peripheral mononuclear cells and autologous serum. Next, cells were diluted in Isocove's Modified Dulbecco's medium (IMDM, Lonza), containing 1 % antibiotic antimycotic solution (Sigma Aldrich). Cells were seeded on glass coverslips (R. Langenbrinck GmbH, thickness of  $0.17 \text{ mm} \pm 0.005 \text{ mm}$ ) placed in a 6-well plate (Greiner Bio-One) at a concentration of  $1.5 \times 10^6$  cells/well to  $2.5 \times 10^6$  cells/well. Cells were incubated for 30 min and washed three times in pre-warmed phosphate-buffered saline (PBS, Thermo Fisher Scientific). Afterwards, cells were incubated for 6 days at  $37 \text{ }^\circ\text{C}$  and 5 %  $\text{CO}_2$  in IMDM containing granulocyte macrophage colony-stimulating factor (GM-CSF, university-clinic pharmacy Mainz) and 2 % autologous serum, which had been heat-inactivated before at  $56 \text{ }^\circ\text{C}$  for 30 min.

### **Treatment with LPS, ATI or ATI TNM**

Primary human macrophages grown on glass coverslips were washed once with pre-warmed PBS. Next, cells were incubated with either 100 ng/ml lipopolysaccharide (LPS-EB; from *E. coli* O111:B4, Invivogen), 12.5  $\mu\text{g/ml}$  ATI (Amylase Trypsin Inhibitor Type I, Sigma Aldrich) or 12.5  $\mu\text{g/ml}$  ATI TNM. All stimuli were diluted in complete cell culture medium and incubation was done at  $37 \text{ }^\circ\text{C}$  and 5 %  $\text{CO}_2$  for 15 min and 30 min. Afterwards, cells were washed once in PBS followed by a two-step fixation process [51], [52]. First, cells were fixed in cold PBS containing 4 % formaldehyde (Thermo Fisher Scientific) and 0.2 % glutaraldehyde (Sigma Aldrich). After 15 min at  $4 \text{ }^\circ\text{C}$  the first fixation buffer was replaced by a second fixation buffer. It contained the same concentration of formaldehyde and glutaraldehyde in PBS as the first one but had been set at room temperature. Subsequently, incubation for the second fixation step was done for 30 min at room temperature. Afterwards, cells were washed three times in PBS and stored at  $4 \text{ }^\circ\text{C}$  in PBS until further usage for immunostaining.

### **Immunostaining**

Fixed cells were quenched for 7 min in 0.1 % (w/v) sodium borohydride ( $\text{NaBH}_4$ , Sigma Aldrich). After three washing steps in PBS, cells were blocked in 2 % bovine serum

albumin (BSA, Cell Signaling Technology) dissolved in PBS for 60 min. Next, cells were incubated for 60 min at room temperature with the primary TLR4-antibody (76B357.1, original concentration of 1 mg/ml, cat. no. ab22048, Abcam) diluted 1 to 100 in blocking buffer. Samples were then washed three times in PBS and subsequently incubated with the secondary antibody (F(ab')<sub>2</sub> anti-mouse Alexa Fluor 647, original concentration of 2 mg/ml, cat. no. A-21237, Thermo Fisher Scientific) diluted 1 to 100 in blocking buffer for 60 min at room temperature. After incubation, the sample was washed again three times in PBS and stained cells were post-fixed with 4 % formaldehyde in PBS for 10 min at room temperature. After three times washing in PBS, the sample was embedded in Vectashield H-1000 (Vector Laboratories) and sealed using picodent twinsil (picodent Dental Produktions- und Vertriebs GmbH).

### **Localization microscopy**

Experiments were conducted on a custom-built localization microscope (for details see Supplementary Figure 7). In brief, for imaging of TLR4 stained macrophages a 647 nm laser (Coherent Obis) was used. For SMLM imaging the laser beam was expanded 3.125-fold, resulting into an illuminated area of ~640  $\mu\text{m}^2$  in the sample plane (area of  $1/e^2$  width of Gaussian profile). The collimated laser beam was coupled into the back port of the microscope (Leica DM RBE) and focused onto the back focal plane of the objective lens (100x/NA 1.49, Olympus). After passing an emission filter (bandpass 700/75 nm, Chroma Technology), emitted fluorescent light was collected on an electron multiplying charge-coupled device (EMCCD) camera (iXon 897 Ultra, Andor Technology) with an effective pixel size of 95 nm.

### **Imaging and data processing**

For each SMLM experiment, a region of Interest (ROI) was placed on visually inspected single cells, covering typically an area of ~50  $\mu\text{m}^2$  to ~400  $\mu\text{m}^2$  of the plasma membrane. For each ROI of a cell 5,000 frames were acquired with a laser intensity of 6.5 kW/cm<sup>2</sup> (measured in the sample plane) and an exposure time of 40 ms.

To obtain the list of localizations, processing of the raw data stacks was done using Matlab (MathWorks) and the custom written software package Integrated Localization Environment (ILE; <https://gitlab.com/microscopy/ILE>). The localization algorithm of ILE, which accomplishes the extraction and position determination of single molecule signals from the raw data stacks is based on fastSPDM [53]. In brief, an initial background image was created from the first eight frames of the raw data stack. The background image was subtracted from the frames of the raw data stack and while looping through the frames of the raw data stack the background image had been continuously adjusted to account for changes in background intensities during imaging. Next, signal peaks were extracted from the resulting background corrected images. A 7x7 px ROI was centered around each signal peak exceeding a standard deviation of 2 times the noise (whereby the noise is considered to follow a Poisson noise model) were considered for subsequent position determination. Positions with subpixel accuracy were determined by calculating the center of mass of each input ROI, which corresponds in the absence of background (due to background subtraction) to a maximum likelihood estimation (MLE). Close by signals were detected by searching each ROI from its center towards its boundaries for local intensity minima. In case of local minima, the ROI was clipped and the signal was recalculated or discarded when the clipping results in a loss of more than 30 % of the ROIs intensity. An initial list of localizations was returned by the algorithm, listing x- and y- position of each detected single molecule as well as information about its photon count and localization precision. Next, the list of localization was post-processed using ILE by first joining localizations

occurring in consecutive frames and within 2.5 times of the mean localization precision. Drift correction was done by splitting the list of localization in 5 subsets and correlating the reconstructions of the subsets [54], [55]. The measured shift among the subsets was interpolated and used to correct the positions of the detected signals in the list of localizations. No further filtering of the list of localizations had been applied. For reconstruction of SMLM images, the single molecule positions were blurred by a Gaussian with a standard deviation corresponding to their respective localization precisions.

### **Spatial point pattern analysis of SMLM data**

For analysis of spatial distribution of the detected single molecule signals a custom written software package in Matlab was used (Integrated Localization Analyzer for Nanoscale Distributions (ILAND), <https://github.com/Jan-NM/ILAND>). The list of localizations was preprocessed in a first step by reconstructing the images (via histogram binning) and cropping a rectangular ROI for each cell that showed a homogenous distribution on large scales i.e. no visible gaps. For each measured cell a new list of localizations was generated containing only the points within the rectangular ROI. Subsequent analysis was done on the single molecule coordinates. Random data were generated from the density and area of the experimental input data exhibiting complete spatial randomness (CSR). In total four different algorithms were used to characterize the point pattern:

#### *Grid-based analysis*

Detected single molecule signals were binned on a uniform grid with a bin size of 10 nm (corresponding to the average rounded localization precision). In parallel, random data were generated from the experimental data and also binned on a grid. The ratio of experimental to random data of each bin was calculated and color-coded displayed. A ratio around one indicates a random distribution of points which corresponds to the color green in the selected color code. Yellow colored areas i.e. a ratio larger than one indicate clustering, whereas blue areas i.e. ratios lower than one indicate dispersion. For better visualization grid values larger than two had been clipped.

#### *Ripley's H-function*

Ripley's H-function [56] up to a distance of 1  $\mu\text{m}$  was calculated to estimate the typical domain size of the point pattern. To account for edge effects, points with a minimum distance of 1  $\mu\text{m}$  from the image border were extracted from the input data. A distance matrix between the extracted point pattern and the input data was pre-computed. The distance matrix contained only entries of distances smaller than 1  $\mu\text{m}$ . Using the distance matrix Ripley's K-function was calculated [47]:

$$K(r) = \frac{1}{N} \sum_{i=1}^N \frac{n_{p_i}(r)}{\lambda}$$

Where N denotes the total number of points that are investigated, n is the number of points within a distance r of a point  $p_i$  and  $\lambda$  the density of points. The K-function was later transformed to obtain Ripley's H-function:

$$H(r) = \sqrt{\frac{K(r)}{\pi}} - r$$

Subsequently, the Ripley's H-functions obtained from different donors from the same treatment were averaged and the maximum of Ripley's H-function was used as an estimate of the cluster size.

#### *Density-based spatial clustering of applications with noise (DBSCAN)*

DBSCAN requires two user input parameters – radius (epsilon) and minimum number of points (minPts). Together, these values form a local density threshold that determines whether the point under investigation is part of a cluster [48]. In brief, initial DBSCAN parameter selection was done as follows: The 4<sup>th</sup> nearest neighbor distances of the detected molecules from the list of localizations of a few experimental data sets were calculated. The nearest neighbor distances were sorted in ascending order and plotted against the number of points within the data set. The distance, where the bend in the plot occurs, was used as a starting value for the radius parameter of DBSCAN. Next, DBSCAN was executed with those starting parameters and further iterative adjustment of the parameters was done by visualizing the cluster and comparing the distance distribution obtained from the points outside of clusters with a random distribution (Supplementary Figure 4). Using this parameter estimation pipeline, a value of 30 nm for the radius (epsilon) and a value of 6 for the minimum number of points (minPts) were determined.

With these input parameters and the list of localizations, the implemented DBSCAN algorithm calculates first a sparse distance matrix, which contains for every point (= single molecule) entries to points that lie within the specified distance (here epsilon = 30 nm). In the next step DBSCAN is applied on the distance matrix and points are assigned to a specific cluster or as noise. Next, the algorithm generates a table containing for every detected cluster its area, number of molecules, diameter, center of mass, density and the distance to the next neighboring cluster as well as an assignment list for every point to which cluster it belongs. This assignment list was used to calculate the distances of points outside of the clusters as shown in Supplementary Figure 4. The maximum allowable cluster diameter was set to 1  $\mu\text{m}$ . If a cluster larger than 1  $\mu\text{m}$  had been detected, its points were assigned as noise.

#### *Radial distribution from the center of mass of the clusters*

To determine the radial distribution of single molecules around the clusters, center of mass coordinates and nearest neighbor cluster distances were extracted for each detected cluster from the DBSCAN analysis. The number of detected molecules within concentric rings around the center of mass of the cluster was calculated and averaged over the entire clusters. The width of the rings was set to 1 nm and the maximum calculated distance from the cluster center was limited to half of the inter-cluster distance. The half of inter-cluster distance  $d_{1/2}^{NN}$  was defined as follows:

$$d_{1/2}^{NN} = r_{cluster} + \frac{1}{2}(d^{NN} - r_{cluster} - r_{cluster}^{NN})$$

Here,  $r_{cluster}$  denotes the cluster radius,  $d^{NN}$  the distance to the next neighboring cluster and  $r_{cluster}^{NN}$  the radius of the next neighboring cluster. Thus, different cluster diameters are considered. Finally, the average number of molecules contained in each ring was normalized to the area of the rings and the difference between the treatment and the medium control was calculated for each ring.

#### **Conventional fluorescence microscopy of TLR4**

Primary human macrophages were derived and isolated from PBMCs as described before. Instead of glass coverslips, cells were seeded on a glass bottom 12-well plate (Cellvis) at a concentration of  $1.5 \times 10^6$  cells/well to  $2.5 \times 10^6$  cells/well. Fixation and

immunostaining of TLR4 was done in the same way as for the localization microscopy experiments. Instead of Vectashield H-1000, cells were imaged in PBS on the Opera Phenix High-Content Screening system (PerkinElmer). TLR4 stained cells (excitation 640 nm, emission 650 nm – 760 nm) were imaged in non-confocal mode using a 20x/1.0 water immersion objective.

### **Nitration of ATI with Tetranitromethane (TNM) and endotoxin quantification**

ATIs (Amylase Inhibitor Type I, Sigma Aldrich) were diluted in ultra-pure water to a final concentration of 1 mg/ml. 4.55 µl TNM/Methanol (4 % v/v) were added to 500 µl of diluted ATI. The mixture was stirred for 3 h at room temperature. Residual TNM was removed using a PD-25 size exclusion column (GE Healthcare). The endotoxin content was quantified using a limulus amoebocyte lysate (LAL) assay (Thermo Fisher Scientific). ATI TNM solutions with an endotoxin content of less than 20 endotoxin units per ml were used for experiments.

### **Sample Size**

Experiments were conducted on primary human macrophages obtained from three different healthy donors. A total of at least 25 cells were evaluated per treatment. Number of cells used for Ripley's analysis and DBSCAN can be found in Supplementary Table 1 ,2 and 3.

### **Ethics statement**

All experimentation was reviewed and approved by the Ethical Committee Landesärztekammer Rheinland-Pfalz, Mainz, Germany (license 837.176.08 (6173)). Consent of participants was given in written form.

### **Acknowledgements**

We thank Dr. Sandra Ritz, Dr. Maria Hanulova, Dr. Jonas Schwirz, Dr. Aleksander Szczurek, Florian Schock and Amine Gourram for continuous support and fruitful discussions. Support by the Max Planck Graduate Center, the Mainz Program for Chemical Allergology and the joint Laboratory of Inflammation and Microscopy is gratefully acknowledged. We also acknowledge the IMB Microscopy and Histology Core Facility for support and the German Research Foundation (DFG) for funding the Opera Phenix High Content Spinning Disk Microscope (Project 402386039). We thank Dr. Frank Helleis, Dr. Thomas Klimach and the workshop of the MPI for Chemistry as well as the E-lab of IMB for help and support in the construction of the SMLM setup.

## References

- [1] E. M. Y. Moresco, D. LaVine, and B. Beutler, "Toll-like receptors," *Curr. Biol.*, vol. 21, no. 13, pp. R488–R493, 2011.
- [2] T. Kawasaki and T. Kawai, "Toll-like receptor signaling pathways," *Front. Immunol.*, vol. 5, no. SEP, pp. 1–8, 2014.
- [3] J. C. Chow, D. W. Young, D. T. Golenbock, W. J. Christ, and F. Gusovsky, "Toll-like receptor-4 mediates lipopolysaccharide-induced signal transduction.," *J. Biol. Chem.*, vol. 274, no. 16, pp. 10689–92, Apr. 1999.
- [4] B. Beutler, X. Du, and A. Poltorak, "Identification of Toll-like receptor 4 (Tlr4) as the sole conduit for LPS signal transduction: genetic and evolutionary studies.," *J. Endotoxin Res.*, vol. 7, no. 4, pp. 277–80, 2001.
- [5] J. da Silva Correia, K. Soldau, U. Christen, P. S. Tobias, and R. J. Ulevitch, "Lipopolysaccharide Is in Close Proximity to Each of the Proteins in Its Membrane Receptor Complex," *J. Biol. Chem.*, vol. 276, no. 24, pp. 21129–21135, Jun. 2001.
- [6] T. L. Gioannini *et al.*, "Isolation of an endotoxin-MD-2 complex that produces Toll-like receptor 4-dependent cell activation at picomolar concentrations," *Proc. Natl. Acad. Sci.*, vol. 101, no. 12, pp. 4186–4191, Mar. 2004.
- [7] B. S. Park, D. H. Song, H. M. Kim, B.-S. Choi, H. Lee, and J.-O. Lee, "The structural basis of lipopolysaccharide recognition by the TLR4–MD-2 complex," *Nature*, vol. 458, no. 7242, pp. 1191–1195, Apr. 2009.
- [8] A. Płóciennikowska, A. Hromada-Judycka, K. Borzęcka, and K. Kwiatkowska, "Co-operation of TLR4 and raft proteins in LPS-induced pro-inflammatory signaling.," *Cell. Mol. Life Sci.*, Oct. 2014.
- [9] J.-M. Ruyschaert and C. Loney, "Role of lipid microdomains in TLR-mediated signalling," *Biochim. Biophys. Acta - Biomembr.*, vol. 1848, no. 9, pp. 1860–1867, Sep. 2015.
- [10] M. Triantafilou, K. Miyake, D. T. Golenbock, and K. Triantafilou, "Mediators of innate immune recognition of bacteria concentrate in lipid rafts and facilitate lipopolysaccharide-induced cell activation.," *J. Cell Sci.*, vol. 115, no. Pt 12, pp. 2603–11, Jun. 2002.
- [11] L. J. Pike, "Rafts defined: a report on the Keystone symposium on lipid rafts and cell function," *J. Lipid Res.*, vol. 47, no. 7, pp. 1597–1598, Jul. 2006.
- [12] M. Schürmann *et al.*, "Helium Ion Microscopy Visualizes Lipid Nanodomains in Mammalian Cells," *Small*, vol. 11, no. 43, pp. 5781–5789, Nov. 2015.
- [13] K. A. Lidke, B. Rieger, T. M. Jovin, and R. Heintzmann, "Superresolution by localization of quantum dots using blinking statistics," *Opt. Express*, vol. 13, no. 18, p. 7052, 2005.
- [14] E. Betzig *et al.*, "Imaging Intracellular Fluorescent Proteins at Nanometer Resolution," *Science.*, vol. 313, no. 5793, pp. 1642–1645, Sep. 2006.
- [15] S. T. Hess, T. P. K. Girirajan, and M. D. Mason, "Ultra-high resolution imaging by fluorescence photoactivation localization microscopy.," *Biophys. J.*, vol. 91, no. 11, pp. 4258–72, Dec. 2006.
- [16] M. J. Rust, M. Bates, and X. Zhuang, "Sub-diffraction-limit imaging by stochastic optical reconstruction microscopy (STORM).," *Nat. Methods*, vol. 3, no. 10, pp. 793–5, Oct. 2006.
- [17] A. Sharonov and R. M. Hochstrasser, "Wide-field subdiffraction imaging by accumulated binding of diffusing probes," *Proc. Natl. Acad. Sci.*, vol. 103, no. 50, pp. 18911–18916, Dec. 2006.
- [18] M. Heilemann *et al.*, "Subdiffraction-resolution fluorescence imaging with

- conventional fluorescent probes,” *Angew. Chemie - Int. Ed.*, vol. 47, no. 33, pp. 6172–6176, 2008.
- [19] P. Lemmer *et al.*, “SPDM: light microscopy with single-molecule resolution at the nanoscale,” *Appl. Phys. B*, vol. 93, no. 1, pp. 1–12, Sep. 2008.
- [20] S. W. Hell and J. Wichmann, “Breaking the diffraction resolution limit by stimulated emission: stimulated-emission-depletion fluorescence microscopy,” *Opt. Lett.*, vol. 19, no. 11, p. 780, Jun. 1994.
- [21] R. Heintzmann and C. G. Cremer, “Laterally modulated excitation microscopy: improvement of resolution by using a diffraction grating,” 1999, pp. 185–196.
- [22] M. G. Gustafsson, “Surpassing the lateral resolution limit by a factor of two using structured illumination microscopy,” *J. Microsc.*, vol. 198, no. Pt 2, pp. 82–7, May 2000.
- [23] M.-T. Zeuner *et al.*, “Biased signalling is an essential feature of TLR4 in glioma cells,” *Biochim. Biophys. Acta - Mol. Cell Res.*, vol. 1863, no. 12, pp. 3084–3095, Dec. 2016.
- [24] J. S. Aaron, B. D. Carson, and J. A. Timlin, “Characterization of differential Toll-like receptor responses below the optical diffraction limit,” *Small*, vol. 8, no. 19, pp. 3041–9, Oct. 2012.
- [25] T. Lang and S. O. Rizzoli, “Membrane protein clusters at nanoscale resolution: more than pretty pictures,” *Physiology (Bethesda)*, vol. 25, no. 2, pp. 116–24, Apr. 2010.
- [26] M. F. Garcia-Parajo, A. Cambi, J. A. Torreno-Pina, N. Thompson, and K. Jacobson, “Nanoclustering as a dominant feature of plasma membrane organization,” *J. Cell Sci.*, vol. 127, no. 23, pp. 4995–5005, Dec. 2014.
- [27] N. Tanimura, S. Saitoh, F. Matsumoto, S. Akashi-Takamura, and K. Miyake, “Roles for LPS-dependent interaction and relocation of TLR4 and TRAM in TRIF-signaling,” *Biochem. Biophys. Res. Commun.*, vol. 368, no. 1, pp. 94–99, 2008.
- [28] H. Fang *et al.*, “Toll-like Receptor 4 (TLR4) Is Essential for Hsp70-like Protein 1 (HSP70L1) to Activate Dendritic Cells and Induce Th1 Response,” *J. Biol. Chem.*, vol. 286, no. 35, pp. 30393–30400, Sep. 2011.
- [29] C.-F. Liu, D. Drocourt, G. Puzo, J.-Y. Wang, and M. Riviere, “Innate Immune Response of Alveolar Macrophage to House Dust Mite Allergen Is Mediated through TLR2/-4 Co-Activation,” *PLoS One*, vol. 8, no. 10, p. e75983, Oct. 2013.
- [30] B. Raghavan, S. F. Martin, P. R. Esser, M. Goebeler, and M. Schmidt, “Metal allergens nickel and cobalt facilitate TLR4 homodimerization independently of MD2,” *EMBO Rep.*, vol. 13, no. 12, pp. 1109–1115, Oct. 2012.
- [31] Y. Junker *et al.*, “Wheat amylase trypsin inhibitors drive intestinal inflammation via activation of toll-like receptor 4,” *J. Exp. Med.*, vol. 209, no. 13, pp. 2395–2408, Dec. 2012.
- [32] V. F. Zevallos *et al.*, “Nutritional Wheat Amylase-Trypsin Inhibitors Promote Intestinal Inflammation via Activation of Myeloid Cells,” *Gastroenterology*, vol. 152, no. 5, p. 1100–1113.e12, 2017.
- [33] A. Fasano, A. Sapone, V. Zevallos, and D. Schuppan, “Nonceliac Gluten Sensitivity,” *Gastroenterology*, vol. 148, no. 6, pp. 1195–1204, May 2015.
- [34] D. Schuppan, G. Pickert, M. Ashfaq-Khan, and V. Zevallos, “Non-celiac wheat sensitivity: Differential diagnosis, triggers and implications,” *Best Pract. Res. Clin. Gastroenterol.*, vol. 29, no. 3, pp. 469–476, Jun. 2015.
- [35] V. Leccioli, M. Oliveri, M. Romeo, M. Berretta, and P. Rossi, “A New Proposal for the Pathogenic Mechanism of Non-Coeliac/Non-Allergic Gluten/Wheat Sensitivity: Piecing Together the Puzzle of Recent Scientific Evidence,” *Nutrients*, vol. 9, no. 11, p. 1203, Nov. 2017.

- [36] A. S. Tatham and P. R. Shewry, "Allergy to wheat and related cereals," *Clin. Exp. Allergy*, Sep. 2008.
- [37] M. Cuccioloni *et al.*, "Interfering with the high-affinity interaction between wheat amylase trypsin inhibitor CM3 and toll-like receptor 4: In silico and biosensor-based studies," *Sci. Rep.*, vol. 7, no. 1, pp. 4–6, 2017.
- [38] Y. K. Gruijthuisen *et al.*, "Nitration enhances the allergenic potential of proteins," *Int. Arch. Allergy Immunol.*, vol. 141, no. 3, pp. 265–275, 2006.
- [39] T. Franze, M. G. Weller, R. Niessner, and U. Pöschl, "Protein nitration by polluted air," *Environ. Sci. Technol.*, vol. 39, no. 6, pp. 1673–1678, 2005.
- [40] K. Reinmuth-Selzle *et al.*, "Air Pollution and Climate Change Effects on Allergies in the Anthropocene: Abundance, Interaction, and Modification of Allergens and Adjuvants," *Environ. Sci. Technol.*, vol. 51, no. 8, pp. 4119–4141, 2017.
- [41] K. Ziegler *et al.*, "Nitration of Wheat Amylase Trypsin Inhibitors Increases their Innate and Adaptive Immunostimulatory Potential in vitro," Manuscript submitted for publication., 2018.
- [42] R. Kaufmann, P. Müller, G. Hildenbrand, M. Hausmann, and C. Cremer, "Analysis of Her2/neu membrane protein clusters in different types of breast cancer cells using localization microscopy.," *J. Microsc.*, vol. 242, no. 1, pp. 46–54, Apr. 2011.
- [43] Y. S. Hu, H. Cang, and B. F. Lillemeier, "Superresolution imaging reveals nanometer- and micrometer-scale spatial distributions of T-cell receptors in lymph nodes," *Proc. Natl. Acad. Sci.*, vol. 113, no. 26, pp. 7201–7206, Jun. 2016.
- [44] P. S. Boyd *et al.*, "Clustered localization of EGFRvIII in glioblastoma cells as detected by high precision localization microscopy," *Nanoscale*, vol. 8, no. 48, pp. 20037–20047, 2016.
- [45] H. Husebye *et al.*, "Endocytic pathways regulate Toll-like receptor 4 signaling and link innate and adaptive immunity," *EMBO J.*, vol. 25, no. 4, pp. 683–692, 2006.
- [46] J. Cuschieri, E. Bulger, J. Billgrin, I. Garcia, and R. V. Maier, "Acid Sphingomyelinase Is Required for Lipid Raft TLR4 Complex Formation," *Surg. Infect. (Larchmt)*, vol. 8, no. 1, pp. 91–106, 2007.
- [47] M. A. Kiskowski, J. F. Hancock, and A. K. Kenworthy, "On the Use of Ripley's K-Function and Its Derivatives to Analyze Domain Size," *Biophys. J.*, vol. 97, no. 4, pp. 1095–1103, Aug. 2009.
- [48] M. Ester, H.-P. Kriegel, J. Sander, and X. Xu, "A Density-Based Algorithm for Discovering Clusters in Large Spatial Databases with Noise," *Proc. Second Int. Conf. Knowl. Discov. Data Min.*, pp. 226–231, 1996.
- [49] C. L. Krüger, M. T. Zeuner, G. S. Cottrell, D. Widera, and M. Heilemann, "Quantitative single-molecule imaging of TLR4 reveals ligand-specific receptor dimerization," *Sci. Signal.*, vol. 10, no. 503, 2017.
- [50] B. Heydenreich *et al.*, "Adjuvant effects of aluminium hydroxide-adsorbed allergens and allergoids - differences in vivo and in vitro," *Clin. Exp. Immunol.*, vol. 176, no. 3, pp. 310–319, Jun. 2014.
- [51] P. Sengupta, T. Jovanovic-Talisman, D. Skoko, M. Renz, S. L. Veatch, and J. Lippincott-Schwartz, "Probing protein heterogeneity in the plasma membrane using PALM and pair correlation analysis," *Nat. Methods*, vol. 8, no. 11, pp. 969–975, Sep. 2011.
- [52] K. A. K. Tanaka *et al.*, "Membrane molecules mobile even after chemical fixation," *Nat. Methods*, vol. 7, no. 11, pp. 865–866, Nov. 2010.
- [53] F. Gröll, M. Kirchgessner, R. Kaufmann, M. Hausmann, and U. Kechschull, "Accelerating image analysis for localization microscopy with FPGAs," in

*Proceedings - 21st International Conference on Field Programmable Logic and Applications, FPL 2011*, 2011, no. 2, pp. 1–5.

- [54] M. J. Mlodzianoski *et al.*, “Sample drift correction in 3D fluorescence photoactivation localization microscopy,” *Opt. Express*, vol. 19, no. 16, p. 15009, Aug. 2011.
- [55] Y. Wang *et al.*, “Localization events-based sample drift correction for localization microscopy with redundant cross-correlation algorithm,” *Opt. Express*, vol. 22, no. 13, p. 15982, Jun. 2014.
- [56] B. D. Ripley, “Modelling spatial patterns,” *J. R. Stat. Soc. Ser. B*, vol. 39, no. 2, pp. 172–212, 1977.

# Figures

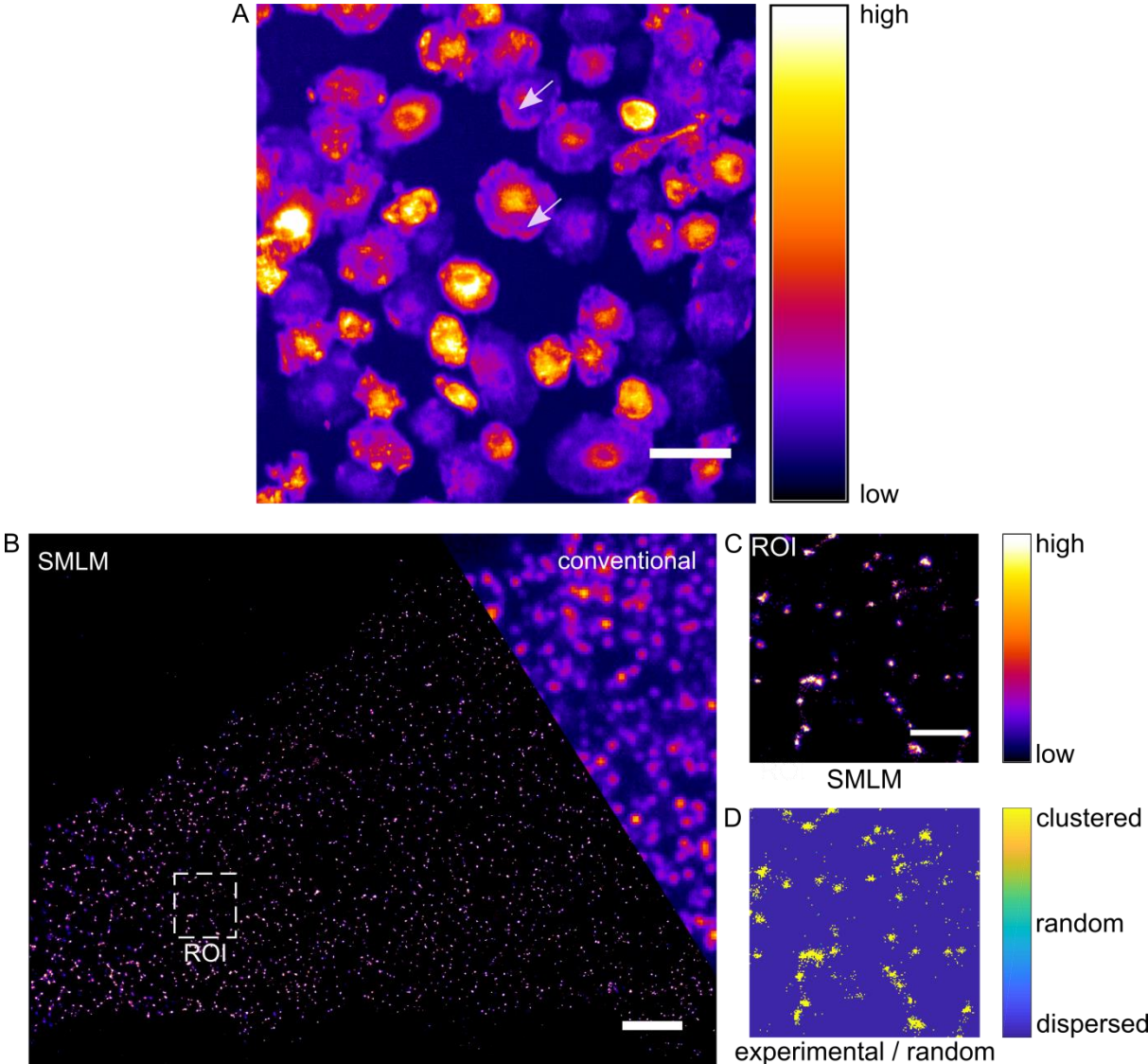


**Figure 1: TLR4 clusters on the cell membrane.** (A) Fluorescence microscopy image of macrophages stained for TLR4. Intensity coded representation reveals differences in TLR4 expression level between cells and variations in its surface representation on individual cells (white arrows). Scale bar = 50  $\mu$ m. (B) Combined SMLM and conventional image of an untreated primary human macrophage stained for TLR4. Scale bar = 2  $\mu$ m. (C) Enlarged area of the ROI indicated in (B). SMLM images are intensity coded i.e. bright areas correspond to an accumulation of single molecule signals. Scale bar = 500 nm. (D) Grid-based cluster analysis of image section shown in (C). Blue areas indicate a dispersed distribution, whereas yellow areas show clustering of TLR4.

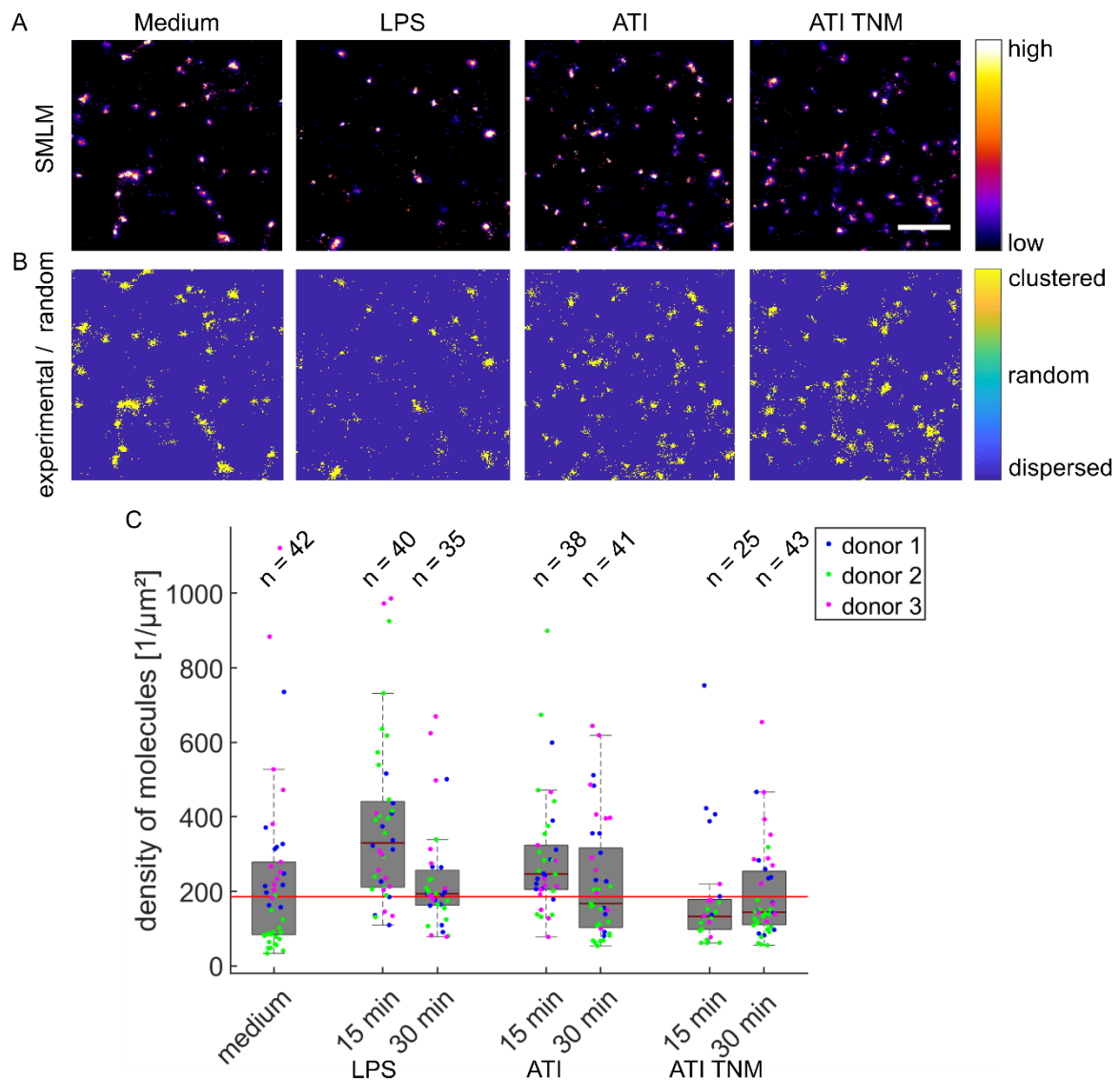


**Figure 2: TLR4 membrane clustering upon LPS or ATI stimulation.** (A) TLR4 SMLM image sections of macrophages treated with LPS-EB (100 ng/ml), ATI (12.5  $\mu\text{g}/\text{ml}$ ) or ATI TNM (12.5  $\mu\text{g}/\text{ml}$ ) for 15 min compared to medium control. The image section of the medium control was taken from the ROI indicated in figure 1B. Scale bar = 500 nm. (B) Grid-based cluster analysis of SMLM images from panel A. Color representation corresponds to that used in figure 1. (C) Mean density of detected molecules on the cell membrane. The horizontal red line indicates the median value of the medium control. The points represent mean molecule densities of individual cells and the number above each box plot denotes the number of measured cells.

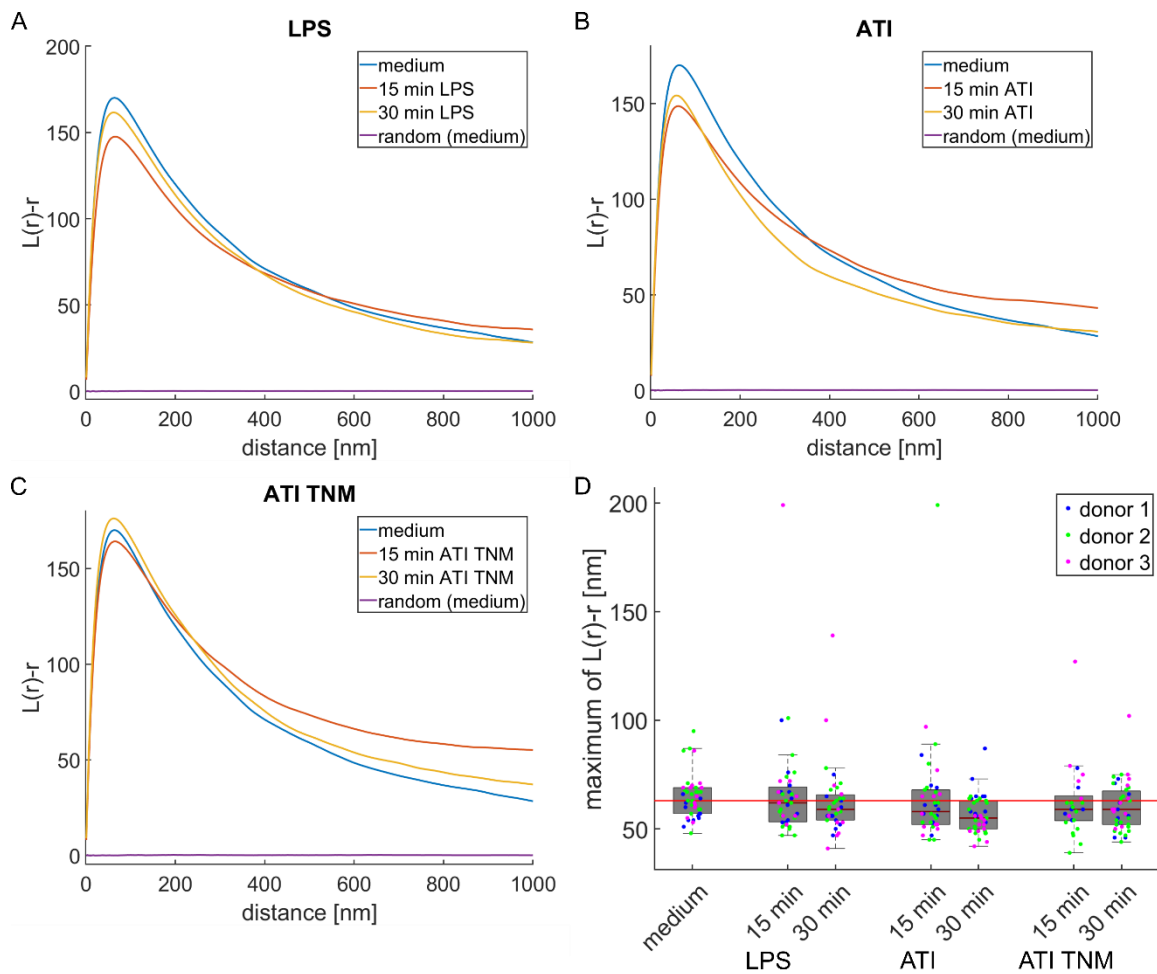


**Figure 3: Size of TLR4 clusters analyzed by Ripley's H-function.** Ripley's H-function of macrophages stimulated for 15 min and 30 min with (A) 100 ng/ml LPS, (B) 12.5  $\mu$ g/ml ATI or (C) 12.5  $\mu$ g/ml ATI TNM. Each function displays the average of three different healthy donors. All plots also show Ripley's H-function, which was calculated from the random data of the medium sample. (D) TLR4 cluster size obtained from the maximum of Ripley's function. The horizontal red line indicates the median value of the medium control. The color-coded points represent the maximum of Ripley's function for individual cells.

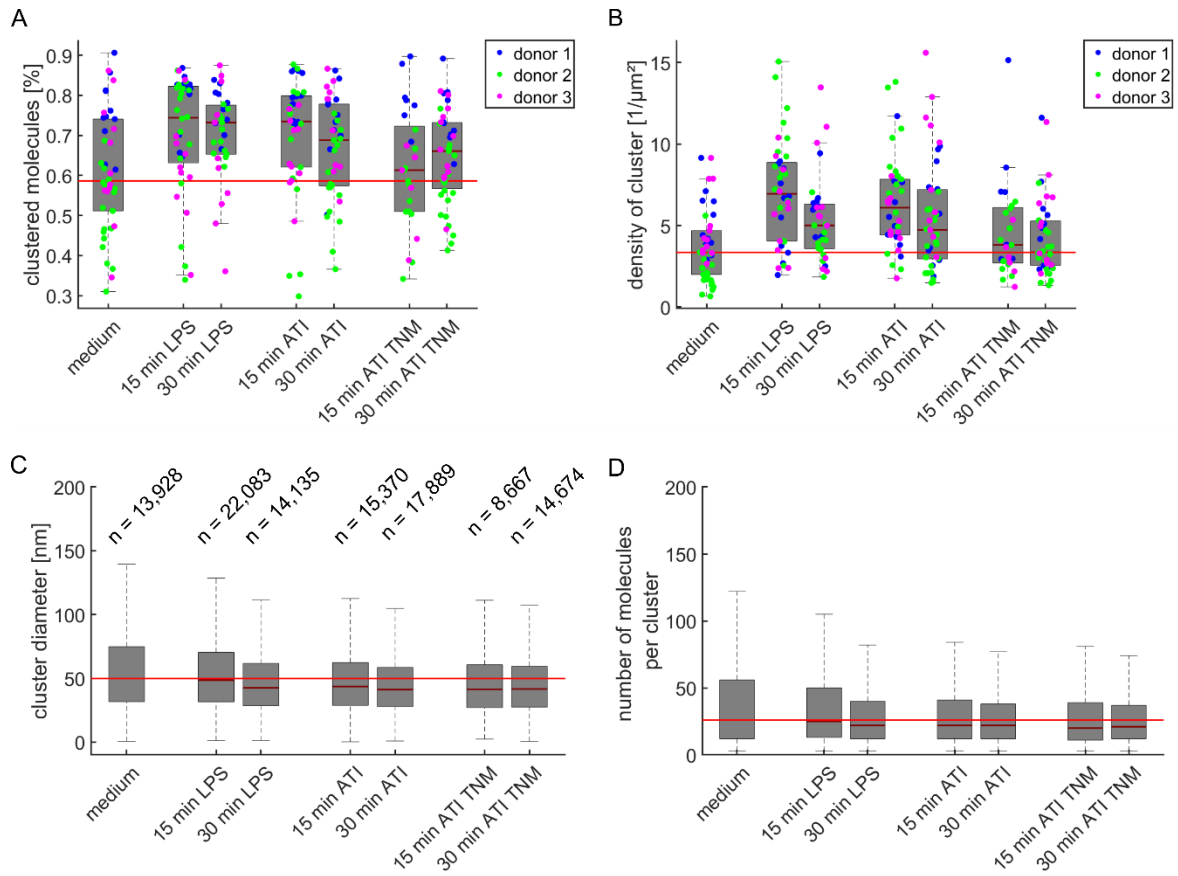


**Figure 4: Cluster properties of TLR4 analyzed by DBSCAN.** (A) Percentage of clustered molecules and (B) density of cluster on the cell membrane. Overlaid dots represent mean values obtained from different cells. The color of the dots corresponds to the respective donors. Size distribution of the (C) cluster diameter and the (D) number of molecules per cluster. Values above the boxes denote the number of measured clusters for panel A and B. In each panel, the red line represents the median of the medium control. More detailed values can be found in Supplementary Table 2 and 3.

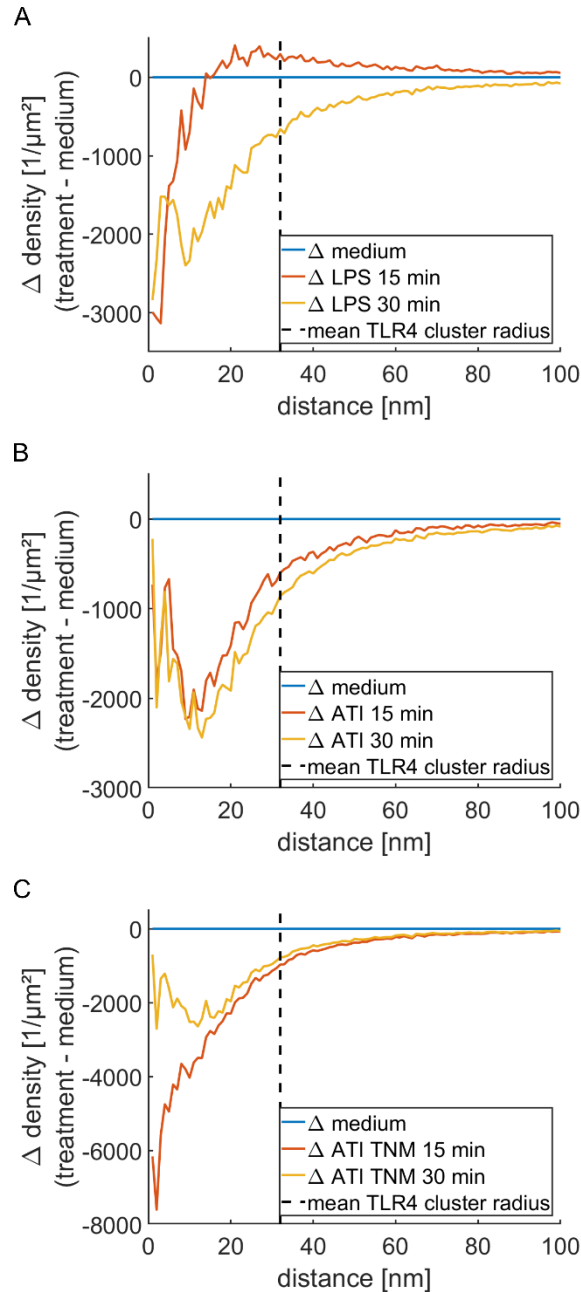


**Figure 5: Relative radial density distribution of TLR4 around cluster centers.** Differences in radial density distribution of TLR4 compared to medium sample shown for (A) LPS, (B) ATI and (C) ATI TNM stimulated samples. The blue line indicates the medium control. Calculations were carried out from the center of mass of the clusters, which had been obtained from DBSCAN analysis. In all panels the dashed line indicates the mean cluster radius of the medium control calculated by Ripley's function. Each line was obtained from the mean of three different healthy donors with a total of at least 8,000 clusters. Absolute distribution can be found in Supplementary Figure 6.

## ***Supplementary Material***

# **Membrane Distribution of TLR4 in Primary Human Macrophages after Stimulation with ATI or LPS using Localization Microscopy**

Tentative author list. To be extended/adjusted.

Jan Neumann<sup>1,2</sup>, Kira Ziegler<sup>1</sup>, Márton Gelléri<sup>2</sup>, Janine Fröhlich-Nowoisky<sup>1</sup>, Fobang Liu<sup>1</sup>, Iris Bellinghausen<sup>3</sup>, Detlef Schuppan<sup>4,5</sup>, Udo Birk<sup>2,†</sup>, Ulrich Pöschl<sup>1</sup>, Christoph Cremer<sup>2,1</sup>, and Kurt Lucas<sup>1</sup>

*<sup>1</sup>Multiphase Chemistry Department, Max Planck Institute for Chemistry, Hahn-Meitner-Weg 1, 55128 Mainz, Germany*

*<sup>2</sup>Institute of Molecular Biology, Ackermannweg 4, 55128 Mainz, Germany*

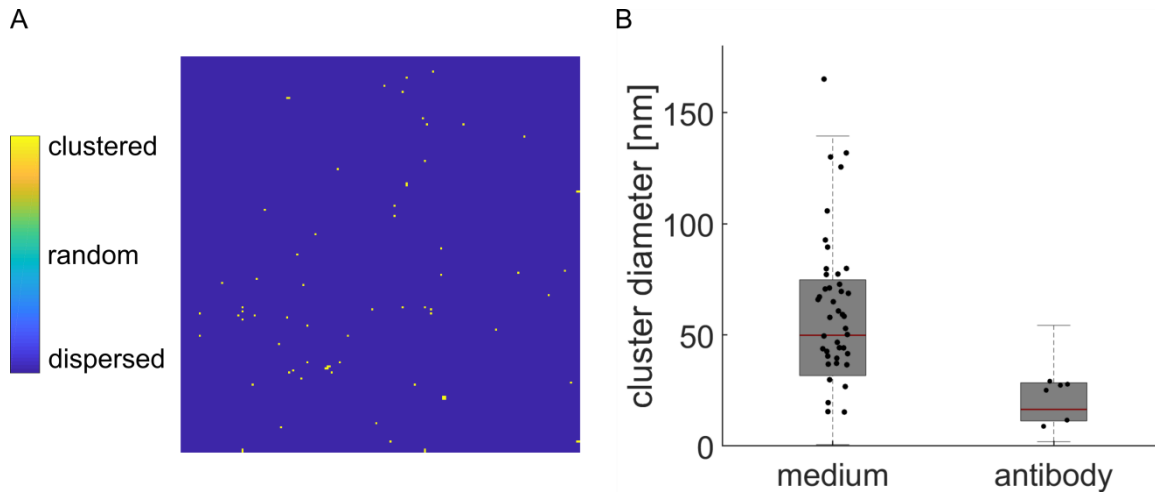
*<sup>3</sup>Department of Dermatology, University Medical Center of the Johannes Gutenberg University, 55131 Mainz, Germany*

*<sup>4</sup>Institute of Translational Immunology, University Medical Center of the Johannes Gutenberg University, Langenbeckstraße 1, 55131 Mainz, Germany*

*<sup>5</sup>Division of Gastroenterology, Beth Israel Deaconess Medical Center, Harvard Medical School, 330 Brookline Ave, Boston, MA 02215, USA*

Correspondence to K. Lucas (k.lucas@mpic.de)

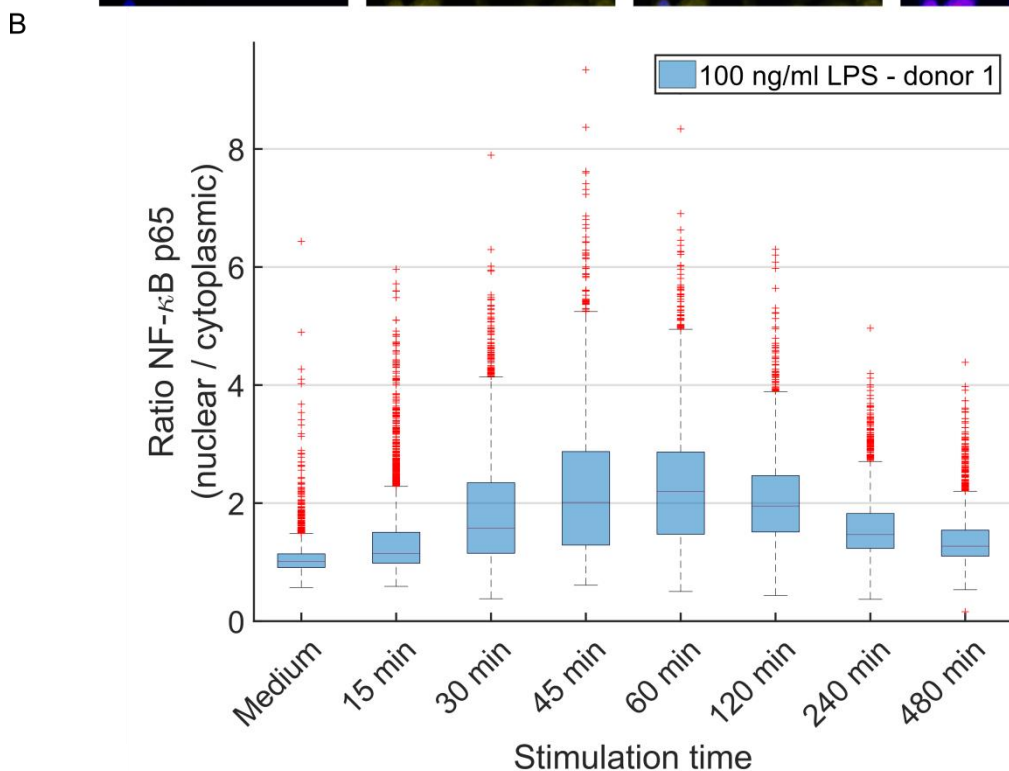
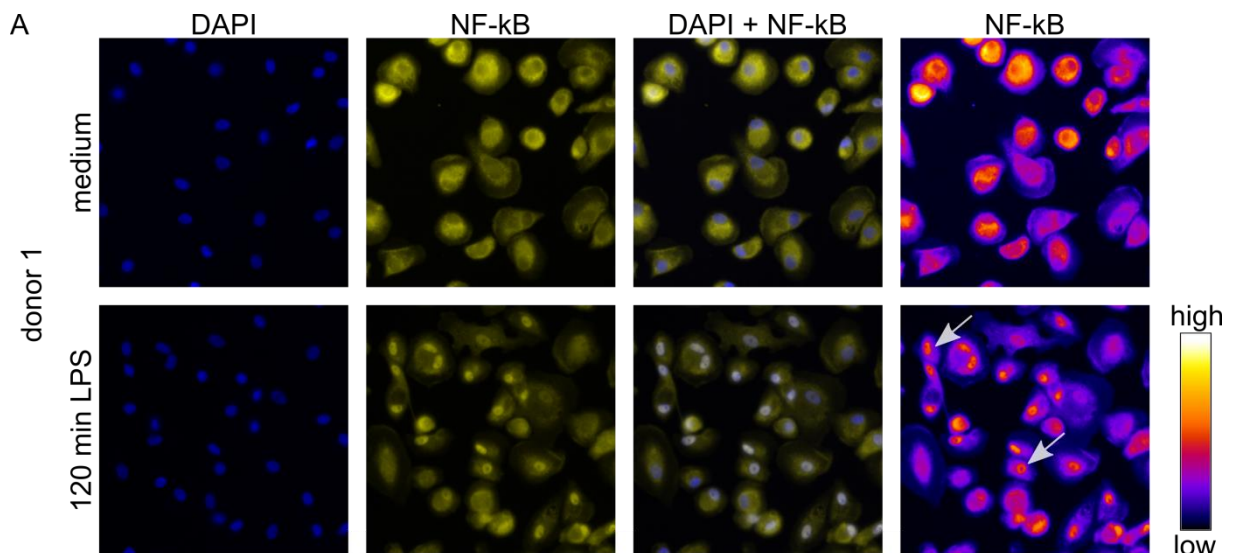
†Current address: Hochschule für Technik und Wirtschaft Chur, Pulvermühlestrasse 57, 7000 Chur, Switzerland



**Supplementary Figure 1: Cluster size due to multiple blinking of the same fluorophore.** (A) Grid-based analysis of sparsely distributed secondary antibodies on a coverslip. 2 μm x 2 μm ROI showing the color-coded ratio of experimental to random data. Yellow areas indicate clusters in the order of a few pixels. The pixel size is 10 nm. (B) Average cluster diameter obtained by DBSCAN. Every point corresponds to the average cluster diameter obtained from a cell (medium) or a field of sparsely distributed secondary antibodies on a coverslip (antibody). Note that the mean localization precision in the medium sample was about 11 nm, whereas the mean localization precision in the antibody sample was about 16 nm. This could adversely influence the cluster diameter measured for the antibody sample.

**Supplementary Note 1: Sample preparation to estimate size of clusters due to multiple blinking.**

To estimate the size of clustering due to multiple blinking of the same fluorophore, coverslips containing sparsely distributed secondary antibodies had been prepared. Therefore, glass coverslips were coated with poly-L-lysine for 15 min to 30 min and rinsed in ddH<sub>2</sub>O afterwards. Meanwhile, secondary antibodies were diluted 1 to 10,000 in ddH<sub>2</sub>O. After vortexing, 100 μl of diluted antibody were pipetted on parafilm. The coverslip was placed on top of it with the coated side facing downwards. Incubation of the sample was done for 1 h to 2 h. Next, the sample was rinsed with PBS, embedded in Vectashield H-1000 and sealed using picodent twinsil. Imaging and data evaluation were performed in the same way as for the cell samples.



**Supplementary Figure 2: Time dependent translocation of NF- $\kappa$ B induced by LPS.** (A) Fluorescence microscopy images of human primary macrophages stimulated for 120 min with either LPS-EB (100 ng/ml). After fixation, cells were stained for NF- $\kappa$ B (pseudocolor yellow). The nucleus is counterstained using DAPI (pseudocolor blue). For medium control NF- $\kappa$ B is mostly located in the cytoplasm, whereas in LPS stimulated samples NF- $\kappa$ B is enriched in the nucleus (indicated by arrows). Scale bar = 50  $\mu$ m. (B) Quantitative evaluation of NF- $\kappa$ B translocation for cells fixed at indicated time points. The ratio of nuclear to cytoplasmic NF- $\kappa$ B is plotted against the stimulation time. Nuclear translocation of NF- $\kappa$ B is visible within 30 min of LPS stimulation.

**Supplementary Note 2: Treatment, immunofluorescence staining and imaging of NF- $\kappa$ B p65.**

*Treatment*

Human primary macrophages were isolated and differentiated as described in the experimental section. Instead of coverslips, cells were seeded on 12-well glass bottom

plates (Cellvis). After 6 days of differentiation, cells were challenged with 100 ng/ml LPS-EB for different times between 15 min and 480 min. Cells were washed once in pre-warmed PBS after incubation with LPS and subsequently fixed using 4 % formaldehyde in PBS for 10 min at 37 °C. Next cells were washed three times in PBS before proceeding with immunostaining of NF- $\kappa$ B.

#### *Immunofluorescence staining*

For immunostaining, cells were permeabilized and blocked for 1 h in PBS containing 5 % bovine serum albumin (BSA; Cell Signaling Technology, Cambridge, UK) and 0.3 % Triton X-100 (Merck, Darmstadt, Germany). Primary antibody (D14E13, Cell Signaling Technology), directed against human p65 subunit of NF- $\kappa$ B, was diluted 1 to 400 in antibody dilution buffer (1 % BSA and 0.3 % Triton X-100 in PBS). Incubation of cells with primary antibody was done overnight at 4 °C. Afterwards, cells were washed three times in PBS, followed by incubation with Alexa Fluor 568 conjugated secondary antibody (Thermo Fisher Scientific, cat. no. A-11011), diluted 1 to 400 in the same buffer as the primary antibody. After 1 h of incubation at room temperature, cells were washed again three times in PBS. Counterstaining of cell nuclei was done using 4',6-diamidino-2-phenylindole (DAPI; Thermo Fisher Scientific) at a concentration of 300 nM in PBS for 3 min. After three washing steps in PBS, stained cells were immediately imaged. PBS was used as imaging buffer.

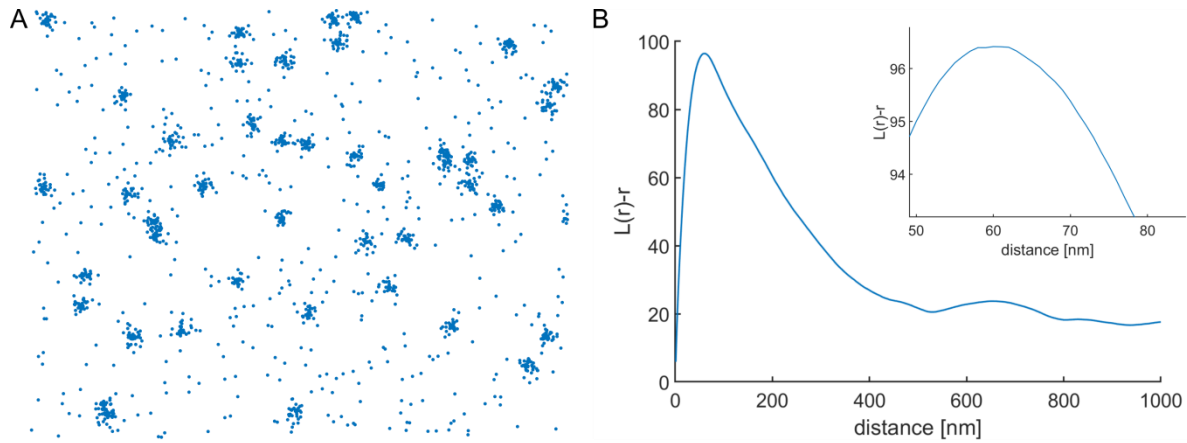
#### *Imaging*

Imaging was done using the Opera Phenix High-Content Screening system (PerkinElmer). Samples were imaged through a 20x/1.0 water immersion objective. Cells stained for NF- $\kappa$ B p65 and DAPI were excited using 561 nm and 405 nm laser lines, respectively. Emitted light was collected on two sCMOS cameras through specific emission filters for NF- $\kappa$ B p65 (570 nm to 630 nm) and DAPI (435 nm to 480 nm). 2 x 2 binning was used for the two cameras and the microscope was operated in a nonconfocal mode. Intensity and exposure time were set to obtain sub-saturating pixels. In each well, images from 72 different ROIs were taken.

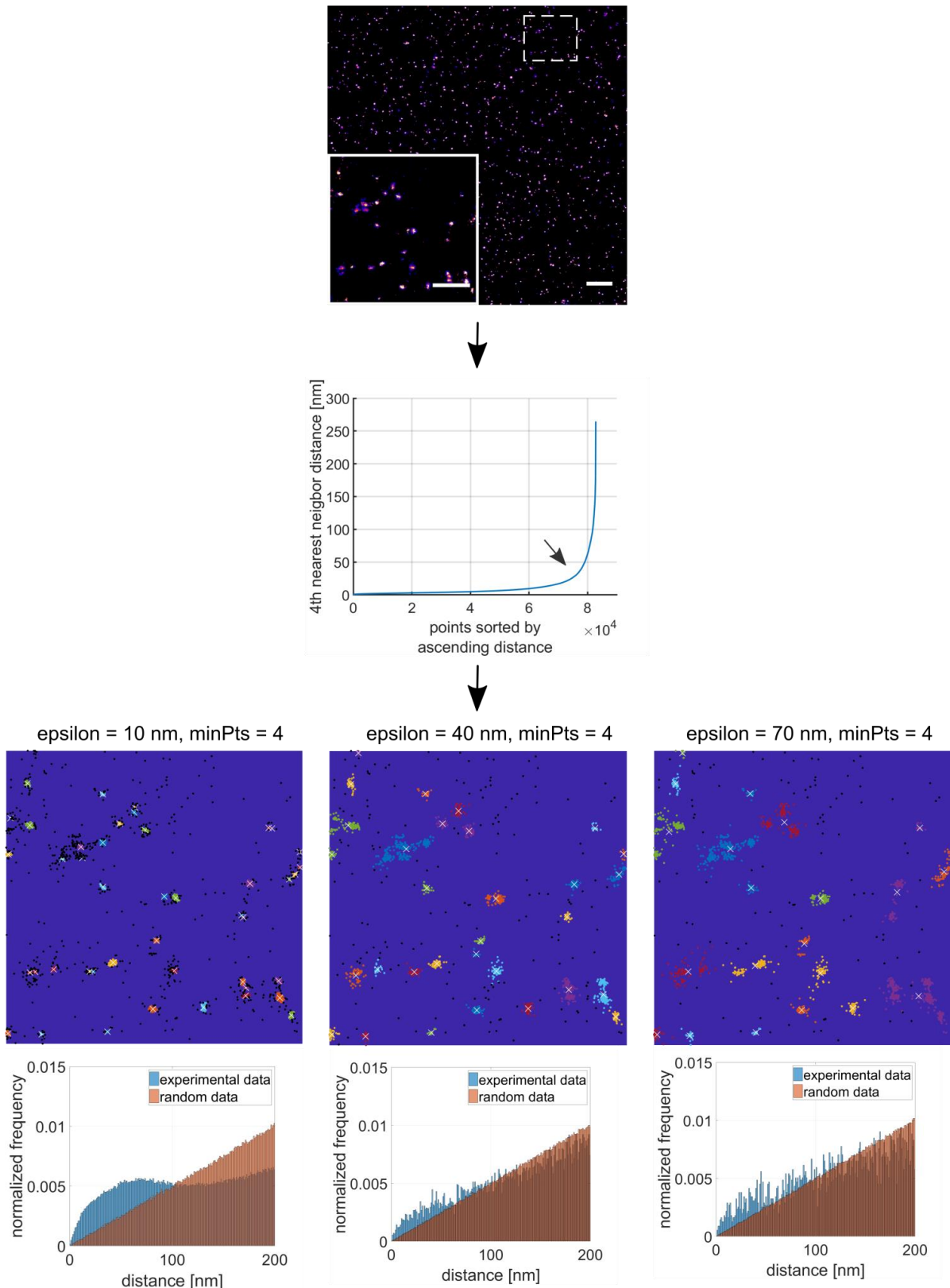
Image processing was done in Harmony software (PerkinElmer). First, stained cell nuclei were identified by segmenting the DAPI channel. Identified nuclei were used as seeds to identify their corresponding cytoplasm masks using the NF- $\kappa$ B p65 channel. Masks were resized to avoid overlapping between them and to stay within the boundaries of the cell. At the end a nuclear mask with a corresponding ring-like cytoplasm mask was obtained. Mean NF- $\kappa$ B p65 intensities within both masks were determined and the ratio of nuclear to cytoplasmic NF- $\kappa$ B p65 was calculated.

**Supplementary Table 1: TLR4 cluster size obtained by Ripley's H-function.**  
 Errors denote standard deviation.

	donor	number of cells	Maximum Ripley's H function [nm]
<b>medium</b>	donor 1	11	58 ± 5
	donor 2	19	67 ± 11
	donor 3	12	66 ± 9
<b>15 min LPS</b>	donor 1	11	66 ± 15
	donor 2	18	62 ± 14
	donor 3	10	75 ± 44
<b>30 min LPS</b>	donor 1	11	58 ± 8
	donor 2	13	64 ± 7
	donor 3	11	67 ± 29
<b>15 min ATI</b>	donor 1	11	61 ± 10
	donor 2	16	69 ± 37
	donor 3	11	62 ± 15
<b>30 min ATI</b>	donor 1	11	64 ± 10
	donor 2	19	55 ± 7
	donor 3	11	51 ± 5
<b>15 min ATI TNM</b>	donor 1	7	62 ± 8
	donor 2	12	53 ± 8
	donor 3	6	79 ± 25
<b>30 min ATI TNM</b>	donor 1	11	58 ± 9
	donor 2	20	58 ± 10
	donor 3	12	65 ± 14

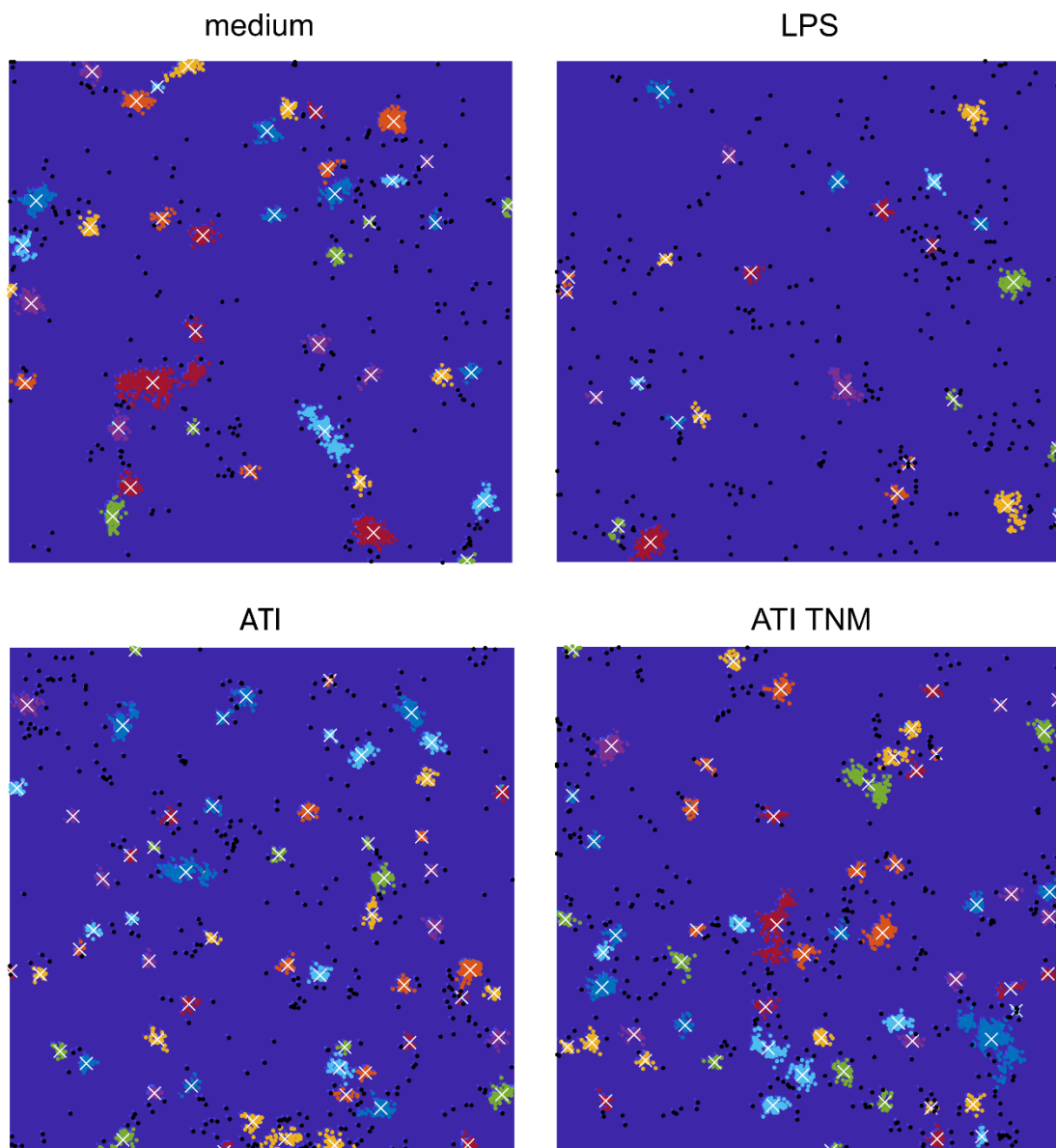


**Supplementary Figure 3: Simulation of clusters.** (A) Section of a 10  $\mu\text{m}$  x 10  $\mu\text{m}$  simulated image. Simulation parameters were set to represent experimental data. The average density is 300 points/ $\mu\text{m}^2$ , with 70 % of points being part of a simulated Gaussian-shaped cluster. Simulated clusters were randomly distributed over the randomly simulated point pattern with an average density of 6 cluster/ $\mu\text{m}^2$ . Cluster diameter has been set to 60 nm. (B) Ripley's H-function of the simulated point pattern. The maximum of Ripley's function lies at about 60 nm.

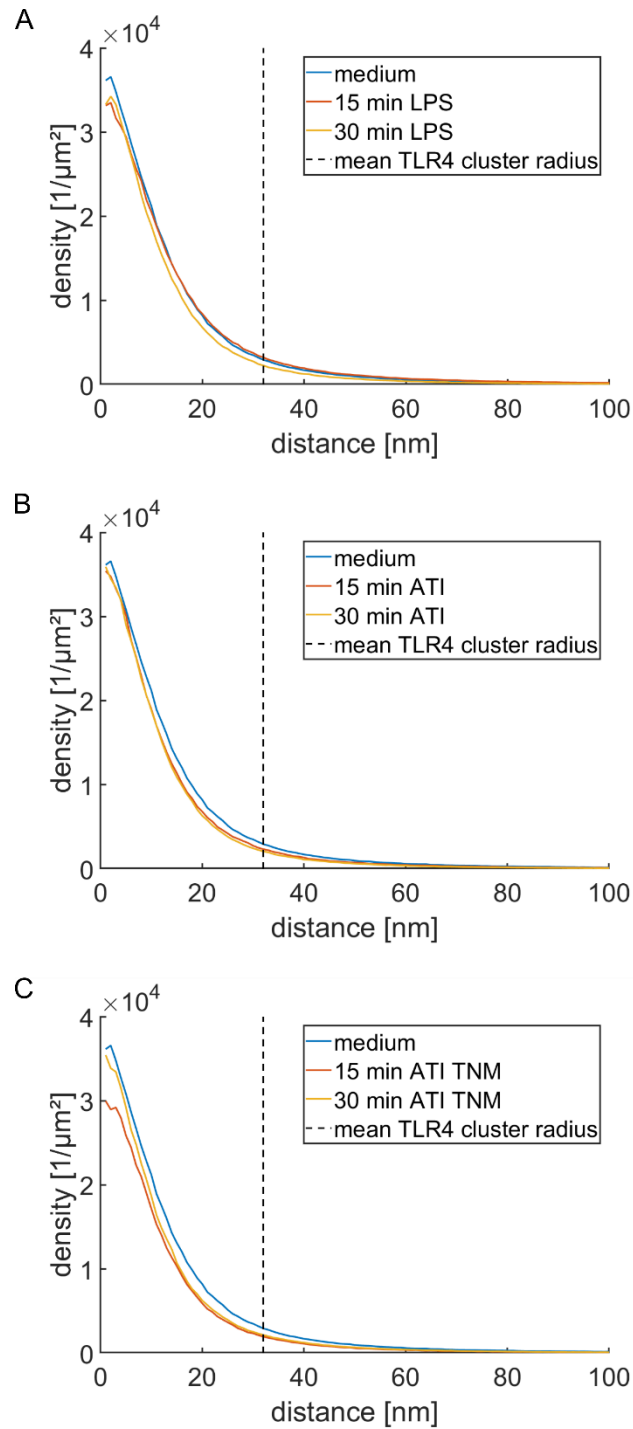


**Supplementary Figure 4: Iterative determination of DBSCAN parameters.** Different TLR4 sample data sets were selected for determination of DBSCAN parameters. Step A shows an 11.6  $\mu\text{m}$  x 11.6  $\mu\text{m}$  SMLM image from such a data set containing about 80,000 detected single molecule signals (scale bar = 1  $\mu\text{m}$ , inset scale bar = 500 nm). To estimate the DBSCAN parameters (minPts and epsilon) a similar approach as shown in Ester et al (1996) [1] was used in a first step. The detected molecule coordinates from the list of localizations were used to determine the 4<sup>th</sup>

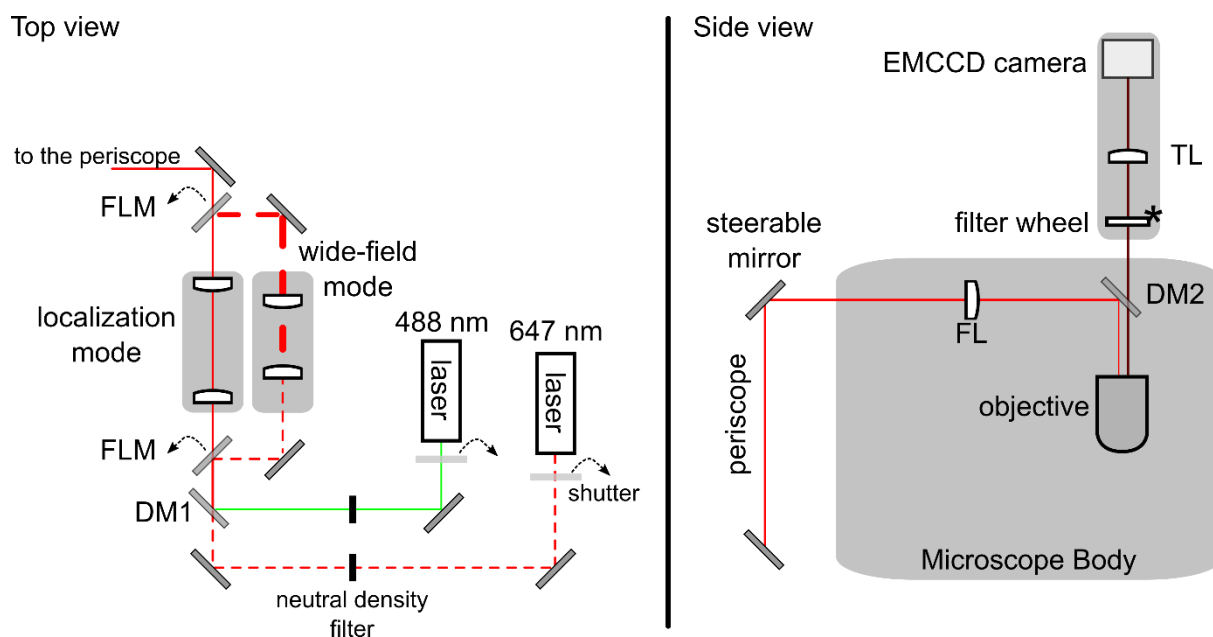
nearest neighbor distances. Those distances were sorted in ascending order and plotted against the number of detected signals. The distance value where the first strong bend in the curve occurs, was taken as a starting point for  $\epsilon$  (step B, indicated by the black arrow). Next, DBSCAN was done using  $\text{minPts} = 4$  and the estimated epsilon obtained from step B. The clusters obtained by DBSCAN were visualized (step C). Every detected cluster is represented by a different color. Black points correspond to molecules which are not part of a cluster or which belong to a cluster with a diameter larger than  $1 \mu\text{m}$ . The white cross indicates the center of mass of the cluster. For better visibility only, the ROI from step A is shown, but calculations were done for all points of the data set. Besides the visualization, distances between all points outside of the detected clusters were calculated and plotted in a histogram (blue). The obtained frequency distribution of distances was then compared to the one expected from a random distribution. To account for edge effects, distances originating from points, which are located within the cut-off distance of 200 nm from the image border, were not calculated. The result of different combinations of epsilon and fixed  $\text{minPts}$  for DBSCAN is depicted in step C. Using an epsilon value of 10 nm, small clusters are identified by DBSCAN that are surrounded by points assigned as noise (indicated by arrows). By visual inspection, those noise points seem as they should belong to the clusters. This can be also seen in the frequency distribution of the distances from the points outside of the cluster (= noise points). At shorter distances points deviate from the random distribution indicating clustering. In case of proper parameter selection for DBSCAN those points should follow a random distribution. As a result, the epsilon parameter was set in this case to small. If epsilon is set to 40 nm more points are assigned to a cluster and the frequency distribution of the distances from the residual noise points approximates a random distribution. If epsilon is set too large i.e. 70 nm, well separated clusters will be detected as one large cluster. The final parameters were found by iteratively adjusting  $\text{minPts}$  and epsilon such that the frequency distribution of distances from points outside of cluster approximates a random distribution, supported by visual inspection of the clusters obtained from DBSCAN.



**Supplementary Figure 5: Visualization of clusters as detected by DBSCAN.** Representation of the detected clusters from the SMLM images from figure 2A. For each identified cluster a color was randomly assigned. The white cross indicates the center of mass of the cluster. Black dots represent detected molecules that are not part of a cluster.



**Supplementary Figure 6: Radial density distribution of TLR4 around cluster centers.** Radial distribution of TLR4 for samples stimulated with (A) LPS, (B) ATI and (C) ATI TNM in comparison to the medium control (blue line). In all plots the dashed line indicates the mean cluster diameter of the medium control calculated by Ripley's function.



### Supplementary Figure 7: Schematic of the custom-built localization microscope setup.

The setup was equipped with a 647 nm laser (Coherent Obis) and a 488 nm laser (Coherent Sapphire). Selection of laser lines was done with custom-built shutters and neutral density filters allowed adjustment of laser intensities. Both laser lines were combined using a dichromatic mirror (DM1; HC BS 580, AHF Analysetechnik). With two motorized flipping mirrors (FLM; Radiant Dyes) the laser beam could be switched between two beam paths consisting of beam expanders for localization or wide-field acquisitions. In wide-field mode the laser beam was expanded 10-fold, illuminating the whole field of view of the camera ( $49.15 \mu\text{m} \times 49.15 \mu\text{m}$ ) homogeneously. For localization measurements the beam was expanded 3.125-fold. This led to an illuminated area of  $\sim 640 \mu\text{m}^2$  in the sample plane (area derived from  $1/e^2$  width of Gaussian profile). The collimated laser beams were coupled into the back port of the microscope (Leica DM RBE) using a periscope. The mirror in the top unit was placed in the focal plane of the focusing lens and piezoelectric actuators (Thorlabs) attached to the mirror allowed to steer the beam between epi-illumination and total internal reflection (TIR) illumination. The collimated laser beam was focused on the back focal plane of a 100x/NA 1.49 objective lens (Olympus) using a  $f = 300 \text{ mm}$  focusing lens (FL, Thorlabs) mounted on a xyz-translator. The objective lens was attached to a piezo objective scanner (Physik Instrumente) for z-focusing of the sample. The sample was mounted on a xy-stepper stage, guided by a commercial controller (Corvus-2 eco TT, ITK Dr. Kassen GmbH). Fluorescence discrimination was done with a dichroic mirror (dual line zt488/647 rpc, AHF Analysetechnik) incorporated into a filter cube (DM2). The filter cube contained also a laser clean-up filter (ZET488/640, AHF Analysetechnik) and a dual-notch filter (488/647 nm, AHF Analysetechnik) to remove remaining excitation light. Emitted fluorescent light was collected on an EMCCD camera (iXon 897 Ultra, Andor Technology) mounted on a custom-built camera adapter, which included an emission filter wheel. The emission filter wheel contained a 500 nm long pass filter (Chroma Technology) for 488 nm illumination and a 700/75 nm bandpass filter for 647 nm illumination. For astigmatism-based 3D localization microscopy [2] a weak cylindrical lens ( $f = 1,000 \text{ mm}$ , Thorlabs) could be placed between the tube lens (TL;  $f = 300 \text{ mm}$ , Thorlabs) and the camera. Interfacing with all hardware devices and data acquisitions were done with  $\mu$ Manager [3].

	number of cells			density of molecules on membrane [1/μm <sup>2</sup> ]			% of clustered molecules			number of molecules per cluster		
	Donor 1	Donor 2	Donor 3	Donor 1	Donor 2	Donor 3	Donor 1	Donor 2	Donor 3	Donor 1	Donor 2	Donor 3
Buffycocot												
control	11	19	12	300 ± 160	80 ± 40	420 ± 300	0.7 ± 0.1	0.5 ± 0.1	0.6 ± 0.1	48 ± 46	21 ± 19	59 ± 87
15 min LPS	11	18	11	300 ± 130	430 ± 210	380 ± 300	0.8 ± 0.1	0.7 ± 0.2	0.6 ± 0.1	44 ± 42	37 ± 45	54 ± 99
30 min LPS	11	13	11	210 ± 110	190 ± 65	300 ± 210	0.8 ± 0.1	0.7 ± 0.1	0.7 ± 0.2	28 ± 26	31 ± 30	40 ± 47
15 min ATI	11	16	11	280 ± 120	340 ± 200	230 ± 105	0.8 ± 0.1	0.7 ± 0.2	0.7 ± 0.1	39 ± 34	33 ± 47	30 ± 36
30 min ATI	11	19	11	270 ± 150	130 ± 60	360 ± 180	0.7 ± 0.1	0.6 ± 0.1	0.7 ± 0.1	37 ± 37	23 ± 21	32 ± 35
15 min ATI TNM	7	12	6	350 ± 220	110 ± 40	150 ± 50	0.8 ± 0.1	0.5 ± 0.1	0.6 ± 0.1	43 ± 42	15 ± 12	29 ± 31
30 min ATI TNM	11	20	12	200 ± 110	120 ± 60	290 ± 160	0.7 ± 0.1	0.6 ± 0.1	0.7 ± 0.1	30 ± 28	23 ± 20	42 ± 57

	diameter [nm]			density of molecules within clusters [x10 <sup>4</sup> 1/μm <sup>2</sup> ]			distance to next neighboring cluster [nm]			density of clusters on the membrane [1/μm <sup>2</sup> ]		
	Donor 1	Donor 2	Donor 3	Donor 1	Donor 2	Donor 3	Donor 1	Donor 2	Donor 3	Donor 1	Donor 2	Donor 3
Buffycocot												
control	57 ± 29	38 ± 20	65 ± 41	2.3 ± 16	2.4 ± 4.3	2.1 ± 23	230 ± 120	360 ± 230	230 ± 120	5 ± 2	2 ± 1	5 ± 2
15 min LPS	57 ± 27	52 ± 32	59 ± 43	1.9 ± 4.5	2.0 ± 2.7	2.0 ± 2.6	220 ± 110	190 ± 90	230 ± 130	6 ± 3	8 ± 3	6 ± 3
30 min LPS	43 ± 24	46 ± 25	55 ± 32	2.4 ± 4.6	2.4 ± 3.9	1.9 ± 2.0	220 ± 120	270 ± 150	200 ± 110	6 ± 2	4 ± 1	6 ± 3
15 min ATI	53 ± 25	48 ± 32	45 ± 27	2.1 ± 17	3.3 ± 85	2.5 ± 3.6	220 ± 120	200 ± 120	230 ± 130	6 ± 3	8 ± 3	5 ± 2
30 min ATI	52 ± 28	39 ± 22	46 ± 24	2.1 ± 7.3	2.7 ± 5.3	2.2 ± 1.9	230 ± 130	260 ± 150	190 ± 100	6 ± 3	4 ± 2	8 ± 4
15 min ATI TNM	58 ± 29	31 ± 16	45 ± 27	1.7 ± 1.5	2.9 ± 4.1	2.4 ± 2.7	200 ± 110	260 ± 160	290 ± 170	7 ± 4	4 ± 2	3 ± 1
30 min ATI TNM	47 ± 26	39 ± 21	56 ± 34	2.5 ± 19	3.1 ± 23	2.1 ± 4.7	240 ± 140	300 ± 180	240 ± 140	5 ± 3	3 ± 2	5 ± 3

**Supplementary Table 2: Donor-specific results from TLR4's density-based clustering analysis.** Errors denote standard deviation.

	number of cells	density of molecules on membrane [ $1/\mu\text{m}^2$ ]	% of clustered molecules	number of molecules per cluster
Control	42	$240 \pm 230$	$0.6 \pm 0.2$	$48 \pm 68$
LPS 15 min	40	$380 \pm 220$	$0.7 \pm 0.1$	$43 \pm 62$
LPS 30 min	35	$230 \pm 140$	$0.7 \pm 0.1$	$33 \pm 37$
ATI 15 min	38	$290 \pm 160$	$0.7 \pm 0.1$	$34 \pm 41$
ATI 30 min	41	$230 \pm 160$	$0.7 \pm 0.1$	$31 \pm 32$
TNM 15 min	25	$180 \pm 160$	$0.6 \pm 0.1$	$31 \pm 35$
TNM 30 min	43	$190 \pm 130$	$0.6 \pm 0.1$	$31 \pm 38$

	diameter [nm]	density of molecules within clusters [ $\times 10^4 1/\mu\text{m}^2$ ]	distance to next neighboring cluster [nm]	density of clusters on the membrane [ $1/\mu\text{m}^2$ ]
Control	$57 \pm 36$	$2.2 \pm 19$	$260 \pm 150$	$4 \pm 2$
LPS 15 min	$55 \pm 34$	$2.0 \pm 3.3$	$200 \pm 110$	$7 \pm 3$
LPS 30 min	$48 \pm 28$	$2.2 \pm 3.6$	$230 \pm 130$	$5 \pm 3$
ATI 15 min	$49 \pm 29$	$2.7 \pm 57$	$220 \pm 120$	$6 \pm 3$
ATI 30 min	$46 \pm 25$	$2.3 \pm 5.3$	$230 \pm 130$	$6 \pm 3$
TNM 15 min	$47 \pm 28$	$2.2 \pm 2.8$	$240 \pm 140$	$5 \pm 3$
TNM 30 min	$47 \pm 28$	$2.6 \pm 18$	$260 \pm 150$	$4 \pm 2$

**Supplementary Table 3: Averaged results from TLR4's density-based clustering analysis.** Errors denote standard deviation.

## References

- [1] M. Ester, H.-P. Kriegel, J. Sander, and X. Xu, "A Density-Based Algorithm for Discovering Clusters in Large Spatial Databases with Noise," *Proc. Second Int. Conf. Knowl. Discov. Data Min.*, pp. 226–231, 1996.
- [2] B. Huang, W. Wang, M. Bates, and X. Zhuang, "Three-Dimensional Super-Resolution Imaging by Stochastic Optical Reconstruction Microscopy," *Science.*, vol. 319, no. 5864, pp. 810–813, Feb. 2008.
- [3] A. Edelstein, N. Amodaj, K. Hoover, R. Vale, and N. Stuurman, "Computer control of microscopes using manager," *Curr. Protoc. Mol. Biol.*, vol. 92, no. 1, pp. 1–17, 2010.

## Nitration of Wheat Amylase Trypsin Inhibitors Increases their Innate and Adaptive Immunostimulatory Potential *in vitro*

Kira Ziegler<sup>1</sup>, Jan Neumann<sup>1,2</sup>, Fobang Liu<sup>1</sup>, Janine Fröhlich-Nowoisky<sup>1</sup>, Christoph Cremer<sup>2</sup>, Joachim Saloga<sup>3</sup>, Kathrin Reinmuth-Selzle<sup>1</sup>, Ulrich Pöschl<sup>1</sup>, Detlef Schuppan<sup>4</sup>, Iris Bellinghausen<sup>3#</sup>, and Kurt Lucas<sup>1#\*</sup>

<sup>1</sup>Multiphase Chemistry Department, Max Planck Institute for Chemistry, Mainz, Germany

<sup>2</sup>Institute of Molecular Biology, Mainz, Germany

<sup>3</sup>Department of Dermatology, University Medical Center of the Johannes Gutenberg University, Mainz, Germany

<sup>4</sup>Institute of Translational Immunology, University Medical Center of the Johannes Gutenberg University, Mainz, Germany

# equally contributing senior authors

★ **Correspondence:**

Dr. Kurt Lucas  
k.lucas@mpic.de

**Author contributions.**

DS, UP, KRS, IB, and KL designed the experiments. KZ, JN, FL, and IB performed the experiments. KZ, JN, FL, JFN, DS, UP, IB, and KL analyzed and interpreted the data. CC, FL, KRS, and IB contributed materials/methods/analysis tools. KZ, IB, and KL wrote the paper. All authors were involved in the editing and proof reading of the manuscript.

# Nitration of Wheat Amylase Trypsin Inhibitors Increases their Innate and Adaptive Immunostimulatory Potential *in vitro*

Kira Ziegler<sup>1</sup>, Jan Neumann<sup>1,2</sup>, Fobang Liu<sup>1</sup>, Janine Fröhlich-Nowoisky<sup>1</sup>, Christoph Cremer<sup>2</sup>, Joachim Saloga<sup>3</sup>, Kathrin Reinmuth-Selzle<sup>1</sup>, Ulrich Pöschl<sup>1</sup>, Detlef Schuppan<sup>4</sup>, Iris Bellinghausen<sup>3#</sup>, and Kurt Lucas<sup>1#\*</sup>

<sup>1</sup>*Multiphase Chemistry Department, Max Planck Institute for Chemistry, Mainz, Germany*

<sup>2</sup>*Institute of Molecular Biology, Mainz, Germany*

<sup>3</sup>*Department of Dermatology, University Medical Center of the Johannes Gutenberg University, Mainz, Germany*

<sup>4</sup>*Institute of Translational Immunology, University Medical Center of the Johannes Gutenberg University, Mainz, Germany*

*#equally contributing senior authors*

**\* Correspondence:**

Dr. Kurt Lucas  
k.lucas@mpic.de

**Key words:** Allergy, amylase trypsin inhibitors, dendritic cells, non-celiac wheat sensitivity, protein nitration, wheat

### Abstract

Amylase trypsin inhibitors (ATI) can be found in all gluten containing cereals and are, therefore, ingredient of basic foods like bread or pasta. In the gut ATI can mediate innate immunity via activation of the Toll-like receptor 4 (TLR4) on immune cells residing in the lamina propria, promoting intestinal, as well as extra-intestinal, inflammation. Inflammatory conditions can induce formation of peroxynitrite (ONOO<sup>-</sup>) and, thereby, endogenous protein nitration in the body. Moreover, air pollutants like ozone (O<sub>3</sub>) and nitrogen dioxide (NO<sub>2</sub>) can cause exogenous protein nitration in the environment. Both reaction pathways may lead to the nitration of ATI.

To investigate if and how nitration modulates the immunostimulatory properties of ATI, they were chemically modified by three different methods simulating endogenous and exogenous protein nitration and tested *in vitro*.

Here we show that ATI nitration was achieved by all three methods and lead to increased immune reactions.

We found that ATI nitrated by tetranitromethane (TNM) or ONOO<sup>-</sup> lead to a significantly enhanced TLR4 activation. Furthermore, in human primary immune cells, TNM nitrated ATI induced a significantly higher T cell proliferation and release of Th1 and Th2 cytokines compared to unmodified ATI.

Our findings implicate a causative chain between nitration, enhanced TLR4 stimulation, and adaptive immune responses, providing major implications for public health, as nitrated ATI may strongly promote inhalative wheat allergies (baker's asthma), non-celiac wheat sensitivity (NCWS), other allergies, and autoimmune diseases. This underlines the importance of future work analyzing the relationship between endo- and exogenous protein nitration, and the rise in incidence of ATI-related and other food hypersensitivities.

### 1 Introduction

Nitration of proteins can occur endogenously in the human body or exogenously in the environment. Air pollutants, like ozone and nitrogen oxides, are able to nitrate allergenic proteins, like the major birch pollen allergen Bet v 1, leading to an increased allergic potential and elevated immune reactions (Franze et al., 2005;Gruijthuijsen et al., 2006;Karle et al., 2012;Ackaert et al., 2014;Reinmuth-Selzle et al., 2014;Reinmuth-Selzle et al., 2017). In the human body, inflammatory conditions can lead to the formation of ONOO<sup>-</sup>, which is the main agent for endogenous protein nitration (Galinañes and Matata, 2002;Salvemini et al., 2006;Reinmuth-Selzle et al., 2014;Ferrer-Sueta et al., 2018). Moreover, several air pollutants and pathogens can induce or favor inflammatory processes and related nitration processes (Franze et al., 2005;Karle et al., 2012;Reinmuth-Selzle et al., 2017). Diseases typically accompanied by a high degree of inflammation are, for example, autoimmune and other chronic inflammatory diseases, like chronic obstructive pulmonary disease (COPD), allergic asthma, inflammatory bowel diseases (IBD), or non-celiac non-allergy wheat sensitivity (NCWS) (Fasano et al., 2015;Schuppan and Zavallos, 2015;Zundler and Neurath, 2017).

We previously showed that amylase trypsin inhibitors (ATI), a family of non-gluten proteins, are responsible for manifestations of mainly extra-intestinal symptoms of NCWS (Fasano et al., 2015;Schuppan et al., 2015;Schuppan and Zavallos, 2015;Leccioli et al., 2017). Moreover, ATI are major allergens in baker's asthma, a classical IgE mediated allergy (Walusiak et al., 2004;Tatham and Shewry, 2008). ATI can be found in all gluten containing grains (wheat, barley, rye), and represent 2-4% of the total protein (Dupont et al., 2011). In plants, ATI regulate the germination processes (Finnie et al., 2002) and defense mechanisms by blocking the amylase and trypsin activity of pathogens (Payan, 2004). The wheat intake of an adult person is about 250 g per day, mainly as

## Nitrated ATI show enhanced immunogenicity

processed bread or pasta which is equivalent to 0.5 g to 1 g ATI (Fasano et al., 2015). Remarkably, ATI are resistant to food processing and to proteolysis in the gut where they stay biologically active (Zevallos et al., 2017). In the gut ATI are able to stimulate immune cells residing in the lamina propria and mesenteric lymph nodes through TLR4 binding and stimulation, and the emigration of the activated myeloid cells (Junker et al., 2012;Cuccioloni et al., 2016;Zevallos et al., 2017).

The innate immune receptor TLR4 recognizes damage and pathogen associated patterns (DAMPs/PAMPs), like lipopolysaccharides (LPS), which are major components in the outer membrane of gram negative bacteria. Upon stimulation, the receptor triggers an NF- $\kappa$ B dependent cascade leading to the release of pro-inflammatory cytokines (Kawai and Akira, 2010;Kawasaki and Kawai, 2014). Importantly, ATI can trigger TLR4 by direct interaction, and provoke innate immunity (Junker et al., 2012;Cuccioloni et al., 2016). In a mouse model of inflammatory bowel disease, ATI enhanced the dextran sodium sulfate-induced intestinal inflammation by increasing the number of activated macrophages and dendritic cells in all sections of the intestine, the lamina propria, and especially in the mesenteric lymph nodes (Zevallos et al., 2017). Moreover, we showed in two mouse studies on experimental airway inflammation that ATI-enriched diets not only enhanced allergen-induced intestinal, but also lung allergic responses in an IgE- and TLR4-dependent manner (Bellinghausen et al., 2018;Zevallos et al., 2018). Thus, the adjuvant effect of ATI is not limited to the intestine, but can also be observed for other organs, fueling ongoing inflammation. These inflammatory conditions might favor the formation of ONOO<sup>-</sup> and, thereby, protein nitration (Galinanes and Matata, 2002;Salvemini et al., 2006;Ischiropoulos, 2009;Ferrer-Sueta et al., 2018), including ATI in the gut, apart from the environmental factors that may induce protein nitration.

To elucidate the effect of nitration, we chemically modified ATI using three different methods simulating endo- (*in vivo*) and exogenous (environmental) nitration mechanisms. These nitrating agents mainly induce the formation of 3-nitrotyrosine (Walcher et al., 2003;Franze et al., 2005;Ischiropoulos, 2009;Radi, 2013;Selzle et al., 2013;Reinmuth-Selzle et al., 2014;Liu et al., 2017). The aim of our study was to examine whether nitrated ATI exhibit an altered innate and adaptive immunostimulatory capacity. Modified ATI were quantified for their nitration degree using HPLC-DAD and ELISA. Furthermore, various *in vitro* studies were performed. A novel HeLa TLR4 reporter cell line was established for determination of innate immune stimulation. Adaptive immune reactions were analyzed in a mixed lymphocyte reaction by the use of primary immune cells isolated from whole blood of healthy donors. TLR4 activation, NF- $\kappa$ B translocation, expression of surface maturation markers, Th1, Th2, relevant cytokines, and T cell proliferation were measured.

## 2 Materials and Methods

### 2.1 Nitration and Analysis of nitrated ATIs

#### 2.1.1 Nitration with Tetranitromethane (TNM) of ATI

ATI were obtained from Sigma Aldrich (Amylase Inhibitor Type I, Sigma-Aldrich, Darmstadt, Germany). Aliquots of aqueous ATI solutions (1 mg/mL, 0.5 mL) were mixed with 4.55  $\mu$ L TNM/Methanol (4%, *v/v*) and stirred for 3 h at room temperature. To remove excess TNM after the reaction, a PD-25 size exclusion chromatography column (GE Healthcare, Little Chalfont, Great Britain) was used according to the manufacturer's instructions. Finally, the ATI were eluted with endotoxin free water (MilliQ, Biopak, Merck, Darmstadt, Germany).

### 2.1.2 Nitration with O<sub>3</sub>/NO<sub>2</sub> of ATI

ATI aqueous solutions (0.5 mg/mL, 1 mL) were exposed to a gas mixture of O<sub>3</sub> and NO<sub>2</sub>, as described previously (Liu et al., 2017). Briefly, O<sub>3</sub> was produced from synthetic air passed through a UV lamp (LOT-Quantum Design, Darmstadt, Germany) at ~1.98 L/min. The air flow was then mixed with a N<sub>2</sub> flow (20 mL/min) containing ~5 ppmV NO<sub>2</sub> (AirLiquide, Düsseldorf, Germany). The resulting air gas mixtures were bubbled directly through the aqueous ATI solutions at a flow rate of 60 mL/min using a Teflon tube (ID: 1.59 mm). The concentrations of O<sub>3</sub>/NO<sub>2</sub> were monitored by commercial monitoring instruments (Ozone analyzer, 49i; NO<sub>x</sub> analyzer, 42i-TL, Thermo Fisher Scientific, Darmstadt, Germany respectively).

### 2.1.3 ONOO<sup>-</sup> nitration of ATI

ATI solutions were prepared in 50 mM ammonium bicarbonate buffer at pH 7.8 (Carl Roth, Karlsruhe, Germany). For one reaction 300 µL of ATI solution [1 mg/mL] were mixed with 2.85 µL ONOO<sup>-</sup> (160-200 mM, Merck) in brown reaction vessels (Eppendorf, Hamburg, Germany) and incubated for 110 min on ice. Immediately after the reaction, the samples were desalted using a PD-10 size exclusion mini column (GE Healthcare), following the manufacturer manual with endotoxin free water.

### 2.1.4 HPLC-DAD analysis

All nitrated ATI samples were analyzed using HPLC coupled to diode array detection (HPLC-DAD, 1200 series, Agilent Technologies, Santa Clara, California, USA). The nitration degree is defined as the concentration of nitrotyrosine as a fraction of the sum of the concentrations of nitrotyrosine and tyrosine. The values were determined using peak areas of signals at wavelengths 280 nm and 357 nm. A detailed description of the analytical method can be found in Selzle et al 2013 (Selzle et al., 2013).

### 2.1.5 Endotoxin quantification

Endotoxin was quantified by Limulus Amebocyte Lysate chromogenic endotoxin quantitation kit (Thermo Fisher Scientific). ATI samples were tested at several dilutions and compared to an *E. coli* endotoxin standard (011:B4) provided with the kit. The endotoxin levels in the final concentration used for all experiments were less than 20 Endotoxin units per mL.

### 2.1.6 Protein analysis

To determine the ATI protein concentrations before and after nitration, a bicinchoninic acid assay (Thermo Fisher Scientific) was used according to the manufacturer's instructions. The optical density at 562 nm was determined using a Synergy Neo plate reader (Biotek, Bad Friedrichshall, Germany).

ATI oligomers were detected using sodium dodecyl sulfate polyacrylamide gel electrophoresis (5-20%, Bio-Rad, Munich, Germany), referring to the instruction manual. A 5 µg portion of each sample was prepared in 2x Laemmli buffer (Bio-Rad) containing 100 mM Dithiothreitol (Sigma Aldrich), heated on 96°C for 5 min, and loaded on the gel. After separation, the gel was stained for 3 h in Coomassie blue (Bio-Rad) and unstained in an aqueous solution containing 10% methanol (Merck) and 20% acetic acid (Carl Roth) over night. For image acquisition and for analysis, a ChemiDoc system and Image Lab software 5.2.1 (both Bio-Rad) were used, respectively.

### 2.2 Cell culture

#### 2.2.1 HeLa TLR4 dual luciferase reporter cell line (HeLa TLR4 dual)

Cells were grown in Dulbecco's Modified Eagle's Medium (DMEM, Thermo Fisher Scientific) containing 25 mM D-glucose, 1 mM sodium pyruvate supplemented with 10% heat-inactivated fetal calf serum (FCS), (Biochrom, Berlin, Germany), 1% Penicillin/Streptomycin (Thermo Fisher Scientific), and 140 µg/mL Hygromycin B (Invivogen, Toulouse, France) in a humidified atmosphere of 5% CO<sub>2</sub> at 37 °C.

For simultaneous determination of TLR4 stimulation and viability, a novel monoclonal dual reporter cell line was established. Therefore, the HeLa TLR4 cell line (Novusbio, Wiesbaden, Germany), expressing Renilla luciferase under the control of an IL-8 promoter reporting TLR4 activity, was stably transfected with a plasmid, constitutively expressing Firefly luciferase, and, thereby, measuring viability (pCMB-firefly-luc-hygro, kindly provided by Ernesto Bockamp, University Medical Center of the Johannes Gutenberg University). Lipofectamine 3000 (Thermo Fisher Scientific) was used as the transfecting reagent according to the manufacturer's protocol.

##### 2.2.1.1 Combined TLR4 and viability assay

20,000 HeLa TLR4 dual reporter cells were seeded in a flat bottom 96-well plate (Greiner, Frickenhausen, Germany) in 100 µL complete DMEM. On the next day, the cells were treated with different nitrated ATI at a final concentration of 7.5 µg/mL. Mock nitrations and medium served as negative controls, and LPS EB (25 ng/mL, Invivogen) as a positive control. After 7 h, the plate was washed with 200 µL of warm PBS containing calcium and magnesium (Thermo Fisher Scientific). Then the cells were lysed by adding passive lysis buffer (Dual-luciferase reporter assay, Promega, Mannheim, Germany) and frozen at -80°C. An analysis of both luciferase reporter activities in the cell lysate was performed according to the manufacturer's manual (Promega). The relative luciferase activity was calculated by dividing the Renilla luciferase (TLR4) signal by the Firefly luciferase (viability) signal. The resulting values were normalized to the value obtained for LPS treated cells.

To inhibit TLR4 signaling, HeLa TLR4 dual cells were pre-incubated with the TLR4 antagonist TAK242 (0.36 µg/mL, Merck), or, as a negative control, its solvent dimethylsulfoxide (4.4 µg/mL, Thermo Fisher Scientific) for 150 min. To provide a stronger stimulation, the doses of ATI were doubled in these experiments [15 µg/mL].

#### 2.2.2 Generation of monocyte derived dendritic cells (DC)

Buffy coats from ten healthy donors were obtained from the Transfusion Center (University Medical Center of the Johannes Gutenberg University, Mainz, Germany) with approval from the local ethical committee (Landesärztekammer Rheinland-Pfalz). Peripheral blood mononuclear cells (PBMC) were isolated by Ficoll-Paque 1.077 g/mL (Biochrom) density centrifugation. The autologous plasma was heat-inactivated at 56°C for 30 min, centrifuged at 1500xg, and stored at 4°C. To enrich CD14<sup>+</sup> monocytes, 5 x 10<sup>6</sup> PBMC per well were incubated in a 12-well plate (Greiner) in 1.5 mL Iscove modified Dulbecco medium (IMDM, Lonza, Basel, Switzerland) enriched with 1% antibiotic/antimycotic solution (Sigma Aldrich) and 3% autologous plasma for 40 min in a cell incubator under 5% CO<sub>2</sub> atmosphere at 37°C. Cells were washed 3 times with warm PBS (without calcium magnesium, Thermo Fisher Scientific), and maintained in IMDM, supplemented with 10 ng/mL IL-4 (Miltenyi, Bergisch Gladbach, Germany), 200 U/mL granulocyte-macrophage colony-stimulating factor (GM-CSF, Leukine®, Immunex Corp., Seattle, WA, USA), and 2% autologous plasma. On day 6, immature DC were pulsed with ATI [15 µg/mL], TNM nitrated ATI [15 µg/mL],

## Nitrated ATI show enhanced immunogenicity

equivalent amounts of mock nitrated solution, or were left untreated. To induce DC maturation, the cells were additionally treated with tumor necrosis factor (TNF)-alpha, 10 ng/mL, Miltenyi Biotec), IL-1 $\beta$  (10 ng/mL, Miltenyi Biotec) and prostaglandin E<sub>2</sub> (1  $\mu$ g/mL, Cayman Chemical, Ann Arbor, MI, USA). After 48 h, DC were harvested, washed twice in cold PBS, and used for T cell stimulation assays as well as for analysis of surface marker expression.

### 2.2.2.1 Surface marker staining and analysis by flow cytometry

5 x 10<sup>4</sup> DC or 5 x 10<sup>5</sup> T cells were stained with specific mouse anti-human monoclonal antibodies (mAbs) for 20 min at 4°C. The following antibodies were used: AlexaFluor 647-conjugated CD4 (MT310; Santa Cruz Biotechnology, Inc., Santa Cruz, CA, USA), fluorescein isothiocyanate (FITC)-conjugated human leukocyte antigen D-related (HLA-DR) (L243), phycoerythrin (PE)-conjugated CD80 (L307.4), and allophycocyanin-conjugated CD83 (HB15e, all from BD Biosciences). As a negative control, matured cells were used. Then, cells were washed, and analyzed by BD Accuri™ C6 Plus Flow Cytometer (BD Biosciences).

### 2.2.2.2 Isolation of CD4<sup>+</sup> T cells and co-culture with autologous native ATI- or TNM nitrated ATI-pulsed DC

Autologous CD4<sup>+</sup> T cells were obtained from PBMC using antibody-coated paramagnetic MicroBeads (MACS; Miltenyi Biotec) according to the manufacturer's protocol. Separation was confirmed by flow cytometry (purity, >98% CD4<sup>+</sup> T cells).

1 x 10<sup>5</sup> T cells and 1 x 10<sup>4</sup> mDC were co-cultured in 96-well plates (Greiner) in triplicates in 200  $\mu$ L IMDM containing 5% autologous plasma. Five days later, 50  $\mu$ l of supernatant was taken for quantification of cytokine production. For the determination of proliferation, the co-culture was pulsed with 37 kBq/well of [<sup>3</sup>H]-thymidine (ICN Biomedicals, CA, USA) for 6 h and [<sup>3</sup>H]-TdR incorporation was measured using a beta counter (1205 Betaplate, LKB Wallac, Turku, Finland).

### 2.2.2.3 Quantification of soluble cytokines by magnetic multiplex assay

For quantification of cytokines, multiplex assay kits (R&D systems, Biotechne, Wiesbaden, Germany) were used. Supernatants from immature DC cultures were tested for TNF-alpha, IL-6, IL-8, IL-1 $\beta$  and monocyte chemoattractant protein 1 (MCP1). Supernatants of mature DC-T cell co-cultures were analyzed for interferon gamma (IFN-gamma), IL-10, IL-17, IL-6, IL-4, IL-5, and IL-13. The samples were prepared according to the manufacturer's manual and analyzed on a MAGPIX device (Luminex, Austin, Texas, USA).

## 2.3 Quantification of ATI induced NF- $\kappa$ B translocation

Nuclear NF- $\kappa$ B translocation in macrophages was determined by fluorescence microscopy. Therefore, PBMCs were isolated and seeded in 12-well glass bottom plates (Cellvis, California, USA) at a concentration of 1.5 x 10<sup>6</sup> – 2 x 10<sup>6</sup> cells per well in IMDM enriched with 200 U/mL GM-CSF and 2% autologous plasma. After six days, cells were stimulated for 2 h either with ATI, ATI TNM [12.5  $\mu$ g/mL], or with LPS EB (100 ng/mL, Invivogen) as a positive control. Untreated cells (medium) served as a negative control. Next, cells were washed once in pre-warmed PBS and fixed using 4% formaldehyde solution (Thermo Fisher Scientific) in PBS for 10 min at 37°C. Subsequently, cells were rinsed three times with PBS, then blocked and permeabilized in PBS containing 0.3% Triton X 100 (Merck) and 5% bovine serum albumin (BSA, Cell Signaling Technology, Danvers, Massachusetts) for 1 h at room temperature. Afterwards, cells were incubated

## Nitrated ATI show enhanced immunogenicity

with primary rabbit anti-NF- $\kappa$ B p65 mAb (D14E12, Cell Signaling Technology) diluted in PBS comprising 1% BSA and 0.3% Triton-X 100 (Merck) overnight at 4°C. Thereafter, cells were washed three times in PBS for 5 min each and incubated for 1 h at room temperature with anti-rabbit Alexa Fluor 568 antibody (A-11011, Thermo Fisher Scientific) diluted in PBS comprising 1% BSA and 0.3% Triton X-100. Cells were washed again three times in PBS for 5 min each and cell nuclei were counterstained using 4',6-diamidino-2-phenylindole (DAPI, Thermo Fisher Scientific) according to the manufacturer's instructions. Imaging of stained macrophages was performed at an Opera Phenix High-Content Screening system (Perkin Elmer, Waltham, Massachusetts, USA). PBS was used as an imaging buffer. For image analysis, Harmony high-content analysis software (Perkin Elmer, Waltham, Massachusetts, USA) was used. Nuclei were identified by DAPI staining, and a ring-like mask around each identified nucleus was created to obtain the corresponding cytoplasm area. Afterwards, the mean intensities of NF- $\kappa$ B within both masks were determined and the nuclear to cytoplasmic ratio of NF- $\kappa$ B was calculated. The described image processing steps are illustrated in figure S1.

### 2.4 Statistics

GraphPad Prism version 6.07 (GraphPad, San Diego, California) was used for statistical analysis. To determine the standard deviation between the different treated groups, an ANOVA was performed. Unpaired t-tests were performed for TLR4 activation measurements using the HeLa TLR4 dual reporter cell line. For all data sets based on primary immune cells, paired t-tests were carried out. Differences between groups were considered as significant when \* $p < 0.05$ , \*\* $p < 0.01$ , or \*\*\* $p < 0.001$ . The number of experiments performed for each data set is described at the end of each figure legend.

## 3 Results

### 3.1 Nitration of ATI by different nitrating agents

The degree of ATI nitration varied for the different nitrating agents and methods used. High nitration was observed with TNM and ONOO<sup>-</sup>. Lowest nitration was obtained for O<sub>3</sub>/NO<sub>2</sub> (Table 1). All three nitration methods were able to modify ATI and induce about 3 % to 13 % of covalently linked ATI oligomers (Figure S2 A+B).

### 3.2 Nitration of ATI enhances TLR4 stimulatory activity

Compared to unmodified ATI, TNM, and ONOO<sup>-</sup>, nitrated ATI induced a significantly higher TLR4 activation in HeLa TLR4 dual reporter cells. However, ATI nitrated with O<sub>3</sub> and NO<sub>2</sub> exhibited a lower TLR4 activation compared to native ATI (Figure 1A). All mock nitrations showed no TLR4 activation (Figure S3).

Administration of the TLR4 antagonist TAK242 completely diminished TLR4 activation induced by ATI or by the positive control LPS (Figure 1B).

### 3.3 Nitrated and unmodified ATI induce similar activation of macrophages and immature DC

In unstimulated primary human macrophages, NF- $\kappa$ B is mostly located in the cytoplasm. Upon treatment with ATI or TNM nitrated ATI, a significantly enhanced NF- $\kappa$ B translocation from cytoplasm to the cell nucleus was observed using fluorescence microscopy (Figure 2 A). Nitrated ATI exhibited only slightly higher NF- $\kappa$ B translocation compared to native ATI, which was also observed in the individual donor dependent responses (Figure 2 B+C).

## Nitrated ATI show enhanced immunogenicity

Immature DC treated with unmodified or TNM nitrated ATI expressed significantly higher amounts of CD80, CD83 and HLA-DR on their surface in comparison to untreated cells (Figure 3 A+B). For DC treated with mock nitrated samples, no changes were observed (Figure S4 A+B). Furthermore, the release of the pro-inflammatory cytokines IL-1 $\beta$ , IL-6, IL-8, and TNF-alpha by immature DC was similarly elevated upon ATI or ATI TNM treatment compared to untreated cells (Figure 3 C-F). No significant changes were observed for MCP-1 release or cells treated with mock nitrations (Figure S4 C-G).

### 3.4 Nitrated ATI enhance proliferation and induce an enhanced Th1 and Th2 cytokine expression profile in CD4<sup>+</sup> T cells stimulated with autologous mature DC

To analyze the immunogenicity of nitrated versus unmodified ATI, CD4<sup>+</sup> T cells were co-cultured with autologous mature DC treated before with ATI or ATI-TNM. Proliferations as well as production of Th1 and Th2 cytokines were analyzed. In general, CD4<sup>+</sup> T cells from almost all donors showed an enhanced proliferative response and cytokine release after stimulation with ATI-pulsed compared to untreated DC. Only DC treated with nitrated ATI induced a significantly increased T cell proliferation (Figure 4A). Moreover, the release of the Th2 cytokines IL-5, IL-6, IL-10, and IL-13 as well as the Th1 cytokine IFN-gamma was significantly enhanced after stimulation with DC treated with ATI-TNM (Figure 4 B-F). Comparing both ATI-treated groups, we found a significant higher release for IL-5, IL-6, IL-10, and IFN-gamma upon the ATI-TNM stimulus (Figure 4 B-D+F). There were no significant changes in IL-4 and IL-17A release between all groups (Figure S5 A+B). Mock nitration did neither influence cytokine release nor T cell proliferation (Figure S5 C-H).

## 4 Discussion

In the present study, we analyzed the impact of nitration on the immunogenicity of ATI, and could show that ATI can be nitrated by exogenous and endogenous nitrating agents. Furthermore, we demonstrated that nitration of ATI lead to enhanced innate and adaptive immune responses compared to unmodified ATI.

By using a novel HeLa TLR4 dual luciferase reporter cell line, we could demonstrate that TNM and ONOO<sup>-</sup> mediated ATI nitration induced significant enhanced TLR4 stimulation, which seems to correlate with the higher nitration degrees as determined by HPLC-DAD and ELISA. Pre-incubation of the cells with the TLR4 antagonist TAK242 inhibited ATI-induced TLR4 signaling, providing further evidence that ATI stimulate TLR4 directly, as reported in previous studies (Junker et al., 2012;Cuccioloni et al., 2016). The complete abolishment of TLR4 activity by TAK242 furthermore allows the conclusion that nitrated ATI also impact the TLR4 agonistic properties directly. As nitration always induces the formation of nitrotyrosine (Walcher et al., 2003;Franze et al., 2005;Ischiropoulos, 2009;Radi, 2013;Selzle et al., 2013;Reinmuth-Selzle et al., 2014;Liu et al., 2017;Ferrer-Sueta et al., 2018), it may be hypothesized that nitrotyrosine embedded into the ATI secondary structure itself serves as an amplifier. This hypothesis is supported by our results, showing the lack of enhanced TLR4 stimulation in HeLa TLR4 dual reporter cells upon treatment with unmodified ATI combined with pure nitrotyrosine (Figure S6).

Moreover, nitration of proteins is known to change their structure and function (Radi, 2013). Further investigations would be necessary to clarify to which degree nitration of ATI alters their interaction with TLR4 (Cuccioloni et al., 2016), which may explain the observed enhanced TLR4 agonistic activity.

## Nitrated ATI show enhanced immunogenicity

One essential step in TLR4 signaling is the nuclear translocation of the transcription factor NF- $\kappa$ B, controlling the expression of many genes relevant in innate and adaptive immunity (Kawai and Akira, 2010; Kawasaki and Kawai, 2014; Sakai et al., 2017). Therefore, we performed several studies on primary immune cells from healthy human donors *in vitro*. Using fluorescence microscopy, we visualized and quantified nuclear translocation of NF- $\kappa$ B in primary human macrophages after the addition of ATI or nitrated ATI. Under the conditions chosen, native and nitrated ATI provoked comparable nuclear translocation of NF- $\kappa$ B.

Previous studies showed that, not only NF- $\kappa$ B, but also the interferon regulatory factor (IRF-3) gets activated upon ATI treatment (Junker et al., 2012). Therefore, future investigations should also investigate whether nitrated ATI effect the IRF-3 pathway.

Moreover, we found that the NF- $\kappa$ B controlled cytokines IL-1 $\beta$ , IL-6, IL-8, TNF-alpha, and the DC maturation markers CD80 and CD83 (Sakai et al., 2017) were strongly enhanced after treatment of immature DC with ATI and nitrated ATI, which is consistent with previous studies (Junker et al., 2012; Zevallos et al., 2018). This finding indicates that ATI in general induce the maturation of DC, which is an essential step in the induction of T cell mediated immunity, both via Th1 and Th2 T helper cells, as occurs in autoimmunity and allergy, underpinning the intrinsic immune adjuvant function of (nutritional) ATI (Zevallos et al., 2017; Bellinghausen et al., 2018; Zevallos et al., 2018).

To investigate the modulation of adaptive immunity by nitrated ATI, we analyzed syngeneic DC-T cell co-cultures. Here, only TNM ATI treated DC induced significantly enhanced T cell proliferation. Moreover, treatment of DC with ATI or nitrated ATI caused a significantly higher release of Th2 relevant cytokines IL-5, IL-6, IL-10, and IL-13, and of the Th1 cytokine IFN-gamma. For unmodified ATI, this finding is in line with our prior studies on nutritional and inhalative allergies (Bellinghausen et al., 2018; Zevallos et al., 2018). Remarkably, nitrated ATI significantly enhanced the production of both Th1 and Th2 cytokines compared to unmodified ATI.

Therefore, it can be concluded that nitrated ATI possess an overall enhanced immune stimulatory potential, including Th1 mediated diseases, as was shown by us before for unmodified ATI in murine inflammatory bowel disease (Zevallos et al., 2017). These results make it highly probable that nitrated ATI may more strongly promote inhalative wheat allergies (baker's asthma), NCWS, other allergies, and autoimmune diseases.

Similar findings were reported for other nitrated allergens in the context of allergic airway inflammation or anaphylaxis, but the exact underlying molecular mechanisms are still elusive (Franze et al., 2005; Gruijthuisen et al., 2006; Karle et al., 2012; Ackaert et al., 2014; Reinmuth-Selzle et al., 2014; Reinmuth-Selzle et al., 2017). Allergen oligomerization as a side product during the nitration process (e.g. cross-linking of protein-bound tyrosine to form a dimer, or the formation of disulfide bridges) was observed for several proteins, and is discussed as one possible mechanism (Selzle et al., 2013; Ackaert et al., 2014; Kampf et al., 2015; Liu et al., 2017). In this respect, it was suggested that one structural aspect of allergens is their capability to form dimers or oligomers, thereby enhancing their allergenicity (Scheurer et al., 2015). Ackaert et al. 2014 reported twofold higher stability for nitrated, as compared to unmodified, Bet v 1, making the allergen more resistant to proteolytic degradation, thus permitting enhanced and prolonged presentation on DC, followed by an enhanced T cell response (Karle et al., 2012; Ackaert et al., 2014). Interestingly, higher molecular weight aggregates instead of oligomers of Bet v 1 (Ackaert et al., 2014), and the hypoallergenic Bet v 1d (Zaborsky et al., 2010) were reported to favor Th1 immunogenicity. Indeed, for all nitration methods used, we found fractions of covalently linked ATI oligomers after the reaction.

## Nitrated ATI show enhanced immunogenicity

Taken together, our results demonstrate that ATI are potent stimulators of innate and adaptive immune responses. In contrast to unmodified ATI, the nitrated ATI exhibit stronger immune stimulatory effects. The observed enhanced immunogenicity of ATI provides a causative chain between stronger TLR4 agonistic effects, leading to enhanced Th1 and Th2 cell activation upon nitration. Future investigations are needed to test how far the degrees of nitration obtained in our study match endogenous ATI nitration under inflammatory conditions, or exogenous nitration, which may occur under certain conditions of wheat growing and processing, e.g., via intensive fertilization, environmental pollution, or nitration during food processing.

### **Ethics statement**

Buffy coats were obtained from the Transfusion Center (University Medical Center of the Johannes Gutenberg University, Mainz, Germany) with approval by the local ethical committee (Landesärztekammer Rheinland-Pfalz approval number 837.176.08 (6173)). The consent of participants was always in written form.

### **Author contributions**

DS, UP, KRS, IB, and KL designed the experiments. KZ, JN, FL, and IB performed the experiments. KZ, JN, FL, JFN, DS, UP, IB, and KL analyzed and interpreted the data. CC, FL, KRS, and IB contributed materials/methods/analysis tools. KZ, IB, and KL wrote the paper. All authors were involved in the editing and proof reading of the manuscript.

### **Acknowledgements**

The authors acknowledge helpful discussions with the members of the Mainz Program for Chemical Allergology (MPCA) and support from the Max Planck Graduate Center with the Johannes Gutenberg University Mainz (MPGC). KZ and JN acknowledge the support by the IMB Microscopy and Histology Core Facility, as well as the DFG for funding the Opera Phenix High Content Spinning Disk Microscope (Project 402386039).

### **Conflict of Interest Statement**

The authors have no conflicting financial interests to disclose.

### **Funding disclosure**

This work was supported by the Max Planck Graduate Center with the Johannes Gutenberg University Mainz (MPGC). DS was supported for ATI-related work by grants from the German Research Foundation (DFG) (DFG-Schu 646/17-1, DFG-Schu-646/20-1, the Collaborative Research Center TR128 “Multiple Sclerosis” project A08), and the Leibniz Foundation (project Wheatscan). IB was supported by DFG grant BE 4504/3-1.

### **Data Availability Statement**

All datasets analyzed for this study are included in the manuscript and the supplementary files.

References

- Ackaert, C., Kofler, S., Horejs-Hoeck, J., Zulehner, N., Asam, C., Von Grafenstein, S., Fuchs, J.E., Briza, P., Liedl, K.R., Bohle, B., Ferreira, F., Brandstetter, H., Oostingh, G.J., and Duschl, A. (2014). The impact of nitration on the structure and immunogenicity of the major birch pollen allergen Bet v 1.0101. *PLoS One* 9, e104520.
- Bellinghausen, I., Weigmann, B., Zevallos, V., Maxeiner, J., Reissig, S., Waisman, A., Schuppan, D., and Saloga, J. (2018). Wheat amylase-trypsin inhibitors exacerbate intestinal and airway allergic immune responses in humanized mice. *J Allergy Clin Immunol*.
- Cuccioloni, M., Mozzicafreddo, M., Ali, I., Bonfili, L., Cecarini, V., Eleuteri, A.M., and Angeletti, M. (2016). Interaction between wheat alpha-amylase/trypsin bi-functional inhibitor and mammalian digestive enzymes: Kinetic, equilibrium and structural characterization of binding. *Food Chem* 213, 571-578.
- Dupont, F.M., Vensel, W.H., Tanaka, C.K., Hurkman, W.J., and Altenbach, S.B. (2011). Deciphering the complexities of the wheat flour proteome using quantitative two-dimensional electrophoresis, three proteases and tandem mass spectrometry. *Proteome Sci* 9, 10.
- Fasano, A., Sapone, A., Zevallos, V., and Schuppan, D. (2015). Nonceliac gluten sensitivity. *Gastroenterology* 148, 1195-1204.
- Ferrer-Sueta, G., Campolo, N., Trujillo, M., Bartesaghi, S., Carballal, S., Romero, N., Alvarez, B., and Radi, R. (2018). Biochemistry of Peroxynitrite and Protein Tyrosine Nitration. *Chem Rev* 118, 1338-1408.
- Finnie, C., Melchior, S., Roepstorff, P., and Svensson, B. (2002). Proteome analysis of grain filling and seed maturation in barley. *Plant Physiol* 129, 1308-1319.
- Franze, T., Weller, M.G., Niessner, R., and Poschl, U. (2005). Protein nitration by polluted air. *Environ Sci Technol* 39, 1673-1678.
- Galinanes, M., and Matata, B.M. (2002). Protein nitration is predominantly mediated by a peroxynitrite-dependent pathway in cultured human leucocytes. *Biochem J* 367, 467-473.
- Gruijthuisen, Y.K., Grieshuber, I., Stocklinger, A., Tischler, U., Fehrenbach, T., Weller, M.G., Vogel, L., Vieths, S., Poschl, U., and Duschl, A. (2006). Nitration enhances the allergenic potential of proteins. *Int Arch Allergy Immunol* 141, 265-275.
- Ischiropoulos, H. (2009). Protein tyrosine nitration--an update. *Arch Biochem Biophys* 484, 117-121.
- Junker, Y., Zeissig, S., Kim, S.J., Barisani, D., Wieser, H., Leffler, D.A., Zevallos, V., Libermann, T.A., Dillon, S., Freitag, T.L., Kelly, C.P., and Schuppan, D. (2012). Wheat amylase trypsin inhibitors drive intestinal inflammation via activation of toll-like receptor 4. *J. Exp. Med* 209, 2395-2408.
- Kampf, C.J., Liu, F., Reinmuth-Selzle, K., Berkemeier, T., Meusel, H., Shiraiwa, M., and Poschl, U. (2015). Protein Cross-Linking and Oligomerization through Dityrosine Formation upon Exposure to Ozone. *Environ Sci Technol* 49, 10859-10866.
- Karle, A.C., Oostingh, G.J., Mutschlechner, S., Ferreira, F., Lackner, P., Bohle, B., Fischer, G.F., Vogt, A.B., and Duschl, A. (2012). Nitration of the pollen allergen bet v 1.0101 enhances the presentation of bet v 1-derived peptides by HLA-DR on human dendritic cells. *PLoS One* 7, e31483.
- Kawai, T., and Akira, S. (2010). The role of pattern-recognition receptors in innate immunity: update on Toll-like receptors. *Nat Immunol* 11, 373-384.
- Kawasaki, T., and Kawai, T. (2014). Toll-like receptor signaling pathways. *Front Immunol* 5, 461.
- Leccioli, V., Oliveri, M., Romeo, M., Berretta, M., and Rossi, P. (2017). A New Proposal for the Pathogenic Mechanism of Non-Coeliac/Non-Allergic Gluten/Wheat Sensitivity: Piecing Together the Puzzle of Recent Scientific Evidence. *Nutrients* 9.

- Liu, F., Reinmuth-Selzle, K., Lai, S., Weller, M.G., Poschl, U., and Kampf, C.J. (2017). Simultaneous determination of nitrated and oligomerized proteins by size exclusion high-performance liquid chromatography coupled to photodiode array detection. *J Chromatogr A* 1495, 76-82.
- Payan, F. (2004). Structural basis for the inhibition of mammalian and insect alpha-amylases by plant protein inhibitors. *Biochim Biophys Acta* 1696, 171-180.
- Radi, R. (2013). Protein tyrosine nitration: biochemical mechanisms and structural basis of functional effects. *Acc Chem Res* 46, 550-559.
- Reinmuth-Selzle, K., Ackaert, C., Kampf, C.J., Samonig, M., Shiraiwa, M., Kofler, S., Yang, H., Gadermaier, G., Brandstetter, H., Huber, C.G., Duschl, A., Oostingh, G.J., and Poschl, U. (2014). Nitration of the birch pollen allergen Bet v 1.0101: efficiency and site-selectivity of liquid and gaseous nitrating agents. *J Proteome Res* 13, 1570-1577.
- Reinmuth-Selzle, K., Kampf, C.J., Lucas, K., Lang-Yona, N., Frohlich-Nowoisky, J., Shiraiwa, M., Lakey, P.S.J., Lai, S., Liu, F., Kunert, A.T., Ziegler, K., Shen, F., Sgarbanti, R., Weber, B., Bellinghausen, I., Saloga, J., Weller, M.G., Duschl, A., Schuppan, D., and Poschl, U. (2017). Air Pollution and Climate Change Effects on Allergies in the Anthropocene: Abundance, Interaction, and Modification of Allergens and Adjuvants. *Environ Sci Technol* 51, 4119-4141.
- Sakai, J., Cammarota, E., Wright, J.A., Cicuta, P., Gottschalk, R.A., Li, N., Fraser, I.D.C., and Bryant, C.E. (2017). Lipopolysaccharide-induced NF-kappaB nuclear translocation is primarily dependent on MyD88, but TNFalpha expression requires TRIF and MyD88. *Sci Rep* 7, 1428.
- Salvemini, D., Doyle, T.M., and Cuzzocrea, S. (2006). Superoxide, peroxynitrite and oxidative/nitrative stress in inflammation. *Biochem Soc Trans* 34, 965-970.
- Scheurer, S., Toda, M., and Vieths, S. (2015). What makes an allergen? *Clin Exp Allergy* 45, 1150-1161.
- Schuppan, D., Pickert, G., Shfaq-Khan, M., and Zevallos, V. (2015). Non-celiac wheat sensitivity: differential diagnosis, triggers and implications. *Best. Pract. Res. Clin. Gastroenterol* 29, 469-476.
- Schuppan, D., and Zevallos, V. (2015). Wheat amylase trypsin inhibitors as nutritional activators of innate immunity. *Dig. Dis* 33, 260-263.
- Selzle, K., Ackaert, C., Kampf, C.J., Kunert, A.T., Duschl, A., Oostingh, G.J., and Poschl, U. (2013). Determination of nitration degrees for the birch pollen allergen Bet v 1. *Anal Bioanal Chem* 405, 8945-8949.
- Tatham, A.S., and Shewry, P.R. (2008). Allergens to wheat and related cereals. *Clin. Exp. Allergy* 38, 1712-1726.
- Walcher, W., Franze, T., Weller, M.G., Poschl, U., and Huber, C.G. (2003). Liquid- and gas-phase nitration of bovine serum albumin studied by LC-MS and LC-MS/MS using monolithic columns. *J Proteome Res* 2, 534-542.
- Walusiak, J., Wiszniewska, M., Krawczyk-Adamus, P., and Palczynski, C. (2004). Occupational allergy to wheat flour. Nasal response to specific inhalative challenge in asthma and rhinitis vs. isolated rhinitis: a comparative study. *Int J Occup Med Environ Health* 17, 433-440.
- Zaborsky, N., Brunner, M., Wallner, M., Himly, M., Karl, T., Schwarzenbacher, R., Ferreira, F., and Achatz, G. (2010). Antigen aggregation decides the fate of the allergic immune response. *J Immunol* 184, 725-735.
- Zevallos, V.F., Raker, V., Tenzer, S., Jimenez-Calvente, C., Ashfaq-Khan, M., Russel, N., Pickert, G., Schild, H., Steinbrink, K., and Schuppan, D. (2017). Nutritional Wheat Amylase-Trypsin Inhibitors Promote Intestinal Inflammation via Activation of Myeloid Cells. *Gastroenterology* 152, 1100-1113.

## Nitrated ATI show enhanced immunogenicity

- Zevallos, V.F., Raker, V.K., Maxeiner, J., Scholtes, P., Steinbrink, K., and Schuppan, D. (2018). Dietary wheat amylase trypsin inhibitors exacerbate murine allergic airway inflammation. *Eur J Nutr*.
- Zundler, S., and Neurath, M.F. (2017). Pathogenic T cell subsets in allergic and chronic inflammatory bowel disorders. *Immunol Rev* 278, 263-276.

**Table****Table 1: Levels of ATI nitration by different nitrating agents**

Agent	Reaction condition	Nitration degree (%) <sup>a)</sup>	Nitrotyrosine [ $\mu\text{g}/\text{ml}$ ] <sup>b)</sup>
TNM	4.55 $\mu\text{L}$ [4%], 3 h	19.5 $\pm$ 0.2	0.36 $\pm$ 0.03
O <sub>3</sub> /NO <sub>2</sub>	O <sub>3</sub> [200 ppb], NO <sub>2</sub> [50 ppb], 4 h	8.6 $\pm$ 0.5	7.8E-04 $\pm$ 2.4E-04
ONOO <sup>-</sup>	2.85 $\mu\text{l}$ [200mM], 1.8 h	26.2 $\pm$ 6,2	0.23 $\pm$ 0.12

a) The ND values here were corrected according to the background for pre-nitrated signals of native ATI ( $n = 2$ ). Blank samples were conducted under the same nitration conditions, and no signal at 280 nm and 357 nm was detected for all the mock samples.

b) The values are expressed in equivalents of nitrotyrosines [ $\mu\text{g}$ ] nitrated BSA nBSA per 1  $\mu\text{g}$  of nitrated ATI solution ( $n = 2$ ). The values were corrected against unmodified ATI solution. Mock samples showed no nitration.

Figures

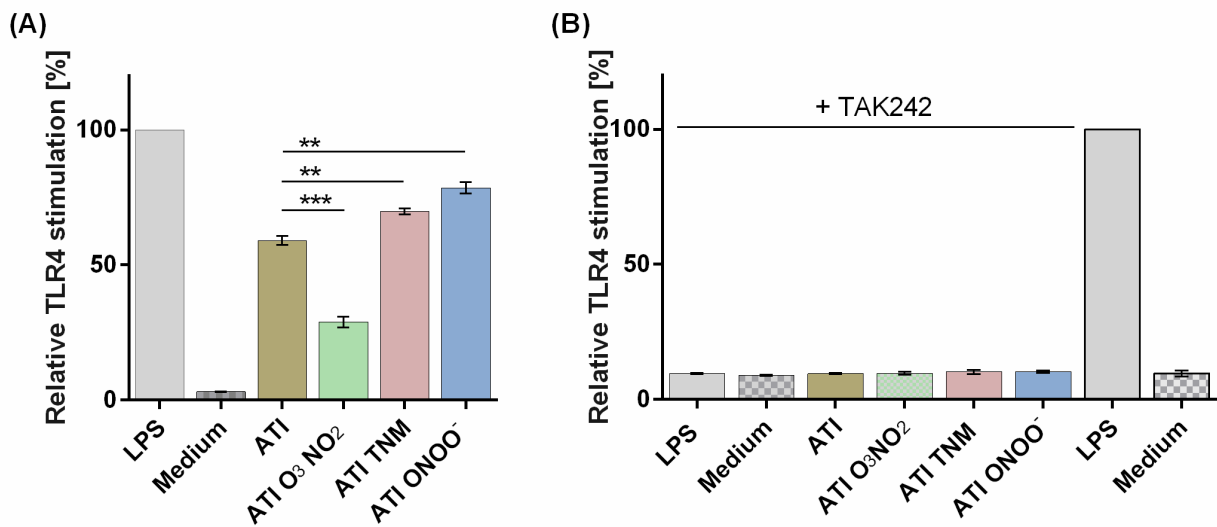


**Figure 1: Different nitrated ATIs induce distinct TLR4 activation in HeLa TLR4 dual reporter cells.**

A: HeLa TLR4 dual reporter cells were treated for 7 h with nitrated or unmodified ATIs [7.5 µg/mL] or LPS [25 ng/mL] as a positive control. B: Cells were pre-incubated for 2.5 h with TAK242 [0.36 µg/mL] or its solvent DMSO [4.4 µg/mL]. Then the cells were stimulated with nitrated or unmodified ATIs [15 µg/mL], or LPS [25 ng/mL] for 7 h. The relative luciferase activity was calculated by dividing the Renilla luciferase (TLR4) signal by the Firefly luciferase (viability) signal. The resulting values were normalized to the value obtained for LPS- treated cells. Shown are the means ± SD of three independent experiments measured in triplicates using two independently nitrated probes. \*\*\*P<0.001, \*\*P<0.01.

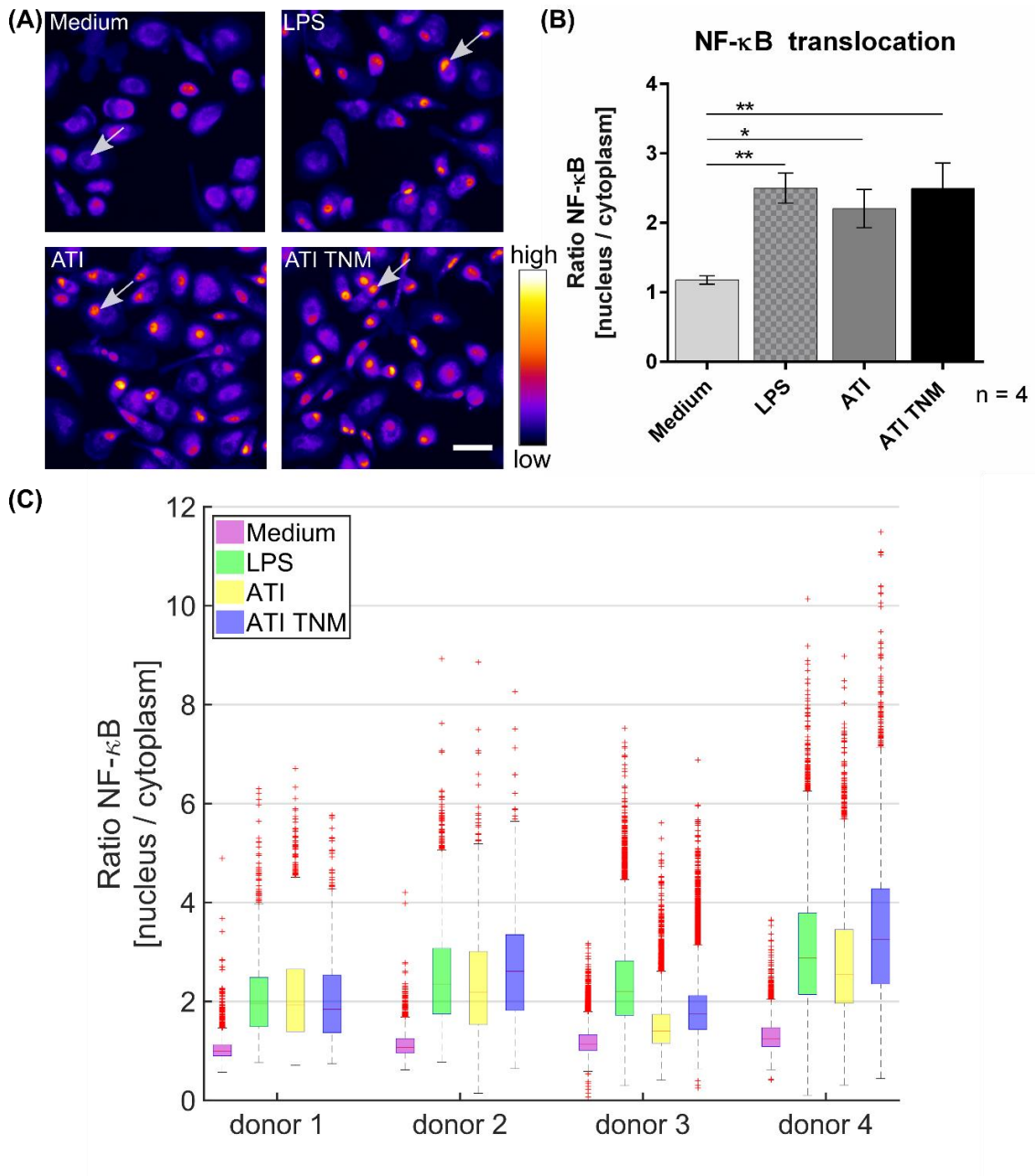


**Figure 2: Increased NF-κB p65 translocation into the cell nucleus in ATI and ATI TNM treated primary human macrophages.**

A: Fluorescence microscopy images of macrophages treated for 2 h with LPS (positive control, 100 ng/mL), ATI or ATI TNM [12.5 μg/mL] and stained for NF-κB. In untreated conditions (medium) NF-κB resides mostly in the cytoplasm, whereas an increased translocation of NF-κB p65 into the nucleus can be observed for LPS, ATI, and ATI TNM treated cells (indicated by arrows). Brightness and contrast were adjusted to the same level for every image within the panel. Scale bar = 50 μm. B: Quantitative evaluation of NF-κB translocation from the cell cytoplasm to the nucleus by Harmony high-content analysis software (Perkin Elmer). Shown are the means ± SEM from four independent experiments/donors, \*P<0.05, \*\*P<0.01. C: Donor-dependent response to LPS (green), ATI (yellow) and ATI TNM (blue) treatment.

## Nitrated ATI show enhanced immunogenicity

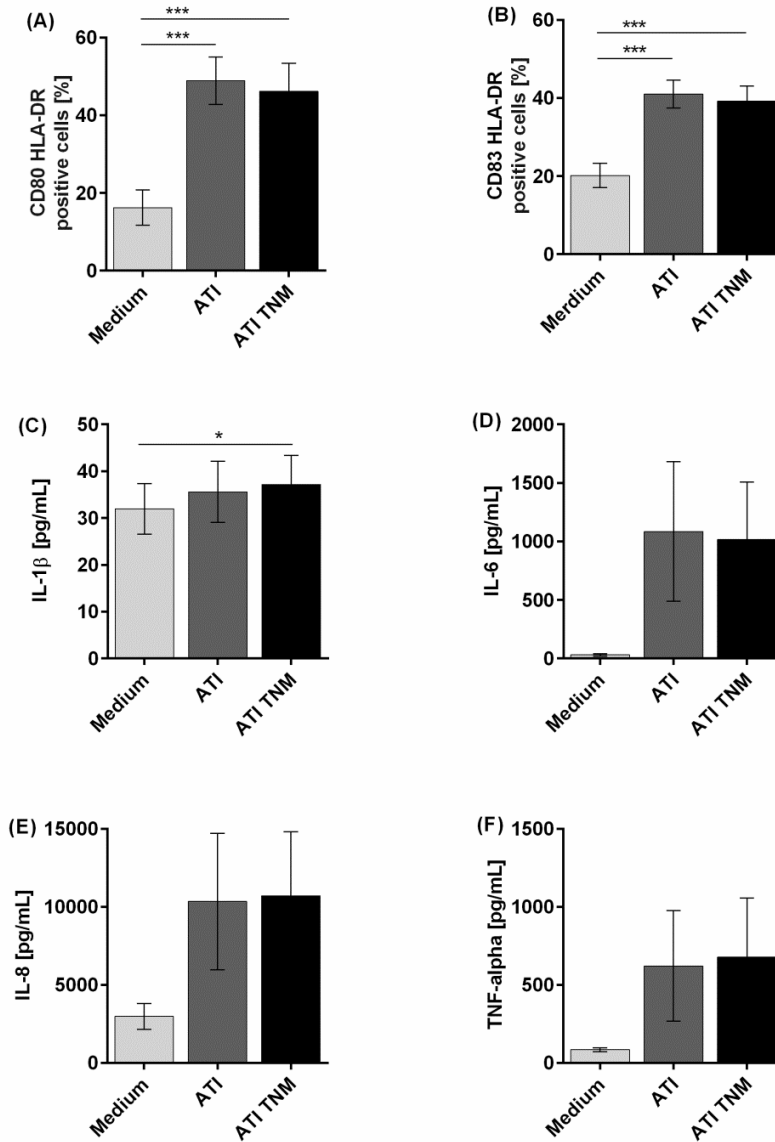


**Figure 3: Enhanced expression of maturation markers as well as pro-inflammatory cytokines by human immature DCs upon stimulation with ATI and ATI TNM.**

Immature DCs were pulsed with ATI or ATI TNM [15  $\mu\text{g}/\text{mL}$ ] on day 6. 48 h later cells were stained for expression of the indicated surface markers and analyzed by flow cytometry (A+B). Before, supernatants were taken for determination of IL-1 $\beta$ , IL-6, IL-8, and TNF-alpha by magnetic multiplex assay (C-F). Shown are the means  $\pm$  SEM from ten independent experiments/donors, \*P<0.05, \*\*\*P<0.001.

## Nitrated ATI show enhanced immunogenicity

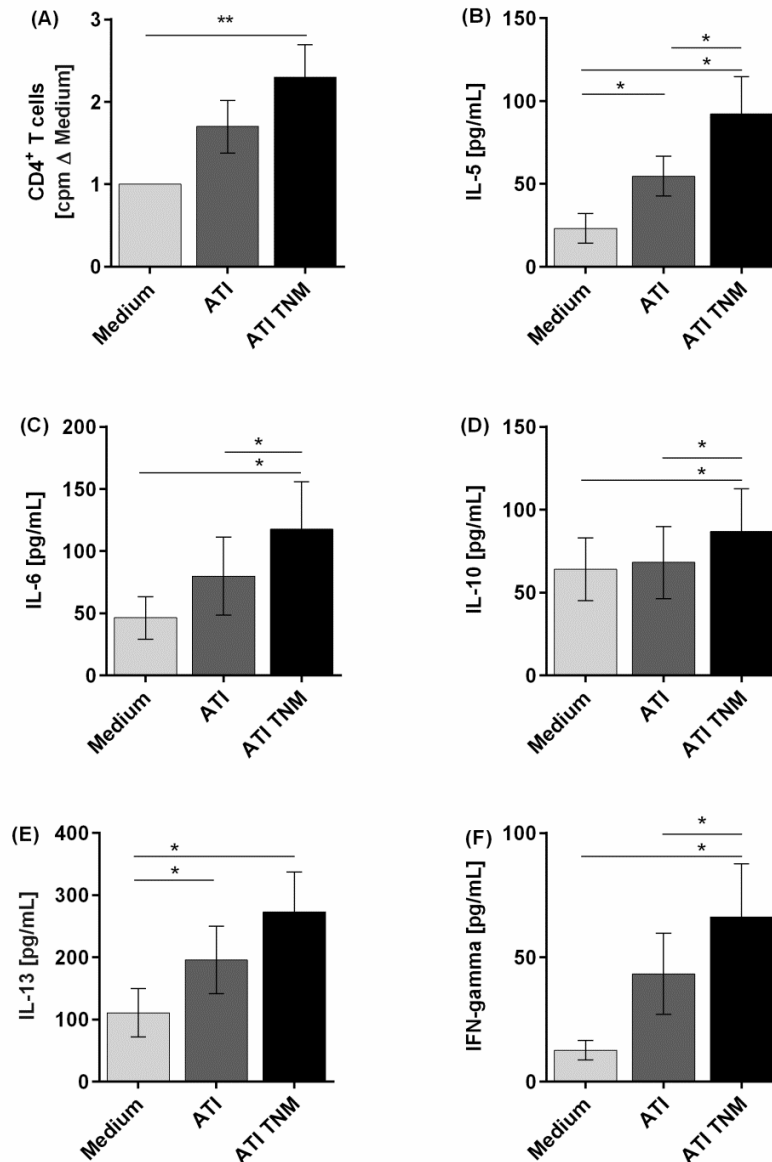


**Figure 4: Enhanced T cell proliferation as well as Th1 and Th2 cytokine production of CD4<sup>+</sup> T cells stimulated with autologous ATI TNM-pulsed mature DC.**

Immature DC were pulsed with ATI or ATI TNM [15  $\mu$ g/mL] and matured with pro-inflammatory cytokines as described in Materials and Methods. After 48 h, mature DC were washed and co-cultivated with autologous CD4<sup>+</sup> T cells for 5 days. A: T cell proliferation was measured by [<sup>3</sup>H]-thymidine incorporation, and proliferation index was calculated related to untreated cells. B-F: Supernatants (50  $\mu$ L) were collected before thymidine administration to determine the production of IL-5, IL-6, IL-10, IL-13 and IFN-gamma by multiplex assay. Results are presented as means  $\pm$  SEM from ten independent experiments/donors. In some cases, cytokine concentrations were below the detection limit so that  $n < 10$  (IL-5  $n=8$ , IL-13  $n=5$ , IFN-gamma  $n=9$ ), \* $P < 0.05$ , \*\* $P < 0.01$ .

*Supplementary Material*

**Nitration of wheat amylase trypsin inhibitors increases their innate and adaptive immunostimulatory potential *in vitro***

**Kira Ziegler<sup>1</sup>, Jan Neumann<sup>1,2</sup>, Fobang Liu<sup>1</sup>, Janine Fröhlich-Nowoisky<sup>1</sup>, Christoph Cremer<sup>2</sup>, Joachim Saloga<sup>3</sup>, Kathrin Reinmuth-Selzle<sup>1</sup>, Ulrich Pöschl<sup>1</sup>, Detlef Schuppan<sup>4</sup>, Iris Bellinghausen<sup>3#</sup>, and Kurt Lucas<sup>1#\*</sup>**

<sup>1</sup>*Multiphase Chemistry Department, Max Planck Institute for Chemistry, Mainz, Germany*

<sup>2</sup>*Institute of Molecular Biology, Mainz, Germany*

<sup>3</sup>*Department of Dermatology, University Medical Center of the Johannes Gutenberg University, Mainz, Germany*

<sup>4</sup>*Institute of Translational Immunology, University Medical Center of the Johannes Gutenberg University, Mainz, Germany*

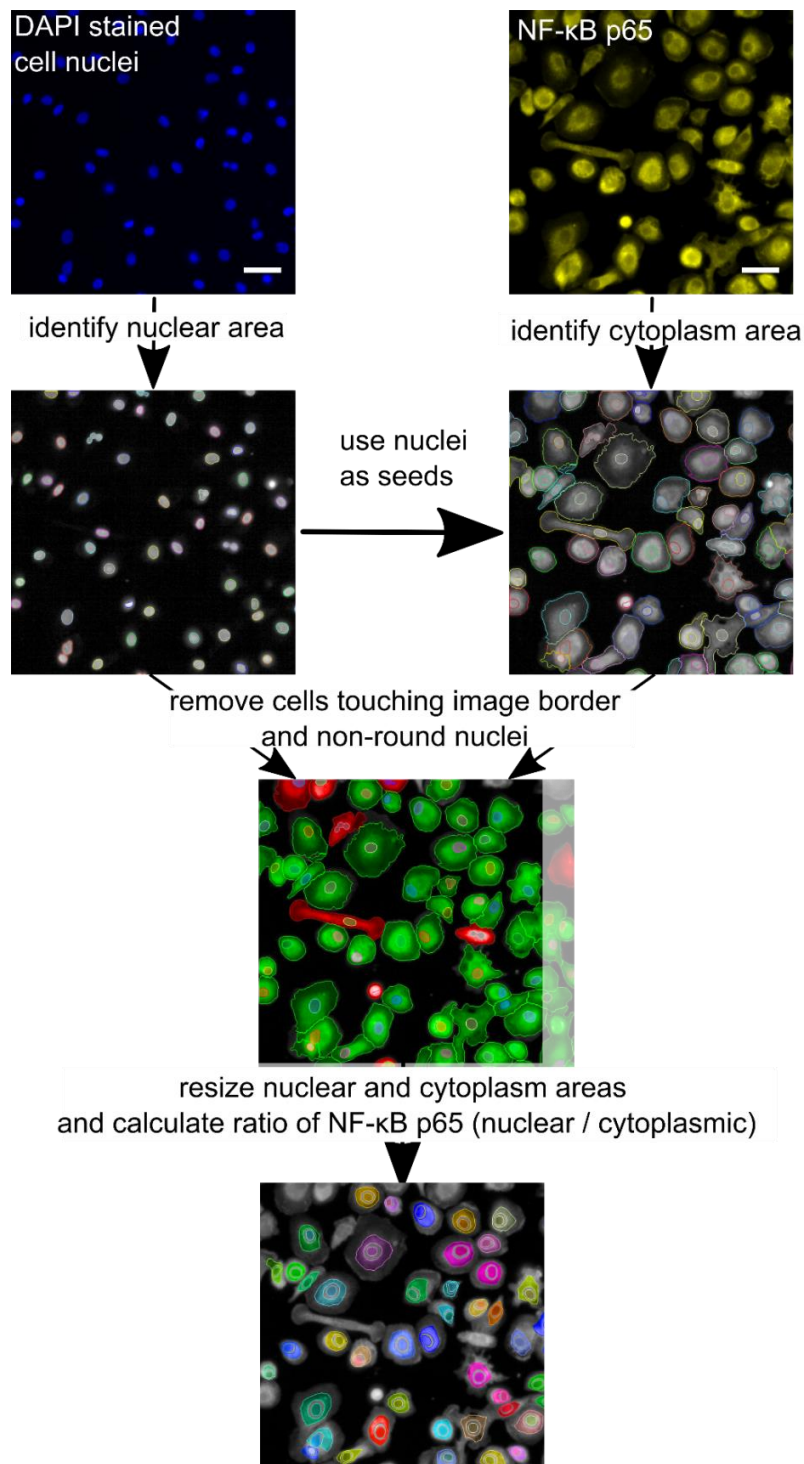
*#equally contributing senior authors*

**\* Correspondence:**

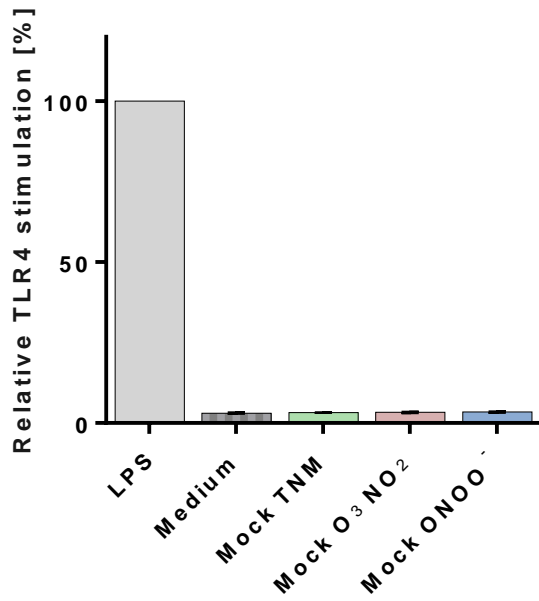
Dr. Kurt Lucas

k.lucas@mpic.de

## Nitrated ATI show enhanced immunogenicity



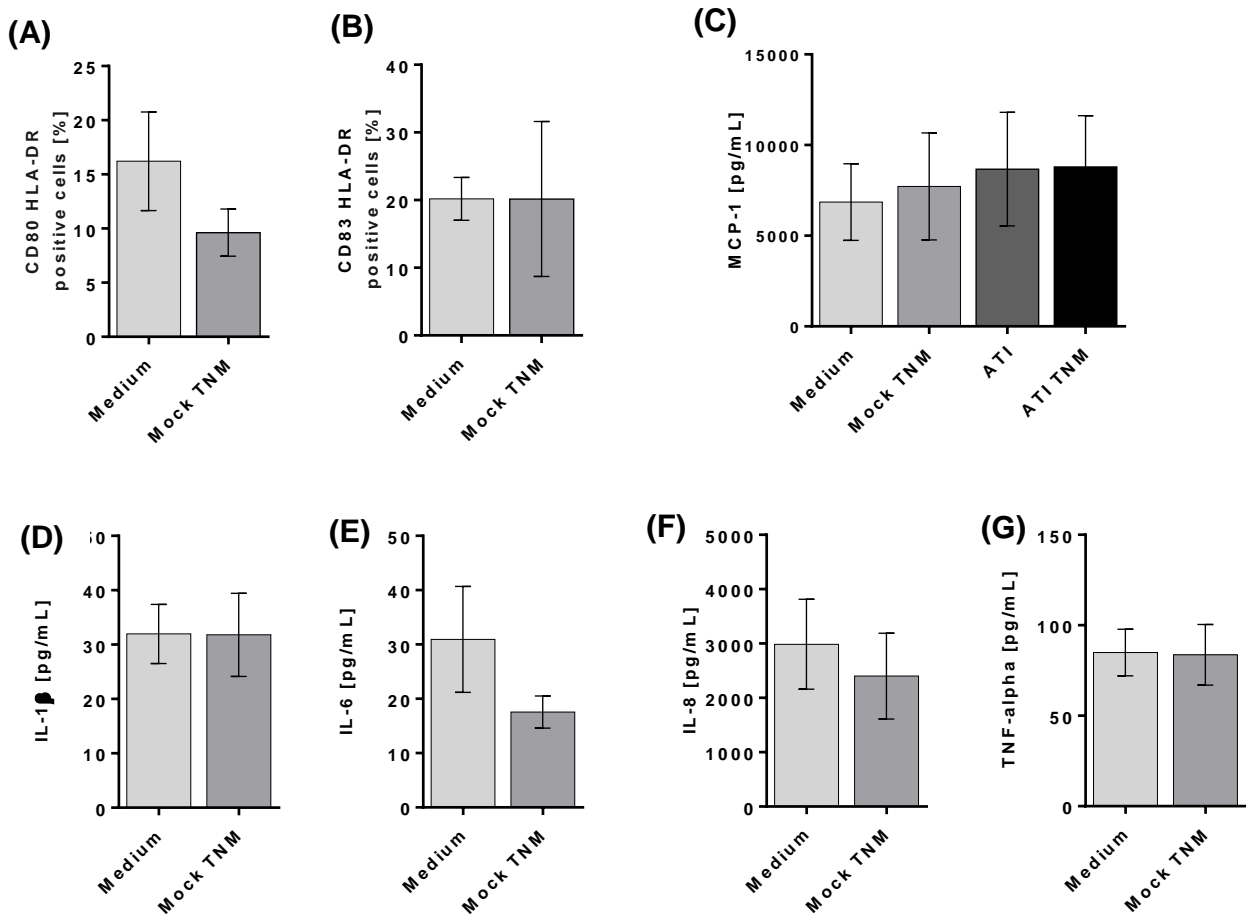
**Supplementary Figure 1. Image processing steps to quantify nuclear translocation of NF-κB.** DAPI (pseudocolor blue) and NF-κB (pseudocolor yellow) input images were taken at the Opera Phenix High-content screening system (Perkin Elmer, Waltham, Massachusetts, USA). The output image contains the nuclear and cytoplasm masks, which were used to calculate the mean NF-κB p65 intensities within the cytoplasm and the nucleus. Scale bar = 50 μm.



**Supplementary Figure 2. TLR4 stimulation by Mock nitrations on HeLa TLR4 dual reporter cells.**

HeLa TLR4 dual reporter cells were treated for 7 h with equivalent volumes of mock nitrated solution, LPS [25 ng/mL] served as positive control. The relative luciferase activity was calculated by dividing the Renilla luciferase (TLR4) signal to the Firefly luciferase (viability) signal. The resulting values were normalized to the value obtained for LPS treated cells. Shown are the means  $\pm$  SD of three independent experiments carried out in triplicates, using two independently nitrated probes.

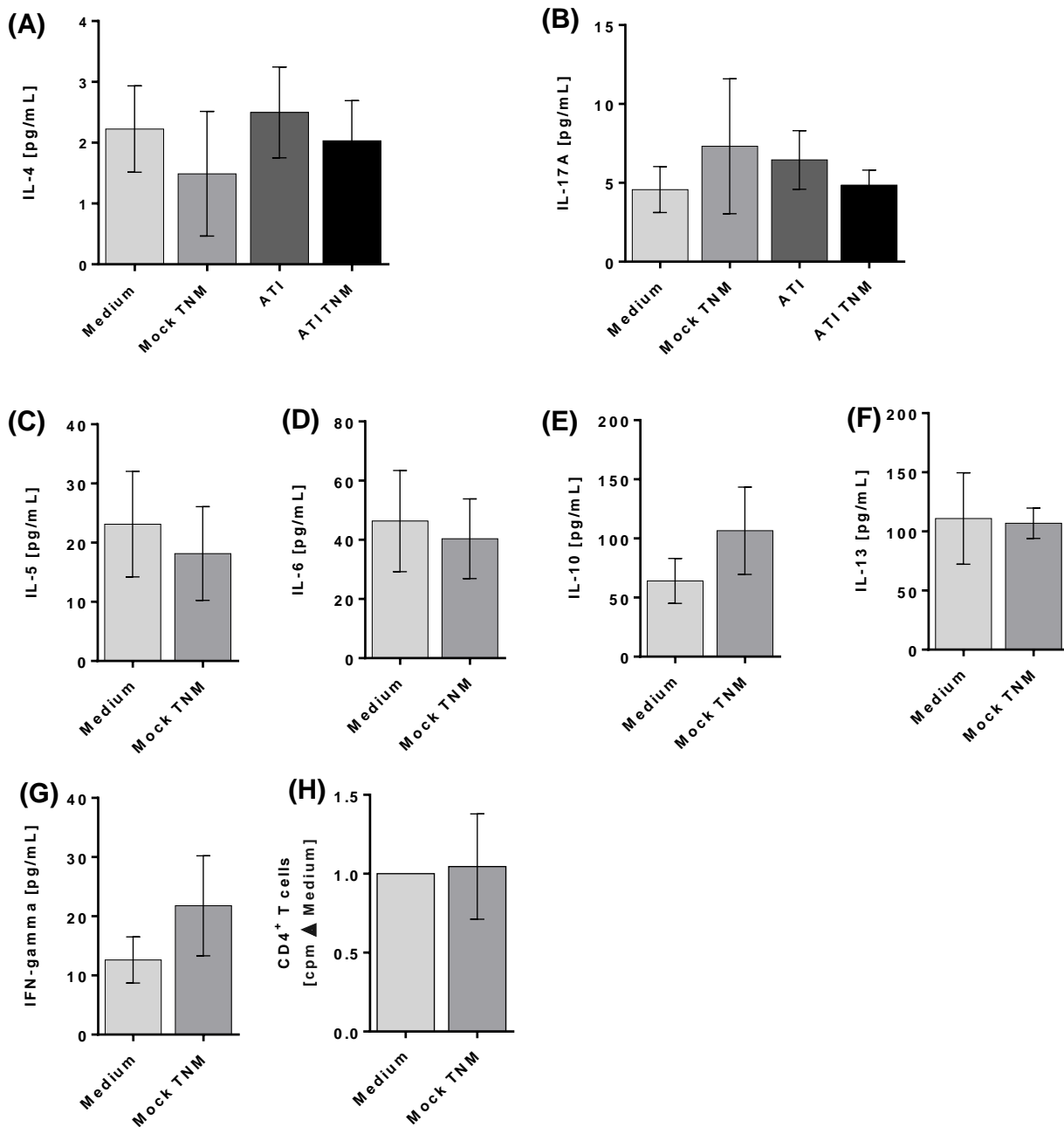
## Nitrated ATI show enhanced immunogenicity



### Supplementary Figure 3. Expression of maturation markers as well as pro-inflammatory cytokines by human immature DCs upon stimulation with Mock TNM

Immature DCs were left untreated or pulsed with ATI or ATI TNM [15  $\mu$ g/mL] or equivalent volumes of mock nitrated solution on day 6. 48 h later the cells were stained for expression of the indicated surface markers and analyzed by flow cytometry (A+B). Before, supernatants were taken for determination of MCP-1, IL-1 $\beta$ , IL-6, IL-8 and TNF-alpha by magnetic multiplex assay (C-G). Shown are the means  $\pm$  SEM from  $n \geq 6$  independent experiments/donors, \* $P < 0.05$ , \*\*\* $P < 0.001$ .

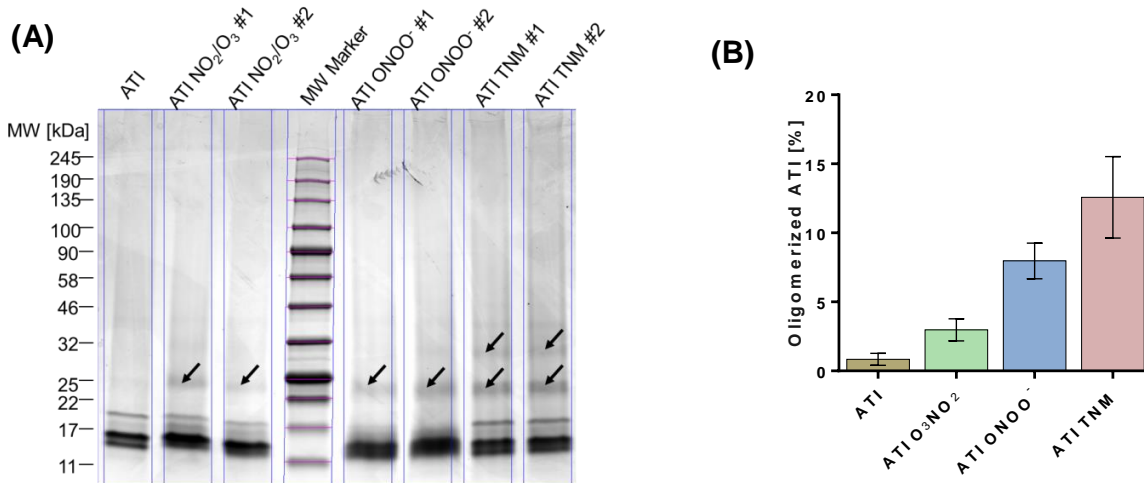
## Nitrated ATI show enhanced immunogenicity



### Supplementary Figure 4. T cell proliferation as well as Th1 and Th2 cytokine production of CD4<sup>+</sup> T cells stimulated with autologous Mock TNM pulsed mature DC.

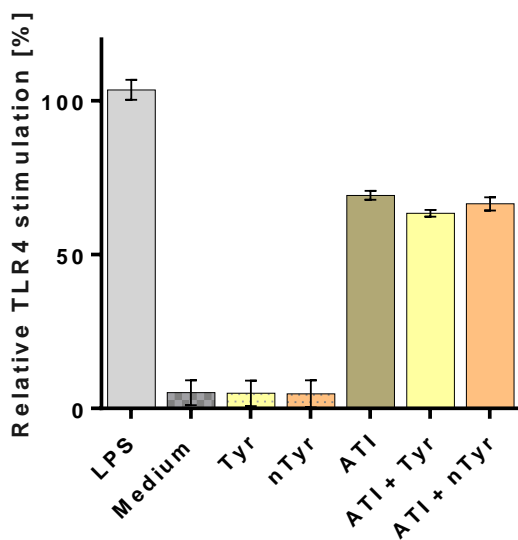
Immature DC were left untreated or pulsed with ATI or ATI TNM [15  $\mu\text{g}/\text{mL}$ ] or equivalent volumes of mock nitrated sample and matured with pro-inflammatory cytokines as described in Materials and Methods. After 48 h, mature DC were washed and co-cultivated with autologous CD4<sup>+</sup> T cells for 5 days. A-G: Supernatants (50  $\mu\text{L}$ ) were collected before thymidine administration to determine the production of IL-4, IL-17A, IL-5, IL-6, IL-10, IL-13 and IFN-gamma by multiplex assay. H: T cell proliferation was measured by [<sup>3</sup>H]-thymidine incorporation and proliferation index was calculated related to untreated cells. Results are presented as means  $\pm$  SEM from  $n \geq 6$  independent experiments/donors.

## Nitrated ATI show enhanced immunogenicity



### Supplementary Figure 5. SDS PAGE of unmodified ATI and nitrated ATI samples.

5  $\mu\text{g}$  of each ATI sample was analyzed by sodium dodecyl sulfate polyacrylamide gel electrophoresis (SDS PAGE). Molecular weight (MW) is shown in kDa. A: Oligomers can be found for all nitrated ATI samples (indicated with arrows). B: Quantification of oligomers was carried out by Image lab software (Biorad). Results are presented as means  $\pm$  SEM from  $n = 2$  independent SDS PAGE and nitration experiments.



### Supplementary Figure 6. TLR4 stimulation by ATI combined with pure nitrotyrosine

HeLa TLR4 dual reporter cells were treated for 7 h with ATI [7.5  $\mu\text{g}/\text{mL}$ ] with or without addition of tyrosine or nitrotyrosine [30  $\mu\text{M}$ ], LPS [25  $\text{ng}/\text{mL}$ ]. The relative luciferase activity was calculated by dividing the Renilla luciferase (TLR4) signal to the Firefly luciferase (viability) signal. The resulting values were normalized to the value obtained for LPS treated cells. Shown are the means  $\pm$  SD two independent experiments carried out in duplicates.